

AD _____

Award Number: DAMD17-95-C-5095

TITLE: Contributive Research in Aviation Medicine,
Bioengineering, Human Performance Analytic and Modeling
Systems

PRINCIPAL INVESTIGATOR: Thomas H. Harding, Ph.D.

CONTRACTING ORGANIZATION: UES, Incorporated
Dayton, Ohio 45432-1894

REPORT DATE: December 2002

TYPE OF REPORT: Final

PREPARED FOR: U.S. Army Medical Research and Materiel Command
Fort Detrick, Maryland 21702-5012

DISTRIBUTION STATEMENT: Approved for Public Release;
Distribution Unlimited

The views, opinions and/or findings contained in this report are those of the author(s) and should not be construed as an official Department of the Army position, policy or decision unless so designated by other documentation.

20030604 085

REPORT DOCUMENTATION PAGEForm Approved
OMB No. 074-0188

Public reporting burden for this collection of information is estimated to average 1 hour per response, including the time for reviewing instructions, searching existing data sources, gathering and maintaining the data needed, and completing and reviewing this collection of information. Send comments regarding this burden estimate or any other aspect of this collection of information, including suggestions for reducing this burden to Washington Headquarters Services, Directorate for Information Operations and Reports, 1215 Jefferson Davis Highway, Suite 1204, Arlington, VA 22202-4302, and to the Office of Management and Budget, Paperwork Reduction Project (0704-0188), Washington, DC 20503

1. AGENCY USE ONLY (Leave blank)		2. REPORT DATE December 2002	3. REPORT TYPE AND DATES COVERED Final (1 Jul 95 - 30 Nov 02)	
4. TITLE AND SUBTITLE Contributive Research in Aviation Medicine, Bioengineering, Human Performance Analytic and Modeling Systems			5. FUNDING NUMBERS DAMD17-95-C-5095	
6. AUTHOR(S) : Thomas H. Harding, Ph.D.				
7. PERFORMING ORGANIZATION NAME(S) AND ADDRESS(ES) UES, Incorporated Dayton, Ohio 45432-1894 E-MAIL: tharding@ues.com			8. PERFORMING ORGANIZATION REPORT NUMBER	
9. SPONSORING / MONITORING AGENCY NAME(S) AND ADDRESS(ES) U.S. Army Medical Research and Materiel Command Fort Detrick, Maryland 21702-5012			10. SPONSORING / MONITORING AGENCY REPORT NUMBER	
11. SUPPLEMENTARY NOTES Original contains color prints. All DTIC reproductions will be in black and white.				
12a. DISTRIBUTION / AVAILABILITY STATEMENT Approved for Public Release; Distribution Unlimited				12b. DISTRIBUTION CODE
13. ABSTRACT (Maximum 200 Words) The U.S. Army Aeromedical Research Laboratory (USAARL) at Fort Rucker, Alabama, is tasked with a broad range of applied research and engineering programs designed to answer biomedical questions dealing with aviator and soldier performance issues in an operational environment. In carrying out its mission, the Laboratory encounters unique and complex research requirements that demand maximum flexibility in its response capability. In order to achieve such flexibility, UES, Inc. was contracted to provide engineering and scientific research support in the areas of aviation medicine; biological and human factors engineering; crash modeling and research on airbags, restraint systems and head supported weight; aeromedical equipment air worthiness evaluations; research on flat panel and advanced cockpit displays, evaluations of developmental optical systems, and visual performance with military displays; and biochemical support of research in pharmaceutical intervention in army air crew. This report provides a brief summary of the extensive work performed by UES engineers and scientists during this task order contract. This report covers work completed during a seven year, five month research effort.				
14. SUBJECT TERMS: helmet mounted displays, flat panel displays, HMD, IHADSS, HIDSS, HGU56-P, helmet, crash worthiness, head supported weight, helicopter, army aviation, airbags/models, melatonin, aeromedical equipment, USAARL, crash dynamics/modeling, grayshades, HMD model, luning, HMD simulation/tester, air worthiness certification				15. NUMBER OF PAGES 302
				16. PRICE CODE
17. SECURITY CLASSIFICATION OF REPORT Unclassified	18. SECURITY CLASSIFICATION OF THIS PAGE Unclassified	19. SECURITY CLASSIFICATION OF ABSTRACT Unclassified	20. LIMITATION OF ABSTRACT Unlimited	

FOREWORD

Opinions, interpretations, conclusions and recommendations are those of the author and are not necessarily endorsed by the U.S. Army.

() Where copyrighted material is quoted, permission has been obtained to use such material.

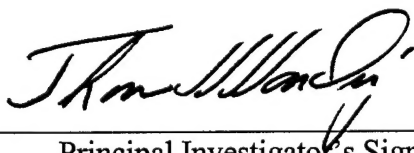
() Where material from documents designated for limited distribution is quoted, permission has been obtained to use the material.

() Citations of commercial organizations and trade names in this report do not constitute an official Department of the Army endorsement or approval of the products or services of these organizations.

() In conducting research using animals, the investigator(s) adhered to the 'Guide for the Care and Use of Laboratory Animals,' prepared by the Committee on Care and Use of Laboratory Animals of the Institute of Laboratory Animal Resources, National Research Council (NIH Publication No. 86-23, Revised 1985).

(x) For the protection of human subjects, the investigator(s) have adhered to policies of applicable Federal Law 32 CFR 219 and 45 CFR 46.

() In conducting research utilizing recombinant DNA technology, the investigator(s) adhered to current guidelines promulgated by the National Institutes of Health.



Principal Investigator's Signature
Contract DAMD1 7-95-C-5095

24 Dec 2002

Date

TABLE OF CONTENTS

	Page
FORWARD	ii
INTRODUCTION.....	1
<u>Task 1: Airworthiness Certification Evaluation Program</u>	
INTRODUCTION.....	1-1
EVALUATION OF MEDICAL EQUIPMENT	1-1
Omni-Vent Model Series D/mri Ventilator	1-2
Impact Uni-Vent Model 780 Ventilator.....	1-2
Pneupac Model PortaPAC Ventilator	1-2
Impact Model 326/326M Portable Suction System	1-3
Ivac Medsystem Model 2863B Infusion Pump	1-4
Protocol Model 106LCD Vital Signs Monitor.....	1-5
Physio-Control Model Lifepak 10-59 Defibrillator	1-6
SIMS BCI Model 3303GR Pulse Oximeter.....	1-7
Impact Model 754/754M Ventilator	1-8
Protocol Model Propaq 206EL Vital Signs Monitor	1-9
Infusion Dynamics Power Infuser Model M100B-3A Infusion Pump.....	1-10
Cardiac Science Model Powerheart Defibrillator	1-11
Lifesaving Systems Oxylator Model EM-100	1-12
Nonin Model 2500 Pulse Oximeter	1-12
Nonin Model 9500 Pulse Oximeter	1-13
Life Support for Trauma and Transport.....	1-14
UH60Q MEDEVAC Helicopter	1-15
Spacelabs Medical Model 90309 Vital Signs Monitor	1-16
Heartstream Model Forerunner.....	1-16
Allied Healthcare Model Bear 33 Ventilator	1-17
Zoll Model PD2000 Defibrillator	1-18
SUMMARY	1-18
REFERENCES.....	1-19

TASK 1 FIGURES

Figure	Page
1-1 Impact 326/326M Suction System.....	1-3
1-2 Ivac Medsystem Model 2863B Infusion Pump	1-4
1-3 Protocol Model 106LCD Vital Signs Monitor.....	1-5
1-4 Physio-Control Model Lifepak 10-59 Defibrillator	1-6
1-5 SIMS BCI Model 3303GR Pulse Oximeter.....	1-7
1-6 Impact Model 754/754M Ventilator	1-8
1-7 Protocol Model Propaq 206EL Vital Signs Monitor	1-9
1-8 Infusion Dynamics Power Infuser Model M100B-3A Infusion Pump.....	1-10
1-9 Cardiac Science Model Powerheart Defibrillator	1-11
1-10 Lifesaving Systems Oxylator Model EM-100	1-12
1-11 Nonin Model 2500 Pulse Oximeter	1-13
1-12 Nonin Model 9500 Pulse Oximeter	1-14

TABLE OF CONTENTS (Continued)

Figure	Page
1-13 Life Support for Trauma and Transport.....	1-15
1-14 Heartstream Model Forerunner.....	1-16
1-15 Allied Healthcare Model Bear 33 Ventilator	1-17

Task 2: Investigation of Visual Performance Issues for Electro-Optical Displays

	Page
INTRODUCTION.....	2-1
IHADSS SPECIFICATIONS.....	2-1
IHADSS Optical Specifications.....	2-3
IHADSS Electro-Optical Specifications.....	2-4
ANVIS SPECIFICATIONS	2-5
ANVIS Optical Specifications.....	2-6
ANVIS Electro-Optical Specifications	2-7
Visual Performance with the ANVIS	2-8
SUMMARY	2-10
REFERENCES.....	2-11

TASK 2 FIGURES

Figure	Page
2-1 Drawing of the IHADSS IHU and visor in place	2-2
2-2 Drawing of the ANVIS attached to the SPH-4 helmet	2-6
2-3 Percent ANVIS distortion as a function of angular position	2-7
2-4 Spatial contrast sensitivity as a function of spatial frequency for different night sky conditions.....	2-9
2-5 Visual flicker sensitivity viewing alphanumeric characters through the ANVIS.....	2-9

TASK 2 TABLES

Table	Page
2-1 Summary table of IHADSS performance	2-10
2-2 Summary table of ANVIS performance	2-11

Task 3: Biochemical Research and Analytical Support for USAARL Research Programs

	Page
INTRODUCTION.....	3-1
MELATONIN ADMINISTRATION TO HEALTHY FEMALES DOES NOT ALTER MENSTRUAL CHARACTERISTICS	3-1
METHODS	3-2
Subjects.....	3-2
Melatonin and Dose Administration.....	3-2
Procedures.....	3-3
BIOCHEMICAL ASSAYS	3-3

TABLE OF CONTENTS (Continued)

	Page
LH and FSH Assays.....	3-3
Pregnancy Testing.....	3-3
Melatonin Assay	3-4
DATA ANALYSIS	3-4
RESULTS	3-4
Melatonin metabolite concentrations.....	3-4
Awareness of symptoms following melatonin.....	3-5
Length of menses and menstrual cycle after melatonin.....	3-5
Use of IMx technology with urine samples	3-8
Melatonin effects on LH and FSH	3-9
THE CORRELATION BETWEEN PLASMA AND SALIVARY MELATONIN, AND URINARY 6-SULPHATOXYMELATONIN EXCRETION IN THE HUMAN	3-13
DISCUSSION	3-15
REFERENCES	3-18

TASK 3 FIGURES

Figure	Page
3-1 Melatonin metabolite level in urine. Mean aMT6s concentration for each of the seven daily samples during the 6 in-house post-administration days for one member of the placebo group and one member of the melatonin group. Error bars indicate f the standard error of the mean	3-5
3-2 Change in menstrual cycle length based upon first day of menses for all members of both the melatonin and placebo groups between cycle 1 and 2 and between cycle 2 and 3. The dotted lines indicate 3 days which we have selected to indicate physiological significance.....	3-7
3-3 Change in menstrual cycle length based upon timing of LH peak for members of both the melatonin and placebo groups between cycles 1-2 and 2-3. The dotted lines indicate 13 days which we have selected to indicate physiological significance	3-8
3-4 Change in length of menses for all members of both the melatonin and placebo groups between cycles 1 and 2 and between cycles 2 and 3.....	3-8
3-5 Daily LH and FSH levels over three cycles for volunteer number 4. LH and FSH levels for each day of the three cycles of participation for one of the placebo volunteers	3-10
3-6 Daily LH and FSH levels over three cycles for volunteer number 11. LH and FSH levels for each day of the three cycles of participation for the volunteer (melatonin group) demonstrating the strongest LH and FSH peaks.....	3-10
3-7 Mean LH levels during the seven day in-house stay for both melatonin and placebo groups	3-11
3-8 Mean FSH levels during the seven day in-house stay for both melatonin and placebo groups.....	3-11
3-9 Mean peak LH levels for three cycles of participation. Mean peak LH levels based upon first void urine samples for both the melatonin and placebo groups for each of the three cycles as well as the mean peak value based upon multiple daily samples during the in-house phase of cycle 2.....	3-12

TABLE OF CONTENTS (Continued)

TASK 3 TABLES

Table	Page
3-1 Menstrual cycle characteristics	3-6
3-2 LH and FSH peak values	3-13
3-3 Cycle day of LH peak	3-14

Task 4: Investigation of Visual Performance Issues for Flat Panel Technology Displays

	Page
INTRODUCTION	4-1
PHYSICAL EVALUATION OF DEVELOPMENTAL DISPLAY SYSTEMS	4-1
The Microvision Scanning Laser HMD	4-2
The Microvision System	4-3
Functional operation	4-4
Optical-path description and energy efficiencies	4-6
Optical and physical measurements	4-8
Pinch Correction	4-18
Other Measures	4-21
The Kaiser Electronics CRT HIDSS	4-22
Optical characteristics	4-23
Miniature CRT image source	4-24
HMD System	4-24
Evaluation of HIDSS Developmental Sources	4-32
Introduction	4-32
Image Sources	4-33
Honeywell, Inc. electroluminescent (EL) display tests	4-34
Kaiser Electronics, Inc. LCD tests	4-41
Comparative test summary and discussion	4-47
The Honeywell High Pass HMD	4-48
System Tests	4-55
THE DEVELOPMENT OF HMD EVALUATION SYSTEMS	4-58
The Mobile IHADSS Tester	4-58
Laboratory HMD Tester	4-61
FIGURES OF MERIT	4-64
What FOMs measure	4-66
Examples	4-70
The MTF	4-71
The Observer's CSF	4-72
Combining the MTF and CSF into an FOM to quantify conveyable Information	4-72
The effect of visual tasks on spatial resolution requirements	4-75
The effect of technology on spatial resolution FOMs	4-76
FOMs for CRTs and FPDs	4-77
Differences of FPD technology	4-77
Which CRT FOMs apply to FPDs?	4-78
Differences in image addressing and updating in CRTs and FPDs	4-83

TABLE OF CONTENTS (Continued)

	Page
Differences in image gray scales and contrast in CRTs and FPDs.....	4-83
New FOMs needed for dynamic imagery on FPDs	4-85
Gray scale and spatial resolution of dynamic imagery on FPDs	4-86
Considerations in developing the new FOMs.....	4-87
CONCLUSIONS	4-88
VISUAL EVALUATION OF LEGIBILITY WITH LCD FLAT PANEL DISPLAYS	4-90
Introduction.....	4-90
Methods.....	4-90
Results.....	4-96
Discussion.....	4-100
VISUAL EVALUATIONS OF PERFORMANCE METRICS AS A FUNCTION OF HELMET MOUNTED DISPLAY FOV CONFIGURATION	4-102
The Effect Of FOV On Target Acquisition	4-106
Methods.....	4-106
Results and Discussion	4-115
Conclusion	4-122
Visual Search In HMDs With Partial Overlapped Binocular FOV	4-122
Visual search experiment.....	4-123
Methods.....	4-123
Results.....	4-131
Discussion.....	4-135
AN OPERATIONAL GRAYSHADES AND SEE-THROUGH COLOR MODEL	4-137
Model Implementation.....	4-138
The Basic Model	4-139
Grayshades	4-140
Skylight	4-141
Image and symbology simulation	4-142
Conclusion	4-145
REFERENCES	4-147

Task 4 Figures

Figure	Page
4-1 An artist's conception depicting the ability of scanning laser HMDs to present symbology of sufficient luminance to be seen against daytime backgrounds	4-3
4-2 Microvision prototype scanning laser HMD.....	4-4
4-3 Functional block diagram of the scanning laser HMD system	4-6
4-4 Photographs of optical set-up showing relationship between the HMD optics and camera lens. In the top photograph, note the image of the exit pupil centered on an artificial 3mm iris. For all of the data shown in this report, a 5mm iris was used. The device holding the camera allowed viewing of any FOV position while still maintaining correct alignment	4-9
4-5 Vertical and horizontal MTFs measured previously (Harding, et al., 2001). Note the difference between the two curves at the Nyquist frequency (horizontal = 0.05 and vertical = 0.20)	4-10

TABLE OF CONTENTS (Continued)

Figure		Page
4-6	Horizontal and vertical lines captured by a grayscale camera. These lines reflect the best imagery we obtained from the system.....	4-11
4-7	MTFs measured from the left side of the HMD. Like before, the vertical MTF shows about 0.20 modulation at the Nyquist frequency. The horizontal MTF showed modest improvement with about a 0.12 modulation at the Nyquist.....	4-11
4-8	Peaks and troughs used to measure the CTF contrast.....	4-12
4-9	Horizontal and vertical CTFs measured for grill patterns in the left side's central area. Note the sharp fall-off at the Nyquist frequency.....	4-13
4-10	Photographically enhanced images of 1off-1on grill patterns in the horizontal (A) and vertical (B) orientations. Of note is the pixel structure observed in B. Here a strong horizontal element is noticed. This element makes recognition of orientation difficult. Profile amplitudes are not necessarily to scale	4-14
4-11	CTFs measured using the standard deviation technique for grill patterns presented to the left side. Here the noise estimates are plotted as a function of grill spatial frequency. As a side note, the noise frequency spectra is highly correlated with the pixel spacing and is thus composed of higher spatial frequencies (near the Nyquist frequency). Since the Nyquist frequency is well within human spatial frequency bandwidth, we feel justified in using our noise estimates in this fashion.....	4-15
4-12	CTF signal-to-noise ratios based upon the data shown in Figure 4-11. Microvision engineers provided us photographic images of grill patterns used in their data analysis. Using their images, we calculated the signal-to-noise ratios for the highest two spatial frequencies. With the exception of the aberrant point, their data fell on top of our data points	4-16
4-13	Photographic images of 5 by 5 character sets presented normally (bottom) and 90 degrees rotated (top). Note the slight misalignment of character elements.....	4-17
4-14	Graphs of scanned lines representing dual scans with no pinch correction (A) and dual scans with pinch correction (B). Note the difference between distance A and B in (A), whereas with pinch correction (B), the distances are the same. Original graphs supplied by Microvision, Inc	4-18
4-15	Line numbering and pattern for evaluating line pairs. (A) Graph of dual scanning with pinch correction. The lines are numbered 0, 1, 2, 3 depicting the four line conditions. (B) Horizontal grill pattern comprised of 2 lines followed by five lines off and the pattern repeated. Original graph (A) supplied by Microvision, Inc	4-19
4-16	Photographic images of line pairs near the left edge of the left side display. (A). Non-pinch corrected condition coupled with a torqued scanner housing (see text for explanation). (B). Typical non-pinch corrected pattern consisting of alternation thick and thin line pairs. (C). Pinch-corrected condition with proper calibration and alignment.....	4-19
4-17	Photographic images of 5 by 5 text characters. (A) Non-pinch corrected text imagery. (B) Pinch corrected text imagery	4-20
4-18	MTFs measured from the left side of the HMD. The vertical MTF as a modulation of about 0.23 modulation at the Nyquist frequency (approximately 15.6 cycles/degree) and the horizontal MTF has a modulation of about 0.17 at the same frequency. These MTFs show slight improvements over the MTFs measured without pinch correction (see Figure 4-7).....	4-21
4-19	The Kaiser Electronics HIDSS	4-23

TABLE OF CONTENTS (Continued)

Figure	Page
4-20 ARU mounting configurations.....	4-23
4-21 CRT luminance response curve	4-24
4-22 Luminance profiles for the horizontal (A) and vertical (B) FOV	4-25
4-23 Monocular FOVs with binocular overlap region	4-26
4-24 Day time and nighttime contrast ratios for the HIDSS HMD.....	4-27
4-25 Luminance uniformity	4-27
4-26 Horizontal and vertical MTFs.....	4-29
4-27 See-through spectral transmittance as a function of (a) horizontal and (b) vertical rotation	4-30
4-28 Honeywell, Inc., miniature 1280 X 1024 EL image source.....	4-33
4-29 Kaiser Electronics, Inc., miniature 1280X1024 LCD image source.....	4-34
4-30 Photomicrograph of pixel structure. Pixel illumination is artificial and provided from above. Please note the calibration scale.....	4-35
4-31 Enlarged photomicrograph subsection with light enhancement. Two pixels are highlighted (pixels A and B). Using computer mensuration, we measured pixel pitch to be 24.1 pm, which also equates to the pixel size	4-35
4-32 Photomicrographs of pixel defects in the Honeywell EL display.....	4-36
4-33 Off-axis normalized luminance.....	4-37
4-34 The luminance response curve (Gamma) measured for the Honeywell EL panel (#42)	4-38
4-35 Contrast as a function of spatial frequency for the grill pattern. The 25 X lens actually shows less contrast which is contrary to expectation	4-39
4-36 MTF curves measured for the vertical and horizontal line-spread curves.....	4-40
4-37 Spectral distribution of the EL display	4-40
4-38 Photomicrograph of 12:m LCD showing a pixel patch of about 8 by 6 pixels. Illumination is artificial and is from directly above.....	4-41
4-39 Enlarged sub-section of Figure 4-38. Note the active pixel area is the white rectangle. Illumination is artificial, and the square area, designated as a single pixel, may or may not be co-located with the actual pixel area, although the square is the size of the actual pixel area	4-42
4-40 Digitally enhanced image of back-lit on-pixels. The real image was too dim to illustrate due to the high magnification. The color of the pixels was altered as a result of the enhancement	4-42
4-41 Off-axis luminance as a function of angular orientation. Luminance is reportedly higher here owing to the numerical aperture of the standard lens and measurement distance used to collect these data. The lens used here was selected in order to collect data with a smaller angle of regard	4-44
4-42 Luminance response curve for the Kaiser Electronics LCD.....	4-45
4-43 Vertical CTF for the Kaiser LCD	4-46
4-44 The Vertical MTF for the Kaiser 12µm LCD.....	4-46
4-45 The hp-HMD mounted to a HGU-56p helmet in a bi-ocular arrangement. Please note that the HMD was not adjusted properly for this subject. On the right is shown a photograph of the hp-HMD source, a miniature electro-luminescent flat panel display	4-48

TABLE OF CONTENTS (Continued)

Figure	Page
4-46 The hp-HMD mounded to a bar used for testing the device. Please note that the optic is composed of fused optical lenses. The lenses were glued to each other in order to make a single optical device.....	4-49
4-47 Photomicrograph of the EL sources pixel structure. The bright square outlines a single pixel	4-49
4-48 Photomicrograph of a small patch of pixels with every other row of pixels turned on. At the Nyquist frequency, it can clearly be seen that there is good contrast. This photomicrograph has been enhanced in Adobe Photoshop by adjusting the contrast curve to brighten the on-pixels, (a method similar to histogram equalization where the luminance range is stretched). The original photo would be difficult to discern any contrast when reproduced	4-50
4-49 Luminance response function showing relative luminance over better than a 10,000 to 1 range.....	4-52
4-50 Michaelson contrast at six different spatial frequencies representing 32 on – 32 off, 16 on - 16 off, 8 on - 8 off, 4 on - 4 off, 2 on - 2 off, and 1 on - 1 off	4-53
4-51 Line spread function measured for the single vertical column	4-53
4-52 Horizontal MTF calculated from the line spread shown in Figure 4-50.....	4-54
4-53 Spectral distribution of the display source	4-54
4-54 Measurement of field curvature for the four horizontal trans-sections and the one vertical trans-section	4-57
4-55 Computer rendition of the IHADSS test image	4-58
4-56 Photograph showing relationship between the two cameras and the IHADSS HMD. Please note that in this arrangement, the image is evaluated after passing through the combiner lens (as opposed to evaluating the test image following its reflection off of the combiner lens).....	4-59
4-57 IHADSS mobile tester	4-60
4-58 Battery and charging compartment mounted underneath the computer and switching platform.....	4-60
4-59 UES designed and developed laboratory HMD tester. The test system allows positioning of an optical test device anywhere within the FOV of an HMD. Here the photograph shows a high resolution camera system mounted to an XYZ linear positioning stage. The stage in turn is mounted to a curved rail which allows the system to rotate laterally within the FOV. The curved rail is mounted to a swing that allows vertical positioning within the FOV. The position of the camera is monitored by digital readouts of lateral and vertical degrees (measured to the nearest 1/100 of a degree).....	4-61
4-60 In the this photograph, one side of the Microvision phase II HMD is mounted and the formed exit pupil is formed in the center of a 3mm camera iris. The exit pupil is seen as a focused light-green circular spot of light.....	4-62
4-61 The arrows show the position of the two precision potentiometers.....	4-62
4-62 Control electronics for the laboratory HMD tester. The main parts include 4 analog operational amplifiers and gain control potentiometers along with a voltage zeroing circuit	4-63
4-63 Mechanical device for positioning the camera lens' iris	4-63
4-64 Typical modulation transfer function curve.....	4-71

TABLE OF CONTENTS (Continued)

Figure	Page
4-65 A representative measured modulation transfer function for a CRT	4-72
4-66 The contrast sensitivity function.....	4-73
4-67 The modulation transfer function area.....	4-74
4-68 A rectangular spatial matrix of triad color (RGB) picture elements (pixels)	4-78
4-69 MTF curves for P43 phosphor (Beasley et al., 1995).....	4-81
4-70 MTF curves for P1 phosphor (Beasley et al., 1995).....	4-82
4-71 Temperature response of a liquid crystal display (Rash and Verona, 1987).....	4-82
4-72 Alphabetical letters created for the psychophysical experiment. Alphabet on left is composed of 5X5 pixels and alphabet on right is composed of 7X7 pixels	4-91
4-73 Luminance response as a function of computer gray level for the five flat panel displays.....	4-93
4-74 Target and background luminances for five flat panel displays	4-94
4-75 Nominal geometry of the 5X5 letter E. The distance G equals the pixel pitch and the distance S equals five times the pixel pitch. For the purpose of this illustration, the fill factor is 1; i.e., the illumination of the subpixels occupy all of the allotted space.....	4-94
4-76 Equivalent Snellen acuity line for the three stimulus conditions.....	4-95
4-77 Subject acuity as a function of viewing distance	4-96
4-78 Average error rate for each of the stimulus conditions. Data are averaged across displays and across subjects.....	4-97
4-79 Overall psychophysical performance on each of the color displays. Each data point represents the average performance scored across all three viewing distances and all five subjects.....	4-99
4-80 Overall psychophysical performance at the furthest viewing distance for each of the displays. The data were averaged across all five subjects.....	4-99
4-81 Predicted MTF for the 5 flat panel displays.....	4-101
4-82 In normal unaided vision the two monocular fields are partially overlapped producing a divergent FOV consisting of three regions, the central binocular overlap region and two lateral monocular regions.....	4-103
4-83 Pilot's view of visual world in an HMD with a partially binocular overlapped FOV. Each eye sees a circular monocular field against a black background. The real world image to each eye matches in the binocular region, but in the monocular regions, the real world image of each eye is matched to the black background of the other eye leading to visual effects such as binocular combination and binocular rivalry. Luning, the temporally varying subjective darkening near binocular overlap borders, can result. Also, fragmentation of the FOV into three phenomenally distinct regions and reduced target visibility in monocular regions can occur.....	4-104
4-84 Perspective and schematic illustrations of the optical table configuration consisting of the monitor, eight mirrors, focusing lenses, and binoculars. Top image of monitor is directed to left eye, and bottom image is directed to right eye....	4-108

TABLE OF CONTENTS (Continued)

Figure	Page
4-85	Examples of the total FOV with targets and clutter. The top shows the total FOV with nine alphanumeric symbols, six fusion locks (crosses), and random clutter (ellipses). Target is the "6" in the left bottom position. The horizontal extent is 32.8 degrees of visual angle, and the vertical extent is 10 degrees of visual angle. In the PO FOV configurations, this is presented to the subject via two monocular fields, each 23.4 degrees of visual angle in horizontal extent 4-110
4-86	Examples of reduced FOV seen in FO FOVs. The top shows the FO FOV, where both monocular fields present the same center region (23.4 degrees of visual angle in the horizontal extent) to each eye. The bottom shows how much the binocular portion of the FOV is shrunk in the PO FOVs. Figure 4-85 shows how the FOV is enlarged by PO 4-111
4-87	The two monocular fields on the monitor are each optically directed to an ocular of the binoculars for viewing by the subject 4-112
4-88	Mean response time to acquire target (FOV x Block) 4-116
4-89	Mean response time to acquire target (FOV x Position)..... 4-117
4-90	Mean number of misses before target acquisition (FOV x Position)..... 4-120
4-91	Mean percent of first scores (FOV x Position) 4-121
4-92	FOV dimensions. Four target positions in degrees of visual angle from the center are shown on the right and four symmetrical positions are shown on the left. The top shows a partial overlap FOV and the bottom shows a full overlap FOV 4-125
4-93	Example of a total FOV with blurred symbols. Target is the numeral "4" indicated by an arrow 4-126
4-94	The total FOV divided into the three regions seen in the partial overlap displays, the central binocular overlap region and the two flanking monocular regions. The vertical lines were not present in the displays. The left monocular field consists of the left and central regions, and the right monocular field consists of the central and right regions. In the divergent FOVs, the left eye saw the left monocular field, and the right eye saw the right monocular field. In the convergent FOVs, the left eye instead saw the right monocular field, and the right eye saw the left monocular field..... 4-126
4-95	A full overlap FOV where both monocular fields consist of the same central portion of the total FOV. The symbols are sharp. Target is the numeral "2" indicated by the arrow 4-127
4-96	Mean RT to acquire target (FOV x Block). P is the practice block..... 4-133
4-97	Mean RT to acquire target (FOV x Position)..... 4-133
4-98	Mean number of errors per target acquired (FOV x Position)..... 4-134
4-99	Mean percent errorless target acquisition (FOV x Position) 4-134
4-100	Main index page for the model. From here, the user can quickly navigate the model and select variables 4-139
4-101	Basic scenario for outside the cockpit imagery 4-140
4-102	Basic scenario for inside the cockpit imagery 4-140
4-103	Actual model results for the sample conditions mentioned above 4-142
4-104	Transmissivity curves for the AH-64 windscreen, the Comanche tinted visor, the Microvision HMD, and the combined transmissivity curve 4-143

TABLE OF CONTENTS (Continued)

Figure	Page
4-105 Spectral scale factors (left), original image (middle) and filtered image (left). Filtering was performed using the hardware transmissivity curve shown in Figure 4-104. The scale factors used to filter the image were Red = 1.57, Green = 0.91, and Blue = 0.52	4-146
4-106 Original (left), filtered image (center) and composite image (right). Filtering was performed using an IHADSS HMD, an AH-64 Apache windscreen and a Comanche clear visor. Note the greenish tint and lack of red in the filtered image. The scale factors used to filter the image were Red = 0.70, Green = 1.37, and Blue = 0.93. The composite image represents HMD symbology against a see-through background. The composite resulted from 200 fL symbology against 5000fL peak ambient luminance. Under these conditions, the predicted HMD gray level is – (minus) 3.836. Please compare with Figure 4-107	4-146
4-107 Same as in Figure 4-106, except that the Comanche tinted visor was used instead of the clear visor. The symbology is now discernable. Using the tinted visor, the HMD grayshades increased from –minus 3.836 to positive 1.187. Note the difference between the filtered image here and the filtered image in Figure 4-106. The only difference is the HMD. The scale factors used to filter the image were Red = 0.73, Green = 1.11, and Blue = 1.16	4-146

Task 4 Tables

Table	Page
4-1 Summary of requirements for AIHS scanning laser HMD.....	4-4
4-2 Evaluation Summary.....	4-21
4-3 Summary findings from the HIDSS Evaluation	4-31
4-4 Additional findings from the HIDSS Evaluation.....	4-32
4-5 On-axis luminance of each of the 25 illuminated squares	4-36
4-6 Lateral contrast.....	4-37
4-7 Vertical contrast	4-37
4-8 On-axis luminance (fL) for each of the windows	4-43
4-9 Lateral contrast ratios.....	4-44
4-10 Vertical Contrast ratios	4-45
4-11 Deviations from the average luminance as a percent.....	4-51
4-12 Deviations from the average contrast	4-51
4-13 Common CRT FOMs classified into four categories	4-65
4-14 Common FPD FOMs classified into four categories	4-65
4-15 Most important variables affecting CRT image quality (adapted from Curtin and Infante, 1996)	4-79
4-16 Listing of the five active matrix displays and their particulars.....	4-90
4-17 Viewing distances for the five flat panel displays (given in centimeters)	4-92
4-18 Counter-balanced design for subject-display-day interaction.....	4-92
4-19 Summary of target and background luminances used in the acuity study. Target and background luminances are given in cd/m^2	4-93
4-20 Visual angle of distances S and G in Figure 4 measured in degrees	4-95
4-21 Measured fill factors for each of the flat panel displays.....	4-96

TABLE OF CONTENTS (Continued)

Table	Page
4-22 Mean response times in seconds, collapsed over blocks, and planned comparisons	4-118
4-23 Mean percentage increase in response time, collapsed over blocks	4-118
4-24 Mean log of response times (in seconds), collapsed over blocks, and planned comparisons	4-119
4-25 Mean number of misses (out of a maximum of S), collapsed over blocks	4-120
4-26 Mean percent of first scores, collapsed over blocks	4-120
4-27 RT ANOVAs	4-132
4-28 Number or Errors ANOVAs	4-134
4-29 Percent errorless target acquisition ANOVAs	4-135
4-30 Hardware variables included in current model	4-138
4-31 Skylight conditions with default luminance and color temperature specifications.....	4-142

Task 5: Mathematical Modeling and Computer Simulation Of Human Bio-Dynamics And Crash Environments

	Page
INTRODUCTION.....	5-1
MASS AND LOCATION CRITERIA OF HEAD-SUPPORTED DEVICES USING ARTICULATED TOTAL BODY SIMULATIONS	5-2
Introduction.....	5-2
Biodynamic Simulations.....	5-2
Occupant model	5-2
Energy-attenuation seat.....	5-2
Restraint system	5-3
Impact Conditions.....	5-3
Head-supported mass	5-5
Center of mass position.....	5-5
Discussion	5-5
HSD mass and CM position.....	5-5
Effects of lateral CM position.....	5-6
Effects of seat-stroking distance	5-6
EFFECTS OF SEAT STROKE DISTANCE ON THE ALLOWABLE MASS OF HEAD SUPPORTED DEVICES	5-7
Introduction.....	5-7
Biodynamic simulations.....	5-7
Impact conditions.....	5-7
Helmet mass.....	5-7
CM location	5-8
Seat stroke.....	5-8
Restraint system	5-8
Complete motion.....	5-8
Inertial loading.....	5-8
Injury assessment.....	5-8
Response parameters.....	5-8

TABLE OF CONTENTS (Continued)

	Page
Results and discussions.....	5-9
Conclusions.....	5-12
INFLUENCE OF AIRBAGS ON SELECTION OF MASS AND CM	
PLACEMENTS OF HEAD SUPPORTED DEVICES.....	5-13
Introduction.....	5-13
Objectives	5-13
Test matrix	5-14
Impact conditions.....	5-14
Helmet mass.....	5-14
CM location	5-14
Seat stroke.....	5-14
Airbag position.....	5-14
Restraint system	5-14
Complete motion.....	5-14
Inertial loading.....	5-14
Discussions	5-15
Influence of impact condition	5-15
CM dependency	5-15
Influence of airbags.....	5-15
Conclusions.....	5-16
EFFECTS OF OPTICAL RELAY TUBE (ORT) DISPLAY MODIFICATIONS ON	
THE RISK OF FACIAL AND NECK INJURY	5-16
Introduction.....	5-16
Biodynamic simulations.....	5-17
Modeling of the ORT displays.....	5-17
Head-supported mass	5-21
Impact conditions.....	5-21
Energy-attenuating seat.....	5-22
Restraint system	5-23
Response parameters.....	5-23
Injury assessment	5-24
Facial injury reference values	5-24
Neck injury reference values	5-24
Assessment methodology.....	5-26
Conclusions.....	5-26
REFERENCES.....	5-28

Task 5 Figures

Figure	Page
5-1 Acceleration pulse and subject orientation modeled in impact condition 1	5-3
5-2 Acceleration pulse and subject orientation modeled in impact condition 2	5-4
5-3 Acceleration pulse and subject orientation modeled in impact condition 3	5-4
5-4 Acceleration pulse and subject orientation modeled in impact condition 4	5-4
5-5 Acceleration pulse and subject orientation modeled in impact condition 5	5-4
5-6 Axial tensile neck force	5-6

TABLE OF CONTENTS (Continued)

Figure	Page
5-7 Fore/Aft neck shear force.....	5-6
5-8 Time history for neck compression-tension force	5-9
5-9 Neck load duration plots for 2.5 cm and 25 cm stroke distance	5-10
5-10 Dimensions of plane used to model standard monocular ORT display. (Figure is not to scale.).....	5-18
5-11 Dimensions of plane used to model proposed flat-panel ORT display. (Figure is not to scale.).....	5-19
5-12 Position of design eye-point relative to the center of the ellipsoid used to model the occupant's head. Left: front view, right: side view. (Figures are not to scale).....	5-19
5-13 Diagram of standard monocular ORT display relative to the design eye-point of the co- pilot/gunner. (Figures are not to scale)	5-20
5-14 Diagram of flat-panel display relative to the design eye-point of the co-pilot/ gunner. (Figures are not to scale).....	5-20
5-15 Schematics of the acceleration profiles simulated	5-22
5-16 Subject orientation	5-23
5-17 Injury assessment reference values for neck fore/aft shear force	5-25
5-18 Injury assessment reference values for neck axial tension	5-25
5-19 Injury assessment reference values for neck axial compression.....	5-26

Task 5 Tables

Table	Page
5-1 Summary of response parameters which failed the injury test for the two stroking distance and the four helmet masses	5-11
5-2 Comparison of HSD mass limits for the 2.5 cm and 25 cm seat stroking distances for each impact condition.....	5-12
5-3 Impact Condition Summary	5-21
5-4 Injury assessment reference values for neck flexion and extension moment	5-25

Task 6: Biomedical Engineering Research Support for Head Supported Device Mass Properties Design and Operational Criteria

	Page
INTRODUCTION.....	6-1
INSTRUMENTATION DEVELOPED AND USED	6-2
Simulated HSD platform.....	6-2
Accelerometers/bite bar	6-2
Electromyographic equipment	6-4
Response time and tracking	6-4
PROCEDURES	6-5
RESULTS	6-6
DISCUSSION OF RESULTS	6-9
REFERENCES.....	6-10

TABLE OF CONTENTS (Continued)

Task 6 Figures

Figure	Page
6-1 Side view of the helmet simulator	6-2
6-2 Picture of bite bar assembly	6-3
6-3 Location of bite bar accelerometers with respect to EAM and AOC. EAM represents origin of the anatomical coordinate reference system XZ. (is a pitch angle relating the bite bar coordinate system X'Z' to XZ. Filled circles	6-3
6-4 Picture of electrode application	6-4
6-5 Typical vibration responses over time	6-6
6-6 Head pitch acceleration (left panel) and helmet weight moment (right panel) are displayed against helmet mass and helmet CM (relative to head AOC). The unloaded (no helmet) case is also shown as the zero mass helmet.....	6-7
6-7 Pitch acceleration magnitude versus helmet mass. Averaged among 12 subjects for each helmet CM position relative to head AOC (left plot) and averaged for all helmet CM positions (right plot). Error bars are SD	6-7
6-8 Pitch acceleration magnitude versus helmet CM position. Averaged among 12 subjects for each helmet mass (left plot) and averaged for all helmet masses (right plot). Error bars are SD	6-8
6-9 Graph of mean power frequency (x, in Hz), over time (y, in seconds) of the EMG with individuals subject's pre-test in open circles and post-test in closed circles	6-8
6-10 Guideline for head supported mass configurations.....	6-9

Task 6 Tables

Table	Page
6-1 Helmet mass properties for the swept sine vibration exposure.....	6-5

Task 7: Investigation of Occupant Restraint Issues in Vehicle Occupant Safety and Performance

	Page
<i>Subtask A: Head Supported Mass and Soldier Health</i>	
INTRODUCTION	7a-1
BACKGROUND RESEARCH	7a-2
MATERIALS	7a-2
HSM attachment platform.....	7a-2
Muscular fatigue	7a-3
Randomly appearing targets	7a-4
UH-60 flight performance data acquisition	7a-5
Psychophysical questionnaire	7a-5
PROCEDURES	7a-6
Muscular	7a-6
Randomly appearing targets	7a-7
Psychophysical measurements.....	7a-7
CONCLUSION	7a-8
REFERENCES	7a-8

TABLE OF CONTENTS (Continued)

Task 7a Figures

Figure	Page
7a-1 Picture of the strength and electromyographic data equipment.....	7a-4
7a-2 Locations of proposed target displays (as dots).....	7a-5

Task 7a Tables

Table	Page
7a-1 Describing the experimental weight moments as a function of head supported weight and CM distance.....	7a-3

Task 7: Investigation of Occupant Restraint Issues in Vehicle Occupant Safety and Performance

	Page
<i>Subtask B: Vehicular Occupant Restraint Systems</i>	
INTRODUCTION	7b-1
METHODOLOGY	7b-1
Occupant and restraint system modeling	7b-2
HUMAN TOLERANCE LIMITS	7b-3
Neck Injury Indicator	7b-3
Thoracic Injury Criteria	7b-3
Viscous Criteria (VC) / Soft Tissue Criterion.....	7b-3
Thoracic Trauma Index (TTI).....	7b-3
Pelvis Injury Criteria.....	7b-4
Restraint Quotient (RQ)	7b-4
Torso Angle Criteria	7b-4
MESH DENSITY OPTIMIZATION	7b-4
Observations	7b-7
SELECTION OF PULSE SHAPES FOR CRASH SIMULATIONS	7b-8
Introduction.....	7b-8
Approach.....	7b-10
Simulation Set-up.....	7b-11
Output Parameters.....	7b-13
Analysis and Discussion	7b-13
Conclusion	7b-15
TEST PROTOCOL	7b-15
Objective	7b-16
Approach.....	7b-16
Test Equipment Description	7b-16
Input Pulse	7b-18
Test Procedure	7b-20
Data Collection Requirements	7b-20
Data Analysis	7b-21
Organizational Responsibilities	7b-24
REFERENCES	7b-24

TABLE OF CONTENTS (Continued)

Task 7b Figures

Figure	Page
7b-1 Shoulder Belt Mesh in HyperMesh 4.0.....	7b-6
7b-2 Still Frames of the shoulder belt presimulation	7b-7
7b-3 Isometric, top and side view of the restraint system & restrained dummy.....	7b-12
7b-4 Pulse shapes with same V but different peak 'g'	7b-14
7b-5 Horizontal, Lateral and 30 degree Pitch down orientations.....	7b-19
7b-6 Crash Pulse Corridor (Half-Sine).....	7b-19

Task 7b Tables

Table	Page
7b-1 Simulation Parameters	7b-5
7b-2 Mesh Characteristics	7b-6
7b-3 Mesh Density (Elements/inch of belt length)	7b-6
7b-4 Simulation Output.....	7b-7
7b-5 Percentage Change in the Output.....	7b-8
7b-6 Pulse Characteristics	7b-9
7b-7 Velocity Change Triangular Pulse	7b-10
7b-8 Velocity Change Haver-Sine Pulse.....	7b-10
7b-9 Velocity Change Half-Sine Pulse	7b-10
7b-10 Pulse Summary	7b-11
7b-11 Finite Element Belt Specifications.....	7b-12
7b-12 List of parameters declared in the input deck of Madymo for analysis.....	7b-13
7b-13 ATD Instrumentation	7b-17
7b-14 List of Restraint Systems to be tested at CAMI horizontal accelerator	7b-18
7b-15 List of performance evaluation parameters.....	7b-22

BIBLIOGRAPHY OF PUBLISHED REPORTS	Bibliography-1
--	-----------------------

INTRODUCTION

The U.S. Army Aeromedical Research Laboratory (USAARL) at Fort Rucker, Alabama, is tasked with a broad range of applied research and engineering programs designed to answer biomedical questions dealing with aviator and soldier performance issues in an operational environment. In carrying out its mission, the Laboratory encounters unique and complex research requirements that demand maximum flexibility in its response capability. In order to achieve flexibility, USAARL contracted for contributive research in a variety of soldier performance and capability assessments with UES, Inc. The period of effort of this contract was July 1, 1995 through November 30, 2002. During this time seven taskings have been received by UES under this Task Order Contract. Below is a summary table of the timeframes for the seven tasks and the people who directly worked on each task.

Table 1.

Task assignment and duration of effort with assigned personnel (*denotes former employee).

Task	Task Title	Duration	People Assigned
1	Airworthiness Certification Evaluation Program	1 Jul 95 - 30 Nov 02	Bruce Hall Jeaneen Lesniak Joseph Haley, Jr.* Khalid Barazanji* Blake Murphree* Martin Quattlebaum*
2	Investigation of Visual Performance Issues for Electro-Optical Displays	17 Jul 95 - 6 Oct 95	Thomas Harding John Martin Howard Beasley
3	Biochemical Research and Analytical Support For USAARL Research Programs	25 Sep 95 - 30 Sep 98	Albert Kirby*
4	Investigation of Visual Performance Issues for Flat Panel Technology Displays	15 Dec 95 - 30 Nov 02	Thomas Harding John Martin Howard Beasley Victor Klymenko
5	Mathematical Modeling and Computer Simulation of Human Bio-Dynamics and Crash Environments	26 Jan 96 - 15 Apr 98	Amir Mobasher* Fred Brozoski*
6	Biomedical Engineering Research Support for Head Supported Device Mass Properties Design and Operational Criteria	15 Sep 96 - 1 Apr 99	Khalid Barazanji* Janet Dobson* Janice Marquis*
7	Investigation of Occupant Restraint Issues in Vehicle Occupant Safety and Performance	12 Jun 01 - 30 Nov 02	Stuart Fraser Ketan Mane* Randy Randhawa Bradley Bumgardner

As these tasks each have different research requirements, and are disjointed from one another from a story line point of view, we have organized this final report by Tasks. To assist with navigation through the document, we have assigned page numbers by Task number. Thus "Task 2 – Page 4" will be the fourth page under the Task 2 heading. Likewise, we have numbered Figures and Tables using this same scheme. The table of contents provides a good starting point for understanding the content and nature of the material presented in this final report.

During the course of this contract, UES scientists and engineers have published a large number of reports. Our effort has been most productive in keeping with the demands of the USAARL research mission. A separate bibliography is presented at the end of this report, which lists open literature publications, laboratory reports, and presentations made by UES employees as a direct result of this contract effort. It would be redundant and to large a task to review all of the work performed under this contract in a single document. Therefore, this report provides a summary overview of the work accomplished. Below is a list of major research accomplishments listed in bullet format.

- Performed laboratory/aircraft testing on the following items
 - Omni-Vent Model Series D/mri Ventilator
 - Impact Uni-Vent Model 780 Ventilator
 - Pneupac Model PortaPAC Ventilator
 - Impact Model 326/326M Portable Suction System
 - Ivac Medsystem Model 2863B Infusion Pump.
 - Protocol Model 106LCD Vital Signs Monitor.
 - Physio-Control Model Lifepak 10-59 Defibrillator.
 - SIMS BCI Model 3303GR Pulse Oximeter.
 - Impact Model 754/754M Ventilator.
 - Protocol Model Propaq 206EL Vital Signs Monitor.
 - Infusion Dynamics Power Infuser Model M100B-3A Infusion Pump.
 - Cardiac Science Model Powerheart Defibrillator.
 - Lifesaving Systems Oxylator Model EM-100.
 - Nonin Model 2500 Pulse Oximeter.
 - Nonin Model 9500 Pulse Oximeter.
 - Life Support for Trauma and Transport.
 - Spacelabs Medical Model 90309 Vital Signs Monitor.
 - Heartstream Model Forerunner.
 - Allied Healthcare Model Bear 33 Ventilator.
 - Zoll Model PD2000 Defibrillator.
- Performed analysis on medical package on the UH60Q MEDEVAC Helicopter
- Acquired an Airworthiness Release on the following items
 - Impact 326/326M Suction System
 - Ivac Medsystem Model 2863B Infusion
 - Protocol Model 106LCD Vital Signs Monitor
 - Physio-Control Model Lifepak 10-59 Defibrillator.
 - SIMS BCI Model 3303GR Pulse Oximeter.

- Impact Model 754/754M Ventilator
- Protocol Model Propaq 206EL Vital Signs Monitor.
- Infusion Dynamics Power Infuser Model M100B-3A Infusion Pump
- Cardiac Science Model Powerheart Defibrillator
- Lifesaving Systems Oxylator Model EM-100.
- Life Support for Trauma and Transport
- Evaluated figures-of-merit for the IHADSS and ANVIS
- Completed melatonin correlations with various performance metrics.
- Designed and co-developed prototype of field portable IHADSS tester (Patent Application Submitted)
- Developed laboratory HMD tester.
- Developed HMD grayshades model.
- Developed HMD color scene simulation model.
- Completed study of legibility with flat panel displays.
- Evaluated multiple versions of the Microvision AIHS retinal scanning display (HMD)
- Evaluated the effect of biocular HMD designs on visual performance.
- Evaluated the CRT based Kaiser Electronics Comanche HIDSS
- Evaluated the Honeywell High Pass HMD
- Developed new figures-of-merit for the pixelated displays.
- Evaluated developmental miniature flat panel sources for the Comanche HIDSS
- Developed model of spatial contrast sensitivity
- Developed a high fidelity model of the UH-60 helicopter cockpit
 - Finite element energy-absorbing seat
 - 5-point restraint with buckle
 - 50th percentile hybrid III faceted male dummy
 - 5th percentile hybrid III faceted female dummy
 - Cockpit airbag system
 - Madymo simulation
- Developed a test protocol for dynamic sled testing
- Developed selection criteria for inquiry assessment reference values

TASK 1

Airworthiness Certification Evaluation Program

INTRODUCTION

The overall objective of this task is to provide the technical expertise in the test and evaluation of medical equipment being considered for use aboard U.S. Army medical evacuation (MEDEVAC) helicopters.

Medical devices continue to evolve in technological advancement and complexity. Generally, medical devices are designed to function in an environmentally controlled stationary hospital environment and not in the constantly changing harsh dynamic helicopter environment. For this reason, there are concerns that medical devices may adversely affect the operation of aircraft systems, and conversely, the aircraft may adversely affect the proper operation and efficacy of the medical equipment. Failure of medical devices during in-flight medical care may result in exposing patients and aircrew to hazardous situations. All medical equipment identified for use on MEDEVAC rotary-wing aircraft must undergo a series of laboratory and aircraft tests, before the aircraft controlling authority - the U.S. Army Aviation and Missile Command (USAMCOM), can issue a fleet-wide airworthiness release.

EVALUATION OF MEDICAL EQUIPMENT

Over the course of this contract effort, UES has provided technical evaluation of commercial of the shelf and developmental medical equipment. UES engineers have worked with U.S. Army program managers and system developers in the assessment of the medical devices. Our findings have led to the modification of numerous devices. These improvements have led to better care being given to the wounded, as well as improved safety to the medical personnel and aircraft.

First the medical equipment undergoes a series of laboratory tests and aircraft tests. These tests are based on commercial and military standards. The laboratory tests include: initial inspection, battery life, human factors, high temperature, low temperature, altitude, vibration, humidity, electromagnetic interference (radiated susceptibility and conducted susceptibility), and electromagnetic compatibility (radiated emissions and conducted emissions). The tests have been updated as new standards are released also tests are added when warranted. After completion of laboratory tests, USAARL decides if a limited airworthiness release will be requested from USAMCOM. If a limited airworthiness release is granted, the medical equipment then undergoes a series of aircraft tests including: spectrum analyzer, squib, aircraft susceptibility, medical device susceptibility, and human factors. After completion of aircraft testing a fleet wide airworthiness release may be requested. The paragraphs below will be a chronological history of results from medical devices tested by UES personnel.

Omni-Vent Model Series D/mri Ventilator

The device is a pneumatically powered volume, time cycled ventilator. The device is powered from an external gas source pressurized at 25-140 pounds per square inch. The On/Off rotary control knob allows for initial gas flow to start ventilation. Three rotary knobs controlling inspiratory time, expiratory time, and inspiratory flow, control the volume delivery and breath rate. The device had dimensions of 4 x 5 x 7 inches with a weight of 4.5 pounds.

Because the device is pneumatically powered, limited laboratory tests were conducted. The laboratory tests performed were high temperature, low temperature, humidity, altitude, vibration, and human factors. The device failed to meet criteria for low temperature, human factors and altitude. The device stopped operation during the low temperature test. During the altitude test, the device failed to deliver a set tidal volume. During the human factors testing, deficiencies identified were: control knobs too small, controls not clearly labeled, control knobs difficult to operate with one hand, pressure relief valve not labeled, no indication of current pressure setting, no indication of proper operation, and expiratory time control knob set to its indicated maximum value caused ventilator to shut down.

After laboratory testing, an airworthiness release from USAMCOM was not requested due to the device failures. The device was considered incompatible with the MEDEVAC UH-60A helicopters and no further testing was performed. Results of testing can be found in USAARL Report No. 96-08.

Impact Uni-Vent Model 780 Ventilator

The device is a lightweight portable ventilator. The device delivers ventilation from an external gas source or internal compressor. A three position switch with an off, external oxygen, internal compressor positions is used to power on the device. The device breath volume and breath rate are preset and not adjustable. The device will operate on internal battery, 115/230 volts alternate current (VAC) 50-400 hertz (Hz), and 12 to 30 volts direct current (VDC).

During initial inspection, the device failed to operate consistently in each external power mode. The delivered breath volume varied up to 43 percent. Initial inspection was the only laboratory test performed.

Because of device failure during initial inspection, testing was stopped and no further testing was performed. An airworthiness release from USAMCOM was not requested. The device was considered incompatible with the MEDEVAC UH-60A helicopters. Results of testing can be found in USAARL Report No. 96-10.

Pneupac Model PortaPAC Ventilator

The device is a lightweight portable ventilator. The device delivers ventilation from an external gas source or internal compressor. A three position switch with an off, external oxygen, internal compressor positions is used to power on the device. The device breath volume and breath rate are adjustable via a single rotary knob with six preset conditions. The device will

operate on internal battery or 23 to 28 VDC. The device had dimensions of 13.75 x 8.5 x 6 inches with a weight of 18.74 pounds.

The following laboratory tests were performed on this device: initial inspection, battery life, human factors, high temperature, low temperature, humidity, vibration, altitude, electromagnetic interference, and electromagnetic compatibility. The device met test criteria for initial inspection, battery life, low temperature, humidity, altitude, and electromagnetic interference. The device had human factors issues involving visual displays, controls, maintainability, conductors, fasteners, test equipment, fuses, circuit breakers, labels, coding, and safety. During the high temperature testing, a circuit breaker popped in the battery compartment. During vibration testing, the circuit breaker in the battery compartment repeatedly popped. During electromagnetic compatibility testing, the device produced conducted and radiated emissions.

After laboratory testing, an airworthiness release from USAMCOM was not requested due to the device failures. The device was considered incompatible with the MEDEVAC UH-60A helicopters and no further testing was performed. Results of testing can be found in USAARL Report No. 96-12.

Impact Model 326/326M Portable Suction System

The device is a lightweight portable vacuum pump contained in a rigid plastic case. The device can supply continuous or intermittent vacuum. Knobs located on the front face of the device control all device functions. The device can operate on internal battery, external 11 to 30 VDC, and 115 VAC 50-400 Hz. The device is shown in Figure 1-1.

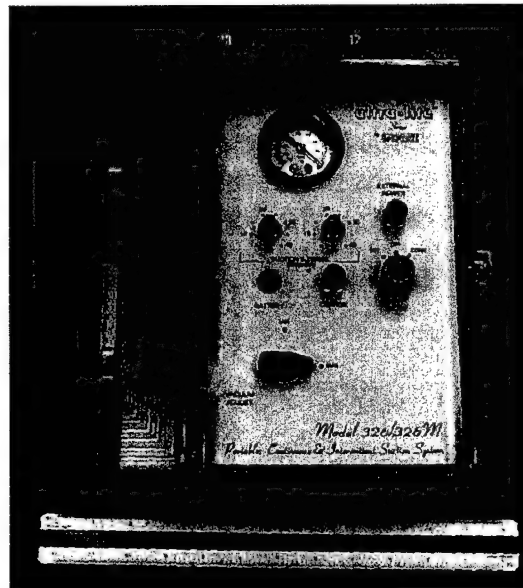


Figure 1-1. Impact 326/326M Suction System.

The following tests were performed on this device: initial inspection, electrical safety, battery life, human factors, high temperature, low temperature, humidity, vibration, altitude, electromagnetic interference, and electromagnetic compatibility. The device met criteria for initial inspection, battery life, electrical safety, high temperature, humidity, vibration, radiated susceptibility, conducted susceptibility, and conducted emissions. During the low temperature test, the device failed to operate using external alternating current (AC), the device did operate properly on battery power. During the altitude test, the device failed to deliver set free airflow. During human factors testing, the battery charge indicator and charge indicator lamp were found to be operationally unreliable, the vacuum gauge indicator needle would stick, the external power input was threaded poorly, plastic cover was not sturdy enough, and battery chafing within battery box may lead to battery failure. The device failed to meet criteria for the radiated emissions test.

After laboratory testing, an airworthiness release from USAMCOM was requested and granted. During the aircraft testing aboard USAARL UH-60, the aircraft did not affect the device, the device did not affect the aircraft, and no new human factors issues were found. A fleet wide airworthiness release was requested from USAMCOM and granted. Results of testing can be found in USAARL Report No. 98-06.

Ivac Medsystem Model 2863B Infusion Pump

The device is a three-channel infusion pump designed to operate on internal battery or external AC power. The device is controlled by a series of membrane keys surrounding the liquid crystal display. The device had dimensions of 7.88 x 6.0 x 2.1 inches with a weight of 5.13 pounds. The device is shown in Figure 1-2.



Figure 1-2. Ivac Medsystem Model 2863B Infusion Pump.

The following tests were performed on this device: initial inspection, electrical safety, battery life, human factors, high temperature, low temperature, humidity, vibration, altitude, electromagnetic interference, and electromagnetic compatibility. The device met criteria for initial inspection, electrical safety, battery life, electrical safety, high temperature, humidity, vibration, radiated susceptibility, and conducted susceptibility. During the low temperature test, the device failed to meet criteria. During human factors testing, the device was found to be deficient in visual displays, fuses and circuit breakers, and labels and coding. The device failed to meet criteria for the radiated and conducted emissions test.

After laboratory testing, an airworthiness release from USAMCOM was requested and granted. During the aircraft testing aboard USAARL UH-60, the aircraft did not affect the device, the device did not affect the aircraft, and no new human factors issues were found. A fleet wide airworthiness release was requested from USAMCOM and granted. Results of testing can be found in USAARL Report No. 98-07.

Protocol Model 106LCD Vital Signs Monitor

The device is a lightweight portable vital signs monitor. The device can monitor a patient's heart rate, invasive and non-invasive blood pressure, temperature, carbon dioxide, and saturated oxygen level. On a liquid crystal display, three waveforms can be viewed at once. Five front panel pushbuttons control device operation. The device will operate on 115 VAC 60 Hz or internal battery. The device had dimensions of 9.8 x 8.3 x 6.8 inches with a weight of 10.1 pounds. The device is shown in Figure 1-3.

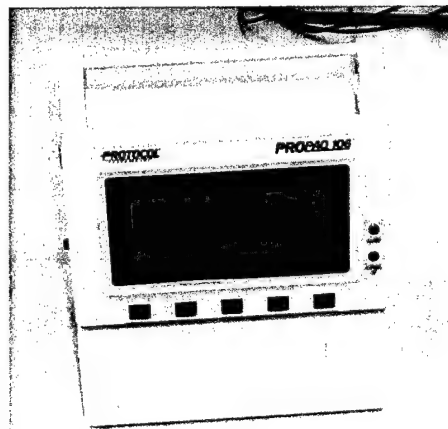


Figure 1-3. Protocol Model 106LCD Vital Signs Monitor.

The following tests were performed on this device: initial inspection, electrical safety, battery life, human factors, high temperature, low temperature, humidity, vibration, altitude, electromagnetic interference, and electromagnetic compatibility. The device met test criteria for initial inspection, electrical safety, battery life, human factors, humidity, and conducted susceptibility. During the altitude test, the device produced an altimeter equipment alert. During vibration and high temperature testing, the carbon dioxide sensor failed to operate. During low temperature testing, the carbon dioxide sensor did not operate and the liquid crystal display

became unreadable. The device produced radiated and conducted emissions in excess of test criteria. The device was susceptible during the radiated susceptibility testing.

After laboratory testing, an airworthiness release from USAMCOM was requested and granted. During the aircraft testing aboard USAARL UH-60, the aircraft did not affect the device, the device did not affect the aircraft, and no new human factors issues were found. A fleet wide airworthiness release was requested from USAMCOM and granted. Results of testing can be found in USAARL Report No. 98-08.

Physio-Control Model Lifepak 10-59 Defibrillator

The device is a portable cardiac life support system intended for use in the diagnosis and treatment of cardiac dysrhythmias. The device can monitor a patient's heart rate rhythm, deliver noninvasive pacing, and deliver defibrillation energy. A cardioscope displays the heart rhythm and device status. Top and front panel pushbuttons control device operation. The device will operate on 115 VAC 60 Hz or internal battery. The device had dimensions of 4.0 x 16.0 x 14.0 inches with a weight of 20.0 pounds. The device is shown in Figure 1-4.



Figure 1-4. Physio-Control Model Lifepak 10-59 Defibrillator.

The following tests were performed on this device: initial inspection, electrical safety, battery life, human factors, high temperature, low temperature, humidity, vibration, altitude, electromagnetic interference, and electromagnetic compatibility. The device met test criteria for initial inspection, battery life, human factors, high temperature, low temperature, humidity, vibration, altitude, and conducted susceptibility. The device produced radiated and conducted emissions in excess of test criteria. The device was susceptible during the radiated susceptibility testing. The device did not meet electrical safety criteria; an excessive leakage current was measured. The leakage current was caused by the external power supply.

After laboratory testing, an airworthiness release from USAMCOM was requested and granted. During the aircraft testing aboard USAARL UH-60, the aircraft did not affect the

device or the device did not affect the aircraft. The spectrum analyzer test indicates possible interference with the Personnel Locator System. Human factors issues included: when securing device through handle the defibrillation paddles cannot be accessed and heart rhythm monitoring can be difficult during high vibration flight. A fleet wide airworthiness release was requested from USAMCOM and granted. Results of laboratory testing can be found in USAARL Report No. 2000-28. Results of aircraft testing can be found in USAARL Report No. 2001-13.

SIMS BCI Model 3303GR Pulse Oximeter

The device is a lightweight portable pulse oximeter. The device provides oxygen saturation, pulse rate, and pulse strength measurements of the patient. The device can provide measurements on any patient, from neonates to adults. The device has user-adjustable light emitting diode display that indicate oxygen saturation and pulse measurements. The device can operate on 115 VAC or internal battery. The device has a weight of 19 ounces and dimensions of 3.3 x 7.25 x 1.85 inches. The device is shown in Figure 1-5.



Figure 1-5. SIMS BCI Model 3303GR Pulse Oximeter.

The following tests were performed on this device: initial inspection, electrical safety, battery life, human factors, high temperature, low temperature, humidity, vibration, altitude, electromagnetic interference, and electromagnetic compatibility. The device met test criteria for initial inspection, electrical safety, human factors, altitude, vibration, high temperature, low temperature, humidity, and conducted emissions. The device did not meet the manufacturer's specification for battery life. The device produced radiated emissions in excess of test criteria. The device was susceptible to radiated and conducted test generated signals.

After laboratory testing, an airworthiness release from USAMCOM was requested and granted. During the aircraft testing aboard USAARL UH-60, the aircraft did not affect the device or the device did not affect the aircraft. Human factors issues included: external power adapter will not fit in aircraft recessed outlet panel, reading of the display can be difficult during

high vibration flight. A fleet wide airworthiness release was requested from USAMCOM and granted. Results of laboratory testing can be found in USAARL Report No. 2001-11. Results of aircraft testing can be found in USAARL Report No. 2002-07.

Impact Model 754/754M Ventilator

The device is a portable ventilator, compressor, and air/oxygen mixer. The device has three modes of operation: assist-control ventilation, synchronized intermittent mandatory ventilation, and continuous positive airway pressure ventilation. All modes are altitude adjusted to minimize the patient's work of breathing. The device can operate from internal rechargeable batteries or external AC and DC. The device has dimensions of 8.87 x 11.5 x 4.5 inches and a weight of 13.0 pounds. The external power supply has dimensions of 8.75 x 2.25 x 5.75 inches and a weight of 3.0 pounds. The device is shown in Figure 1-6.

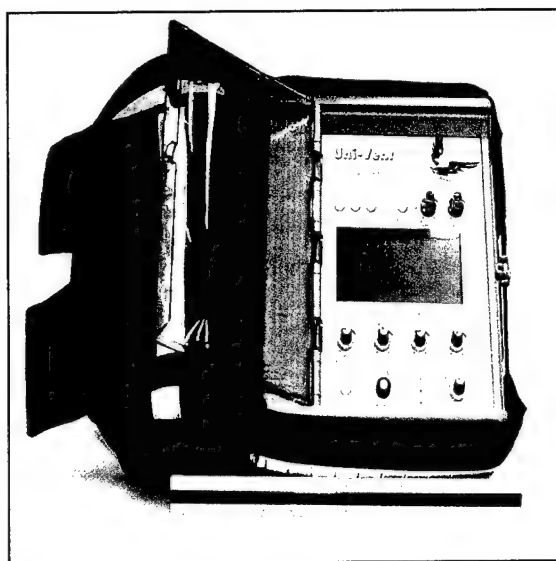


Figure 1-6. Impact Model 754/754M Ventilator.

The following tests were performed on this device: initial inspection, electrical safety, battery life, human factors, high temperature, low temperature, humidity, vibration, altitude, electromagnetic interference, and electromagnetic compatibility. The device met test criteria for initial inspection, electrical safety, battery life, high temperature, low temperature, humidity, vibration, altitude, and conducted susceptibility. The human factors failure concerned the adjustment of the liquid crystal display, when adjusting the display the device did not deliver ventilation to the patient. The device produced radiated and conducted emissions in excess of test criteria. The device was susceptible to radiated test generated signals.

After laboratory testing, an airworthiness release from USAMCOM was requested and granted. During the aircraft testing aboard USAARL UH-60, the aircraft did not affect the device or the device did not affect the aircraft. The spectrum analyzer test indicates possible interference with the one of the aircraft radios. Human factors issues included: securing strap caused screen legibility to be difficult and device operation difficult with cold weather gloves. A

fleet wide airworthiness release was requested from USAMCOM and granted. Results of laboratory testing can be found in USAARL Report No. 2002-17. Results of aircraft testing can be found in USAARL Report No. 2002-18.

Protocol Model Propaq 206EL Vital Signs Monitor

The device is a multi-parameter vital signs monitor for use with neonatal, pediatric and adult patients. The device can monitor oxygen saturation, heart rhythm, carbon dioxide, invasive blood pressure, noninvasive blood pressure, and temperature. On a liquid crystal display, three waveforms can be viewed at once. Five front panel pushbuttons control device operation. The device can operate on internal battery or external AC power. The device has dimensions of 9.65 x 8.25 x 7.56 inches and a weight of 13.5 lbs. The device is shown in Figure 1-7.

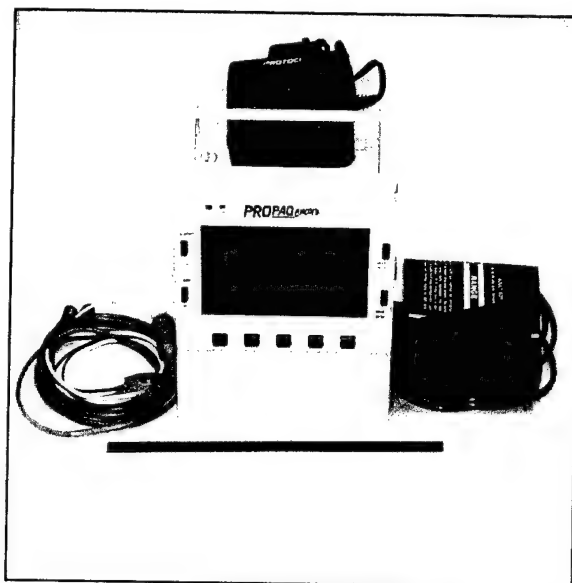


Figure 1-7. Protocol Model Propaq 206EL Vital Signs Monitor.

The following tests were performed on this device: initial inspection, electrical safety, battery life, human factors, high temperature, low temperature, humidity, vibration, altitude, electromagnetic interference, and electromagnetic compatibility. The device met test criteria for initial inspection, electrical safety, battery life, human factors, humidity, and altitude. During the high and low temperature test, the carbon dioxide failed to meet test criteria, though the device did meet the stated manufacturer's specifications. During vibration testing, components of the printer assembly broke. The device produced radiated and conducted emissions in excess of test criteria. The device was susceptible to radiated and conducted test generated signals.

After laboratory testing, an airworthiness release from USAMCOM was requested and granted. During the aircraft testing aboard USAARL UH-60, the aircraft did not affect the device or the device did not affect the aircraft. Human factors issues included: securing strap caused screen legibility to be difficult, device operation difficult with cold weather gloves, and reading of the display can be difficult during high vibration flight. A fleet wide airworthiness

release was requested from USAMCOM and granted. The USAARL report of laboratory testing is in press. The USAARL report of aircraft testing is in preparation.

Infusion Dynamics Power Infuser Model M100B-3A Infusion Pump

The device is a lightweight portable infusion pump. The device is designed for rapid infusion of intravenous fluids with flow rates adjustable from 0.2 to 6.0 liters per hour. The device is not designed for use with blood products or medications. The device can operate on six AAA batteries or external power adapter (only tested operating on internal battery). The device has dimensions of 2.0 x 2.75 x 3.75 inches. The device with batteries installed has a weight of 12 ounces. The device is shown in Figure 1-8.

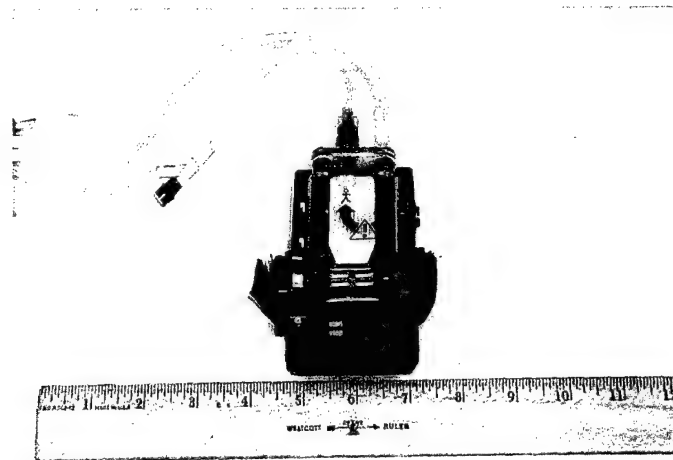


Figure 1-8. Infusion Dynamics Power Infuser Model M100B-3A Infusion Pump.

The following tests were performed on this device: initial inspection, electrical safety, battery life, human factors, high temperature, low temperature, humidity, vibration, altitude, electromagnetic interference, and electromagnetic compatibility. The device met test criteria for initial inspection, electrical safety, battery life, high temperature, low temperature, humidity, vibration, and altitude. The human factors issue was with the battery tray lock mechanism, which broke, was repaired, and is difficult to operate. The device produced radiated emissions in excess of test criteria. The device was susceptible to radiated test generated signals. The device was tested on battery power only.

After laboratory testing, an airworthiness release from USAMCOM was requested and granted. During the aircraft testing aboard USAARL UH-60, the aircraft did not affect the device or the device did not affect the aircraft. The spectrum analyzer test indicates possible interference with the Personnel Locator System and three of the aircraft radios. Human factors issues included: device operation difficult with cold weather gloves. A fleet wide airworthiness release was requested from USAMCOM and granted. The USAARL report of laboratory testing is in preparation. The USAARL report of aircraft testing is in preparation.

Cardiac Science Model Powerheart Defibrillator

The device is a lightweight portable automated external defibrillator. The device automatically analyzes a heart rhythm to determine if defibrillation is needed, all the user must do is deliver the shock. Voice and text instructions alert the user after a shockable rhythm is determined. The device features one button operation. The device operates on internal battery only. The device had dimensions of 3.3 x 10.6 x 12.4 inches with a weight of 7.7 pounds. The device is shown in Figure 1-9.

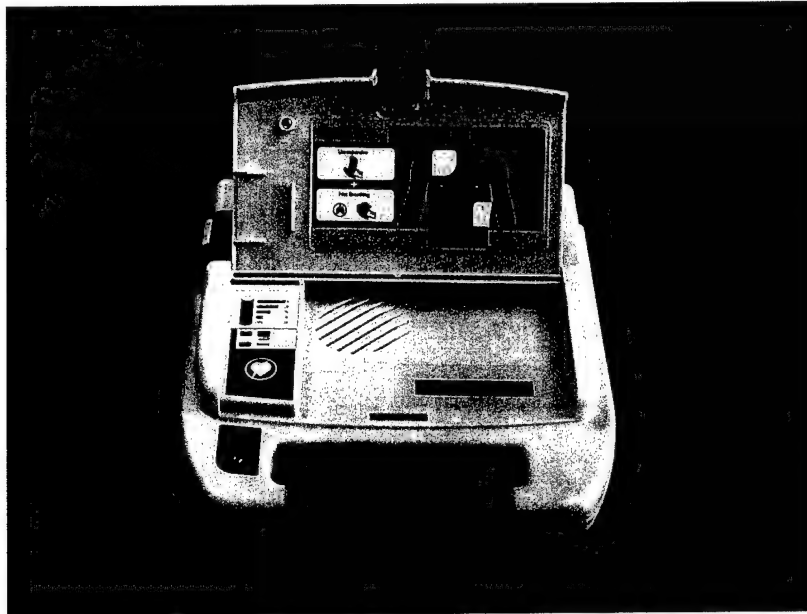


Figure 1-9. Cardiac Science Model Powerheart Defibrillator.

The following tests were performed on this device: initial inspection, electrical safety, battery life, human factors, high temperature, low temperature, humidity, vibration, altitude, electromagnetic interference, and electromagnetic compatibility. The device met test criteria for initial inspection, electrical safety, battery life, human factors, high temperature, low temperature, humidity, vibration, and altitude. The device produced radiated emissions in excess of test criteria. The device was susceptible to radiated test generated signals.

After laboratory testing, an airworthiness release from USAMCOM was requested and granted. During the aircraft testing aboard USAARL UH-60, the aircraft did not affect the device or the device did not affect the aircraft. Human factors issues included: device operation difficult with cold weather gloves and reading of the display can be difficult during high vibration flight. A fleet wide airworthiness release was requested from USAMCOM and granted. The USAARL report of laboratory testing is in preparation. The USAARL report of aircraft testing is in preparation.

Lifesaving Systems Oxylator Model EM-100

The device is an oxygen powered resuscitator/inhalator that requires no power source other than the supply of compressed oxygen in an appropriate cylinder or wall outlet. The device has adjustable airway limiting pressure. The device has a weight of 0.55 pounds. The device has a diameter of 2.25 inches and a length of 4.25 inches. The device is shown in Figure 1-10.

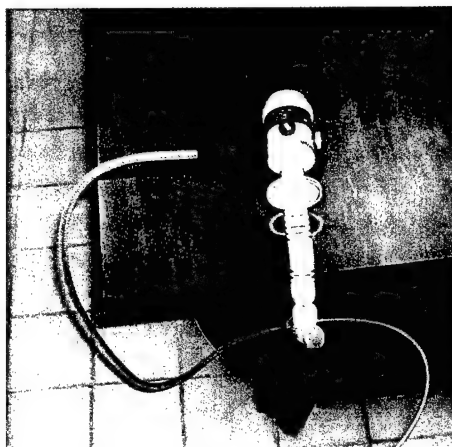


Figure 1-10. Lifesaving Systems Oxylator Model EM-100.

The following tests were performed on this device: initial inspection, human factors, high temperature, low temperature, humidity, vibration, and altitude. The device met test criteria for initial inspection, human factors, high temperature, low temperature, humidity, vibration, and altitude.

After laboratory testing, an airworthiness release from USAMCOM was requested and granted. During the aircraft testing aboard USAARL UH-60, the aircraft did not affect the device or the device did not affect the aircraft. A fleet wide airworthiness release was requested from USAMCOM and granted. The USAARL report of laboratory testing is in preparation. The USAARL report of aircraft testing is in preparation.

Nonin Model 2500 Pulse Oximeter

Is a lightweight portable device for use in measuring oxygen saturation of arterial hemoglobin and pulse rate. The device can be used on adults, pediatric, and neonatal patients in a variety of settings. Oxygen saturation and pulse rate are shown in a light emitting diode display. The device operates on four AA batteries. The device has dimensions of 5.4 x 2.8 x 1.3 inches with a weight of 7.4 ounces. The device is shown if Figure 1-11.

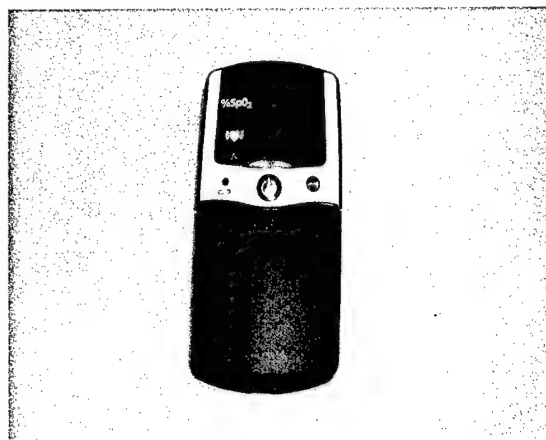


Figure 1-11. Nonin Model 2500 Pulse Oximeter.

The following tests were performed on this device: initial inspection, electrical safety, battery life, human factors, high temperature, low temperature, humidity, vibration, altitude, electromagnetic interference, and electromagnetic compatibility. The device met test criteria for initial inspection, electrical safety, battery life, human factors, high temperature, low temperature, humidity, vibration, altitude, and radiated emissions. The device was susceptible to radiated test generated signals.

After laboratory testing, an airworthiness release from USAMCOM was requested and granted. During the aircraft testing aboard USAARL UH-60, the aircraft did not affect the device or the device did not affect the aircraft. A fleet wide airworthiness release was requested from USAMCOM and granted. The USAARL report of laboratory testing is in preparation. The USAARL report of aircraft testing is in preparation.

Nonin Model 9500 Pulse Oximeter

Is a lightweight portable device for use in measuring oxygen saturation of arterial hemoglobin and pulse rate. The device can be used on adults and pediatric patients in a variety of settings. Oxygen saturation and pulse rate are shown in a light emitting diode display. The device operates on two AAA batteries. The device has dimensions of 1.3 x 1.3 x 2.2 inches with a weight of 2.0 ounces. The device is shown if Figure 1-12.



Figure 1-12. Nonin Model 9500 Pulse Oximeter.

The following tests were performed on this device: initial inspection, electrical safety, battery life, human factors, high temperature, low temperature, humidity, vibration, altitude, electromagnetic interference, and electromagnetic compatibility. The device met test criteria for initial inspection, electrical safety, battery life, human factors, high temperature, low temperature, humidity, vibration, altitude, and radiated emissions. The device was susceptible to radiated test generated signals.

After laboratory testing, an airworthiness release from USAMCOM was requested and granted. During the aircraft testing aboard USAARL UH-60, the aircraft did not affect the device or the device did not affect the aircraft. A fleet wide airworthiness release was requested from USAMCOM and granted. The USAARL report of laboratory testing is in preparation. The USAARL report of aircraft testing is in preparation.

Life Support for Trauma and Transport

The device is a portable individual intensive care unit. The device serves as a resuscitation platform for stabilization and evacuation for trauma casualties. The device travels with the casualty to the care facility. The device includes an onboard physiological monitoring unit, suction unit, defibrillation unit, fluid administration unit, ventilator unit, portable clinical analyzer, and oxygen system. The device can operate from internal batteries (30 minutes) or the following external power sources (1) $115 \pm 10\%$ VAC 60 hertz (Hz), (2) 108 to 118 VAC 400 Hz, (3) $230 \pm 10\%$ VAC 50 Hz, and (4) 25 ± 5 VDC. The device has an internal environmental control system for operation in harsh environments. The device has data logging for retrieval of patient information. Patient information and device status can be monitored from a laptop computer. The device with stretcher, oxygen bottle and regulator has a weight of 174 pounds (lbs). The device is securable to the litter pan using the carousel litter straps. The device is shown in Figure 1-13.

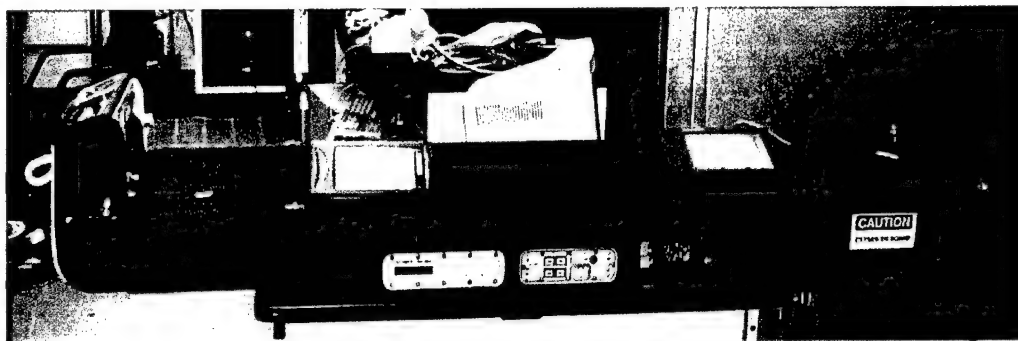


Figure 1-13. Life Support for Trauma and Transport.

The following tests were performed on this device: initial inspection, electrical safety, battery life, human factors, high temperature, low temperature, humidity, vibration, altitude, electromagnetic interference, and electromagnetic compatibility. The EUT met criteria for the following tests: acceptance inspection, electrical safety, and altitude. The EUT did not meet criteria for the following tests: human factors, battery life, vibration, humidity, high temperature, low temperature, conducted emissions, conducted susceptibility, radiated emissions, and radiated susceptibility. During cold weather test, the infusion pump, suction pump, clinical analyzer, and carbon dioxide sensor failed to function. During hot weather test, the clinical analyzer and carbon dioxide sensor failed to function. During high humidity test, the clinical analyzer failed to function. During the altitude test, the Display and Data Logging System (DDLS) display failed to function. During vibration test, the defibrillator assembly contacted the center bay cover, DDLS screen was unreadable, and wire breakage in the DDLS. The manufacturer later modified the defibrillator assembly to allow for more clearance from the center bay cover and modified wire connections of the DDLS. The laboratory testing was performed at Brooks Air Force Base and two manufacturer facilities in metropolitan Los Angeles, California. UES personnel traveled to these sites to assist in testing.

After laboratory testing, an airworthiness release from USAMCOM was requested and granted. During the aircraft testing aboard USAARL UH-60, the aircraft did not affect the device or the device did not affect the aircraft. A fleet wide airworthiness release was requested from USAMCOM and granted. The USAARL report of laboratory testing is in preparation. The USAARL report of aircraft testing is in preparation.

UH60Q MEDEVAC Helicopter

The UH-60Q is a fulltime medical aircraft based on the UH-60 airframe. The aircraft can accommodate a crew of three and up to six litter patients or seven ambulatory patients. The aircraft has a medical interior consisting of: suction system, onboard oxygen generating system, litter system, medical attendant seats, environmental control system, external rescue hoist, equipment control panels, medical cabinet, litter lighting system, and electrical outlets.

UES personnel have been involved in a couple of series of tests on the UH-60Q airframe. The first test was a Production Qualification Test performed at Sikorsky Helicopters facility in

Stratford, CT. During this test, UES personnel assisted in testing of the medical interior. Results of this test can be found in the Final Report, Production Qualification Test of the UH-60 Helicopter, TECOM Project No. 4-AI-170-UTT-143. The second test was a cold weather test performed at McKinley Laboratories on Eglin Air Force Base. The purpose of this test was to access the performance of the medical interior in a cold environment. A USAARL report with results is in preparation.

Spacelabs Medical Model 90309 Vital Signs Monitor

The Spacelabs Medical Model 90309 vital signs monitor is a multi-parameter vital signs monitor for use with neonatal, pediatric and adult patients. The device can monitor oxygen saturation, heart rhythm, carbon dioxide, invasive blood pressure, noninvasive blood pressure, and temperature. On a liquid crystal display, three waveforms can be viewed at once. Front panel pushbuttons control device operation. The device can operate on internal battery or external AC power.

The following tests were performed on this device: initial inspection, electrical safety, and vibration. The device met criteria for initial inspection and electrical safety. During vibration testing the device failed to meet criteria. The device ceased operation during the test. The device was sent to manufacturer for repairs. The manufacturer later decided to stop testing and not pursue an airworthiness release. A USAARL report with results is in preparation.

Heartstream Model Forerunner

The device is a lightweight portable automated external defibrillator. The device automatically analyzes a heart rhythm to determine if defibrillation is needed, all the user must do is deliver the shock. Voice and text instructions alert the user after a shockable rhythm is determined. The device features one button operation. The device operates on internal battery only. The device had dimensions of 2.53 x 8.75 x 8.0 inches with a weight of 4.4 pounds. The device is shown in Figure 1-14.

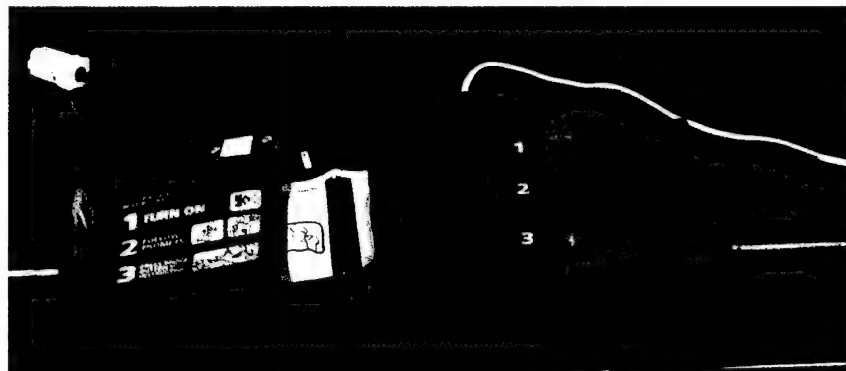


Figure 1-14. Heartstream Model Forerunner.

The following tests were performed on this device: initial inspection, electrical safety, battery life, human factors, high temperature, low temperature, humidity, vibration, altitude, electromagnetic interference, and electromagnetic compatibility. The device met test criteria for initial inspection, electrical safety, battery life, human factors, high temperature, low temperature, humidity, vibration, and altitude. The device produced radiated emissions in excess of test criteria.

Before a limited airworthiness release could be received, the manufacturer decided to stop the testing process. The manufacturer was ceasing production of the model tested and would start the testing process with a new model. The USAARL report of laboratory testing is in preparation.

Allied Healthcare Model Bear 33 Ventilator

The portable device provides ventilation to adult and pediatric patients. The device has three modes of operation: control ventilation, assist-control ventilation, and synchronized intermittent mandatory ventilation. The device can operate from internal rechargeable batteries or external AC. The device has dimensions of 14.0 x 12.8 x 7.5 inches and a weight of 32.0 pounds. The device is shown in Figure 1-15.

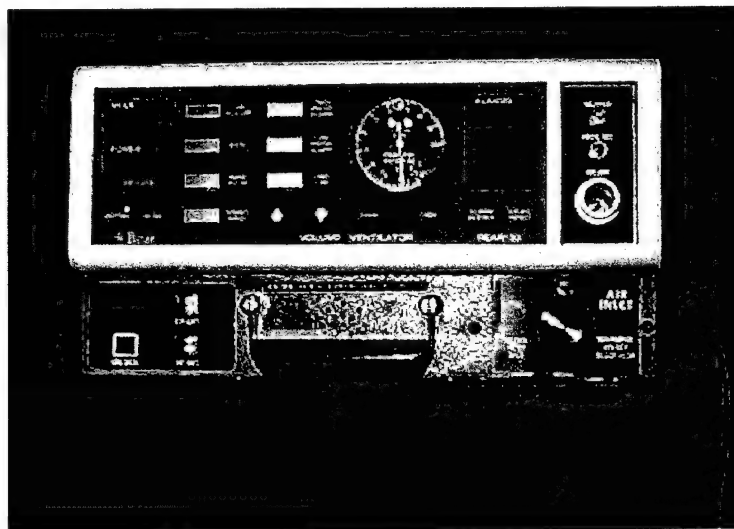


Figure 1-15. Allied Healthcare Model Bear 33 Ventilator.

The following tests were performed on this device: initial inspection, electrical safety, battery life, human factors, high temperature, low temperature, humidity, vibration, altitude, and electromagnetic compatibility. The device met test criteria for initial inspection, electrical safety, battery life, human factors, high temperature, humidity, and altitude. After the low temperature tests, part of the device's liquid crystal displays did not operate. During the vibration testing, the device did not deliver the set air volume. The device produced radiated emissions in excess of test criteria.

Due to failure during vibration testing, the device was returned to the manufacturer. The manufacturer later decided not to pursue an airworthiness release and no further testing was performed. The USAARL report of laboratory testing is in preparation.

Zoll Model PD2000 Defibrillator

The device is a portable cardiac life support system intended for use in the diagnosis and treatment of cardiac dysrhythmias. The device can monitor a patient's heart rate rhythm, deliver noninvasive pacing, and deliver defibrillation energy. Top and front panel pushbuttons control device operation. The device will operate on 115 VAC 60 Hz or internal battery. The device had dimensions of 4.2 x 13.2 x 12.2 inches with a weight of 13.0 pounds.

The following tests were performed on this device: initial inspection, electrical safety, battery life, human factors, high temperature, low temperature, humidity, vibration, altitude, electromagnetic interference, and electromagnetic compatibility. The device met test criteria for initial inspection, electrical safety, battery life, human factors, high temperature, low temperature, humidity, vibration, and altitude. The device produced excessive leakage currents during the electrical safety test. The device battery life did not meet the manufacturer rated time for noninvasive pacing. The device produced radiated and conducted emissions in excess of test criteria. The device was susceptible to radiated test generated signals.

Due to the numerous failures during laboratory testing a limited airworthiness release was requested. The device was considered to be incompatible with the UH-60 airframe. The USAARL report of laboratory testing is in preparation.

SUMMARY

The work of UES personnel has resulted in numerous improvements to the medical equipment being used by the U.S. Army MEDEVAC program. This has resulted in improved medical care to the injured. UES personnel have been part of 14 publications, with several more in preparation.

REFERENCES

Association for the Advancement of Medical Instruments, Human Factors Engineering Guidelines and Preferred Practices for the Design of Medical Devices, February 1988, Arlington, VA, AAMI-HE-1988.

Association for the Advancement of Medical Instruments, Safe Current Limits for Electromedical Apparatus, December 1993, Arlington, VA, AAMI-ES1-1993.

Department of the Army, Environmental Protection and Enhancement, June 1982, Washington, DC, Army Regulation 200-1.

Department of the Army, Maintenance Management Procedures for Medical Equipment, April 1987, Washington, DC, TB 38-750-2.

Department of Defense, Design Criteria Standard, 31 October 1996, Washington DC, MIL-STD-1472E.

Department of Defense, EMI Characteristics Measurement of, February 1971, Washington, DC, MIL-STD-462, Notice 3.

Department of Defense, EMI Characteristics Requirements for Equipment, February 1971, Washington, DC, MIL-STD-461C, Notice 5.

Department of Defense, Environmental Test Methods and Engineering Guideline, 14 July 1989, Washington, DC, MIL-STD-810E.

Department of Defense, Environmental Engineering Considerations and Laboratory Tests, 01 January 2000, Washington, DC, MIL-STD-810F.

Department of Defense, Requirements for the Control of Electromagnetic Interference Emissions and Susceptibility, 11 January 1993, Washington DC, MIL-STD-461D.

Department of Defense, Requirements for the Control of Electromagnetic Interference Characteristics of Subsystems and Equipment, 20 August 1999, Washington D.C, MIL-STD-461E.

Mitchell, G. W., and Adams, J.E, Technical Test and Evaluation of Aeromedical Equipment, 1988, Fort Rucker, AL, USAARL Letter Report LR-88-16-1-2.

National Association of Fire Protection, Standard for health care facilities, February 1987, Quincy, MA, NAFP 99.

U.S. Army Medical Command, Aeromedical Evacuation Device Airworthiness Testing Program at USAARL, 13 October 1995, Memorandum.

TASK 2

Investigation of Visual Performance Issues for Electro-Optical Displays

INTRODUCTION

To successfully integrate new technologies into military programs, several objectives must be met. We must have baseline measures of current inventory equipment to identify the specific electro-optical operating characteristics which impact user visual performance. Additionally, some studies will have to be conducted in areas that we currently cannot quantify definite measures of performance. These baselines will allow the Air Warrior Evaluation Team to assess the added value of new technology displays under development, as these representative displays also must be evaluated for visual performance.

Regardless of the final selection for Air Warrior's Helmet Mounted Display (HMD), all of the emerging candidate technologies have at least one function in common – presenting information in the form of imagery and/or symbology to the user. Unfortunately, the spiraling advances in the engineering characteristics of new displays have not been accompanied by a parallel understanding of the effectiveness of these displays in information transfer. We must provide the baseline information from the decades of CRT use as a primary reference to compare figures-of-merit for evaluation of the new displays and eventually identify which figures-of-merit are appropriate to the new technology and which are not.

Therefore, the purpose of Task 2 is to compile optical, electro-optical and visual performance figures-of-merit which fully characterizes the currently fielded IHADSS and ANVIS display imagery and user performance with these displays.

The results of UES, Inc. effort in Task 2 can be found in USAARL Technical Report No. 96-13. The information reported here is garnered from that reporting.

The U.S. Army currently fields two helmet mounted display systems. These are the Integrated Helmet and Display Sighting System (IHADSS), which is employed on the AH-64 Apache, and the Aviator's Night Vision Imaging System (ANVIS), which is employed on all U.S. Army rotary wing aircraft, including the AH-64. The IHADSS has been fielded since 1985 and ANVIS came into general use during the latter 1980's. The ANVIS is based on third generation image intensification tubes; systems based on second generation image intensification tubes preceded ANVIS and were fielded as early as 1971. The performance and figures-of-merit specifications of the IHADSS and the ANVIS provide a basis for judging performance of future aviation electro-optical devices.

IHADSS SPECIFICATION

The IHADSS consists of various electronic components and a helmet/display system, called the Integrated Helmet Unit (IHU). The IHU includes a helmet, visor housings with visors,

miniature cathode-ray-tube (CRT), and helmet display unit (HDU) Figure 2-1. The HDU serves as an optical relay device which conveys the image formed on the CRT through a series of lenses, off a beamsplitter (often called a combiner), and into the aviator's right eye. The combiner is a multilayered dichroic filter which is maximized for reflectance at the peak emission of the P-43 phosphor. The IHADSS operates in conjunction with two forward looking infrared (FLIR) sensors located on the nose of the aircraft. One sensor, called the Pilot's Night Vision System (PNVS), provides pilotage imagery, while the second sensor, the Target Acquisition and Designation System (TADS), provides targeting imagery. Infrared detectors, mounted on the IHU helmet, allow the FLIR sensors to be slaved to the pilot's head movements. Aircraft parameter symbology, along with the imagery from the FLIR sensor, is presented to the pilot by means of the HDU. The HDU is designed so that the image of the 30-degree vertical by 40-degree horizontal field-of-view (FOV) of the sensor subtends a 30- by 40-degree field at the pilot's eye. The IHADSS is a monocular display, presenting imagery to the right eye only. At night and under inclement weather conditions, the HDU imagery may be the sole source of information by which the pilot flies the aircraft. The visual quality of this imagery is of supreme importance.



Figure 2-1. Drawing of the IHADSS IHU and visor in place.

Performance specifications for the IHADSS have been divided into two categories: optical and electro-optical. Optical specifications deal with the propagation of the relay and see-through optics. Electro-optical specifications deal with the image as generated by the CRT. We also included a limited discussion on the visual performance with the IHADSS.

IHADSS OPTICAL SPECIFICATIONS

Combiner lens transmittance. Transmittance of light through the HDU combiner lens from the ambient scene is orientation dependent. We estimate that the plane of the combiner lens is approximately 23 degrees off parallel to the front surface of the eye. Harding et al., (1995) measured transmittance at different angles in 2-degree increments. The notched transmittance curve allows greater reflectance of the output of the IHADSS tube, and therefore, greater IHADSS luminance reaches the eye. The average transmittance between 400 and 700 nanometers (nm) is 36 percent.

Distortion. IHADSS distortion was measured using an Ann Arbor optical tester, the image of a Ronchi ruling was viewed after having passed through the optics of the HDU combiner lens twice. Comparing the imaged ruling to standards in MIL-V-43511C revealed nonsignificant levels of distortion. A value of less than 1 was assigned the distortion image.

Optical aberrations. Field curvature and spherical aberration were measured using a diptometer to measure errors in focus with changes in orientation (field curvature) or changes in decentration (spherical aberration). The central portion of field-of-view showed little effects of field curvature, however, more than 1 diopter of field curvature was noted in the periphery. The difference between the vertical and horizontal focuses at each degree of rotation is a measure of astigmatic error. Again, astigmatic error was minimal in the central field-of-view but increased to a high of one diopter in the periphery.

Magnification. HDU generated images show little or no deviation from unity magnification. The sensor to display fields-of-view aspect ratio and magnification are maintained.

Field-of-view. IHADSS field-of-view was measured by filling the CRT with a uniform light pattern and then measuring luminance output as a function of IHADSS rotation. Harding et al., (1995) measured the horizontal and vertical fields of view of the displayed IHADSS image to be approximately 40 and 31 degrees, respectively.

Eye relief. Optical eye relief is defined as the distance along the optical axis from the last optical element (e.g., IHADSS HDU combiner lens) to the exit pupil. Perhaps of more functional importance is the notion of 'physical eye relief' which is defined as the distance from the closest display system component to the exit pupil. Physical eye relief determines system compatibility with auxiliary devices, e.g., corrective lenses, protective masks, etc. Harding et al., (1995) measured optical and physical eye relief under two different conditions. The conditions were with the combiner lens (a) fully retracted, and (b) fully extended. These two conditions represent the far and near extremes of eye relief. Under condition 'a', optical eye relief equaled 40.12 mm and physical eye relief equaled 13.18 mm. Under condition 'b', optical eye relief equaled 25.76 mm and physical eye relief equaled a - 5.99 mm. The negative physical eye relief in condition 'b' underscores the potential problem associated with relying upon optical eye relief measurements.

Exit pupil (size and shape). The size of the exit pupil was measured by focusing on the exit pupil with a short working distance telescope which was mounted to a precision stage. When viewed

through the telescope, the exit pupil appeared as a circular patch of light. Harding et al., (1995) measured the horizontal and vertical extent of the patch of light using the precision stage which had an incremental accuracy of just a few microns. The horizontal and vertical diameters were virtually identical thus providing a circular diameter of 10.57 mm.

Focus adjustment range. There is a focus adjustment on the barrel of the IHADSS HDU which allows the user to bring the imagery into sharp focus. Harding et al., (1995) measured this range to be -6.250 to +3.625 diopters.

IHADSS ELECTRO-OPTICAL SPECIFICATIONS

Dynamic luminance range. The luminance range of the miniature CRTs is rather high and is limited by spectral filtering, the HDU amplification circuits and the typical operational/user settings. By focusing at the exit pupil formed by the HDU, Harding et al., (1995) found a maximum luminance output of about 640 fL at saturation. This output was achieved by providing a 1-volt peak-to-peak NTSC signal to the CRT amplification circuits.

Dynamic modulation transfer function (MTF). The dynamic MTF of the HDU is defined by a spatiotemporal surface whose amplitude is modulation depth at each combination of spatial and temporal frequencies. From a visual standpoint, luminance contrast is of greater importance than modulation depth. Harding et al., (1995) measured a form of luminance contrast, termed Michaelson contrast, over a range of spatial and temporal frequencies. Below 2 Hz, the curves are well grouped. Above 2 Hz they noticed a slight increase in contrast which is atypical for most CRT curves and must be due to the amplification circuits. The drive electronics for the IHADSS CRT must have a high temporal response.

Contrast ratios. By focusing a photometer through the exit pupil to the center of the HDU's field-of-view, Harding et al., (1995) measured contrast ratios under different luminance conditions. By setting the luminance and contrast to maximum, they found a contrast ratio at saturation to be about 3.0 (640/210). To define the contrast ratio over a more usable operational range, two levels were chosen (15 and 150 fL peak luminance) to correspond with lighting conditions encountered while flying with ANVIS and under daytime conditions. For setting the output, they set the contrast to zero and adjusted the peak brightness to 1 fL. They then adjusted contrast until they achieved a luminance of either 15 fL or 150 fL at the peak. Under these conditions, they found contrast ratios of 13.6 (15/1.1) and 33.3 (150/4.5), respectively.

Gray shades. By defining gray shade increments as multiples of $2^{0.5}$, the number of gray shades can be calculated from the contrast ratios specified above. For contrast ratios of 13.6 and 33.3, we found 8 and 11 gray levels, respectively.

Display chromaticity. The spectral output of the HDU with the P-43 phosphor is narrow banded with a peak transmittance at 544 nm. This peak corresponds with the peak of the P-43 phosphor. The width of the spectrum is about 4 to 6 nm at a level equal to 50 percent of the peak. The sidebands of the P-43 phosphor are filtered out by the HDU optical filter. Chromaticity coordinates for the spectrum are $x=0.2774$, $y=0.7089$ and $u'=0.1013$, $v'=0.5826$ for the 1931 and 1976 CIE coordinates, respectively.

Display uniformity. Display/luminance uniformity was measured in the vertical and horizontal meridian of the field-of-view. The luminance fell off abruptly at the extremes of the field-of-view. Independent values were obtained for each meridian by measuring luminance uniformity to within one degree of the field-of-view border. The vertical mean luminance was $129 + 13.2$ fL and the horizontal mean luminance was $124 + 19.6$ fL. The larger horizontal standard deviation is due to the greater luminance fall-off in the peripheral field-of-view.

Visual performance with the IHADSS. Actual IHADSS performance may vary greatly from the performance measurements presented above, depending upon aviator settings, head and face anthropometry, and HDU/combiner lens adjustments. The performance metrics mostly affected by the user are luminance, contrast ratios and field-of-view.

Visual resolution. Visual resolution and contrast of IHADSS imagery are dependent on ambient light levels, background luminance and texture, and control settings of display contrast and brightness, and PNVS sensor settings of gain and bias level (Rash et al., 1990). Rash and Behar (1990) showed 90 percent of Apache aviators misadjusted the HDU focus setting by a mean of -2.25 diopters. Even without this potential problem, Snellen visual acuity with the Apache PNVS/IHADSS system is cited as 20/60 (Greene, 1988).

Field-of-view. A very important lesson learned during the early fielding of the IHADSS was the impact of fitting on the ability of the aviator to achieve the full 30- x 40-degree field-of-view (Rash et al., 1987). Unless considerable care is taken in fitting of the IHADSS IHU and HDU to the user, with special concern paid to head and face anthropometry and final extension of the combiner, a serious loss of field-of-view can occur. In addition, the integration of chemical protective masks with the IHADSS can cause similar losses in achievable field-of-views (Rash and Martin, 1987).

ANVIS SPECIFICATIONS

The ANVIS is a binocular helmet mounted display based on third generation image intensification tubes (Figure 2-2). These tubes use the principle of photomultiplication to amplify low-level ambient light. ANVIS is sensitive to spectral energy between 550 to 950 nanometers. Photons falling on a photocathode produce electrons which are multiplied within a microchannel plate and then strike a phosphor screen, producing an amplified image of the outside scene (Verona and Rash, 1989). The ANVIS currently uses a P-22 phosphor but is planned to be changed to the faster P-43 phosphor. The spectral output of the ANVIS which reaches the eye corresponds to the phosphor's spectrum, not to the spectrum of the ambient scene.

Performance specifications for the ANVIS have been divided into two categories: optical and electro-optical. Optical specifications deal with the physical light conversion path and with user controls. Electro-optical specifications deal with the image as generated by the amplification tube, microchannel plate and phosphor display. We also include a discussion on visual performance with the ANVIS.

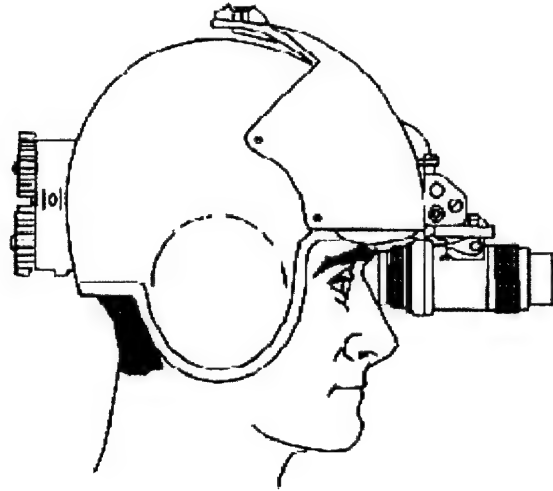


Figure 2-2. Drawing of the ANVIS attached to the SPH-4 helmet.

ANVIS OPTICAL SPECIFICATIONS

Distortion. Distortion in the ANVIS is best described by a curve which shows distortion in percent as a matter of angular position (Figure 2-3). As can be seen, little distortion is apparent even at extreme angular positions. MIL-A-49425 (CR) states that distortion shall be no greater than 4 percent across the field-of-view. Martin et al., (1994) found distortion values less than 2 percent.

Magnification. Sighting through the ANVIS should have unity gain and any deviation from this would be an estimate of magnification. Measurements taken by Martin et al., (1994) using a precision test method, found a magnification of 2 percent or less. MIL-A-49425 (CR) states that magnification shall be less than +5 percent.

Eye relief. Physical eye relief distance for the ANVIS can be specified as the greatest vertex distance where the entire 40-degree field-of-view is still visible. The distance from the anterior surface of the cornea to the surface of the last lens element of the ANVIS is specified as the vertex distance. Beyond a vertex distance of 20 mm, the field-of-view is proportionately reduced (Kotulak, 1992; McLean, 1995). Thus, 20 mm is a good estimate of eye relief.

Exit pupil. The ANVIS does not form an exit pupil per se at the eye, however, an effective exit pupil size can be defined at any specified vertex distance within the cone defined by the marginal rays.

Focus adjustment range. In MIL-A-449425 (CR), the objective focus range is specified as 28 + 3 cm to infinity. The eyepiece focus range is +2 to -6 diopters.

Interpupillary adjustment. The specifications (MIL-A-49425 (CR)) for the interpupillary adjustment range are 52 to 72 mm.

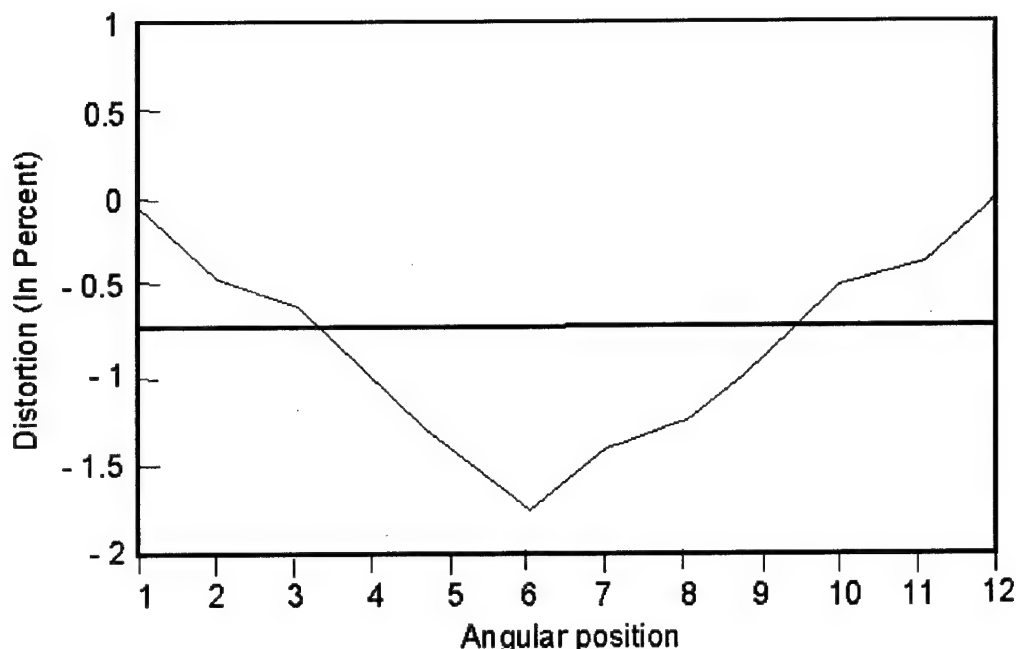


Figure 2-3. Percent ANVIS distortion as a function of angular position. Data taken from Martin et al. (1994).

Collimation. Collimation in the sense of the ANVIS is not a measurement of parallel light rays but rather is a measurement of the alignment between the left and right optics of the ANVIS. The divergence/convergence between the light beams emitted from the two eyepieces is less than 1 degree.

ANVIS ELECTRO-OPTICAL SPECIFICATIONS

Dynamic luminance range. ANVIS display luminance is a function of target and ambient light levels. Rabin (1994) evaluated ANVIS output luminance as a function of steady ambient light levels. The light levels emulated night sky conditions. Through a calibration procedure, Rabin found an approximate three log unit dynamic range for the ANVIS, although under typical night sky conditions, the dynamic range of the ANVIS is less than two log units.

Dynamic MTF. The dynamic MTF of the ANVIS has not been done due to the difficulty in generating mathematically precise near infrared images.

Contrast ratio. Target contrast is dependent upon target size, target reflectance, and lighting conditions. The luminance output of the ANVIS is linear to the point of saturation. For a small high contrast target, ANVIS contrast is high. According to unpublished data by W.E. McLean, contrast ratios of 33 (peak luminance/background luminance) are easily obtained. For small point sources of light, such as ground vehicle lights seen from afar, much higher contrast ratios are achievable.

Gray shades/levels. For a contrast of 33, 11 gray shades are available based upon a one-half octave increment between levels.

Gain. The light amplification gain of the ANVIS is dependent upon the automatic gain control mechanism. For extremely low luminance levels, a gain of 3000 is possible.

Display chromaticity. The ANVIS output using the P-22 phosphor is broadband with the peak wavelength at 537 nm. The chromaticity coordinates are $x=0.3143$, $y=0.5983$ and $u'=0.1316$, $v'=0.5639$ for the 1931 and 1976 CIE coordinate systems, respectively.

Display uniformity. Display uniformity has not been measured for the ANVIS.

Field-of-view. Field-of-view was measured by Martin et al., (1994) and was found to be 40.4 degrees. The technique they used measured the light output of the ANVIS as a function of angular rotation. Extreme light fall-off at the borders of the field-of-view made the field-of-view measurements reliable.

VISUAL PERFORMANCE WITH THE ANVIS

Resolution and ambient light level. Visual acuity with the ANVIS is dependent upon ambient light level and target contrast. In general, the higher the contrast and higher the ambient light level the higher the acuity. For high contrast targets, Snellen acuity is better than 20/40 under full moon lighting conditions and falls off gradually to about 20/80 under overcast starlight conditions. For medium contrast targets, Snellen acuity is about 20/50 under full moon conditions and falls to about 20/300 under overcast starlight conditions.

Spatial contrast sensitivity and ambient light level. Like visual acuity, spatial contrast sensitivity is likewise affected by ambient light levels. The lower the light level, the lower the contrast sensitivity. Figure 2-4 shows spatial contrast sensitivity as a function of four ambient light levels. Note the fall-off in sensitivity with increased spatial frequency.

Temporal contrast sensitivity and ambient light level. True temporal contrast sensitivity has not been measured using ANVIS. What has been measured is flicker sensitivity to an on-off target (Rabin, 1944). The target was a set of seven flickering letter 'Es' each measuring 75 minutes of arc but having different contrasts. The contrasts ranged from 4 to 100 percent in 0.23 log unit increments. The task was to identify the flickering 'E'. Figure 2-5 shows flicker sensitivity to four night sky conditions. Flicker sensitivity is greatest under full moon conditions and falls off as the ambient sky lighting conditions are reduced.

Dynamic target identification. There is no standard psychophysical procedure for specifying target identification performance.

Field-of-view. Field-of-view is dependent upon the distance from the eye to the anterior portion of the last lens element of the ANVIS (sometimes referred to as the vertex distance) (Kotulak, 1992). Within the eye relief distance the field-of-view is around 40 degrees. With vertex distances greater than 20 mm, the field-of-view decreases proportionally to the increase in distance. At 50 mm vertex distance, the field-of-view has fallen to 25 degrees.

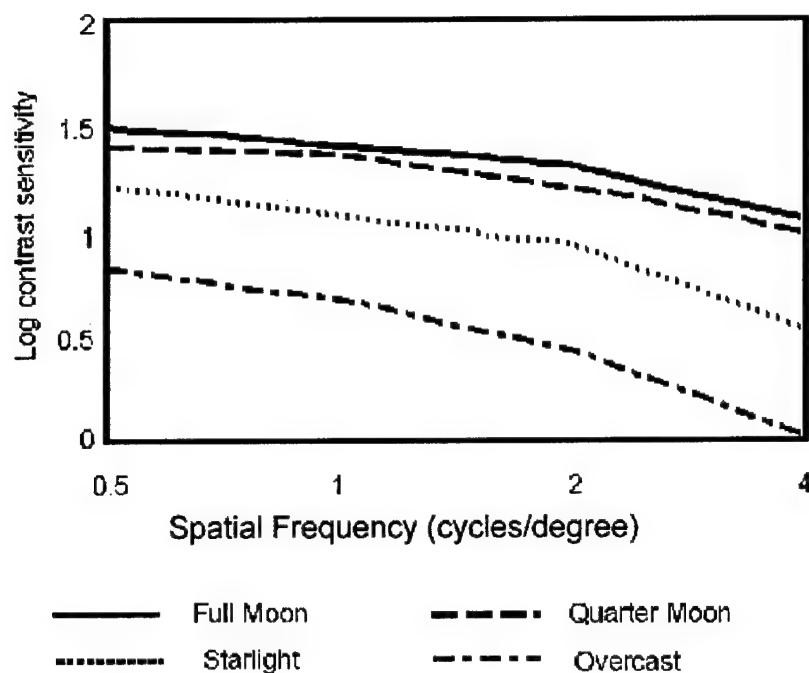


Figure 2-4. Spatial contrast sensitivity as a function of spatial frequency for different night sky conditions. Data from Rabin (1994).

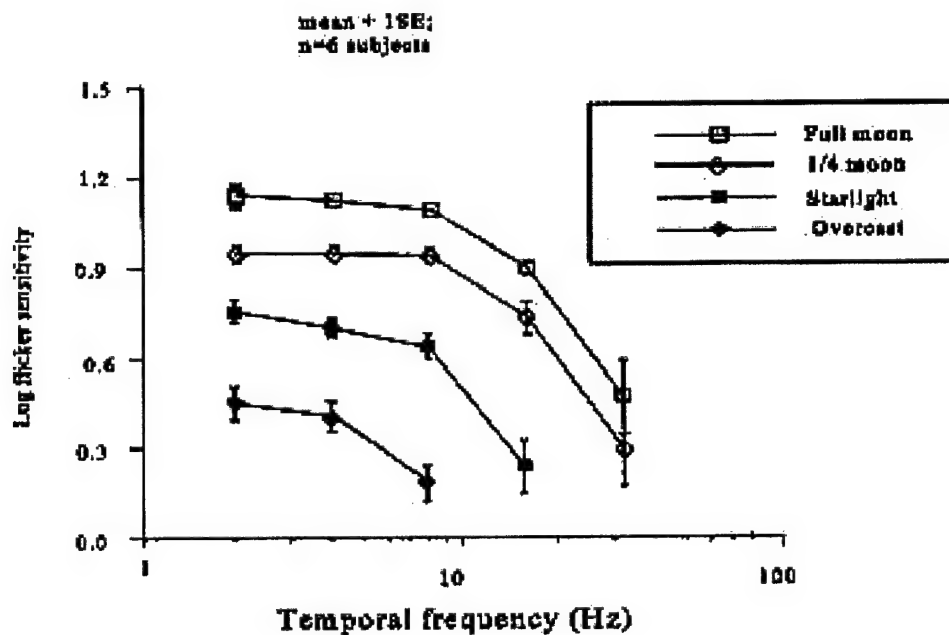


Figure 2-5. Visual flicker sensitivity viewing alphanumeric characters through the ANVIS. Data from Rabin (1994).

SUMMARY

These data presented are a compendium of general performance specifiers for fielded army helmet mounted display systems. The data were taken from published and unpublished reports and represent a summary description of these electro-optical systems. The IHADSS and ANVIS data are summarized in Tables 2-1 and 2-2, respectively. Comparisons between these two systems are not warranted since the systems are based on different operating principles.

Table 2-1.
Summary table of IHADSS performance

Test parameter	Performance measurement/specification
Optical	
Combiner lens transmittance	36 percent between 400 and 700 nm
Distortion	<1 by MIL-V-43511C scale
Optical aberrations	See Figures 2-3 and 2-4
Magnification	Unity
Field-of-view	40 degrees horizontal x 31 degrees vertical
Eye relief	Combiner fully retracted: Optical eye relief of 40.12 mm Physical eye relief of 13.18 mm Combiner fully extended: Optical eye relief of 25.76 mm Physical eye relief of -5.99mm
Exit pupil	
Focus adjustment range	Circular, diameter of 10.57 mm
Electro-optical	
Dynamic luminance range	640 fL peak
Dynamic MTF	See Figure 2-5
Contrast ratios	13.6 for 15 fL peak luminance 33.3 for 150 fL peak luminance
Display chromaticity	$x=0.2774$, $y=0.7089$ and $u'=0.1013$, $v'=0.5826$
Display uniformity	Vertical: 129 ± 13.2 fL Horizontal: 124 ± 19.6 fL

Table 2-2.
Summary table of ANVIS performance

Test parameter	Performance measurement/specification
Optical	
Distortion	Less then 2 percent
Magnification	Less then 2 percent
Eye Relief	20 mm or less
Exit pupil	effective exit pupil defined by vertex distance
Focus adjustment and range	range 28 ± 3 cm to infinity adjustment: +2 to -6 diopters
Electro-optical	
Dynamic luminance range	See Figure 2-8.
Dynamic MTF	Data not available
Gray shades	11 gray shades for naturally illuminated objects
Contrast ratios	33 to 1 for naturally illuminated objects
Gain	3000X
Display chromaticity	$x=0.2774$, $y=0.7089$ and $u'=0.1013$, $v'=0.5826$
Display uniformity	Data not available
Field-of-view	40.4 degrees circular

REFERENCES

- Behar, I. and Rash, C. E. 1990. Diopter focus adjustment of Apache IHADSS. *Aviation Digest*, 1-90-1:14-15.
- Barten, P.G.J. 1990. Evaluation of subjective image quality with the square-root integral method. *J. Opt. Soc. Am. A*, 7:2024-2031.
- Batten, P.G.J. 1993. Effects of quantization and pixel structure on the image quality of color matrix displays. *J. SID*, 1:147-153.
- Charman, W.N. and Olin A. 1965. Tutorial: image quality criteria for aerial camera systems. *Photographic Science and Engineering*, 9:385-397.
- Greene, D.A. 1988. Night vision pilotage system field-of-view (FOV)/resolution tradeoff study flight experiment report. Fort Belvoir, VA: U.S. Army Night Vision Laboratory. NV 1-26.
- Harding, T.H., Beasley, H.H., Martin, J.S., and Rash, C.E. 1995. Physical evaluation of the integrated helmet and display sighting system (IHADSS) helmet display unit (HDU). Fort Rucker, AL: U.S. Army Aeromedical Research Laboratory. USAARL Report No. 95-32.
- Kotulak, J.C. 1993. In-flight field-of-view with ANVIS. Fort Rucker, AL: U.S. Army Aeromedical Research Laboratory. USAARL Report No. 93-8.

Martin, J.S., Beasley, H.H., Verona, R.W. and Rash, C.E. 1994. Semiautomated methodology for measurement of field-of-view, and distortion of night vision devices as defined in MIL-A-49425(CR). Fort Rucker, AL: U.S. Army Aeromedical Research Laboratory. USAARL Report No. 94-25.

McLean, W.E. 1995. Video method of measuring field-of-view of electro-optical devices versus eye clearance. Fort Rucker, AL: U.S. Army Aeromedical Research Laboratory. USAARL Report No. 95-30.

Rabin, J. 1994. Spatial contrast sensitivity through aviator's night vision imaging system (Reprint). Fort Rucker, AL: U.S. Army Aeromedical Research Laboratory. USAARL Report No. 94-19.

Rash, C. E. and Martin, J. S. 1987. The Effect of the M-43 Chemical Protective Mask on the Field-of-View of the Helmet Display Unit of the Integrated Helmet and Display Sighting System. Fort Rucker, AL: U.S. Army Aeromedical Research Laboratory. USAARL LR 87-10-2-5.

Rash, C. E., Martin, J. S., Gower, D. W., Licina, J. R., and Barson, J.V. 1987. Evaluation of the U.S. Army Fitting Program for the Integrated Helmet Unit of the Integrated Helmet and Display Sighting System. Fort Rucker, AL: U.S. Army Aeromedical Research Laboratory. USAARL Report No. 87-8.

Rash, C. E., Verona, R. W., and Crowley, J. S. 1990. Human factors and safety considerations of night vision systems flight using thermal imaging systems, Helmet-Mounted Displays II. R. J. Lewandowski, Editor. Proceedings SPIE. 1290:142-160.

Nelson, S.A. and Cox, J.A. 1992. Quantitative helmet mounted display system image quality model. Helmet-Mounted Displays II. R. J. Lewandowski, Editor. Proceedings SPIE.1695:128-137.

Westerink, J.H.D.M. and Roufs, J.A.J. 1989. Subjective image quality as a function of viewing distance, resolution, and picture size. *SMPTJ*, 98:113-119.

TASK 3

Biochemical Research and Analytical Support for USAARL Research Programs

INTRODUCTION

Task 3 supports efforts to assess the effects of melatonin on women's reproductive physiology and its efficacy in the regulation of sleep during shift-work transitions and troop deployment across time zones. Several studies have been designed to detect any unforeseen effects of melatonin on women's reproductive physiology. In addition, the potential use of melatonin and future deployment scenarios is imminent because of its known efficiency in the prevention of jet lag and treatment of certain sleep disorders. Prior to widespread use, it is critical to clearly understand potential side effects specific to women's physiology. In support of this research, multiple samples of urine and saliva obtained from volunteer subjects must be assayed for the presence of melatonin and its metabolites and other hormones such as LH, FSH, prolactin and estradiol. This task order will ensure that all appropriate data analysis involving melatonin will be conducted and that results will be published in a timely manner.

The overall objective of this task then is to provide biochemical/pharmacological support to investigators studying the effects of melatonin on female reproductive physiology and to investigators studying the use of melatonin to prevent jet lag and shift-lag during rapid deployment and night operations. A secondary purpose is to assist in the evaluation of melatonin effects on pituitary-gonadal function and CNS function.

Detailed contributive results of the Task 3 investigation can be found in USAARL Report Nos. 97-3, 97-4 and 98-30 and 98-36. Here we will present results specific to the Task 3 effort.

MELATONIN ADMINISTRATION TO HEALTHY FEMALES DOES NOT ALTER MENSTRUAL CHARACTERISTICS

Melatonin, a natural hormone which has been shown to resynchronize circadian rhythms and induce sleep in humans (Arendt et al., 1987; Dawson and Encel, 1993; Reiter, 1991; Wurtman, 1986), is currently being marketed widely as a dietary supplement to alleviate desynchronosis (desynchronization of physiological and behavioral rhythms) and assist in obtaining quality sleep. Desynchronosis often results from rapid shifts in work schedules from day to night, or from shifts in the light-dark cycle due to time zone crossing. Symptoms resulting from desynchronosis include fatigue, sleepiness, lethargy, insomnia, gastrointestinal tract disorders, and poor mental performance (for review see Comperatore and Krueger, 1990).

Melatonin therapy has been demonstrated in several studies to be effective in preventing sleep loss and in maintaining alertness following travel across multiple time zones (Arendt and Broadway, 1987; Comperatore et al., 1996a; Petrie et al., 1989). Thus, melatonin can be a potentially effective chronobiotic and ameliorate desynchronosis during travel. Melatonin (N-acetyl-5methoxytryptamine) is an endogenously occurring hormone produced by the pineal

gland in the absence of bright light. In humans, melatonin synthesis reaches peak levels during the night and lowest levels during the day. Known side effects of melatonin chronobiotic doses (5-10 mg) are limited to sleepiness, fatigue, and reduced alertness shortly after administration, but not upon awakening (Arendt et al., 1987; Comperatore et al., 1996a; Petrie et al., 1989). However, in females, due to a potential inhibitory influence of melatonin over the hypothalamo-pituitary-ovarian axis (Aleem, Weitzman, and Weinberg, 1984; Nordlund and Lemer, 1977), melatonin use may be associated with secondary disruptions of the menstrual cycle. Although the exact relationship between melatonin and the monthly cycle in females is unclear, there is considerable evidence for interaction between melatonin and luteinizing hormone (LH) and follicle-stimulating hormone (FSH) (Cagnacci, Elliott and Yen, 1991; Diaz et al., 1993; Nordlund and Lemer, 1977; Penny, Stanczyk, and Goebelsmarm, 1987; Voordouw et al., 1992). Can melatonin be used safely by females to reduce desynchronization resulting from travel, or could short-term use of this nonprescription hormone result in disruption of the menstrual cycle? Such disruption could at the very least increase the already stressful conditions associated with deployment.

Here, we investigated the effect of exogenous melatonin (10 mg) on menstrual characteristics in normally cycling healthy females. Melatonin was given at bedtime (2300 hours) for 7 consecutive nights during the late follicular and early luteal phase of the monthly cycle.

METHODS

SUBJECTS

Subjects were 17 healthy females between the ages of 18 and 36 (mean=27.2), nonpregnant, and not taking any medication that could interfere with normal ovulatory events. Additional requirements were menstrual cycles between 21-36 days with no variation more than 3 days above or below the previous cycle for each volunteer, and no oral contraceptive use within 3 months prior to participation. The study was double blind and placebo controlled, and all participants were assigned randomly and exhaustively to either a melatonin (n=8) or placebo (n=9) group. The 8 melatonin volunteers had a mean age of 26.5, while the mean age of the placebo group was 27.8. All participants gave their informed consent and were advised of their right to withdraw at any time. Participants were asked to refrain from consuming alcohol, caffeinated beverages, or any type of medication with known central nervous system effects during the in-house portion (7 days) of their 3 months of participation. Use of nonsteroidal anti-inflammatory drugs such as ibuprofen were limited also since they have been found to decrease melatonin synthesis (Badia, Myers, and Murphy, 1992).

MELATONIN AND DOSE ADMINISTRATION

Melatonin was obtained from Regis Chemical Company, St. Louis, Missouri, and encapsulated by Regional Services, Inc., Boston, Massachusetts. The 10-mg dose used in this study was selected because of its lack of toxicity (Sugden, 1983), short half-life, lack of side effects, sleep induction effects, and its already demonstrated efficacy in maintaining sleep and alertness in males traveling across multiple time zones (Comperatore et al., 1996). In order to

avoid confounding the study with unwanted changes in sleep onset induced by melatonin's chronobiotic properties, the time of day selected for melatonin or placebo administration (2300 hours) fell in the less sensitive zone of the phase response curve for melatonin (Lewy et al., 1995).

PROCEDURES

The first and third months of participation involved collection of information on the timing of menses and ovulation, menstrual regularity, and LH and FSH levels. On each day of both months, subjects were asked to provide a sample of first void urine. Menstrual regularity data (questionnaire) were used to document the timing of menses and to approximate the scheduling of the 7 days comprising the preovulatory LH surge for the in-house portion of menstrual cycle 2. The timing of menses and the preovulatory LH surge was used to document any advances or delays of the menstrual cycle related to the melatonin administration regimen. Since this information could not be obtained from pregnant volunteers, pregnancy tests were conducted throughout the study beginning on day 1 of cycle 1.

During cycle 2, subjects reported to the sleep laboratory at the U.S. Army Aeromedical Research Laboratory (USAARL), Fort Rucker, Alabama, at 0630 on day 10 and lived in the laboratory until 0800 on day 17 when they were released after a brief medical evaluation. Melatonin (10 mg) or placebo was given at 2300 on days 10 through 16. In addition to first void urine samples, subjects were asked to provide specimens every 2-3 hours from 0630 until 2300. Subjects also were asked to drink at least an 8-oz. glass of water between voids, but they were not encouraged to consume liquids in excess. Vital signs were recorded at bedtime and upon awakening during dose days.

BIOCHEMICAL ASSAYS

LH AND FSH ASSAYS

Hormone levels in urine were used to identify the monthly surge in LH, as well as to determine whether pharmacological levels of melatonin inhibit LH and/or FSH release. Urine samples, collected daily at rise time during the three complete menstrual cycles of the study period, and those collected every 3 hours while awake and just prior to dose during drug administration days, were used. Urinary levels of LH and FSH were measured by direct immunoassay using the Abbott IMx* automated benchtop immunochemistry analyzer system (Fiore et al., 1988). All urine samples were stored at 1-4°C in the USAARL biochemistry lab and assayed the same day or frozen until analysis.

PREGNANCY TESTING

Tests for human chorionic gonadotropin (hCG) were used to detect pregnancy. For maximum sensitivity at critical times during the study (the first day of cycle 1, the first day of melatonin/placebo administration), pregnancy tests were done on samples of blood. Serum levels of hCG were measured by direct immunoassay using the Abbott IMx automated benchtop immunochemistry analyzer system, which has a sensitivity of about 2 mIU/ml for hCG in serum.

MELATONIN ASSAY

Urinary levels of 6-sulphatoxymelatonin (aMT6s) were measured by direct radioimmunoassay (RIA) from specimens collected during days 10-17 of menstrual cycle 2. Urine samples were refrigerated and frozen if not assayed within a day. RIA kits for aMT6s were obtained from American Laboratory Products Company and from Stockgrand Ltd.

DATA ANALYSIS

The LH surge was identified for each menstrual cycle (1-3). For each subject, the day(s) of the LH surge for each month of participation served as a dependent variable. These data, as well as LH assay data obtained throughout days 11-16, were analyzed using a mixed factorial analysis of variance with two levels of the between subjects factor Drug (melatonin and placebo) and six levels of the within subjects factor Day (cycle days 11-16). A similar analysis strategy was used for FSH levels. The aMT6s assays on urine samples collected during days 11-16 of menstrual cycle 2 was used to document elevated levels induced by the administration of the low mg dose of melatonin.

For each subject, menses onset day and duration was recorded for the three consecutive menstrual cycles. The timing of menses was measured from menstrual cycle numbers 1 to 2 and from 2 to 3. The periodicity established by these observations constituted two additional dependent variables capable of reflecting changes in menstrual regularity. Menses periodicity data which occur outside of the expected range of menstrual variability (A 3 days), indicated by participants in the volunteer screening questionnaire, were considered significant. In this case, strict use of statistical analysis would ignore idiosyncratic characteristics of menstrual regularity.

RESULTS

MELATONIN METABOLITE CONCENTRATIONS

Levels of aMT6s were assayed from urine samples provided while volunteers were in-house during cycle 2. Although there was considerable variation between volunteers, there was no question as to the identity of those in the melatonin group. The mean level of aMT6s in the first void of all 17 volunteers on day 10 of cycle 2 (prior to first dose) was 26.8 ~12.8 ng/ml. The highest value recorded for any placebo volunteer during their in-house stay was 47.8 ng/ml. The mean level of aMT6s in the first void of the eight melatonin volunteers on day 11, following their first administration of melatonin, was 20622.4 f 9339.8 ng/ml. Figure 3-1 shows the mean aMT6s concentration for each of the seven daily samples for one member of the placebo group during the 6 in-house test days (11-16), as well as the same information for one member of the melatonin group. Note in Figure 3-1 that not only are aMT6s levels tremendously elevated in the first void from the melatonin volunteer, but they remain elevated throughout the day. Although the elevation in aMT6s in the first void sample is consistent in all melatonin volunteers, the sustained elevation above placebo levels throughout the day is not. Evidence of individual variation is provided by levels of aMT6s returning to placebo level late in the day for some volunteers, but not for others. The first two samples in the morning are the highest in both the

melatonin and placebo groups, and after a midday fall, volunteers in both groups often show an increase in aMT6s in the sample collected at bedtime (see Figure 3-1).

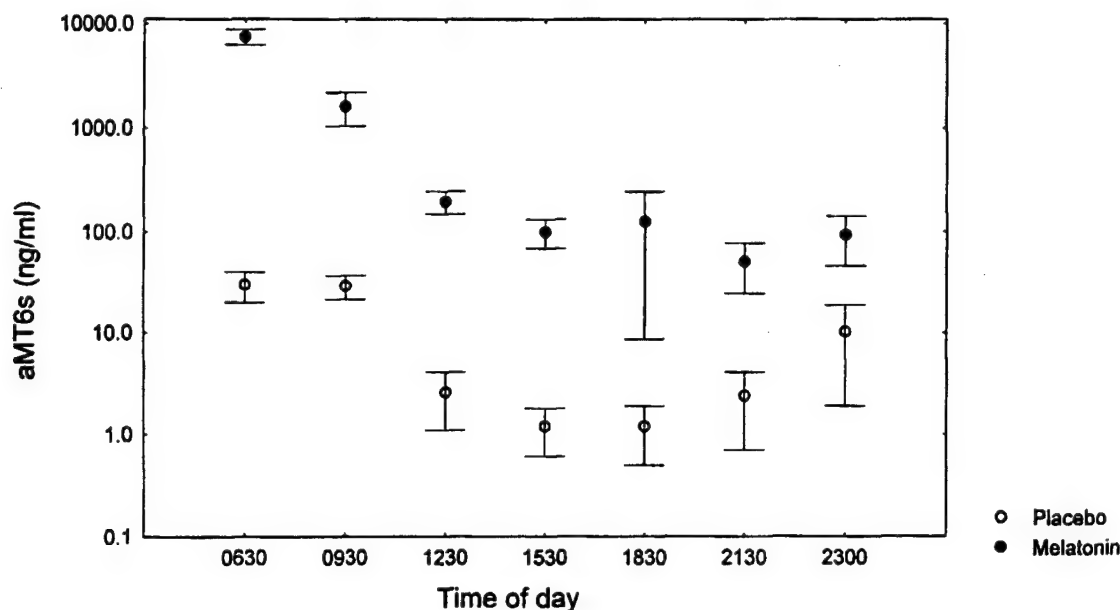


Figure 3-1. Melatonin metabolite level in urine. Mean aMT6s concentration for each of the seven daily samples during the 6 in-house post-administration days for one member of the placebo group and one member of the melatonin group. Error bars indicate the standard error of the mean.

AWARENESS OF SYMPTOMS FOLLOWING MELATONIN

Following the in-house stay during cycle 2, all volunteers were asked if they thought they had received melatonin. Three of the 17 responded "yes," but none of the three were in the melatonin group. Individuals from both the melatonin and placebo group reported sleeping well at night, and having difficulty awakening in the morning. Vital signs were checked upon awakening and before getting out of bed in the morning, and they were never outside of the normal physiological range. One member of the melatonin group felt nauseous on two separate mornings, but did not feel she was taking melatonin. There apparently are no consistent symptoms the next day following 10 mg of melatonin taken at bedtime. It is also quite apparent from our observations that volunteers are unable to distinguish between melatonin and placebo.

LENGTH OF MENSES AND MENSTRUAL CYCLE AFTER MELATONIN

Although our sample size was limited (n=8 for melatonin), there were no consistent changes in either length of menstrual cycle or menses. Since most volunteers indicated that an occasional increase or decrease in the length of their menstrual cycle of up to 3 days was within normal limits, we elected to follow the same guidelines. Therefore, a change of more than 3 days

had to occur before it was considered physiologically significant. Table 3-1 lists the menstrual cycle length based upon the first day of menses (CL-A, 3 cycles), the cycle length based upon the LH surge for cycle 1-2 and 2-3 (CL-B, 2 cycles), and the length of menses (ML, 3 cycles), for each of the 17 participants.

Table 3-1.
Menstrual cycle characteristics

Vol #	Drug	CYCLE 1			CYCLE 2		CYCLE 3		
		CL - A	CL - B	ML	CL - A	ML	CL - A	CL - B	ML
01	M	29	27	4	28	4	25	30	3
02	M	26	26	6	26	5	25	25	6
03	P	28	25	3	29	3	29	31	4
04	P	29	27	5	27	5	32	33	5
05	M	24	24	5	27	5	24	26	4
06	P	30	28	5	26	5	32	30	5
07	P	31	35	4	26	4	24	16	3
09	M	26	28	3	28	4	25	27	5
11	M	26	28	6	28	6	32	32	4
12	M	30	28	6	27	5	31	32	5
15	M	27	27	8	27	7	28	28	7
16	P	25	25	5	27	5	27	27	5
17	P	27	29	5	29	3	29	28	5
19	P	27	26	5	22	4	27	24	6
20	P	26	26	8	24	5	21	24	4
24	P	34	35	6	32	6	31	30	6
28	M	31	27	5	26	6	25	25	7

CL-A Cycle length based upon first day of menses

CL-B Cycle length based upon LH peak

ML Length of menses

Remembering that participants received melatonin starting on day 10 of cycle 2, based upon menses onset, the length of cycle 2 compared to cycle 1 was shorter for three and the same for six placebo subjects (overall mean 2.9 day difference), and shorter for one, and the same for seven melatonin subjects (overall mean 2.0 day difference). Comparing cycle 3 to cycle 2, overall length was greater for three and the same for six in the placebo group (overall mean difference=2.4 days), and greater for two and the same for six in the melatonin group (overall mean difference=2.5 days). Figure 3-2 shows this information plotted as change in cycle length for each subject; it is readily apparent that there is no systematic change for either placebo or melatonin group. The horizontal dotted lines in the figure indicate the minimum change which must be exceeded for physiological significance.

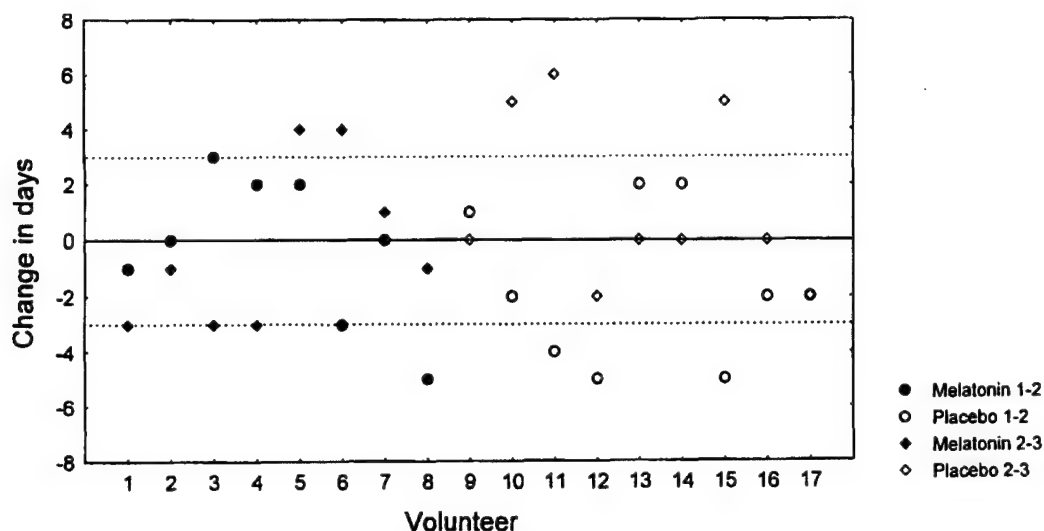


Figure 3-2. Change in menstrual cycle length based upon first day of menses for all members of both the melatonin and placebo groups between cycle 1 and 2 and between cycle 2 and 3. The dotted lines indicate 3 days which we have selected to indicate physiological significance.

Figure 3-3 shows a comparison between cycle lengths as determined by the number of days between LH peaks. The number of days between the identified LH surge is compared between cycles 1 to 2 and 2 to 3. Again using 3 days as a minimum for physiological significance (dotted lines), the melatonin group had two increases and six unchanged, and the placebo group had two increases, two decreases, and five unchanged. As was the case with changes in cycle length determined by first day of menses, there was no systematic change.

Since the in-house dose days occurred after menses in cycle 2, both cycle 1 and cycle 2 serve as controls for menses. Average length of menses for the 3 cycles was 5.4, 5.3, and 5.1 days for the eight melatonin group members, and 5.1, 4.4, and 4.8 for the nine members of the placebo group. The average length of menses for the first 2 cycles taken together was 5.31 for the melatonin group and 4.78 for the placebo group. For cycle 3, the only post-melatonin month, the average length of menses was 5.13 days for the melatonin group and 4.78 days for the placebo group. Figure 3-4 shows changes in menses between cycles 1 and 2 (2 pre-melatonin cycles) and between cycles 2 and 3 (a pre- and a post-melatonin cycle) for all members of both melatonin and placebo groups. No members of either the placebo or melatonin groups demonstrated changes of greater than 2 days in the post-melatonin cycle, and only two placebo volunteers and one melatonin volunteer showed a 2-day change. Inspection of Figure 3-4 shows no apparent difference in melatonin or placebo groups between the pre- and post-melatonin cycles. A two-way analysis of variance applied to the Drug (melatonin and placebo) and the Cycle (pre- and post-melatonin) factors revealed that the melatonin regimen did not significantly change the duration of menses ($F [1,15] = 1.869$; $p = 0.192$).

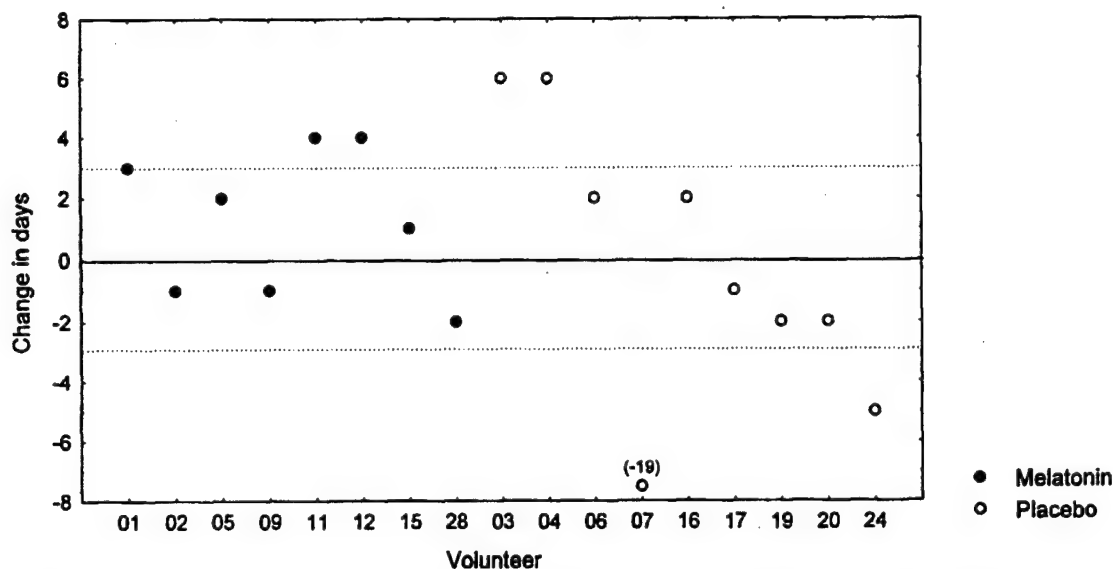


Figure 3-3. Change in menstrual cycle length based upon timing of LH peak for members of both the melatonin and placebo groups between cycles 1-2 and 2-3. The dotted lines indicate 13 days which we have selected to indicate physiological significance.

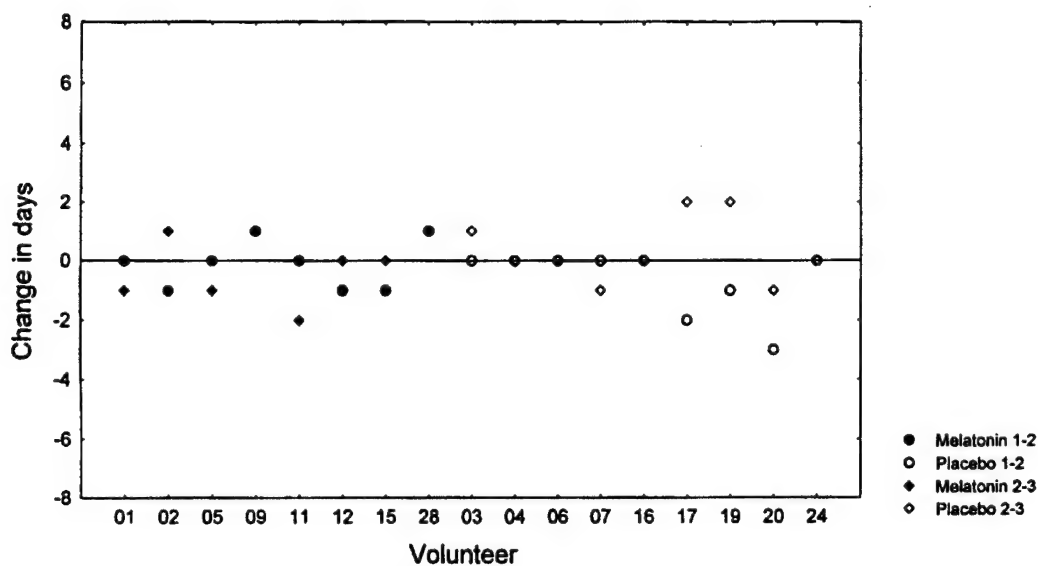


Figure 3-4. Change in length of menses for all members of both the melatonin and placebo groups between cycles 1 and 2 and between cycles 2 and 3.

USE OF IMx TECHNOLOGY WITH URINE SAMPLES

Since there are suggestions in the literature that melatonin may influence levels of LH and FSH, we not only analyzed daily first void urine samples for these hormones, but we also analyzed seven samples daily for each volunteer while in-house. Because the IMx system is recommended for detecting LH and FSH in plasma, we wanted to verify the reliability of the

system for LH and FSH activity in urine. Eight volunteers were asked to check their first void samples with the Whitehall-Robbins Clearplan Easy one-step ovulation predictor, which works by measuring LH in the urine utilizing monoclonal antibody technology. Six of the eight had positive results on the ovulation predictor on the same day that IMx results showed the LH peak. The other two volunteers had positive results on the ovulation predictor within 2 days of the IMx determined LH peak. This is not surprising since LH levels during the mid-cycle surge often remain elevated for 2 days or more. There are no similar indicators for FSH in urine, but since an increase in FSH is expected about the same time as the LH surge, and one was seen in our samples, we assumed the IMx also provided an accurate indication of FSH activity as well.

MELATONIN EFFECTS ON LH AND FSH

Figure 3-5 is a typical plot of LH and FSH levels against day for the entire three cycles of the study from one of our volunteers. In most cases, the baseline activity for LH is quite low and there is a strong elevation during the preovulatory surge. Often the surge persists for 2 or 3 days as in cycle 1 of Figure 3-5 (2 LH peaks separated by a day). Even in cycle 1 of this figure, which demonstrates the smallest of the three peaks, LH is elevated about six times above baseline. FSH results are usually less clear, with two or more monthly increases, less peak amplitude, and less peak separation from baseline activity. Because of these reasons, we are less comfortable addressing differences in FSH activity. Figure 3-6 shows LH and FSH levels against day for the entire three cycles of the study from the volunteer showing the strongest LH and FSH peaks. Note the tremendous separation from baseline for both LH and FSH during all three cycles. Note also, the scale difference between Figures 3-5 and 3-6 (40 mIU vs 100 mIU). Comparison of Figures 3-5 and 3-6 provides a good indication of the individual variation seen in these data.

Figure 3-7 shows mean LH levels across days for both the placebo and melatonin groups for each of the seven sampling times during the in-house stay. Figure 3-8 provides the same information for FSH. There are no statistically significant differences in either case. It is readily apparent from the figures that the mid-cycle surge for LH and FSH appears during the end of the in-house week. LH/FSH increase above baseline is especially pronounced during days 13-16.

Although there appears to be a trend for greater elevation in the melatonin group, especially for LH in Figure 3-7, a three-way analysis of variance applied to the Drug (melatonin and placebo), Day (7 days), and Time of day (7 samples per day) factors did not reveal significant group differences in LH levels ($F [1,6] = 1.0252$; $p = 0.35$) or interactions between the factors ($F [36,216] = 1.011$; $p = 0.458$).

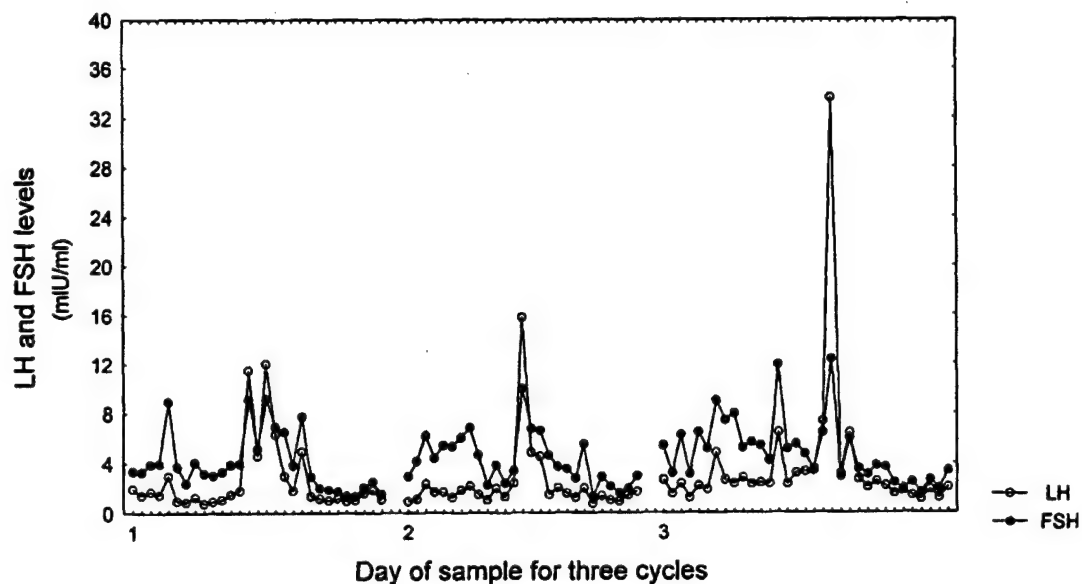


Figure 3-5. Daily LH and FSH levels over three cycles for volunteer number 4. LH and FSH levels for each day of the three cycles of participation for one of the placebo volunteers.

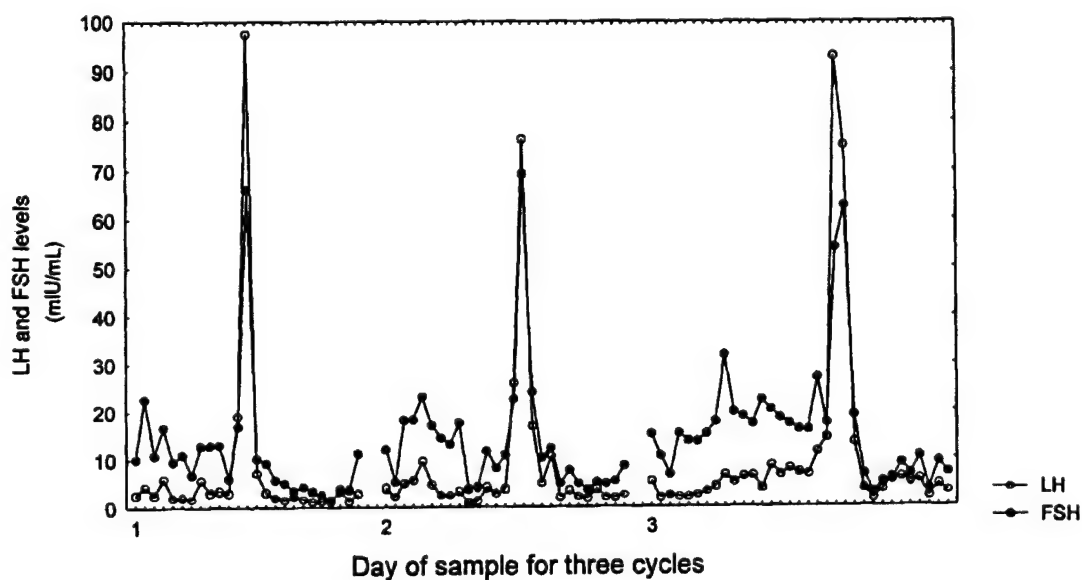


Figure 3-6. Daily LH and FSH levels over three cycles for volunteer number 11. LH and FSH levels for each day of the three cycles of participation for the volunteer (melatonin group) demonstrating the strongest LH and FSH peaks.

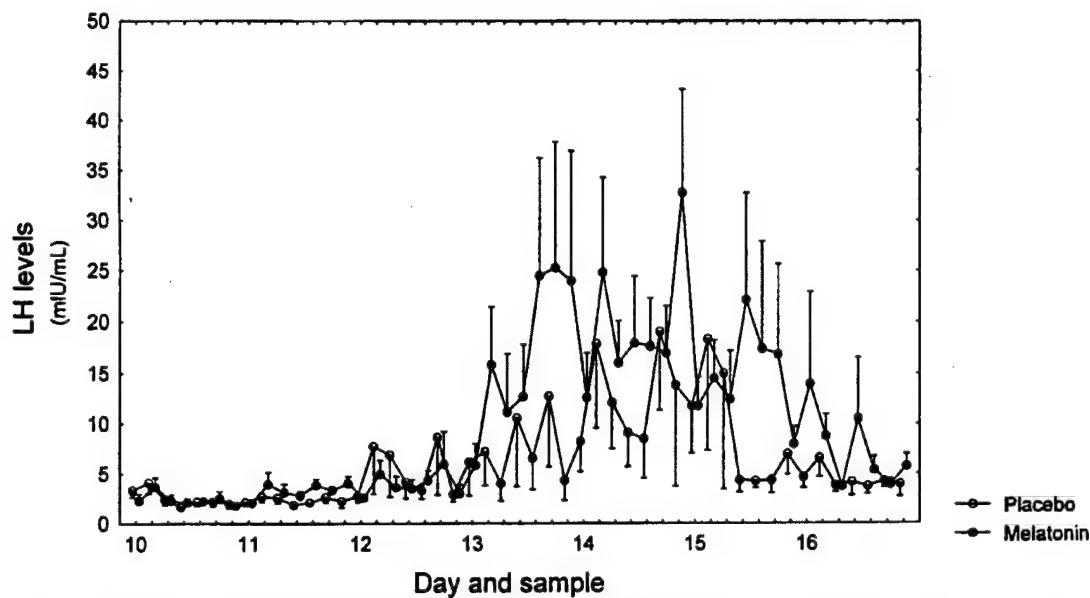


Figure 3-7. Mean LH levels during the seven day in-house stay for both melatonin and placebo groups.

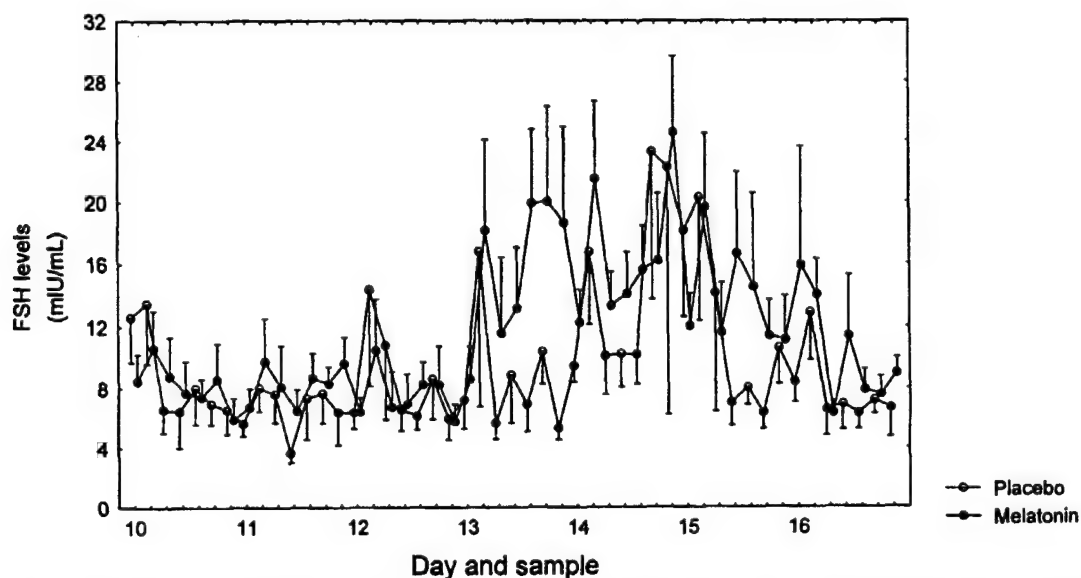


Figure 3-8. Mean FSH levels during the seven day in-house stay for both melatonin and placebo groups.

Our original inspection of the LH data from first void samples suggested decreased levels in the melatonin group during the cycle 2 surge, following their in-house stay and melatonin administration. Closer inspection showed decreased levels for both the melatonin and placebo groups, indicating that the decrease during cycle 2 could not be attributed to melatonin. Figure 3-9 shows the mean peak LH values for the three cycles for both the melatonin and placebo groups, as well as the mean peak values from multiple daily samples while in-house. Note that the in-house values for both melatonin and placebo groups are identical and higher than any of the values for the other 3 months. Table 3-2 lists the LH and FSH peaks determined from first

void samples for each of the three cycles, as well as the LH and FSH peak determined from 7/day urine samples during the in-house stay. Examination of this table (compare the cycle 2 and the cycle 2 in-house columns) reveals that none of the first void samples during cycle 2 caught the LH peak. It was always in a sample later in the day. Fifteen of our 17 volunteers, providing urine samples every 3 hours from 0630 to 2300, demonstrated their LH surge while in-house. Of those 15, 4 exhibited their peak LH level at 0930 and the other 11 were all in the afternoon. Unfortunately, this means we do not know the actual value of the LH peak for cycles 1 and 3, although it was almost certainly higher than recorded in our first void samples. The fact that the peak level of the LH surge during cycle 2, based upon multiple daily samples while in-house, was identical for both melatonin and placebo groups suggests that there is no difference between the two groups.

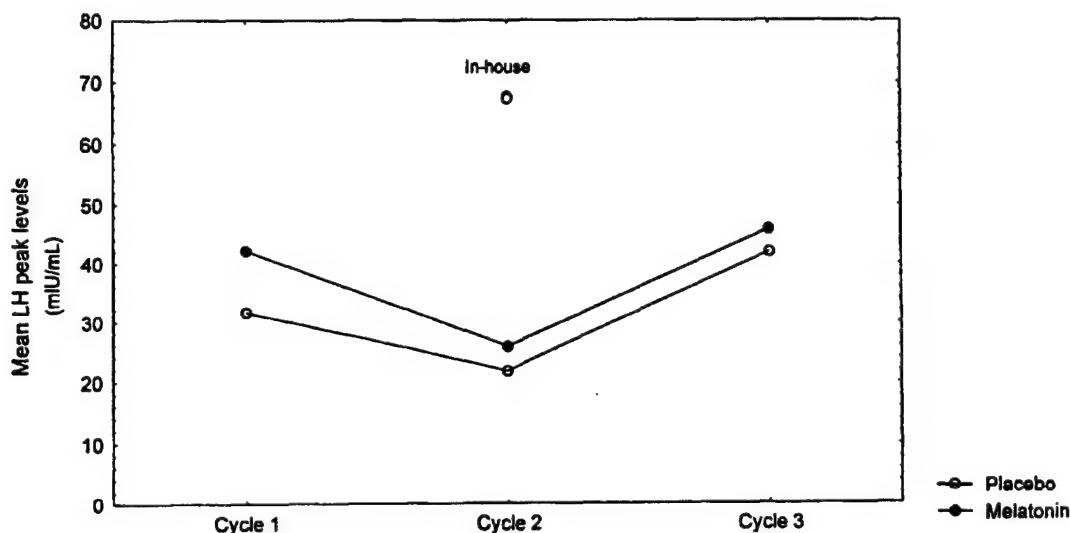


Figure 3-9. Mean peak LH levels for three cycles of participation. Mean peak LH levels based upon first void urine samples for both the melatonin and placebo groups for each of the three cycles as well as the mean peak value based upon multiple daily samples during the in-house phase of cycle 2.

Analysis of FSH results were less consistent. Again, based upon analysis of first void samples, six of eight melatonin volunteers showed decreased FSH levels from cycle 1 to cycle 2, while in the placebo group, there were four decreases, two increases, and three with essentially no change. There were no systematic changes in either group with respect to the timing of the monthly surge (see Table 3-3). For cycle 1 to 2, the melatonin group showed four increases, two decreases, and two with no change, while the placebo group showed four increases, four decreases, and one with no change. For cycle 2 to 3, the melatonin group showed four increases, three decreases, and one with no change, while the placebo group showed four increases, two decreases, and three with no change.

Table 3-2.
LH and FSH peak values

Vol #	Dose	Cycle 1		Cycle 2		Cycle2*		Cycle 3	
		LH	FSH	LH	FSH	LH	FSH	LH	FSH
01	M	29.3	39.9	17.1	21.8	46.1	44.6	46.2	46.7
02	M	77.9	99.3	34.1	19.5	108.7	57.9	92.1	68.2
03	P	19.9	27.2	15.4	26.1	NP	NP	7.8	16.9
04	P	12.0	9.2	15.8	10.0	77.1	43.8	33.6	12.4
05	M	18.9	24.3	13.3	14.8	45.4	41.7	5.3	NP
06	P	28.6	17.0	28.7	17.0	67.9	22.9	55.9	27.9
07	P	48.3	25.1	9.4	11.3	18.4	21.6	88.9	24.8
09	M	18.3	34.7	16.3	13.6	85.1	44.0	9.6	21.3
11	M	97.5	66.2	76.3	69.3	93.2	69.3	92.9	62.7
12	M	19.2	14.3	13.6	11.9	41.7	43.0	25.1	23.7
15	M	38.4	17.3	30.0	21.5	85.7	40.9	71.2	32.4
16	P	50.0	35.4	31.3	19.6	63.3	32.4	23.4	18.6
17	P	48.7	50.1	44.3	43.6	104.9	80.0	66.3	46.7
19	P	57.7	150.0	8.8	10.9	45.6	61.8	67.4	150.0
20	P	5.7	19.8	25.0	49.7	94.4	150.0	17.0	21.2
24	P	14.4	8.9	17.8	11.0	NP	NP	17.4	13.8
28	M	37.9	22.4	6.3	8.6	35.6	42.5	24.1	30.7

Cycle 2* Values determined from multiple daily samples while in-house.

THE CORRELATION BETWEEN PLASMA AND SALIVARY MELATONIN, AND URINARY 6-SULPHATOXYMELATONIN EXCRETION IN THE HUMAN

As melatonin is a natural hormone which can resynchronize circadian rhythms and induce sleep in humans, and may therefore be used to ameliorate desynchronization during rapid deployments as well as rotation from daytime to nighttime duty schedules. The effects of various doses of melatonin or time of administration vary and must be determined to derive the maximum benefit from melatonin therapy. Since it is seldom practical to obtain sufficient blood samples to determine pineal function/melatonin secretion curves, it is essential to know the correlation between salivary melatonin or urinary 6-sulphatoxy melatonin (aMT6s) and blood melatonin. Although correlations have been done previously by other laboratories between plasma or saliva melatonin and aMT6s, assay results are known to vary depending upon the type of assay used as well as other laboratory specific factors. Our primary objective is to perform melatonin or aMT6s assays on previously collected samples of blood, saliva, and urine, and determine the correlation between them. These results will enable us to study the efficacy of various melatonin regimens without the necessity of drawing multiple blood samples from volunteers.

Useful measures of pineal activity are frequently needed in various studies investigating sleep an/or sustained operation, and various endocrinology parameters. Plasma measure of melatonin levels provide this information, however, frequent blood sampling is not always practical or possible. Plasma level of melatonin are low in the daytime and increase as night, peaking at about 0300. Melatonin levels can be determined in saliva utilizing techniques similar to those for plasma, but without the problems associated with frequent blood draws. Also, the major urinary metabolite of melatonin, aMT6s, can be quantified through use of the appropriate assay. However, there is always a question of the correspondence between salivary melatonin, urine metabolites, and the actual melatonin levels in blood. We previously have investigated the use of melatonin in eastward deployments to maintain sleep and cognitive function (Aviat. Space Environ. Med. 67:520), and it effect of hormone levels and menstrual characteristics when administered at 2300 (USAARL Report No. 97-04) or 1300 (USAARL Report in preparation). Anticipating future studies investigating the use of melatonin in various deployment situation, or its endogenous production as a screen for various task, we proposed this correlation study to compare non-invasive assay methods with plasma assays.

Table 3-3.
Cycle day of LH peak

Vol #	Dose Condition	Cycle 1	Cycle 2	Cycle 3
01	M	15	13	15
02	M	13	14	13
03	P	20	18	22
04	P	16	14	20
05	M	15	15	15
06	P	16	14	18
07	P	19	23	11
09	M	13	15	14
11	M	13	16	21
12	M	14	14	18
15	M	13	14	15
16	P	13	13	13
17	P	14	15	15
19	P	14	13	15
20	P	14	15	15
24	P	20	22	19
28	M	19	15	14

The study involved the use of radio-immunoassays (RIA) to quantitate melatonin or metabolite levels. The assays are not trivial, and we are one of the few laboratories in the country doing this work. The opportunity presented itself to do a correlation study on existing

samples, and we thought the study was worth the minimal cost in the context of future melatonin studies.

In a separate study, 20 female volunteers between the ages of 18 to 38 spent two 24-hour days in Lyster hospital and provided hourly samples of blood and saliva and a urine sample every 3 hours. Ten of the volunteers received a single administration of oral melatonin (10mg) on one of the hospital days and the other ten received placebo. Samples were analyzed for levels of prolactin and luteinizing hormone, and additional blood, saliva, and urine samples were frozen at the time of collection. Using RIA kits, samples of serum and saliva were assayed for melatonin activity, and urine samples were assayed for aMT6s. All samples were assayed in duplicate. Mean serum and salivary melatonin and urinary aMT6s concentrations were determined for both the melatonin and placebo groups. Correlations then were determined between serum melatonin and both saliva melatonin and urinary aMT6s, and between saliva melatonin and urinary aMT6s.

Blood and saliva samples were collected hourly from 0800 until 0800 the next day. Urine samples were collected every 3 hours starting at 1000 and ending at 0700 the next day. Hourly mean melatonin levels in blood and saliva and aMT6s levels every 3 hours show clearly, that in humans the diurnal rhythm is serum melatonin, is mirrored in both saliva concentration and aMT6s excretion in the urine. If we base our observation on samples collected on non-dose days so they are not confounded by changing schedules or dose administration, the peak saliva concentration occurs one hour after the peak blood concentration. It should be emphasized that our collection is hourly. Urinary concentrations of aMT6s also occur after the blood melatonin peak, but again we are limited by 3-hour samples. A urinary difference is not surprising, since aMT6s is metabolite and should lag behind the original product. Also, for optimal accuracy, it was essential that volunteers adhere to providing a sample every 3 hours without additional voids, and this was not always possible. There was significant correlation between serum and saliva melatonin concentrations at all times points ($r=0.975$, $P<0.001$). Although somewhat less, correlations between serum and urine concentrations ($r=0.706$, $P<0.05$) and saliva and urine concentrations ($r=0.795$, $P<0.018$) also were significant. These results indicate that both salivary melatonin concentrations and urinary concentrations of aMT6s can be used as an accurate index of phase shifts in blood levels of melatonin.

DISCUSSION

We have demonstrated here an apparent lack of effect of melatonin (10 mg), when given at bedtime to normally cycling healthy females during the late follicular and early luteal phase of the monthly cycle, on menstrual cycle length, length of menses, and timing of the LH and FSH monthly rhythms. There were no reported side effects from melatonin administration, and melatonin volunteers were unable to determine whether they were receiving melatonin or placebo. In addition to hormone levels and menstrual characteristics, cognitive testing was done on the volunteers, both upon awakening in the morning and throughout the day following melatonin administration. Melatonin volunteers performed better than placebo volunteers on some tasks, but not on others.

During this investigation, we determined urinary levels of 6-sulphatoxymelatonin (a major melatonin metabolite found in urine) rather than melatonin itself, because of the difficulties involved with recruiting volunteers willing to submit to frequent blood sampling over 7 days. Following administration of melatonin, melatonin excretion was shown to closely parallel serum melatonin levels for 9 hours (Arendt et al., 1985). After 9 hours, urinary levels tended to be higher than those predicted from serum levels. Urinary levels of aMT6s have been shown to correlate closely, both quantitatively and qualitatively, with plasma melatonin levels in normal humans (Bojkowski and Arendt, 1990; Lee et al., 1995). Based upon the results of our assay for aMT6s, we feel secure in saying that our volunteers in the melatonin group had elevated levels of melatonin upon arising, and probably well into the morning. Whether elevated levels of urinary aMT6s throughout the day provide an accurate indication of melatonin levels in the blood cannot be determined from our data. Published values for a melatonin half life of 60 minutes or less would argue against elevated blood levels 18-24 hours after melatonin administration. However, changes in cognitive performance throughout the day could suggest sustained elevation in blood levels (see Comperatore et al., 1996b).

Peak serum melatonin concentrations vary by as much as 300 to 10,000 times the normal nighttime levels following melatonin administration (Waldhauser et al., 1984; Vakkuri, Leppaluoto and Kauppila, 1985). Since a major portion of the melatonin in blood is metabolized in the liver and excreted in the urine as the sulfate, it is not surprising to find high levels of aMT6s in the urine following melatonin administration, as reported here. We did not consider body weight (possible metabolic differences) while recruiting our volunteers, or attempt to regulate fluid intake while they were in-house. Differences in metabolism could certainly vary the rate at which aMT6s appears in the urine, and since melatonin was administered at 2300, first void samples could be more or less concentrated from one volunteer to the next depending on fluid intake. This could explain much of the variation in aMT6s levels between volunteers. We saw levels of aMT6s in the melatonin group elevated as much as 1400 times above first void levels in the placebo group. Variation in aMT6s levels between subjects also can arise because of variable gastrointestinal absorption of synthetic melatonin. Absorbed ingested melatonin has been reported to vary by as much as 25 fold among subjects (Waldhauser et al., 1984). Quite often daytime values for placebo volunteers were at or below the detection limit for the assay, while similar values for members of the melatonin group remained elevated (see Figure 3-1).

Levels of LH and FSH most often are determined through the use of plasma or serum based assays. Since we were interested in determining levels at least daily for 3 months, blood sampling was not a viable option. Urinary LH has been shown to be a reliable marker for plasma LH, since urinary and plasma LH concentrations change in parallel (Kerin et al., 1980). In a study involving the prediction of ovulation required for aspiration of oocytes during spontaneous menstrual cycles, the Abbott IMx system was shown to be a reliable method for measuring urinary LH and for predicting ovulation (Bischof, Bianchi, and Campana, 1991). More recently, the midcycle serum LH peak was shown to be highly correlated to the measurement of urinary LH metabolites in frozen and thawed first void urine samples (Clough et al., 1992). This was supported in the current study by eight volunteers who used the Whitehall-Robbins Clearplan Easy ovulation predictor and found good agreement between positive results on the predictor and the IMx results. We therefore felt confident in determining daily LH and FSH levels from urine samples using the Abbott IMx system.

Based upon IMx determinations of LH and FSH in urine samples from our volunteers, obtained during in-house stays in cycle 2, we found no systematic changes occurring as a result of melatonin administration. While first void samples always missed the absolute peak values of LH and FSH, as revealed by multiple daily samples while in-house, they did not miss the monthly surge.

There is considerable evidence from the animal literature that melatonin administration alters the timing or inhibits the LH surge and inhibits ovulation in female rats (Chiba, Akema and Toyoda, 1994; Reiter and Sorrentino, 1971; Ying and Greep, 1973). In human females, large doses of melatonin (300 mg and 1 g) have been reported to decrease LH levels (Voordouw et al., 1992; Nordlund and Lemer, 1977). Supporting these findings, young women in athletic training (3-5 year average) have been shown to have higher daytime levels of melatonin and lower levels of LH (Diaz et al., 1993). In contrast, Cagnacci et al. (1991) have reported that melatonin enhances LH during the early follicular phase (days 2-5) without modifying FSH. The effect on FSH generally is reported as minimal or not consistent, in good agreement with our results. As previously discussed, we are unable to address with any certainty the effect of melatonin on absolute levels of LH. We also are unable to predict the effect of melatonin administration at different times of the day or during different times of the monthly cycle. Since it is likely that melatonin would be used earlier in the day during travel across multiple time zones, its specific effect at other times is an important consideration.

The rise in endogenous melatonin in circulation begins after sunset and reaches maximum levels about 0200-0300 (Brown et al., 1985). There is little available melatonin throughout the day. Melatonin receptors are found at many locations both within the central nervous system and in other regions of the body. These receptors, like other classes of receptors, decrease their numbers (down-regulate) with increased availability of melatonin (night) and increase their numbers (up-regulate) with decreased availability of melatonin (daytime) (Gauer et al., 1994; Piketty and Pelletier, 1993; Poon et al., 1994; Term and Niles, 1993). Since the nightly rise in endogenous melatonin was well underway at the time of melatonin administration (2300) in this study, fewer receptor sites were available for interaction with exogenous melatonin. Since melatonin receptors should be up-regulated during daylight hours, exogenous melatonin should have its maximum effect on ovulation and menstrual characteristics at that time. We currently are investigating that possibility by administering melatonin at 1300 hours, during the advance region of the melatonin phase response function.

We have demonstrated that in our hands, administration of melatonin (10 mg) at 2300 during the late follicular and early luteal phase of the monthly cycle to normally cycling healthy females has no apparent effect on menstrual characteristics or ovulation. Under these conditions, administration of melatonin (10 mg) appears to be without significant risk.

REFERENCES

- Aleem, F.A., Weitzman, E.D., and Weinberg, U. 1984. Suppression of basal luteinizing hormone concentrations by melatonin in postmenopausal women. *Fertil. Steril.* 42:923-925.
- Arendt, J., Aldhous, M., English, J., Marks, V., Arendt, J.H., Marks, M., and Folkard, S. 1987. Some effects of jet-lag and their alleviation by melatonin. *Ergonomics.* 30:1379-1393.
- Arendt, J., Bojkowski, C., Franey, C., Wright, J., and Marks, V. 1985. Immunoassay of 6-hydroxymelatonin sulfate in human plasma and urine: Abolition of the urinary 24-hour rhythm with atenolol. *J. Clin. Endocrinol. Metab.* 60: 1166-1173.
- Arendt, J., and Broadway, J. 1987. Light and melatonin as zeitgebers in man. *Chronobiol. Int.* 4:273-282.
- Badia, P., Myers, B.L., and Murphy, P.J. 1992. Effects of nonsteroidal anti-inflammatory drugs on body temperature and melatonin. *Sleep Res.* 21:365.
- Bischof, P., Bianchi, P.G., and Campana, A. 1991. Comparison of a rapid, quantitative and automated assay for urinary luteinizing hormone (LH), with an LH detection test, for the prediction of ovulation. *Human Reprod.* 6:515-518.
- Bojkowski, C.J., and Arendt, J. 1990. Factors influencing urinary 6-sulphatoxymelatonin, a major melatonin metabolite, in normal human subjects. *Clin. Endocrinol.* 33:435-444.
- Brown, R., Kociss, J.H., Caroff, S., Amsterdam, J., Winokur, A., Stokes, P.E., and Frazer, A. 1985. Differences in nocturnal melatonin secretion between melancholic depressed patients and control subjects. *Am J. Psychiatry.* 142:811-816.
- Cagnacci, A., Elliott, J.A., and Yen, S.S.C. 1991. Amplification of pulsatile LH secretion by exogenous melatonin in women. *J. Clin. Endocrinol. Metab.* 73:210-212.
- Chiba, A., Akema, T., and Toyoda, J. 1994. Effects of pinealectomy and melatonin on the timing of the proestrus luteinizing hormone surge in the rat. *Neuroendocrinol.* 59:163-168.
- Clough, K.M., Cole, F.X., Seaver, S.S., Vesprini, A., Kuo, A.Y., and Lasley, B.L. 1992. Enzyme immunoassay method for total alpha gonadotropin in human urine samples. *Fertil. Steril.* 57:1241-1246.
- Comperatore, C.A., and Krueger, G.P. 1990. Circadian rhythm desynchronization, jet lag, shift lag, and coping strategies. In: Scott, I., ed. *Occupational medicine: state of the art reviews*, vol. 5. Philadelphia: Hanley & Belt&, Inc., 323-342.
- Comperatore, C.A., Lieberman, H.R., Kirby, A.W., Adams, B., and Crowley, J.S. 1996a. Melatonin efficacy in aviation missions requiring rapid deployment and night operations. *Aviat. Space Environ. Med.* 67:520-524.

Comperatore, C.A., Allan, L.W., Ferry, C., Strickland, R., Garner, N., Acevedo, H., Hein, L., and Kirby, A.W. 1996b. The effects of a 7-day melatonin regimen on vigilance during & early follicular and late luteal phase of the menstrual cycle. Fort Rucker, AL: U.S. Army Aeromedical Research Laboratory. USAARL Report No. 96-xX.

Dawson, D., and Encel, N. 1993. Melatonin and sleep in humans. *J. Pineal Res.* 15:1-12.

Diaz, B., Garcia, R., Colmenero, M.D., Terrados, N., Fernandez, B., and Marin, B. 1993. Melatonin and gonadotropin hormones in pubertal sports girls. *Rev. Esp. Fisiol.* 49:17-22.

Fiore, M., Mitchell, J., Doan, T., Nelson, R., Winter, G., Grandone, C., Zeng, K., Haraden, R., Smith, J., Harris, K., Leszczynski, J., Berry, D., Safford, S., Barnes, G., Scholnick, A., and Ludington, K. 1988. The Abbott IMx automated benchtop immunochemistry analyzer system. *Clin. Chem.* 34:1726-1732.

Gauer, F., Masson-Pevet, M., Stehle, J., and Pevet, P. 1994. Daily variations in melatonin receptor density of rat pars tuberalis and suprachiasmatic nuclei are distinctly regulated. *Brain Res.* 641:92-98.

Kerin, J.F., Wames, G.M., Cracker, J., Broom, T.G., Ralph, M.M., Matthews, C.D., Seamark, R.F., and Cox, L.W. 1980. 3-hr urinary radioimmunoassay for luteinizing hormone to detect onset of preovulatory LH surge. *Lancet* ii: 430-431.

Lee, B.-J., Parrott, K.A., Ayres, J.W., and Sack, R.L. 1995. Design and evaluation of an oral controlled release delivery system for melatonin in human subjects. *Int. J. Pharm.* 124:119-127.

Lewy, A.J., Sack, R.L., Blood, M.L., Bauer, V.K., Cutler, N.L., and Thomas, K.H. 1995. Melatonin marks circadian phase position and resets the endogenous circadian pacemaker in humans. In: *Circadian clocks and their adjustment*. Wiley, Chichester (Ciba Foundation Symposium 183), p 303-321.

Nordlund, J.J., and Lerner, A.B. 1977. The effects of oral melatonin on skin color and on the release of pituitary hormones. *J. Clin. Endocrinol. Metab.* 45:768-774.

Penny, R., Stanczyk, F., and Goebelsmann, U. 1987. Melatonin: data consistent with a role in controlling ovarian function. *J. Endocrinol. Invest.* 10:499-505.

Petrie, K., Conaglen, J.V., Thompson, L., and Chamberlain, K. 1989. Effect of melatonin on jet lag after long haul flights. *Br. Med. J.* 298:705-707.

Piketty, V., and Pelletier, J. 1993. Melatonin receptors in the lamb pars tuberalis/median eminence throughout the day. *Neuroendocrinol.* 58:359-365.

Poon, A.M., Liu, Z.M., Pang, C.S., Brown, G.M., and Pang, S.F. 1994. Evidence for a direct action of melatonin on the immune system. *Biol. Spinal.* 3: 107-117.

Reiter, R.J. 1991. At the cutting edge melatonin: The chemical expression of darkness. *Mol. Cell. Endocrinol.* 79:C153-C158.

Reiter, R.J., and Sorrentino, S. 1971. Inhibition of luteinizing hormone release and ovulation in PMS-treated rats by peripherally administered melatonin. *Contraception.* 4:385-392.

Sugden, D. 1983. Psychopharmacological effects of melatonin in mouse and rat. *J. Pharmacol. Exp. Ther.* 227:587-591.

Term, C., and Niles, L.P. 1993. Physiological regulation of melatonin receptors in rat suprachiasmatic nuclei: diurnal rhythmicity and effects of stress. *Mol. Cell. Endocrinol.* 98:43-48.

Vakkuri, O., Leppaluoto, J., and Kauppila, A. 1985. Oral administration and distribution of melatonin in human serum, saliva and urine. *Life Sci.* 37:489-495.

Voordouw, B.C.G., Euser, R., Verdonk, R.E.R., Alberda, B.T.H., DeJong, F.H., Drogendijk, A.C., Fauser, B.C.J.M., and Cohen, M. 1992. Melatonin and melatonin-progestin combinations alter pituitary-ovarian function in women and can inhibit ovulation. *J. Clin. Endocrinol. Metab.* 74:108-117.

Waldhauser, F., Waldhauser, M., Lieberman, H.R., Deng, M.H., Lynch, H.J., and Wurtman, R.J. 1984. Bioavailability of oral melatonin in humans. *Neuroendocrinol.* 39:307-313.

Wurtman, R.J. 1986. Introduction: Melatonin in humans. *J. Neural. Transm. [Suppl.]* 21:1-8.

Ying, K.Y., and Greep, R.O. 1973. Inhibition of ovulation by melatonin in the cyclic rat. *Endocrinol.* 92:333-335.

TASK 4

Investigation of Visual Performance Issues for Flat Panel Technology Displays

INTRODUCTION

The overall objective of this task is to provide electro-optical and psychophysical technical data packages in the investigation of visual performance issues related to new flat panel display technologies and advanced display concepts.

There are three major objectives within this task. The first objective is to develop a battery of electro-optical and visual performance measures which will fully characterize visual performance with these displays. The second objective is to develop psychophysical databases on the human visual response to flat panels and to advanced display systems. The third objective is to develop a detailed analysis of technical and human performance issues associated with the integration of flat panel displays into helmet-mounted display designs and other advanced display concepts.

As the work within objectives is overlapping, the work reported here will be divided into sections which provide a more functional division of research efforts performed in support of each of these broad objectives. The work in each section directly relates to these three objectives. The work reported here, shall generally be a summary of work completed and published elsewhere as USAARL Laboratory reports or open literature publications. In a few cases, the work reported here will be the first time that the work has been presented. In these cases, more description shall be provided.

PHYSICAL EVALUATION OF DEVELOPMENTAL DISPLAY SYSTEMS

Over the course of this contract effort, UES has provided detailed assessments of fielded and developmental optical and display systems. Often this work has resulted in the development of new figures-of-merit and optical and physical tests required to fully characterize display performance. UES scientists and engineers have worked hand-in-hand with Army Program Managers and System Developers in the assessment of these devices. Our findings have been used as milestones of development progress and have led to major redirections in developmental efforts. For UES, this collective work has formed the backdrop to our research and engineering development efforts for this task. Having the advantage of working in this applied area, has led to major developments in the laboratory. Therefore, we will start here in detailing the research effort of Task 4.

The Microvision Scanning Laser HMD

The project manager, Aircrew Integrated System (PM-ACIS), Huntsville, Alabama, has established a program with Microvision, Inc., Seattle, Washington, to develop a technology demonstrator to determine the capability of a scanning laser display (VRD) to meet RAH-66 Comanche helmet mounted display (HMD) performance specifications. Under this program, titled Aircrew Integrated Helmet System (AIHS) HGU-56P VRD system, Microvision developed and delivered to the Army a laser based HMD for evaluation by the UES Task 4 team. UES has made separate evaluations of five different developmental versions of the Microvision HMD. These evaluations have resulted in USAARL laboratory reports.

The data presented here constitutes the findings of an evaluation of the phase 2 HMD that is an improvement from the earlier version. The main improvement comes from the integration of new electronics which allow for better control of subpixel spacing and positioning. Essentially, Microvision, Inc. made changes to the system to improve the horizontal MTF of the system. Indeed, improvements were noted in the horizontal MTF with the modulation at the Nyquist frequency approaching 20%.

For each side of the binocular display, light from a laser beam is divided into two beams for simultaneous scanning in both forward and aft (retrace) directions. This scanning technique reduces the bandwidth requirement for the horizontal and vertical scanners housed in the HMD. Beam intensity is adjusted by electro-optical modulators. These modulators in effect control the contrast and duration of each pixel as they are drawn by the sweeping beams. Timing circuits control the duration of pixels which change as a function of lateral position. Due to geometry, pixels in the lateral periphery have shorter durations than pixels in the lateral center. To draw a single vertical line, the horizontal scans must be turned on at certain point and then turned off. To draw the best line possible (narrowest lateral profile), the beams must be well calibrated and aligned and the timing circuits must maintain consistency from the top of the field to the bottom of the field. In past Microvision systems, the vertical line profiles have been substantially wider than the horizontal line profiles and this has been directly observed in the vertical lines MTF (termed the horizontal MTF; since in frequency space, vertical lines are composed of horizontal frequencies).

The current Microvision HMD has new electronics which were developed to address the positioning of pixels more precisely. Positioning pixels in a vertical line more accurately will lead to an improved MTF. Further, Microvision appears to have reduced the timing signature of each pixel and this will also aid in the improvement of the MTF. This can be likened to reducing the fill factor in flat panel displays. However, this reduction has led to other problems, see CTF noise below.

At best, the system seems "fragile", as alignment procedures must be performed prior to each test procedure and does not maintain over night. Warm-up periods seem excessive as often an hour or two was required prior to evaluation. Also, the left side video board failed to produce imagery as good as the right side board during testing. So the right side board was used to drive both sides during the tests reported here.

As expected, Microvision engineers were extremely helpful throughout the testing procedure, but even their telephone assistance failed to produce the quality of imagery we had expected based upon their results and even the results we achieved during the first week of testing.

The Microvision System

Microvision is developing multiple HMD designs based on the technique of scanning lasers. The AIHS configuration, which is the system we have tested thus far, is a monochromatic design based on "green" lasers emitting at 532 nm. However, other ongoing designs incorporate red, green and blue lasers for full color applications. Figure 4-1 extends the artist's conception to depict the ability of scanning laser HMDs to present symbology of sufficient luminance to be seen against daytime backgrounds.

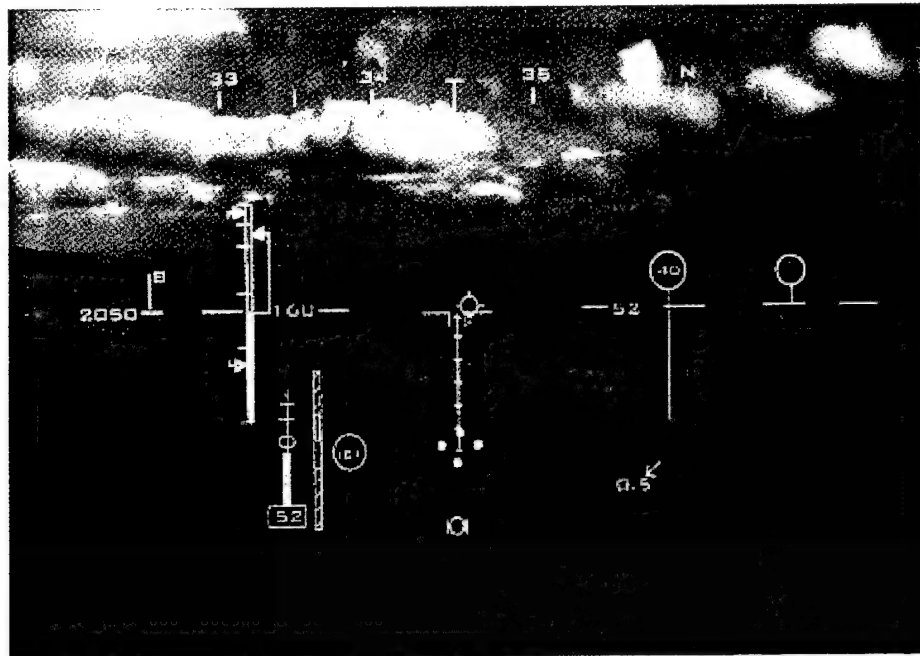


Figure 4-1. An artist's conception depicting the ability of scanning laser HMDs to present symbology of sufficient luminance to be seen against daytime backgrounds.

The current HMD system prototype consists of several primary components: an HMD comprised of a Pilot Retained Unit (PRU) (helmet) and an Aircraft Retained Unit (ARU) (Figure 4-2); an electronic and control module; interconnect cables and three lap top computers, two of which control imagery to the two HMD channels and a third which provides control of the electronic components; and, a power supply that provides an external voltage source for controlling the HMD imagery luminance. Size and number of components continue to decrease as development continues.



Figure 4-2. Microvision prototype scanning laser HMD.

Table 4-1.

Summary of requirements for AIHS scanning laser HMD.

Parameter	Requirement
HMD Type	See-through
Color	Monochrome - Green
Configuration	Binocular
Field-of-view	52° x 30° (H x V)
Overlap	30° minimum
Resolution	1280 x 960
Luminance at the eye	1200 fL
Exit pupil (On axis)	15 mm
Eye relief distance	25 mm
Helmet	HGU-56/P

Functional operation

The AIHS system consists of two channels, one per eye. A functional block diagram of the system is provided in Figure 4-3. The diagram includes the power supply/management and drive (video processing) electronics subsystems, which are shared by the two channels, and those subsystems that are found in each channel: light source (photonics) module, fiber-optic cable, scanner assembly, exit pupil expander (EPE), and relay/viewing optics. A brief description of each subsystem follows:

1. Power supply/management. Supplies required analog (+12V, +/-5V), digital (+5V, +3.3V), and driver (+24V, +12V) voltages to all other subsystems.
2. Drive (video processing) electronics. Receives and processes signals from an image source. The processed signals contain information that controls the intensity and coordinates to position the individual picture elements (pixels) that comprise the image, i.e., provides signals that encode the image information onto the laser beams and control the timing synchronization of the horizontal and vertical scanners in the scanner assembly.
3. Light source (photonics) module. For each channel (eye), this subsystem consists of one diode-pumped solid-state laser (currently a Coherent model 315M-100), 100 milliwatt (mW) continuous wave laser, a slow acoustic-optic modulator (AOM), a holographic beam splitter, a dual AOM, and associated folding and focusing optics. The slow AOM serves to attenuate the intensity (brightness) of the initial laser beam. The beam splitter divides the initial laser beam into two beams. The two beams are directed to the dual AOM which when coupled with the signals from the drive electronics produce the image data pulse stream.
4. Fiber-optic cable. Consists of two single-mode fibers, one per beam. This cable brings the laser beams from the aircraft-mounted enclosures that house the lasers, drive electronics, power supply, etc., up to the scanner assembly and relay/viewing optics located on the head.
5. Scanner assembly. Consists of the horizontal and vertical scanners that "paint" the image by rapidly moving the light source across and down, in a non-interlaced raster pattern. The horizontal scanner is a bi-directional mechanical resonating scanner (MRS) operating typically at 15.75 kilohertz (kHz). The vertical scanner is a linear galvo-mechanism operating at 60 Hz. [Note: Microvision is working on the development of a Micro-Electro-Mechanical Systems (MEMS) technology scanner that will perform the functions of both the horizontal and vertical scanners within a single element. MEMS technology is the integration of mechanical elements, sensors, actuators, and electronics on a common silicon substrate through the utilization of microfabrication technology.]
6. Exit pupil expander (EPE). Currently a diffractive optical element (may be holographic in final design) that increases the size of the effective exit pupil. Nominally, the image would be contained in an area of 1 mm^2 . The EPE increases the natural output angle of the image and enlarges it up to approximately 15 mm in diameter ($\sim 177 \text{ mm}^2$) for ease of viewing. The raster image created by the horizontal and vertical scanners passes through the pupil expander and on to the viewer optics. Note: When the exit pupil is observed, as in the photographic setup, the exit pupil appears as a set of beamlets. Each beamlett contains the entire image.
7. Relay/viewing optics. Consists of multiple refractive and reflective optical elements that relay the final image to the eye. The current optical design is that of a folded catadioptric optical train.

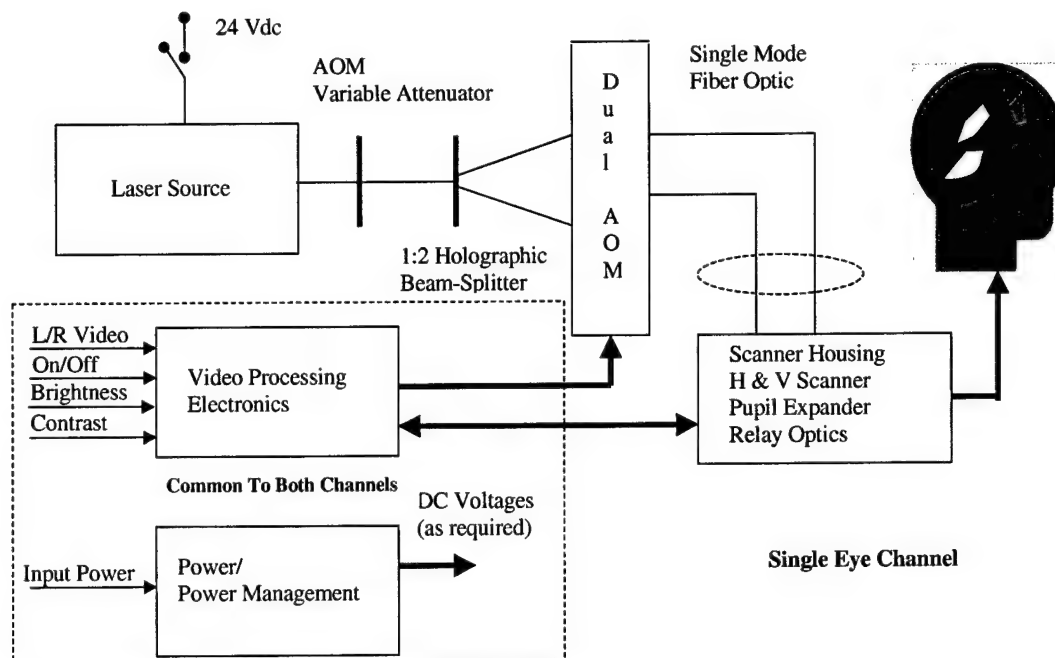


Figure 4-3. Functional block diagram of the scanning laser HMD system.

Optical-path description and energy efficiencies

The functional block diagram in Figure 4-3 is useful for the understanding of the operation of the Microvision AIHS scanning laser HMD. For the purpose of this paper, to propose an approach and methodology to its laser safety evaluation, it may be more interesting and useful to look at the system from the perspective of how the laser light (energy) traverses the optical path from laser source to the eye.

Step 1. Light beam leaves laser as single beam. Laser is 100 mW at 532 nm.

Step 2. Beam is fiber-optically coupled to slow AOM. Efficiency of coupling is approximately 100% resulting in approximately 100% of the energy initially delivered by the laser.

Step 3. Single beam enters slow AOM, which acts as an intensity modulator (45 dB dynamic range). Insertion efficiency is approximately 96%; diffraction efficiency is approximately 90%. Therefore, approximately 86.4% of the energy delivered by the laser leaves the slow AOM.

Step 4. Beam enters holographic beam splitter that produces two primary beams and several extraneous low energy beams. These extraneous beams are absorbed within the AOM. Beam splitter has efficiency of approximately 65%. Therefore, approximately 56% of the energy initially delivered by the laser leaves the beam splitter. However, since this energy is now divided between two beams, each beam exits with only 23% of the initial laser energy.

Step 5. Both beams enter into a single AOM focus lens that results in two spots of 30-35 micron diameter ($1/e^2$). This lens has efficiency of approximately 99%, resulting in approximately 55.6% (27.8% per beam) of the initial laser energy exiting the lens.

Step 6. Each beam then enters a dual AOM where each is modulated by drive signals provided by the video processing electronics. With an insertion and diffraction efficiencies of 90% and 60%, respectively, the dual AOM has a total efficiency of approximately 54%, resulting in 30% (15% per beam) of the initial laser energy exiting the dual AOM.

Step 7. Each of the two modulated beams exiting the dual AOM enters a collimating lens of 99% efficiency. Approximately 29.7% (14.85% per beam) of the initial laser energy exits this lens.

Step 8. Each focused beam enters a fiber-optic coupler that mates the beam to a single-mode optical fiber for transmission to the head-mounted components. With an efficiency of 50%, approximately 14.9% (7.45% per beam) of the initial laser energy is delivered through the coupler.

Step 9-11. Each beam traverses its respective fiber up to the HMD. Combined fiber transmission, duty cycle and connector efficiency is 25.1% resulting in 3.7% (1.85% per beam) of the initial laser energy.

Step 12. Each beam exits the fiber through a fiber focus lens of 94% efficiency resulting in 3.5% (1.75% per beam) of the initial laser energy.

Step 13. Both beams are reflected off a turn mirror (or pinch mirror if pinch correction provided). With greater than 99% efficiency, the resulting energy is 3.5% (1.75% per beam) of the initial laser energy.

Step 14. Both beams are bi-directionally scanned by horizontal and vertical scanning mirrors. Efficiency of scan mirrors is approximately 81%. The resulting energy is 2.8% (1.4% per beam) of the initial laser energy.

Step 15. Both beams pass through a negative lens acting as field flattener lens. Efficiency is 98%. The resulting energy is 2.7% (1.35% per beam) of the initial laser energy.

Step 16. Both beams enter EPE where they are diffracted (or holographically) expanded into an array of beamlets. Each beamlet contains the entire scanned image. EPE efficiency is 80%. The resulting energy is 2.2% (~1% per beam) of the initial laser energy.

Step 17. Beamlets enter the ocular, pass through a series of optical elements, and reflect off the combiner elements. Total ocular efficiency is approximately 22%. The resulting energy finally delivered to the eye is 0.48% (0.24% per beam) of the initial laser energy. A recent evaluation (Harding et al., 2001a) reported a luminance at the eye of 1485 fL. This implies that laser output luminance was of the range of 309,000 fL. By analogy, based on the 100 mW laser output, the system theoretically should deliver approximately 0.48 mW of power to the eye.

Step 18. Several of the beamlets enter the eye providing the viewed image. Since not all of the beamlets enter the eye, total energy delivered to the eye will be less than that predicted by this analysis. Since the higher luminance setting used in the daytime scenario would result in a light adapted pupil of approximately 4 mm diameter, the ratio of the pupil's area to the area of the exit pupil would be 16:225. Therefore, the eye would be receiving only about 7% of the total energy delivered by the system within its full exit pupil.

Note: The efficiencies presented here are representative of values obtained to date. These values may differ from those achieved in the final design.

Optical and physical measurements

The Microvision HMD was evaluated by UES on several occasions. The occasions usually corresponding to annual reviews of Microvision contractual performance progress. As UES testing formed the sole basis for the government's technical review program milestones, the tests performed were typically repetitive in order to gauge improvements to different figures-of-merit. As these reviews are available in laboratory report format, we will confine our discussion of the Microvision system to its current configuration as tested at USAARL. The laboratory reports mentioned above can be reviewed on the USAARL web site (www.usaarl.army.mil). The USAARL reports are 99-18, 2001-06, 2002-01, 2002-13, 2003-01.

The photographic measurement of spatial resolution. To avoid the problems of temporal noise affecting our measurements, we used still photography to capture HMD imagery using a quasi-linear CCD camera and a computer capture card. Software allowed us to evaluate the images by converting the unsigned grayshade values (8 bits of resolution) to whole numbers (0 to 255) for numerical analysis. Image capture was aided by a device, built by UES, that maintained alignment of the camera lens with the HMD's exit pupil (Figure 4-4). In most cases, laser intensity was adjusted to produce photographic images where the graylevels ranged over the whole 8 bit range without saturation. As a word of caution, the noise characteristic of our measurement system was not considered in these calculations. Removing the bitmap noise from the data would likely have a positive affect by showing higher contrast and modulation levels than those reported here. This shortcoming is inherent in the photographic method but can be reduced by using cameras more well suited for mensuration.

The modulation transfer function (MTF). The Microvision HMD uses a display format of 1280 by 960 pixels. Using an approximate field-of-view of 41 by 30.75 degrees, one-degree square of visual angle contains about 975 pixels or 31.22 pixels per linear dimension. This relates to a Nyquist frequency of 15.61 cycles/degree (31.22 pixels per degree/2). In the previous system, the Horizontal MTF showed little modulation at the Nyquist frequency (Figure 4-5.) Comanche specification calls for an eight percent modulation at this frequency.

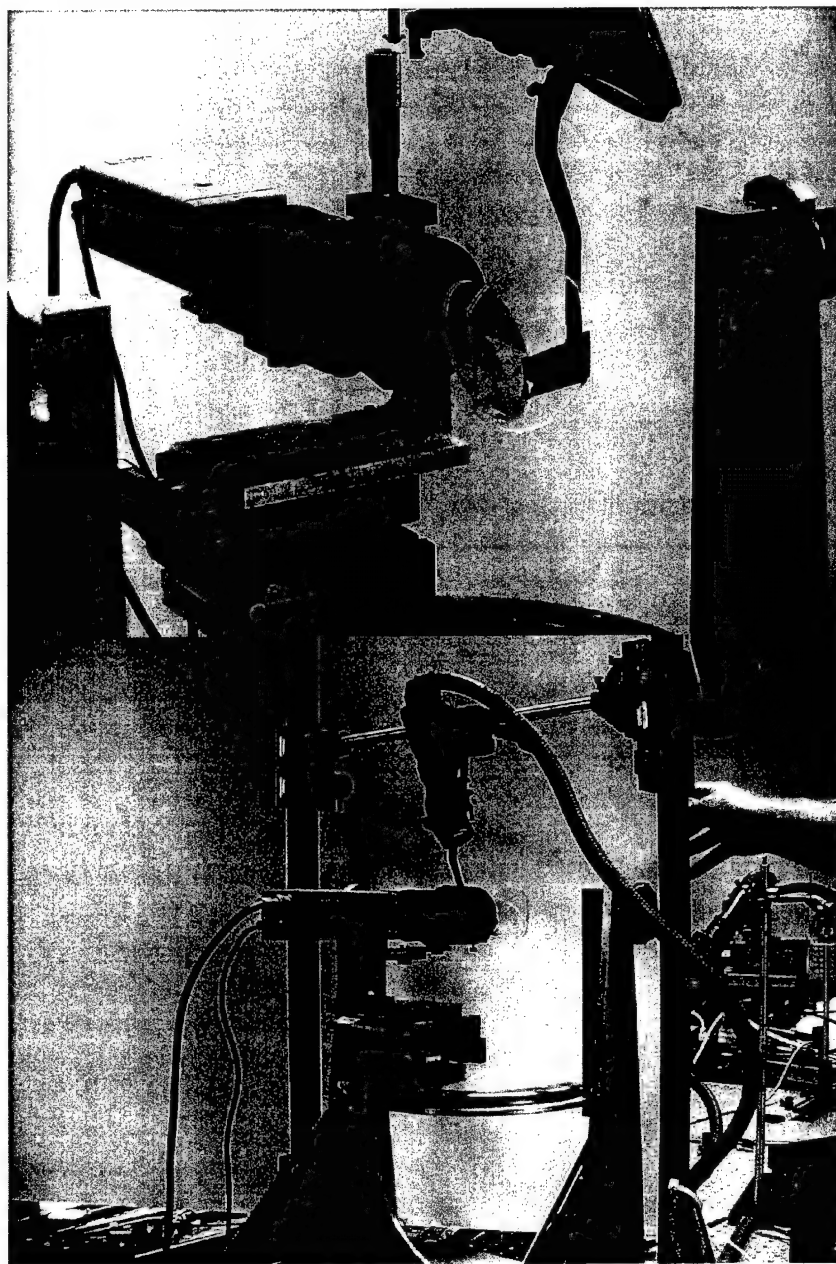


Figure 4-4. Photographs of optical set-up showing relationship between the HMD optics and camera lens. In the top photograph, note the image of the exit pupil centered on an artificial 3mm iris. For all of the data shown in this report, a 5mm iris was used. The device holding the camera allowed viewing of any FOV position while still maintaining correct alignment.

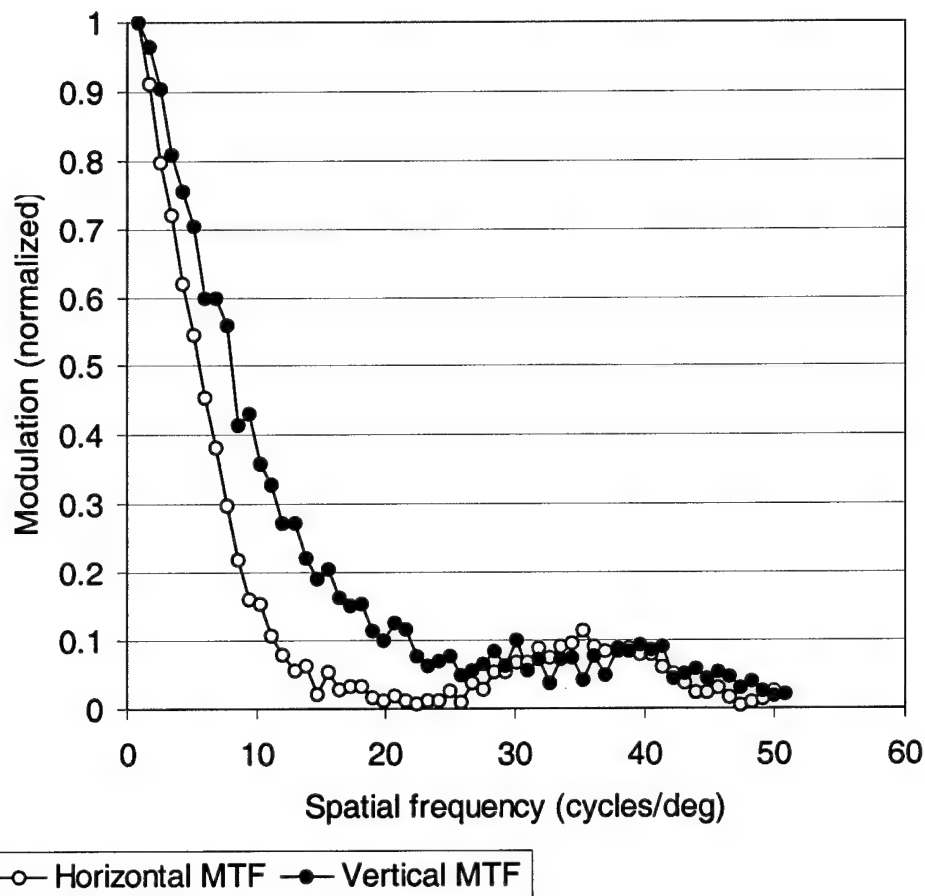


Figure 4-5. Vertical and horizontal MTFs measured previously (Harding, et al., 2001). Note the difference between the two curves at the Nyquist frequency (horizontal = 0.05 and vertical = 0.20).

The MTF of the current system. To make comparative measures and judge Microvision's progress, line spreads were measured for the two orientations with the system well calibrated and the HMD imagery properly aligned with the camera. Figure 4-6 shows photographic images of the horizontal and vertical lines captured from the left side optic. Figure 4-7 shows the MTFs obtained from these photographic images. Note the increase in modulation at the Nyquist for the horizontal MTF.

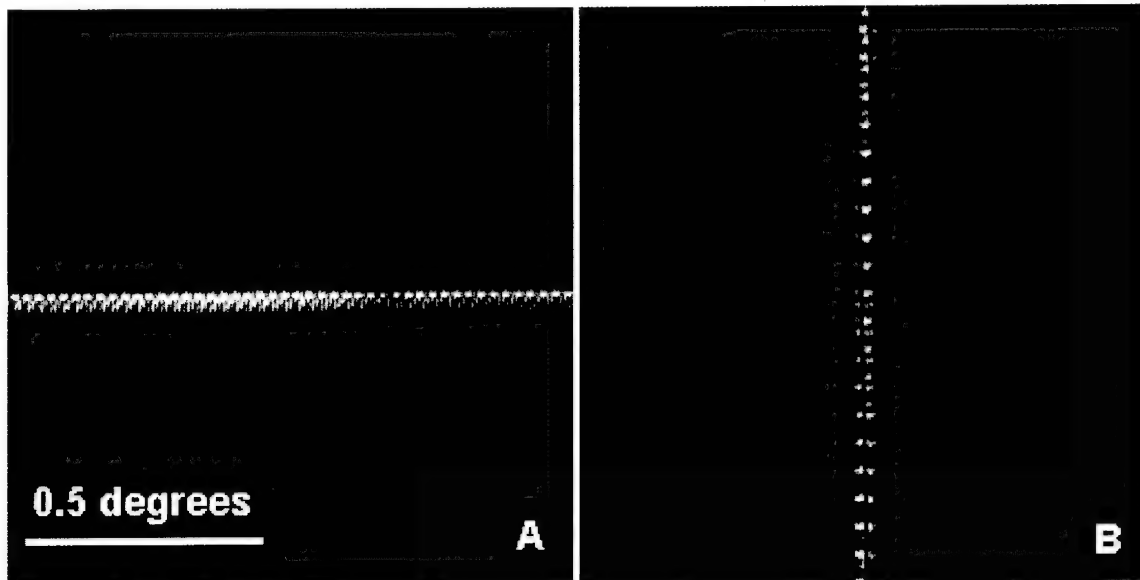


Figure 4-6. Horizontal and vertical lines captured by a grayscale camera. These lines reflect the best imagery we obtained from the system.

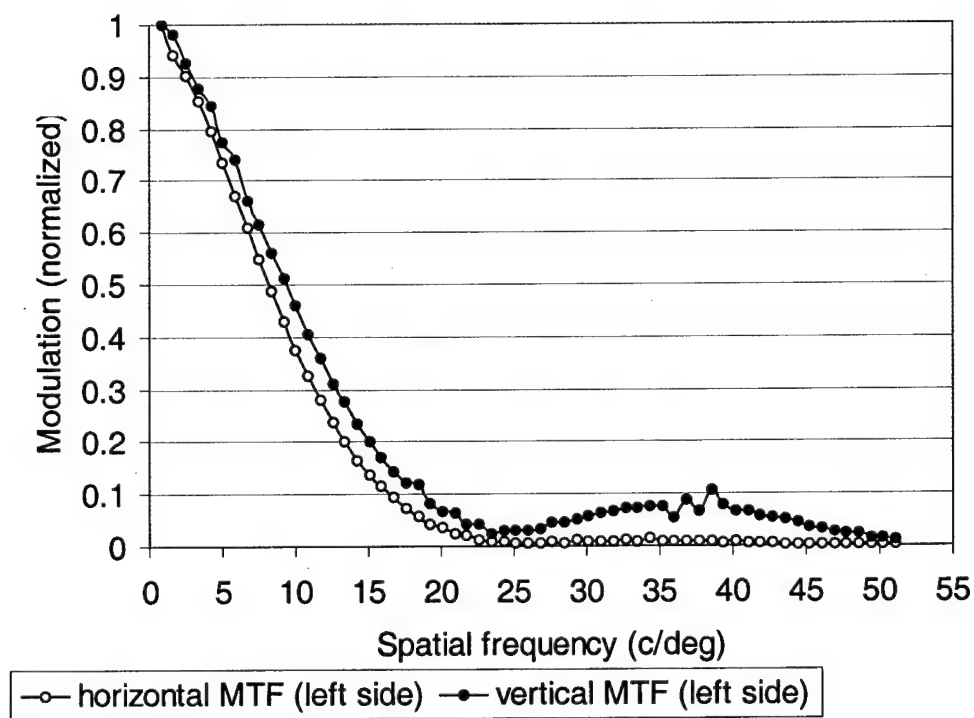


Figure 4-7. MTFs measured from the left side of the HMD. Like before, the vertical MTF shows about 0.20 modulation at the Nyquist frequency. The horizontal MTF showed modest improvement with about a 0.12 modulation at the Nyquist.

The horizontal MTF shows modest improvement in that the performance exceeded the Comanche specification. These curves were taken from lines well centered in the middle of the 1280 by 960 array.

The Contrast transfer function (CTF). The CTF is the measure of contrast in the image plane as a function of spatial frequency. The contrast measurement normally used is Michaelson contrast $\{(L_{\max} - L_{\min}) / (L_{\max} + L_{\min})\}$. In the past, we scanned the square wave image pattern with a slit aperture. We found that this technique yielded problems with the Microvision system, as the system was not typically stable during the time it took to make the precise measurements. Using a photographic method, CTFs were measured using different techniques in order to better characterize the spatial resolution of the system. Following vertical or horizontal alignment, photographic images of grill patterns were collected. As a side note, HMD imagery did not produce orthogonal rows and columns. They were about 2 degrees off normal. Thus realignment was necessary when measuring contrast between rows and columns. In our measurements, alignment was critical because data was collapsed in one dimension to produce an average modulation in the other axis. For example, to measure the contrast for a horizontal grill pattern, data was collapsed horizontally over a number of data points to produce a one-dimensional curve (see Figure 4-8).

The first CTF measurement technique was rather straightforward. Maximum contrast was measured by averaging the peaks and troughs in the collapsed data to determine an average peak and an average trough. Figure 4-8 shows data collected from the 1 on – 1 off grill pattern. The peak was the average of the five peaks identified in the chart. Likewise the trough measurement was the average of the six troughs. Using this technique, horizontal and vertical CTFs were measured for the left side (Figure 4.9). The 0.25 contrast measured for the vertical 1 on – 1 off grill pattern represents a major improvement in the system. Last year (Harding, et al., 2001), an average contrast of about 0.025 for the vertical grill pattern was measured.

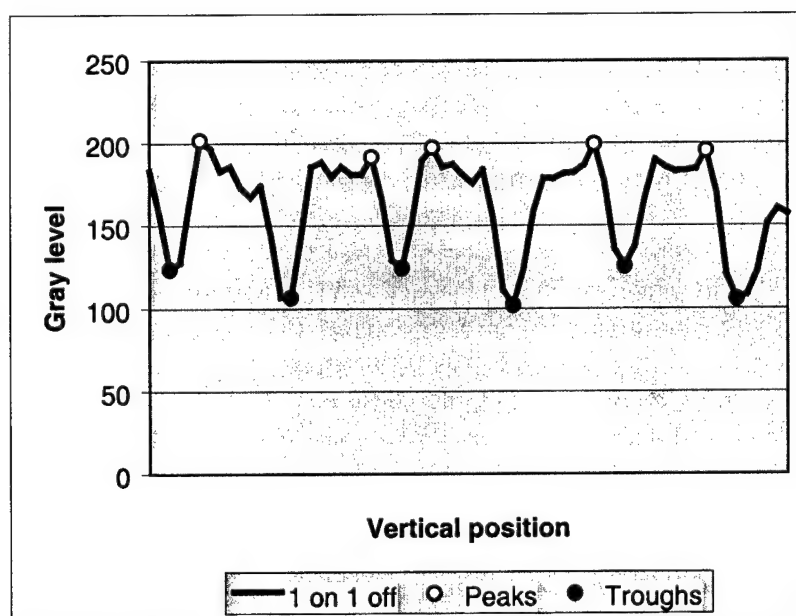


Figure 4-8. Peaks and troughs used to measure the CTF contrast.

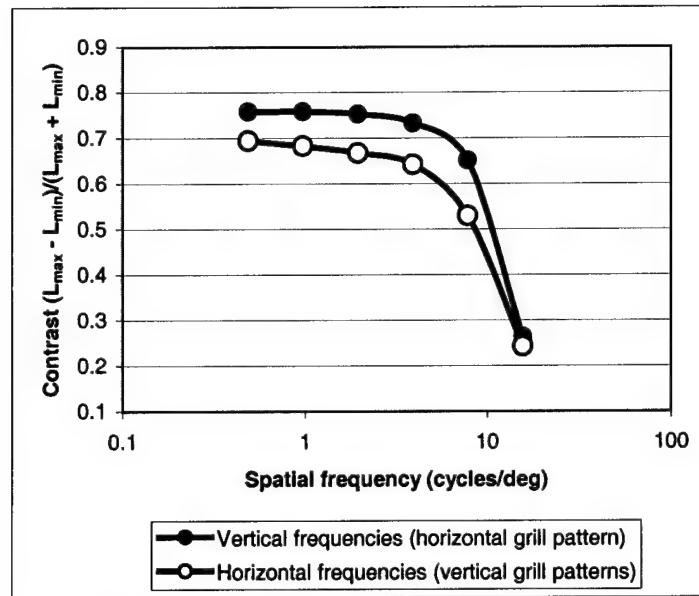


Figure 4-9. Horizontal and vertical CTFs measured for grill patterns in the left side's central area. Note the sharp fall-off at the Nyquist frequency.

CTF noise. When viewing the HMD imagery at the Nyquist limit, it is difficult to discern the orientation of the grill patterns. In fact, for the vertical grill pattern, an observer is more likely to observe a horizontal grill than a vertical grill. This is a problem with the nature of the pixel structure. With older CRT systems, there was never a problem in identifying orientation of grills if given sufficient contrast. However, the Microvision system is a pixilated display much like a flat panel display. Using terminology from flat panels, the pixel geometry in the Microvision system has a fill factor of less than one, i.e., the active pixel does not occupy all of the pixel space represented by the angular subtense of pixel spacing. Thus, the two dimensional spectra of a grill pattern has spatial frequency content in multiple orientations. Older CRTs had spatial frequency content in only one orientation per se. This multi-dimensional frequency content leads to mistaken recognition of orientation. If we consider spatial frequency content that is not in the appropriate orientation as noise, then it is possible to calculate signal to noise ratios for grill patterns.

To ease the noise calculation, we used a shortcut by collapsing data orthogonal to the orientation of the grill pattern. Figure 4.10 depicts this method of measuring signal and noise. In Figure 4-10A, the noise would be the profile at the bottom and the signal would be to the right. The opposite case would be used for the grill pattern shown in Figure 4-10B.

In this analysis, a more robust method of measuring contrast was used which takes into account the variability of the waveform. Standard deviations were calculated for the signal and noise curves. To normalize the data, the standard deviations were divided by the means. Figure 4-11 shows CTFs measured using this technique. Of particular note, the noise contrast for the vertical grill pattern was higher than the signal contrast. This would explain the difficulty in correctly identifying the orientation of the vertical grill pattern. In Figure 4-12 we plotted the signal to noise ratios for the six spatial frequencies and two orientations. Also plotted in this

figure are calculations taken from images provided by Microvision. With the exception of the one wayward point, the data was nearly identical. This provides additional support for the robustness of the method.

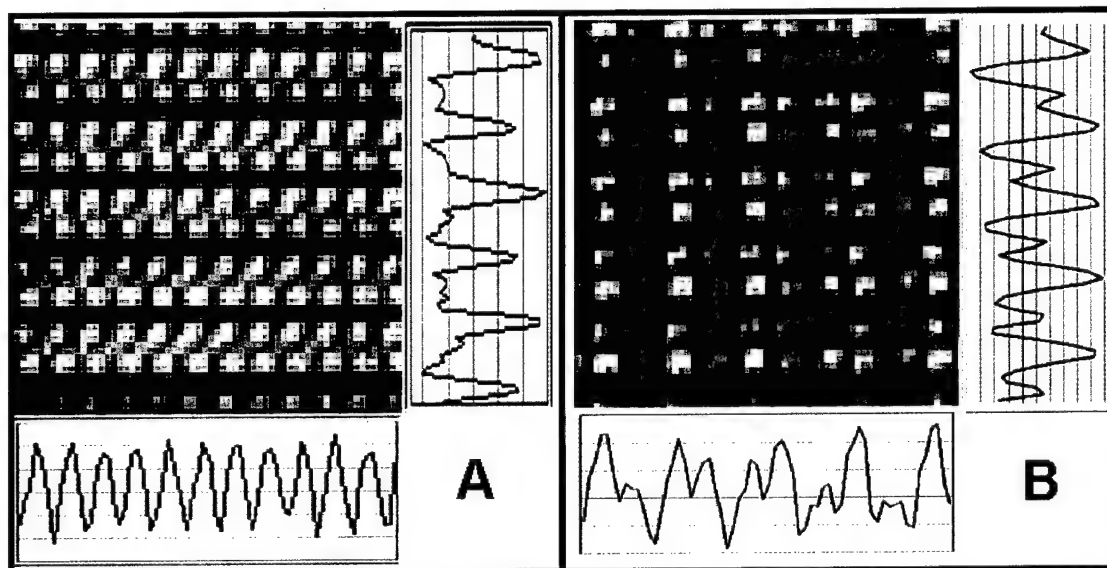


Figure 4-10. Photographically enhanced images of 1off-1on grill patterns in the horizontal (A) and vertical (B) orientations. Of note is the pixel structure observed in B. Here a strong horizontal element is noticed. This element makes recognition of orientation difficult. Profile amplitudes are not necessarily to scale.

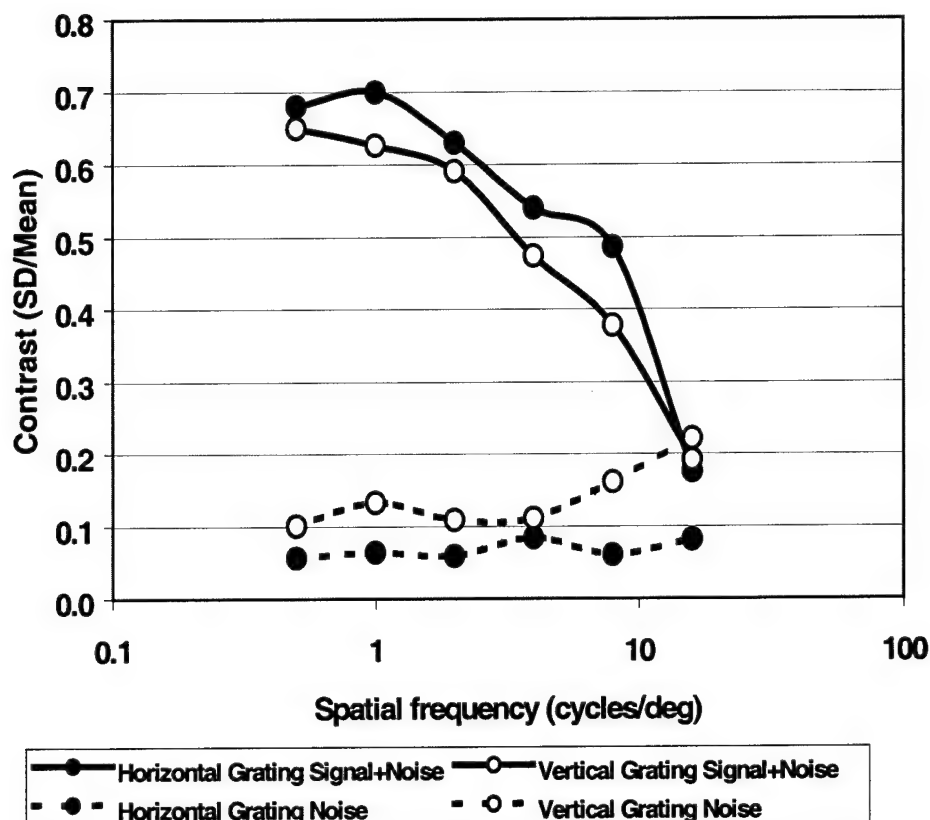


Figure 4-11. CTFs measured using the standard deviation technique for grill patterns presented to the left side. Here the noise estimates are plotted as a function of grill spatial frequency. As a side note, the noise frequency spectra is highly correlated with the pixel spacing and is thus composed of higher spatial frequencies (near the Nyquist frequency). Since the Nyquist frequency is well within human spatial frequency bandwidth, we feel justified in using our noise estimates in this fashion.

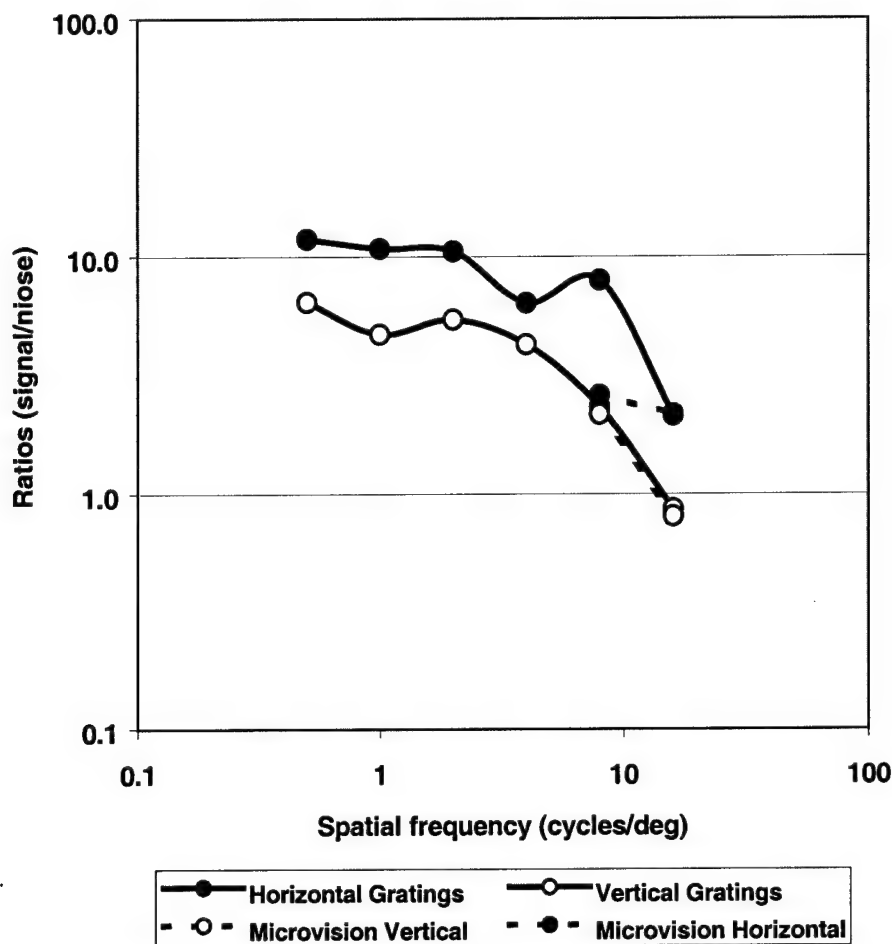


Figure 4-12. CTF signal-to-noise ratios based upon the data shown in Figure 4-11. Microvision engineers provided us photographic images of grill patterns used in their data analysis. Using their images, we calculated the signal-to-noise ratios for the highest two spatial frequencies. With the exception of the aberrant point, their data fell on top of our data points.

Character resolution at the spatial limit. To view the system's ability to produce imagery at the spatial limit of resolution, a target consisting of 5 by 5 characters was constructed and presented normally and at 90 degrees rotation. The smallest gap in these characters is one pixel, the spatial limit. Figure 4.13 shows photographs of this imagery. Although, the system may not have been absolutely aligned properly, the waviness of the characters and loss of pixel definition further suggests the lack of system robustness.

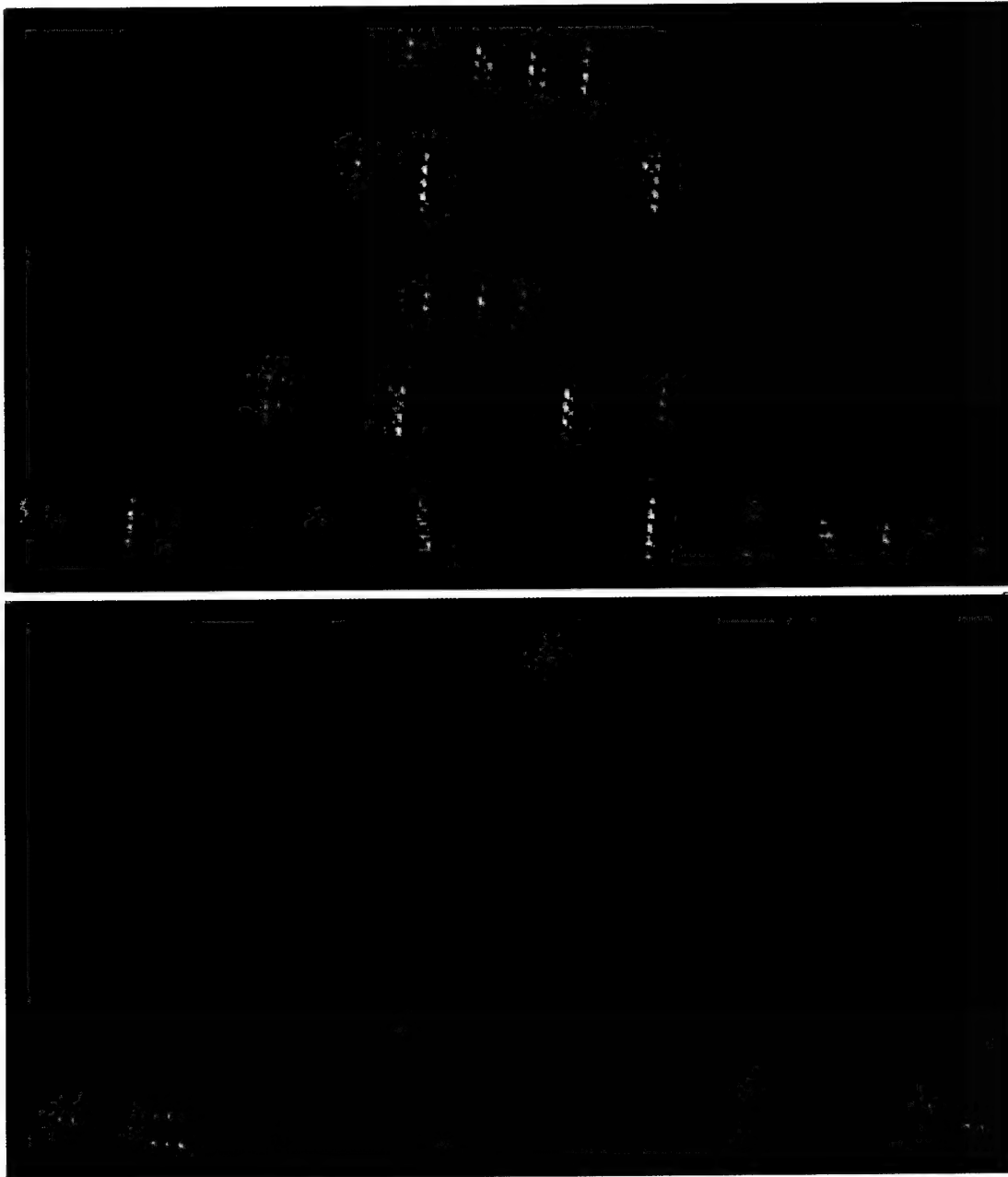


Figure 4-13. Photographic images of 5 by 5 character sets presented normally (bottom) and 90 degrees rotated (top). Note the slight misalignment of character elements.

The data reported here shows an improvement in the MTF which meets the Comanche contrast requirement at the Nyquist frequency. Microvision's new electronics made possible the increase modulation at higher spatial frequencies (observed in the MTF and traditional CTF) when considering only those single orientation spatial frequencies. However, when a noise analysis is used, we see that the horizontal MTF's modulation at the Nyquist limit is handicapped by the noise modulation. The perceptual relevance of this noise pattern is revealed in the inability to identify the orientation of the vertical grill pattern at this frequency.

Pinch Correction

In a scanning display (e.g., cathode ray tubes), lines are generally scanned horizontally and contrast is achieved by increasing or decreasing electron beam intensity as it passes over the display area. The Microvision HMD is the same with the exception that the scanning area is the retina instead of a phosphor, in the case of the CRT, and the beam is a laser instead of an electron beam. For each eye, two laser beams are scanned forward and aft across the retina. As the beams approach an edge they begin to diverge and converge in a geometrically defined way. Figure 4-14 shows graphs of scanned lines with and without pinch correction. Figure 4-14A shows the case where two lines are being scanned simultaneously without pinch correction. As seen in the figure near the right edge, distance A is shorter than distance B, but line separations are the same in the middle of the display. Also notice that scanned lines cross near the edge where the top line crosses the previously scanned bottom line of the line pair. This crossing reduces the usable active area of the display and thereby reduces system efficiency.

Compare this with the pinch correction shown in Figure 4-14B. Here a second harmonic solution has been applied to the scanned lines. Note that near the right edge, distance A and B are now the same. In addition, the line crossing takes place much closer to the edge thereby increasing the usable area of the display thus increasing system efficiency.

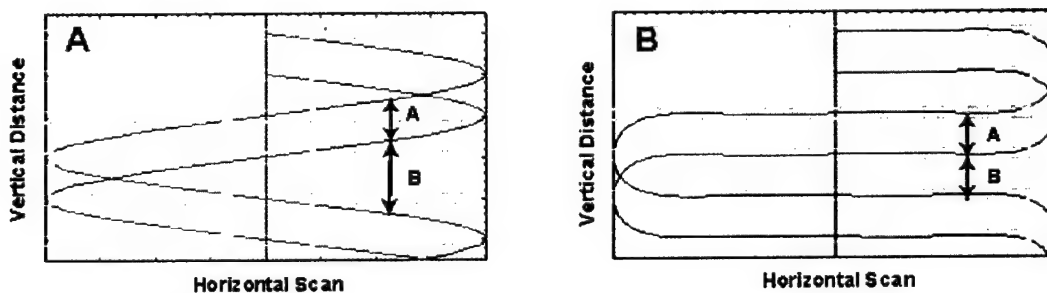


Figure 4-14. Graphs of scanned lines representing dual scans with no pinch correction (A) and dual scans with pinch correction (B). Note the difference between distance A and B in (A), whereas with pinch correction (B), the distances are the same. Original graphs supplied by Microvision, Inc.

To test pinch correction, we devised a horizontal grid pattern composed of two lines on followed by five lines off and the pattern repeated over a given area (Figure 4-15B). Due to the odd number of lines in the pattern, the grill pattern tests different line pairs sequentially. Figure 4-15A shows another graph of the scanning lines with pinch correction. We have numbered the lines 0, 1, 2 and 3. Lines 0 and 1 traverse the screen from left to right and lines 2 and 3 traverse the screen from right to left. The grill pattern displays line pairs 0-1, 3-0, 2-3, and 1-2 sequentially. Line pairs 0-1 and 2-3 scan the same direction, whereas line pairs 3-0 and 1-2 scan in opposite directions. By photographing the displayed grill pattern, the thickness of the line pairs could be measured thereby evaluating the effectiveness of the pinch correction.

If pinch correction is effective, all line pairs should have the same photographic thickness. Figure 4-16 shows images captured from the left edge of the left side. The photograph in Figure 4-16A was taken with pinch correction off. Note that every fourth pair of

lines was thicker than the others. As this pattern did not agree with our prediction of the non-pinch corrected pattern, calibration patterns were examined for inconsistencies. Unfortunately, none were found. After further investigation, we discovered a small piece of black tape stuck to the scanner housing. The tape had torqued the scanner housing and removing the tape and recalibrating, solved the problem. Figure 4-16B shows the proper non-pinch corrected pattern consisting of alternating thick and thin line pairs. Figure 4-16C shows a splendid example of properly aligned optics coupled with pinch correction. Note the uniform thickness of the horizontal line pairs.

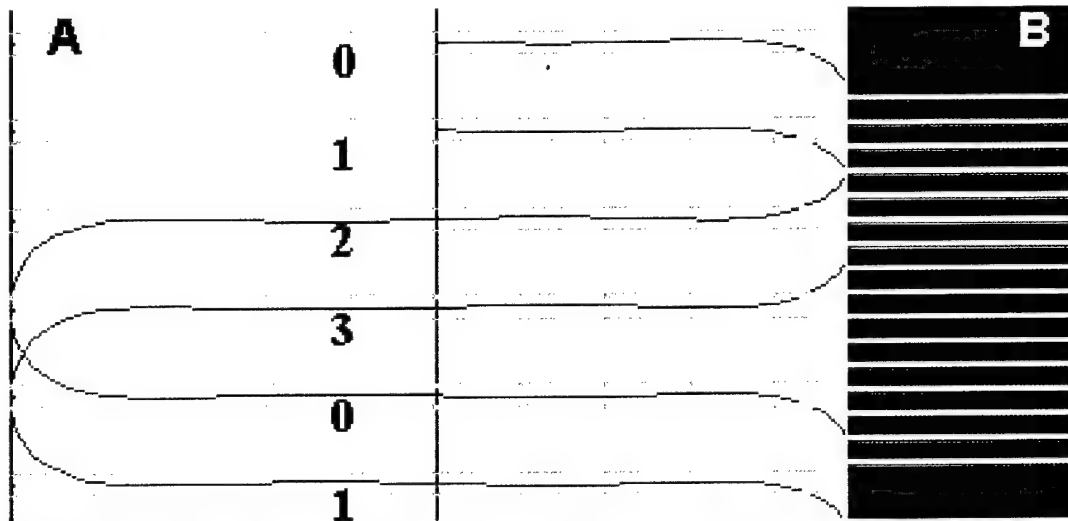


Figure 4-15. Line numbering and pattern for evaluating line pairs. (A). Graph of dual scanning with pinch correction. The lines are numbered 0, 1, 2, and 3 depicting the four line conditions. (B). Horizontal grill pattern comprised of 2 lines followed by five lines off and the pattern repeated. Original graph (A) supplied by Microvision, Inc.

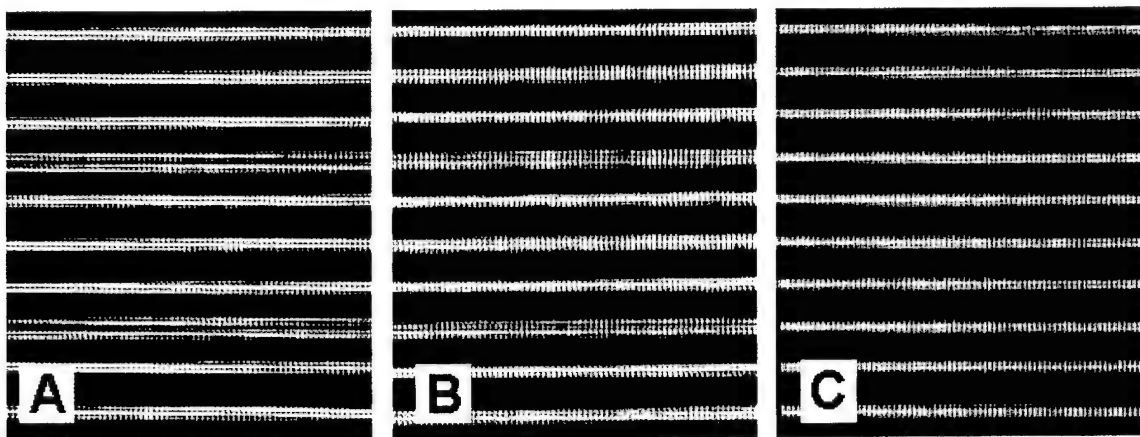


Figure 4-16. Photographic images of line pairs near the left edge of the left side display. (A). Non-pinch corrected condition coupled with a torqued scanner housing (see text for explanation). (B). Typical non-pinch corrected pattern consisting of alternation thick and thin line pairs. (C). Pinch-corrected condition with proper calibration and alignment.

Text images in periphery. To view the effects of pinch correction in another way, 5 by 5 text characters were displayed near the lateral periphery. Figure 4-17 shows photographic

images captured under the two conditions. Letter fragmentation or gaps are seen in the uncorrected condition whereas the pinch-corrected condition shows fairly good character definition.

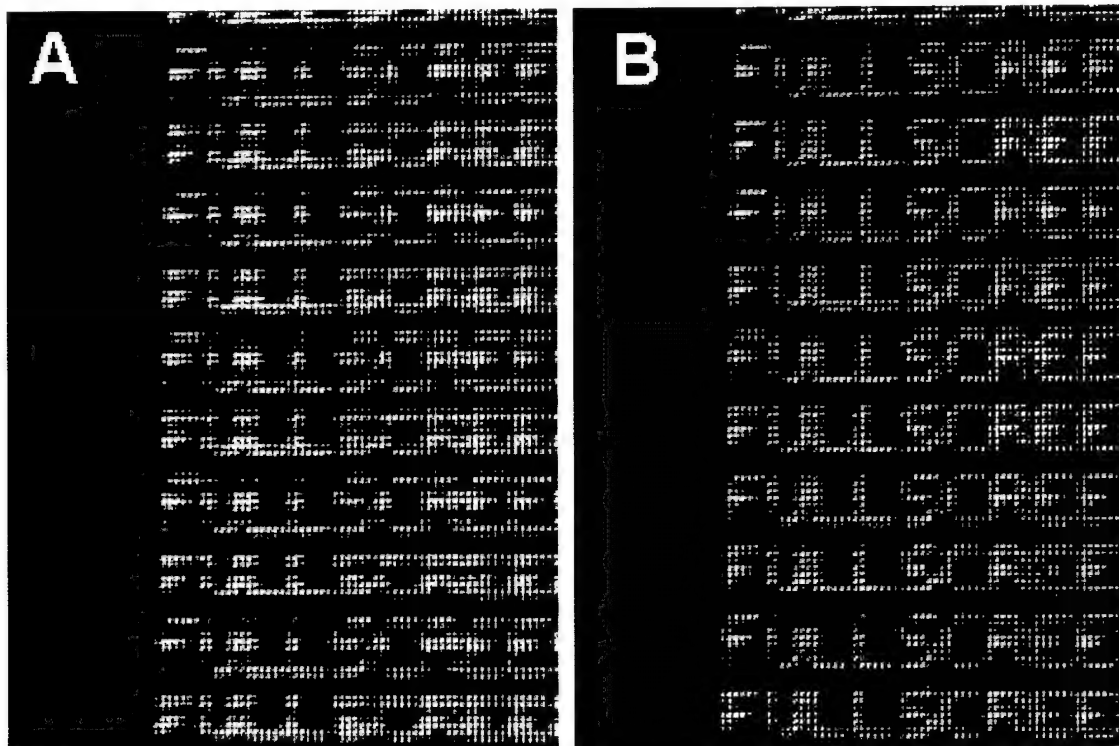


Figure 4-17. Photographic images of 5 by 5 text characters. (A). Non-pinch corrected text imagery. (B). Pinch corrected text imagery.

MTF following pinch correction. To assess the effects of pinch correction on the MTF, the MTF was calculated for the middle of the display. Since pinch correction does not affect line width, it should have no effect on the MTF. Single vertical and horizontal lines were displayed in the middle of the field-of-view. The lines were photographed and processed and the resulting data imported into Microsoft Excel for frequency analysis (Harding, et al., 2001b). Figure 4-18 shows the vertical and horizontal MTFs calculated from the photographic images.

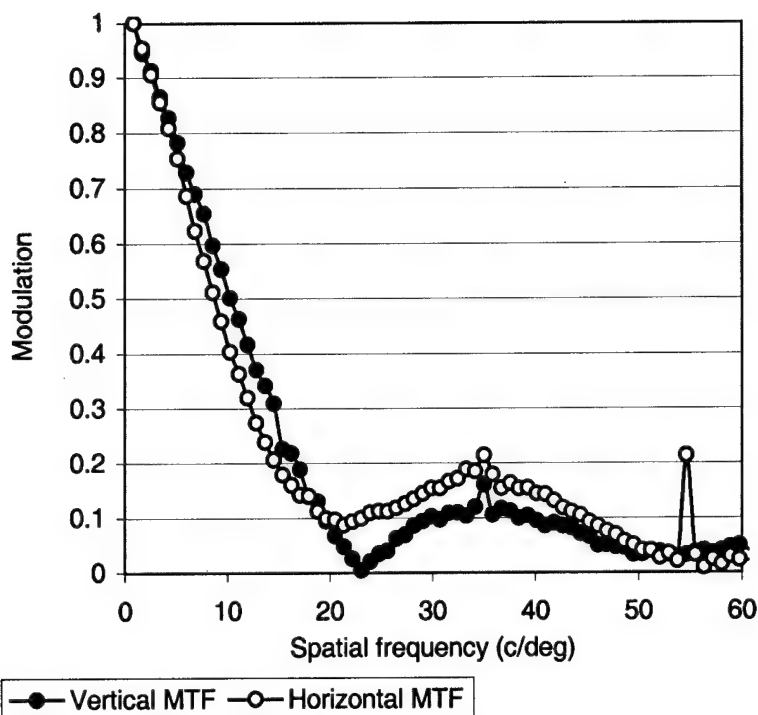


Figure 4-18. MTFs measured from the left side of the HMD. The vertical MTF as a modulation of about 0.23 modulation at the Nyquist frequency (approximately 15.6 cycles/degree) and the horizontal MTF has a modulation of about 0.17 at the same frequency. These MTFs show slight improvements over the MTFs measured without pinch correction (see Figure 4-7).

Other Measures

Table 4-2 shows summary results of measurements taken of the Microvision HMD. These measurements represent the best numbers measured to date for the current version of the HMD.

Table 4-2.
Evaluation Summary

Exit pupil size and shape.	About 15 mm and circular
Eye relief	Physical eye relief: 19mm nominally; Optical eye relief: 42 mm nominally
Field-of-view	Slightly greater than 30 by 40 degrees monocularly
Binocular field-of-view and overlap	Horizontal: 53.24 degrees; Vertical: 31.6 degrees; Overlap 25 degrees
Binocular alignment	Less than milliradian
Transmissivity	Photopic transmission: 59.3% with a tungsten source
Spectral output	Highly monochromatic with a peak at 534 nm
Aberrations	Field curvature was generally negative but did not exceed - 1 diopter. Astigmatic error did not exceed 0.5 diopter.
Maximum luminance at eye	1485 fL

Luminance response curve	Compressive non-linearity
Luminance uniformity	8% of area showed greater than $\pm 20\%$ deviation from the mean
Contrast	Contrast ratios of 20 to 1 measured for a 25 square pattern

The Kaiser Electronics CRT HIDSS

The RAH-66 Comanche is the Army's next generation reconnaissance/attack rotary-wing aircraft. The Comanche Mission Equipment Package (MEP) includes a helmet-mounted display designated as the Helmet Integrated Display Sight System (HIDSS). The Development and Validation Program (DVP) phase HIDSS consists of an integrated helmet, a helmet mounted display (HMD) consisting of a right and a left multifunction display (MFD), a helmet tracking system (HTS), a boresight reticle unit (BRU), and the associated electronics (e.g., expanded display electronics unit [EDEU] and display control panel). Imagery acquired by nose-mounted forward-looking infrared (FLIR) or television sensors is reproduced on miniature displays and then optically relayed to the aviator's eyes. The HTS allows the nose-mounted sensors to be slaved to the aviator's head movements. The BRU provides the capability to align the HTS to the forward aligned direction. The display control panel provides for display adjustments, e.g., brightness and contrast. The HIDSS is required to operate biocularly/binocularly with monocular capability. The HIDSS has a goal to present a 35° (V) X 52° (H) field-of-view (FOV) with an 18° overlap. Exit pupil size is to be 15 mm on axis and 13 mm off axis. A design goal for minimum eye clearance is 22 mm. Kaiser Electronics, San Jose, California, is the manufacturer of the HIDSS evaluated herein. Gentex Corporation, Carbondale, Pennsylvania, manufactures the helmet shell and visor.

The Kaiser Electronics version of the HIDSS has a biocular/binocular integrated helmet and a HMD system. It consists of an aircraft retained unit (ARU) and a pilot retained unit (PRU) (Figure 4-19). The ARU is a front piece consisting of two miniature 1-inch diameter cathode ray tubes (CRTs) and two optical relays attached to a mounting bracket. The final elements of the optical relays are beamsplitters, referred to as combiners. The PRU is the basic helmet with a single-visor assembly. The Kaiser Electronics HIDSS uses two 35° monoculars that provide the required FOV. The system provides adjustments for inter-pupillary distance (IPD) and vertical adjustment position. Rubber "boots" have been installed on the backsides of the combiners to reduce reflections.



Figure 4-19. The Kaiser Electronics HIDSS

Optical characteristics

An optical test bench was used throughout to properly hold, align and actively measure the video response characteristics from the HIDSS. Optical alignment was achieved by affixing the ARU to a U.S. Army Aeromedical Research Laboratory (USAARL) fabricated holder with precision rotation and linear X and Y positioners. See Figure 4-20 for a photograph of the experimental setup. For many of our physical measurements, we found it easier to mount only one optical/CRT channel to the rotating stage. Optical alignment was achieved by producing a centering video pattern consisting of a crosshair that extended to the far periphery of the FOV. Focusing our test equipment to infinity, we aligned our equipment with the video test target. We then focused on the exit pupil and aligned the test equipment with the middle of the exit pupil. Often, this process required several iterations to assure precise optical alignment. As per specifications, a video signal of 1023 scan lines with an aspect ratio of 6:5 was used.

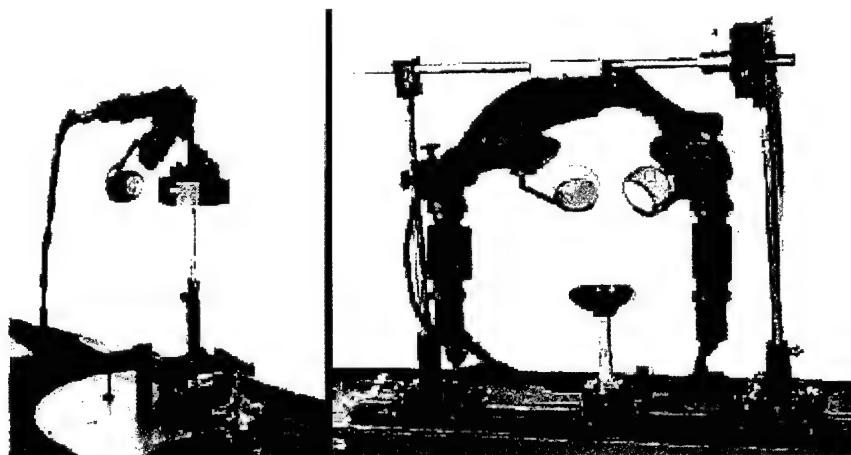


Figure 4-20. ARU mounting configurations.

Miniature CRT image source

Luminance response (Gamma) of the CRT source is shown in Figure 4-21. The curve was monotonic and was approximately linear, although a two component linear fit would probably provide a better description of the data. A linear regression analysis produced a slope of 4.87 with a Y-intercept of 24.61. The Pearson product moment correlation was greater than 0.98. Peak luminance was approximately 3300 fL. This level of light output is required given the efficiency of the catadioptric HMD design.

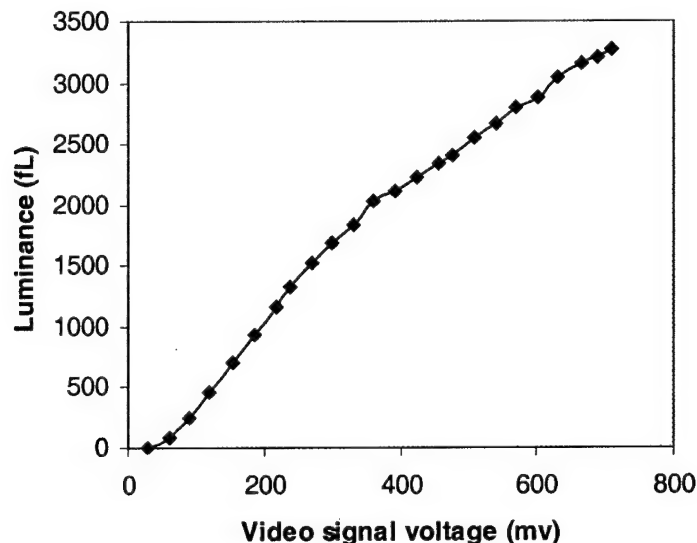


Figure 4-21. CRT luminance response curve.

HMD System

The following tests generally refer to the entire optical system including the CRT image source, relay optics, and combiner.

Field-of-view (physical measure). FOV was measured by rotating the left channel/CRT of the HIDSS about a point that was fixed at the center of the exit pupil. By ray tracing, it could be demonstrated that the image displayed by the channel was contained within a cone whose apex was at the exit pupil and extended out into space. By measuring luminance within this cone, we could measure the extent of the formed image. Following alignment, a uniform field was presented which covered the entire FOV. We measured the luminance of the horizontal FOV by rotating the stage through the spatial extent of the luminance cone. Following this measurement, we mounted the channel/CRT so that the vertical FOV could be measured. The procedure was repeated. Using a dioptrimeter with a crosshair, we measured the horizontal and vertical FOVs by measuring the total rotation required to transit the luminance profile. Figures 4-22 A and B show the measured luminance profiles. The total FOV was found to be 36.7° (H) by 29.5° (V).

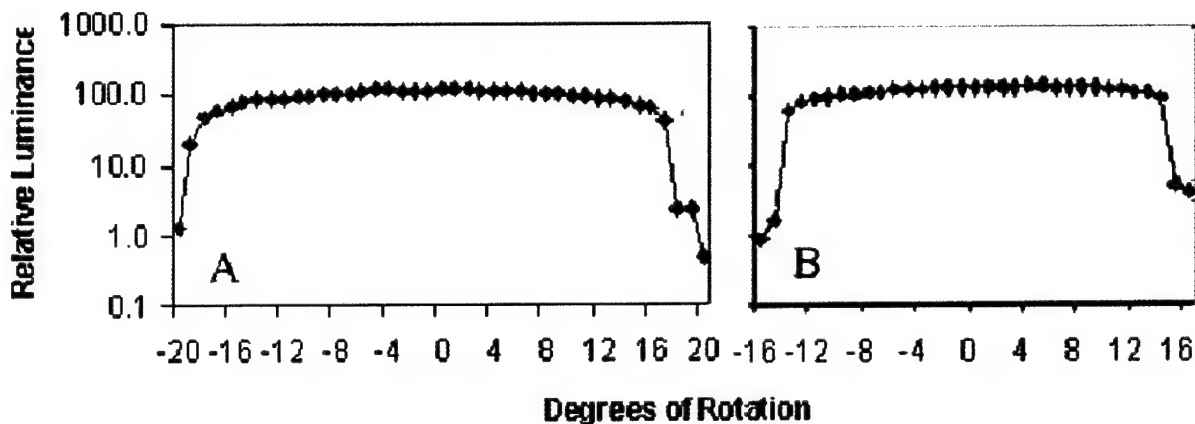


Figure 4-22. Luminance profiles for the horizontal (A) and vertical (B) FOV.

Field-of-view (perceptual measure). The HIDSS ARU was mounted to an optical table so a chin rest could be mounted appropriately for viewing naturally through the combiner systems. A video pattern was generated in the HIDSS which clearly marked the center of the FOV while also showing the peripheral borders. An observer aligned the center of the FOV with a distant central fixation point on the target board. We then marked on the board the left/right and top/bottom FOV borders for each eye. The monocular FOV measured 35.94° (H) by 29.72° (V). We measured a binocular FOV of 54.35° (H) by 29.7° (V).

During this procedure, it was noticed that when the combiner is located at the design exit pupil position (22 mm behind the rubber "boots"), it did not allow upward retraction of the combiner for this observer. This retraction is needed for monocular operation. However, when two observers tested at both the design eye position and the fore-aft position, which would allow combiner retraction, no notable reduction in FOV was found. However, based on our experience with head and facial anthropometry, a percentage of aviators will experience a reduction in FOV when the system is adjusted fore/aft to allow retraction of the combiners.

Using the above technique, we could also map the overlap region of the FOV. Figure 4-23 depicts the results.

Exit pupil size, position and eye relief. A rear projection screen was used to locate the exit pupil position. This was accomplished by moving the rear projection screen along the optical axis until a best focus was achieved. For determining exit pupil size, the dioptometer (with crosshair) was focused on the exit pupil. The crosshair was positioned at the extreme left edge of the exit pupil and the position was marked. The crosshair (diptometer) was translated horizontally across the exit pupil to the extreme right edge of the exit pupil. The translational distance was recorded. The procedure was repeated for the vertical dimension. Eye relief (eye clearance distance) is defined for the purpose of this report to be the straight-line distance from the cornea to the vertical plane defined by the first encountered physical structure of the system. For this test, eye relief was measured for two conditions: with and without the rubber boots in

place. Following the locating of the exit pupil, the distance back to the boots was measured using a millimeter ruler. Three measurements were made and the average reported.

The exit pupil was found to be located at a distance of 27.9 mm from the plane defined by the last (plano) combiner lens. Exit pupil shape was nearly circular with size measurements 15.1 mm vertically and 15.2 mm horizontally. With the rubber boots attached (and needed to reduce extraneous reflections), the eye relief (eye clearance distance) was found to be 22.1 mm.

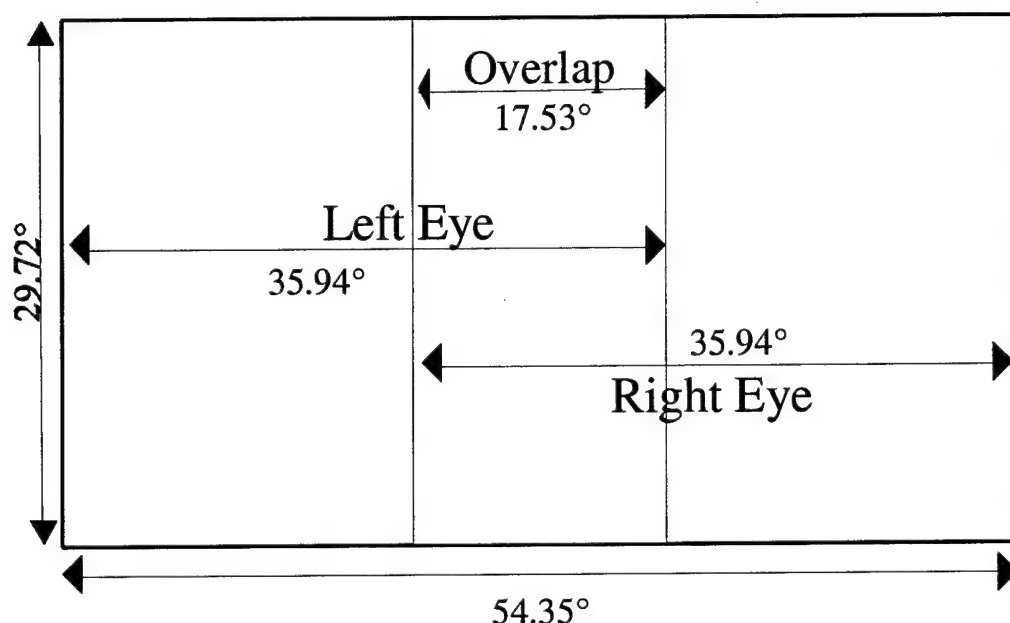


Figure 4-23. Monocular FOVs with binocular overlap region.

Contrast. A video generator and oscilloscope were used to produce bipartite boxes 20 mm square. Using a maximum output level of 710 mv, the total range was divided into 32 gray levels designated 0-31. Each square consisted of two gray level values. The background was set to the mid gray level value of 15. Luminance readings were measured for each side of the resulting square for 16 gray level pairs. The contrast ratio values were defined and calculated as $C_r = \max/\min$. Contrast values were measured for both the “day and “night” switch settings on the control panel. Contrast ratio are provided in Figure 4-24.

Luminance uniformity. A uniform field luminance pattern was produced on the HIDSS left channel/CRT. At each of 25 positions corresponding to the intersections of the 10, 30, 50, 70, and 90% lines, the luminance was measured using the 1980 photometer with a 6' aperture. Figure 4-25 shows a luminance uniformity plot expressed in 20% bands. The maximum deviation from uniformity was 78%. This occurred at the lower right corner of the image. The deviation for most of the image area was less than 40%. In the FOV periphery, significant luminance fall-offs were observed.

Beyond the central region (as defined in Figure 4-25), the luminance uniformity exceeds 20% deviation. Current criteria (Rash, et al., 1996) states that the luminance at any two points within a flat field presented on a display should not vary by more than 20%. By this criterion, a

significant peripheral region of the HIDSS FOV does not meet this criterion. However, by comparison to previous IHADSS uniformity data (Harding, et al., 1996) based only on uniformity measured in the horizontal and vertical meridians, the IHADSS had a coefficient of variation of 15.81%. Using similar analysis with the HIDSS, we find a coefficient of variation of 17.12%. Based upon this analysis, we find only minor differences between the two systems.

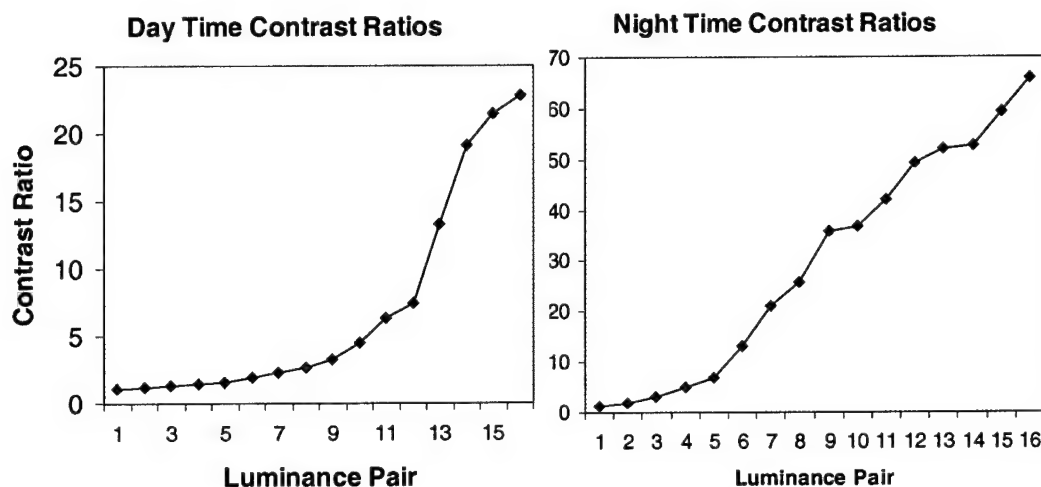


Figure 4-24. Daytime and nighttime contrast ratios for the HIDSS HMD.

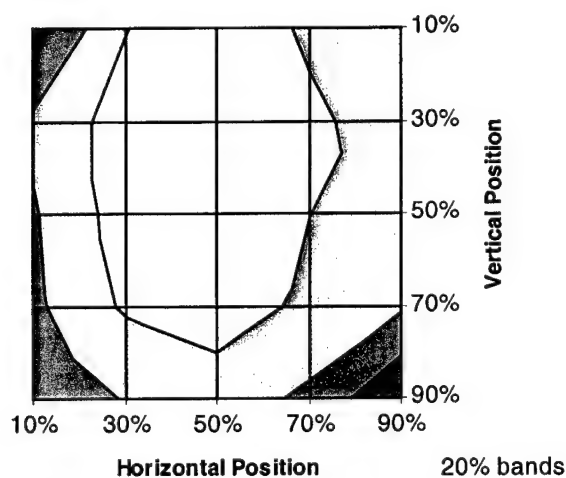


Figure 4-25. Luminance uniformity.

Field curvature and spherical/astigmatic aberrations. A high definition grid pattern was produced on the full active area of the CRT. The optical/CRT channel was mounted on a rotating stage and positioned such that the center of rotation was at the exit pupil. The dioptrometer was mounted to the optical table and aligned with the center of the test grid image. The position of the exit pupil was at the front of the dioptrometer. The dioptrometer was set to zero. From -18° to $+18^\circ$, field curvature along the horizontal axis was measured by focusing on the grid pattern and the power change noted. Astigmatic error was measured by noting any differences between vertical and horizontal grid focus.

By mounting the diptometer to a precision traversing stage, spherical aberration could be measured as a function of decentration. Over a ± 7 mm decentration range (the most allowed with a 15-mm exit pupil), spherical aberration was measured.

No significant field curvature or spherical/astigmatic aberrations were measured: all measured values were less than 0.125 diopter.

Temporal response. A single horizontal scan line was displayed on the HIDSS left channel/CRT. A one-degree circular aperture was aligned on the middle of the horizontal line segment. We calculated that the CRT beam would be within the photometer's aperture for less than 1 δ sec every 33.33 msec. This short measurement period allowed us to measure the phosphor rise and fall times.

By defining the rise time to 90% of the peak, we found a phosphor rise time of approximately 500 δ sec. By defining the phosphor fall time as the time from peak to 10%, we found a phosphor persistence of approximately 6 msec. The measured 6 ms persistence is in line with the ~ 7 ms value cited in Tube Engineering Advisory Council (TEAC) publication No. 116. This is the limiting temporal characteristic of the HIDSS. The phosphor's temporal characteristics provides a sufficient temporal bandwidth for the display frequency of the HIDSS.

The MTF. The left channel/CRT was mounted on a rotating stage such that the axis of rotation coincided with the position of the exit pupil. A single vertical line segment was displayed in the middle of the FOV. The luminance of the line was adjusted to provide a high contrast ratio. The slit aperture in the 1980 photometer was aligned with the line segment. The slit aperture measured approximately 1 arc minute in width by 10 arc minutes in length. The slit was appreciably narrower than the video line segment. We rotated the table to a position 0.5 degrees laterally. The amount of rotation equivalent to 0.5 arc minutes was calculated. Photometric readings were taken at each 0.5 arc minute increment about the line segment. In all, 120 readings were obtained which encompassed 30 arc minutes to either side of the line segment. The resulting luminance profile was a line spread function of the single line segment. The fast Fourier transform (FFT) of the line spread was calculated and then normalized to approximate the uncorrected horizontal MTF. Likewise, the FFT of the finite slit aperture was calculated and normalized. The inverse of the aperture FFT was multiplied by the line spread FFT thus performing a deconvolution and correcting for the effects of the finite aperture. The left channel/CRT then was rotated 90° to obtain the vertical line spread in similar fashion and the FFT procedures repeated.

The normalized horizontal and vertical MTFs are shown in Figure 4-26. As expected, the vertical MTF is slightly higher than the horizontal MTF for spatial frequencies beyond 3 cycles/degree (c/deg). Modulations fell to 50% of the peak at only 6 to 7 cycles per degree and are 90% down at only 10 to 11 cycles per degree. The MTFs appear to be low given the spatial bandwidth of the visual system. We noticed that the lines appeared out of focus and this could account for part of the low spatial resolution.

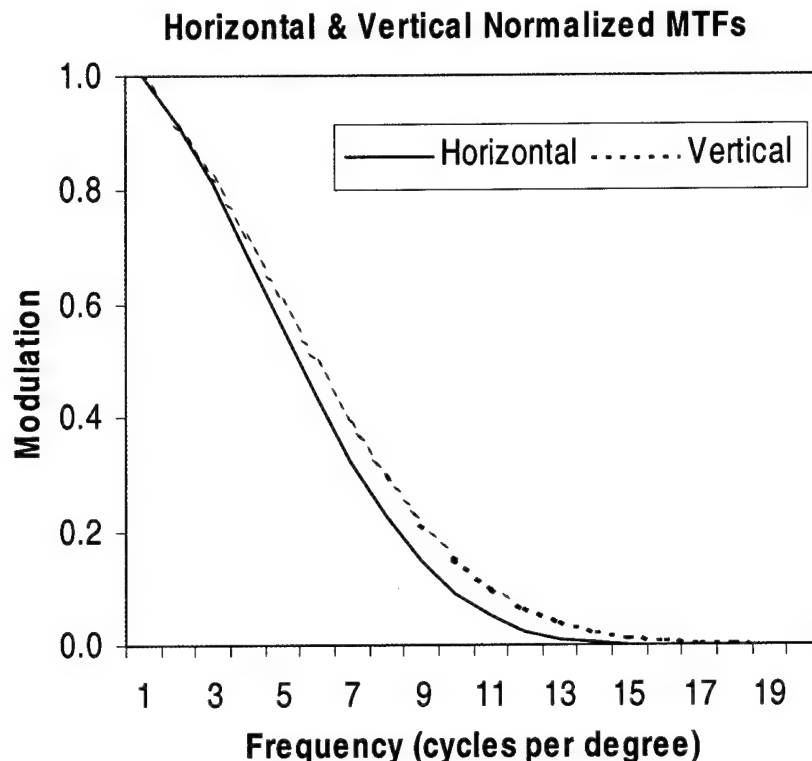


Figure 4-26. Horizontal and vertical MTFs.

See-through spectral/luminance transmittance. The RS-12 standard lamp was placed in front of the combiner lens assembly with the lamp surface orthogonal to the optical axis. The spectral output of the lamp was scanned with the combiner lens assembly in the retracted position ("up" position) and with the lens assembly in the normal (see-through) position. We also measured transmittance as a function of horizontal and vertical rotation to see if the optical coatings are angular dependent.

The see-through spectral transmittance curves for a number of horizontal and vertical angular orientations are shown in Figure 4-27. Note the notch at 544 nm, the peak of the P53 CRT image source phosphor. No significant angular effects were observed in the data. Transmittance on either side of the notch approaches 50%. Transmittance falls-off appreciably above 700 nm and below 420 nm. The average spectral transmittance across the measured spectral band (390 to 730 nm) is 40%. The see-through transmittance of a P53 phosphor display is estimated to be approximately 11%.

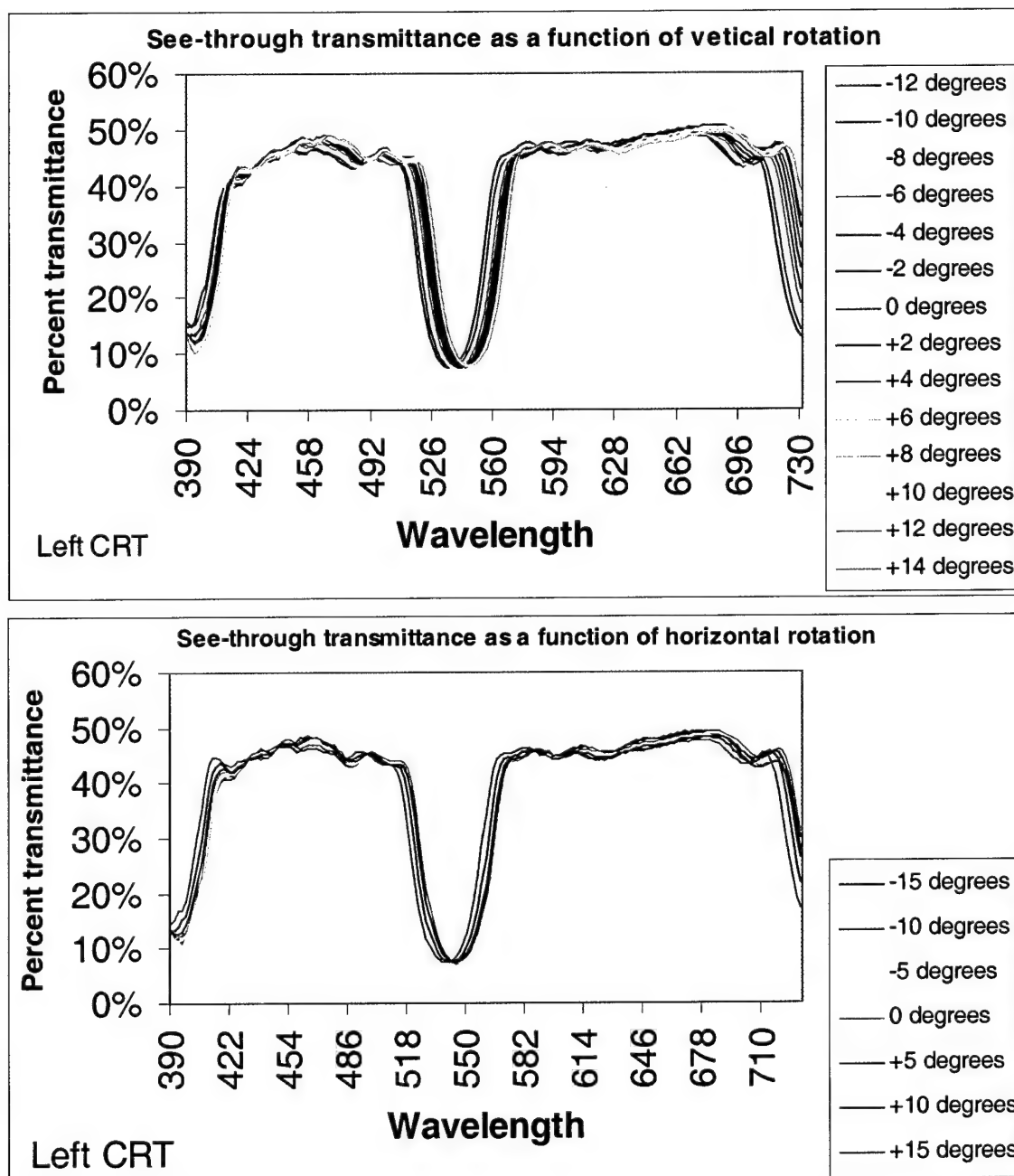


Figure 4-27. See-through spectral transmittance as a function of (a) horizontal and (b) vertical rotation.

Summary of findings. Evaluation results are summarized in Tables 4-3 & 4-4. Image quality consists of a number of attributes which address spatial, temporal, luminance, and spectral figures-of-merit. The HIDSS provided acceptable image quality except for the areas of contrast ratio (shades of gray), luminance uniformity, and MTF. During daytime operation, the HIDSS does not provide a sufficient number of shades of gray. For luminance uniformity a significant drop-off was exhibited in the peripheral FOV. The CRT electron beam appeared out of focus and this contributed to the poor MTF response, down by 50% at only 6-7 cycles/degree.

Additional human factors engineering concerns surfaced during the evaluation. These included restrictions on pilot head movements due to CRT size and location, extraneous reflections, single visor configuration, and IPD extreme adjustment effect on monocular operation.

Table 4-3.
Summary findings from the HIDSS Evaluation

Parameter	Measurement Data
CRT luminance response	Quasi-linear response with a high of 3300 fL
Field of view (physical)	Each Optical Channel: Horizontal FOV = 36.7°; Vertical FOV = 29.5°
Field of view (perceptual)	Binocular FOV = 54.35° by 29.7°
Image overlap	Binocular Overlap = 17.53° with flanking monocular fields of 18.41°
Visual field	Obscurements due to boots; improved look under capability over ANVIS
Interpupillary distance and vertical adjustment	58 to 78 mm IPD range for most optical positions with a 10 mm vertical adjustment range. With the optics raised to their highest extent, the maximum IPD is reduced to 70 mm.
System transmittance & reflectance	From HIDSS CRT to Eye: P-53 phosphor luminance is reduced by 87%.
Exit pupil size, position and eye relief	Size: The exit pupil is circular in shape with diameter of 15.15 mm. Position: 27.9 mm behind the plano lens. Eye Relief: 22.1 mm behind the rubberized extraneous reflections suppressor (boot)
See-through spectral luminance transmittance	The average spectral transmittance is about 40% although the transmittance function has a large trough near the peak of the P-53 phosphor. The see-through transmittance of the peak of the P-53 phosphor is about 11%.
Contrast ratio	Daytime setting: ≈ 22 ; Nighttime setting: ≈ 66 .
Combiner power	0.185 diopter.
Luminance uniformity	Significant drop-off in the periphery. Luminance uniformity was within 20% in the middle of the display.
Field curvature & spherical/astigmatic aberrations	No significant effects.
Temporal response	Phosphor: rise time of 500 \pm sec; fall time of 6 msec.
MTF	Normalized MTF down by 50% at 6 to 7 cycles/degree.
Luminance tracking	Quasi-linear tracking response.

Table 4-4.
Additional findings from the HIDSS Evaluation

System	Parameter	Measurement Data
Visor	Luminous transmittance	Photopic transmittance measured at 90.2%
	Refractive power	Negligible: -0.05 diopter or less.
	Prismatic deviation	No significant effects.
	Distortion	No detectable distortion.
Visual performance	See through visual acuity	20/15 Snellen acuity in each eye.
	See through color discrimination	No color discrimination defects detected.
Pedestrian characteristics	Extraneous reflections	Extraneous reflections were present even with the boots in place.
	Daylight performance	Imagery viewable but perceptible shades of gray not characterized.
	Human factors	Easily donned and doffed; ARU easily attached/detached; lowering/raising of visor acceptable; ease of use of IPD and vertical adjustments rated excellent.
	Single visor configuration	Results in lower usage of visor which increases frequency and severity of facial injuries during mishaps.

Evaluation of HIDSS Developmental Sources

The Aircrew Integrated Helmet System (AIHS) Comanche compatibility program had supported the RAH-66 Comanche Helmet Integrated Display and Sighting System (HIDSS) helmet-mounted display (HMD) program through the investigation of alternative HMD designs, to include the investigation of new technology image sources. UES evaluated the Kaiser and the Honeywell miniature flat panel sources as part of the evaluation for a prime contractor for the Comanche HIDSS. This section summarizes UES findings as outlined in USAARL Report No. 99-06.

Introduction

Miniature CRTs have been used successfully in the monocular Integrated Helmet Display and Sighting System (IHADSS) in the AH-64 Apache. CRTs currently provide the best image quality available. However, CRTs, even miniature ones, present a number of undesirable characteristics. These include high weight and power consumption, heat generation, and, when

helmet-mounted, center of mass offsets. But, more importantly, miniature CRT availability has declined to virtually nil. Miniature CRT demand is limited to military use, making their production financially unfeasible. This would significantly impact the fielding of the current HIDSS CRT design. For this reason, it was prudent to investigate alternate image sources.

Phase I of the alternate program resulted in two subcontractor alternative design proposals. At the end of phase IIA, each subcontractor submitted representative models of their proposed HIDSS design. While both designs showed promise, neither incorporated image sources that were sufficiently matured to fully meet the Comanche requirements (Gentex, 1998). For this reason, phase IIB was expanded to focus on image source enhancements.

The CRT-based DVP HIDSS design was evaluated by the U.S. Army Aeromedical Research Laboratory (USAARL) in the latter part of 1997 (Harding et al., 1998) (see above). This report documents the image quality performance of the miniature electroluminescent (EL) display image source (Figure 4-28) submitted by Honeywell, Inc., Minneapolis, MN, and the miniature liquid crystal display (LCD) image source (Figure 4-29) submitted by Kaiser Electronics, Inc., San Jose, CA.

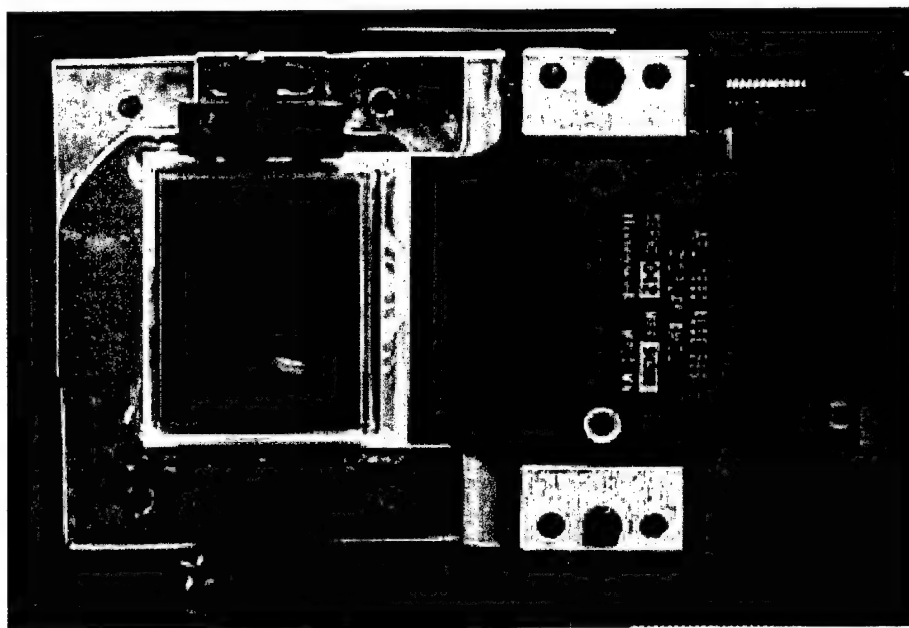


Figure 4-28. Honeywell, Inc., miniature 1280 X 1024 EL image source.

Image Sources

The Honeywell, Inc., EL image source is a nominal 24-micron (urn), 1280 X 1024 resolution display manufactured by Planar Systems, Inc., Beaverton, OR. The Kaiser Electronics LCD image source has the same 1280 X 1024 resolution, but is based on a nominal 12-micron pixel and is manufactured by Kopin Corporation, Tauton, MA. Honeywell provided two test items, identified as #42 and #44. Kaiser Electronics provided two test items, identified as #1 and #39 and a "set up" display, used to validate the electronic configuration.

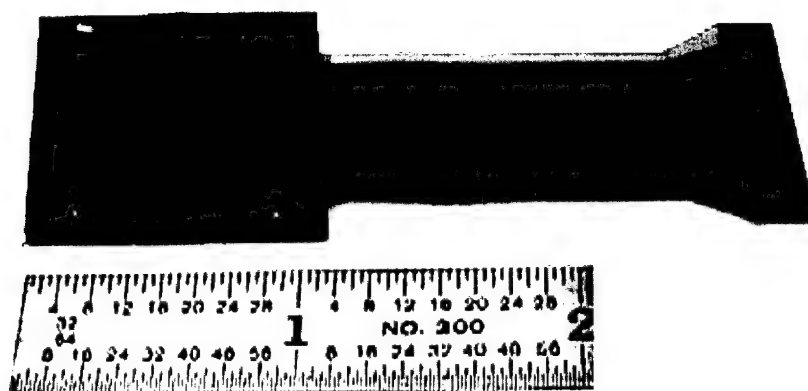


Figure 4-29. Kaiser Electronics, Inc., miniature 1280X1024 LCD image source.

Honeywell, Inc. electroluminescent (EL) display tests

The first EL source (#44) experienced a catastrophic failure during power up. All data reported here are based on test source #42, P/N 1680-ALSE-I-566. Honeywell provided the required drives and control electronics for the evaluation. All testing was performed at USAARL. Some tests were observed by Honeywell, Inc., engineers.

Pixel geometry. Image source was placed on a XY-translator stage beneath a microscope objective. The panel was lighted from above via the microscope's light source. Using a 50X objective lens, a small patch of pixels was imaged by the CCD camera and digitally captured by computer, and the image was saved as a graphics file. Using Adobe Photoshop, the image was analyzed, and measurements of pixel geometry were made using a mensuration technique. Calibration was calculated using a previously stored image of an 1/100 mm microscope stage.

Figure 4-30 is a photomicrograph of a pixel patch on the EL source of about 12 by 9 pixels. The photomicrograph provides details of the microscopic structure not commonly seen under normal viewing conditions. Figure 4-31 shows an enlarged section of the pixel patch shown in Figure 4-30. We measured pixel pitch to be 24.1 μm . The pixel fill factor was virtually impossible to measure owing to the Lambertian output distribution of light of the EL display. Planar engineers reported that the fill factor value was nominally 0.84. The difficulty of accurately measuring a fill factor for this source is the reflectance of emitted light from the areas surrounding the active pixel structure. Our attempts generally provided a measure that was greater than the pixel pitch. This leads to the concept of an "effective" fill factor which we discuss further in the predicted modulation transfer function (MTF) section.

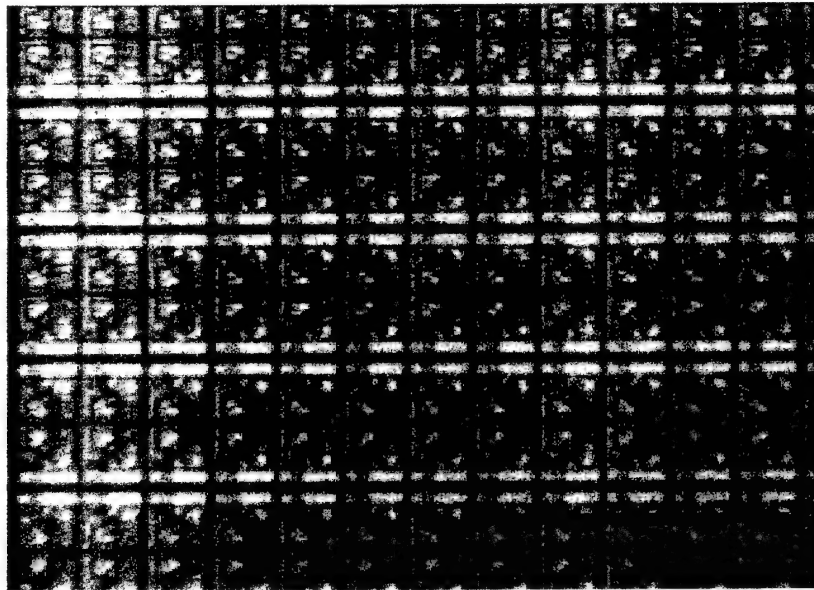


Figure 4-30. Photomicrograph of pixel structure. Pixel illumination is artificial and provided from above. Please note the calibration scale.

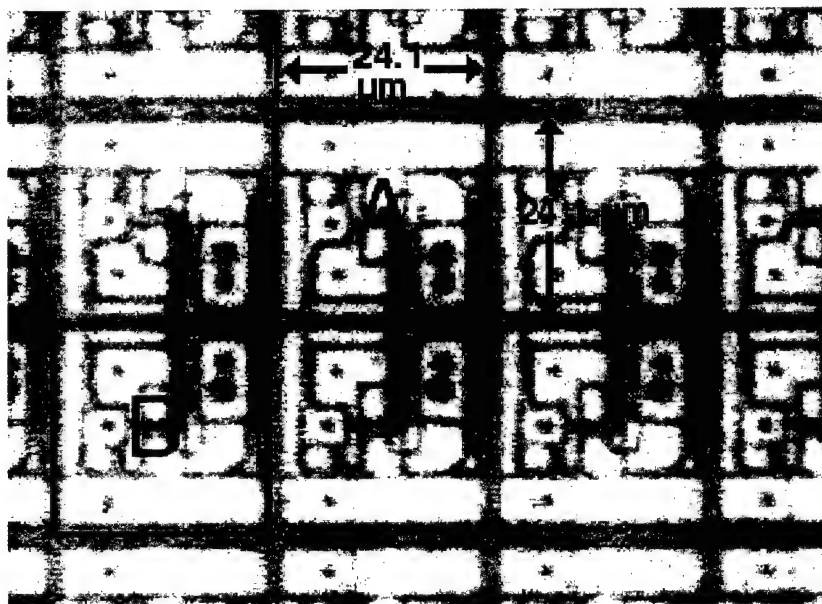


Figure 4-31. Enlarged photomicrograph subsection with light enhancement. Two pixels are highlighted (pixels A and B). Using computer mensuration, we measured pixel pitch to be 24.1 pm, which also equates to the pixel size.

Pixel defects. In Figure 4-32, photo A, note the two primary columns of pixels that are “stuck on” in the display’s lower right quadrant (picture’s lower left quadrant). Photo B shows a cross pattern, and all other pixels are off. Note the many pixels that are permanently on. In photo C, a gray scale pattern is shown. Note the bleed-through of small squares. The squares are part of a 25-square pattern previously displayed for measuring display uniformity. This “burn-in” of a previously displayed pattern was a recurring problem.

The frequency of pixel defects seemed high. While this is a concern, it must be remembered that the device under test was a prototype. Of greater concern was the “burn-in” problem which will significantly degrade performance.

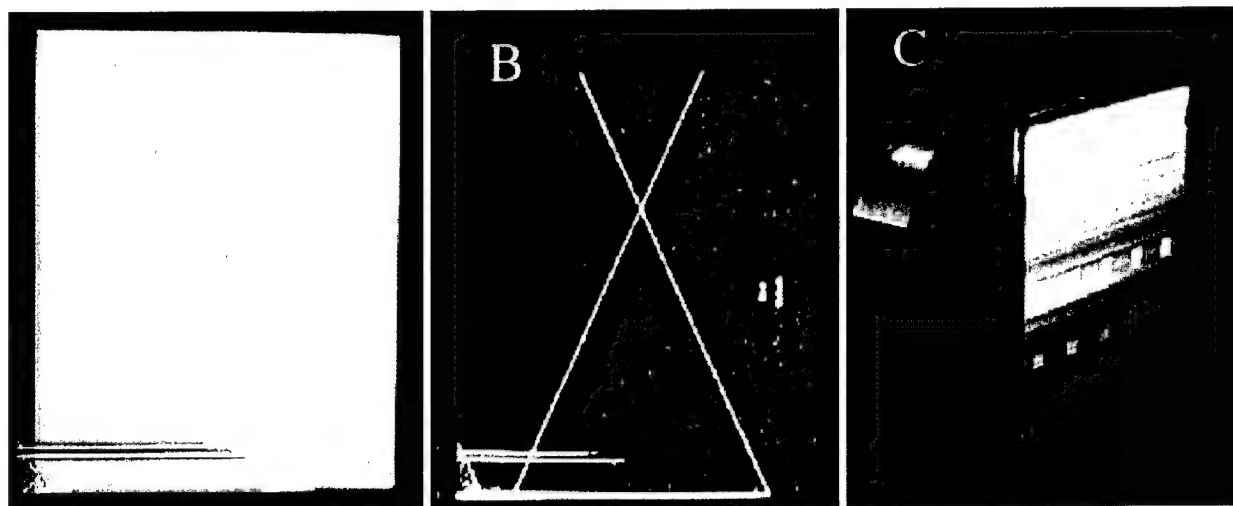


Figure 4-32. Photomicrographs of pixel defects in the Honeywell EL display.

Luminance uniformity. To determine the variation in luminance for both on-axis and off-axis orientations, a pattern consisting of 25 windows, each 80 horizontal by 64 vertical pixels was displayed on the flat panel. Each rectangular block of pixels was set to a maximum gray level of 63. The background was set to a gray level of 0. On-axis luminance measurements were taken for each of the 25 windows. Off-axis luminance measurements were taken for only the center window at each of several horizontal and vertical angles. On-axis luminance (fL) for each of the 25 windows is provided in Table 4-5. On-axis luminance uniformity was exceptional for this display with the largest deviation from the mean of less than 4%.

Figure 4-33 shows the off-axis luminance as a function of angular rotation. The data are plotted as relative luminance where the luminance at zero degrees is set to 0.00. Over a plus or minus 30-degree range, the luminance remained fairly constant with only small deviations (< 3%).

Table 4-5.

On-axis luminance of each of the 25 illuminated squares.

601.28	599.22	588.92	588.92	572.45
603.34	599.22	595.10	590.98	578.63
609.51	605.40	599.22	593.04	580.69
609.51	601.28	603.34	599.22	586.86
609.51	603.34	605.40	590.98	586.86

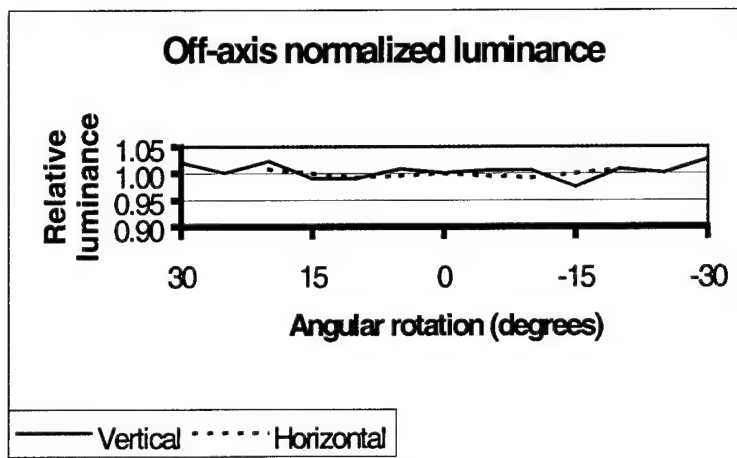


Figure 4-33. Off-axis normalized luminance.

Contrast uniformity. To determine variation in contrast uniformity over a large area of the display, the same 25 square pattern was used. Each rectangular block of pixels was set to a maximum gray level of 63. The background was set to a gray level of 0. Luminance measurements were taken at each of the 25 windows and at locations to the right of each window and beneath each window. For the measurements to the right, the photometer measured a dark area 80 pixels away from the center of the window. For the measurements below each window, the photometer measured an area 64 pixels directly below the center of each window.

Tables 4-6 and 4-7 list the lateral and vertical contrasts for the 25 window pattern. Contrast uniformity shows considerable more deviation owing mostly to the denominator in the contrast ratio.

Table 4-6.
Lateral contrast

202.04	170.93	162.71	170.66	207.46
151.01	127.83	127.19	128.70	165.09
142.65	125.42	119.58	122.65	160.00
145.19	128.14	124.15	126.64	160.00
174.57	155.44	151.55	123.71	146.11

Table 4-7.
Vertical contrast

153.89	117.60	111.63	77.24	62.75
77.26	95.77	97.64	53.75	109.84
122.86	99.33	94.10	95.35	105.66
123.27	104.96	100.69	102.11	100.72
155.67	131.00	126.72	126.43	118.49

Luminance response curve. To determine the luminance response function of the display, a 40 by 40 pixel square was centrally located and set consecutively to a range of gray levels from 0 to 63. All other pixels were set to zero. Luminance was measured with a Pritchard 1980A photometer. The plane of the display was aligned with the photometer focal plane. The 40-pixel square target was centered with the center of the viewing photometer aperture. We measured absolute luminance in footlamberts. Luminance readings were made for each of the 64 gray levels. The Gamma curve is shown in Figure 4-34. The curve displays a shape that may reflect a gray-level bit map error. The error appears every 16 gray level increments. Other data collected also reflected this type of error.

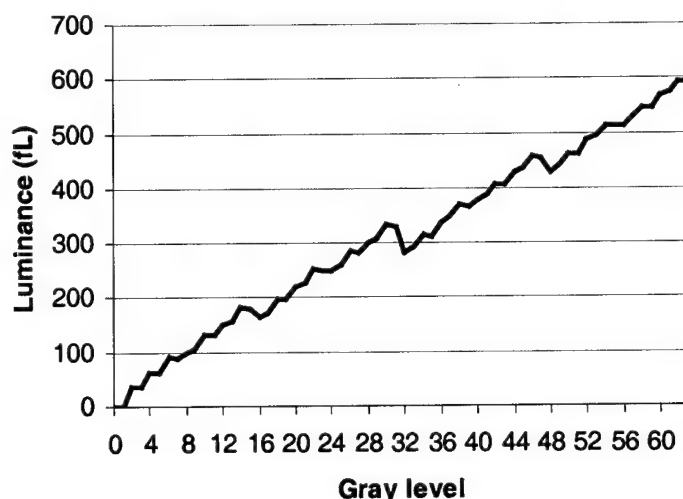


Figure 4-34. The luminance response curve (Gamma) measured for the Honeywell EL panel (#42).

CTF. To determine the Michaelson contrast for a series of grill patterns or square wave gratings. A Pritchard 1980A photometer with an MSIOX and 25X lens with a slit aperture were used to measure the fine patterns. A grill pattern with contrast of 0 for the valleys and 63 for the peaks were used. Spatial frequencies ranged from 20 cycles per display width (32 pixel rows on and 32 pixel rows off) up to a high spatial frequency of 640 cycles per display width (1 pixel row on and 1 pixel row off).

The slit aperture was aligned near the middle of the display and in the center of the lighted half of the frequency pair and the luminance was recorded. This step was repeated for the darkened half of the frequency pair. This procedure was repeated for each spatial frequency (20, 40, 80, 160, 320, and 640 cycles per display width). Testing was performed with the 10X and the 25X lenses. Data collected from the two lenses are shown in Figure 4-35.

The contrast transfer function was good. At the Nyquist frequency (640 cycles/display width), the contrast was about 60%, which is reasonable for this display.

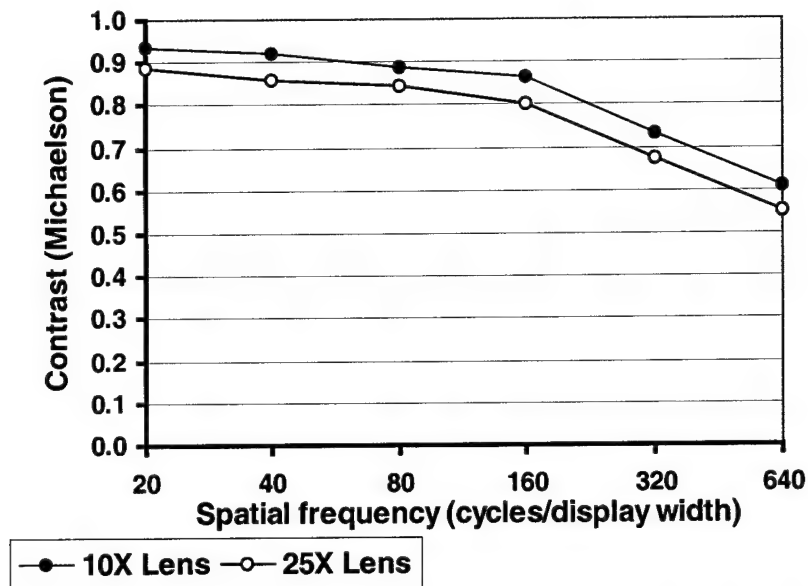


Figure 4-35. Contrast as a function of spatial frequency for the grill pattern. The 25 X lens actually shows less contrast which is contrary to expectation.

MTF. To determine the horizontal and vertical MTFs for the display, a single pixel column or row was turned on while all remaining pixels were turned off. Aligned the slit aperture over the middle of the lighted pixel column. The Pritchard photometer with a 25 X lens with a slit aperture was used to measure the luminance profile of the illuminated line. Assured that the orientation of the slit exactly coincided with the pixel column by translating the stage along the vertical axis and visually confirming that the slit remained in the middle of the pixel column. The slit was returned to the center of the display column and then moved horizontally 128 μ m. The line was then scanned in 1 μ m increments for a total of 256 points which allows a power of 2 fast Fourier transform (FFT) to be performed on the array. This process was then repeated for the horizontal pattern.

The vertical and horizontal MTFs are shown in Figure 4-36. The two curves essentially were identical and this was expected given the horizontal and vertical pixel pitch and fill factor dimensions were the same. The MTF fell to about 40% of the maximum at the Nyquist frequency (approximately 21 cycles/mm). This sharp drop-off was rather expected given the large effective fill factor.

Spectral distribution. To determine the spectral distribution and chromaticity of the display's emitted light, a 100 by 100 pixel window was centrally located and set to a gray level of 63. All other pixels set equal to 0. A Photo Research PR704 Spectrascan was used to measure the color spectrum.

The spectral distribution peaked at 580nm and had a bandwidth at half height of about 50nm. See Figure 4-37. The 1931 CIE chromaticity coordinates are $x = 0.5212$ $y = 0.4760$.

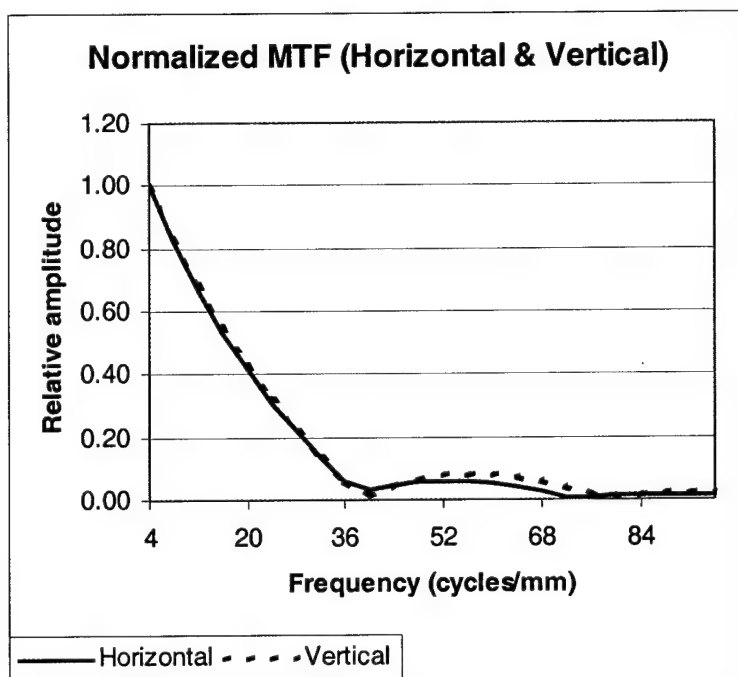


Figure 4-36. MTF curves measured for the vertical and horizontal line-spread curves.

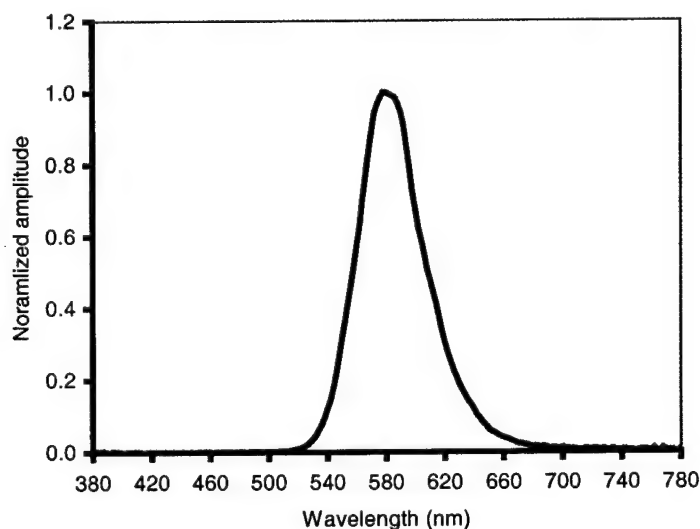


Figure 4-37. Spectral distribution of the EL display.

Perceptible gray levels. To determine the number of perceptible gray levels, a 16 panel gray level pattern (80 pixel/column) was used. Gray level progression for each column was driven by a square root of 2 increments in voltage. Six observers viewed the display and counted the number of gray levels that appeared separate and distinct from all other gray levels. The observers were instructed not to count each bar where a border was observed but rather to judge the number of separable gray levels. The six observers had scattered estimates of the number of gray levels. The estimates average 8.3 gray levels with a standard deviation of 2.5 gray levels.

Kaiser Electronics, Inc. LCD tests

The first LCD source (#1) experienced a failure early in our testing sequence and therefore most of the data presented here were collected on Kaiser's source #9. Kaiser Electronics, Inc., provided the required sources, backlight with fiber optic bundle, and interface electronics for the evaluation. All testing was performed at USAARL. Some tests were observed by a Kaiser Electronics engineer.

Pixel geometry. The image source was placed on a XY-translator stage beneath a microscope objective. The panel was lighted from above via the microscope's light source. Using a 16X and 50X objective lens, a small patch of pixels was imaged by the CCD camera and digitally captured by computer, and the image was saved as a graphics file. Using Adobe Photoshop, the image was analyzed, and measurements of pixel geometry were made using mensuration techniques. Calibration was calculated using a previously stored image of a 1/100 mm microscope stage.

Figure 4-38 is a photomicrograph of an 8 by 6 pixel patch of the LCD source. The photomicrograph provides details of the microscopic structure not commonly seen under normal viewing conditions. Figure 4-39 shows an enlarged section of the pixel patch shown in Figure 4-38. We measured pixel pitch to be $11.85\text{ }\mu\text{m}$. The pixel fill factor was determined to be 0.38 based upon an active pixel area of $6.05\text{ }\mu\text{m}$ wide and $8.75\text{ }\mu\text{m}$ tall. Kopin engineers reported that the fill factor value was 0.32. The fill factor was difficult to measure owing to insufficient light at the high magnification used in our measurements. To overcome this deficiency, we digitally enhanced a patch of on-pixels as shown in Figure 4-40. The on-pixel area corresponds to the active pixel area illustrated in Figure 4-38.

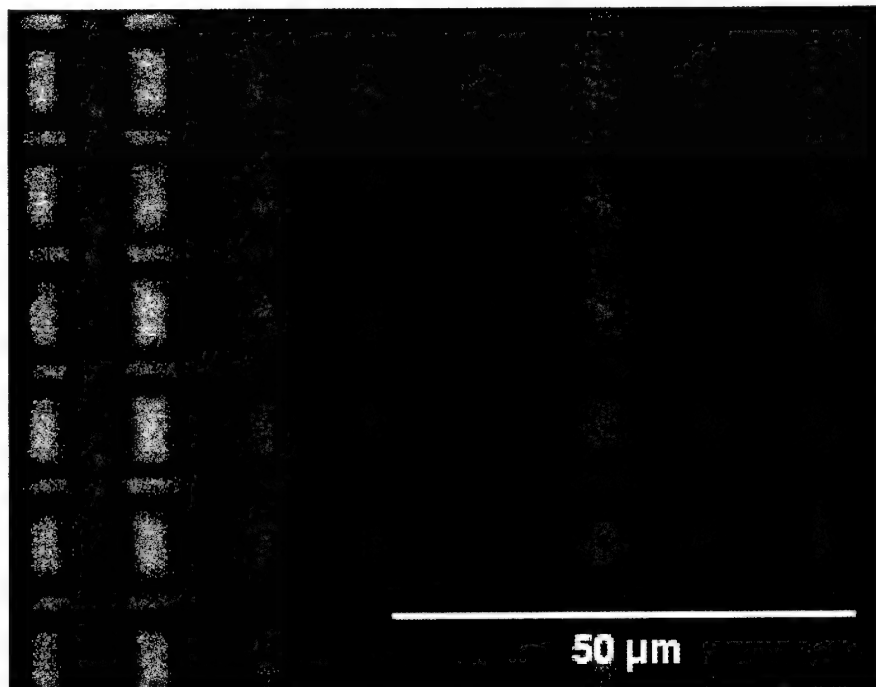


Figure 4-38. Photomicrograph of $12\text{ }\mu\text{m}$ LCD showing a pixel patch of about 8 by 6 pixels. Illumination is artificial and is from directly above.

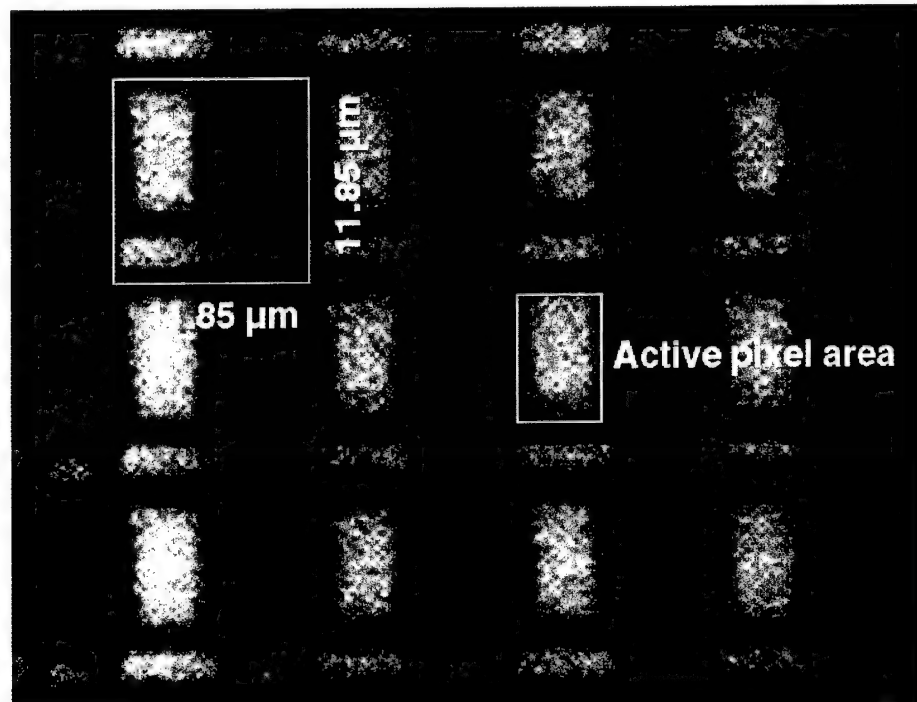


Figure 4-39. Enlarged sub-section of Figure 4-38. Note the active pixel area is the white rectangle. Illumination is artificial, and the square area, designated as a single pixel, may or may not be co-located with the actual pixel area, although the square is the size of the actual pixel area.

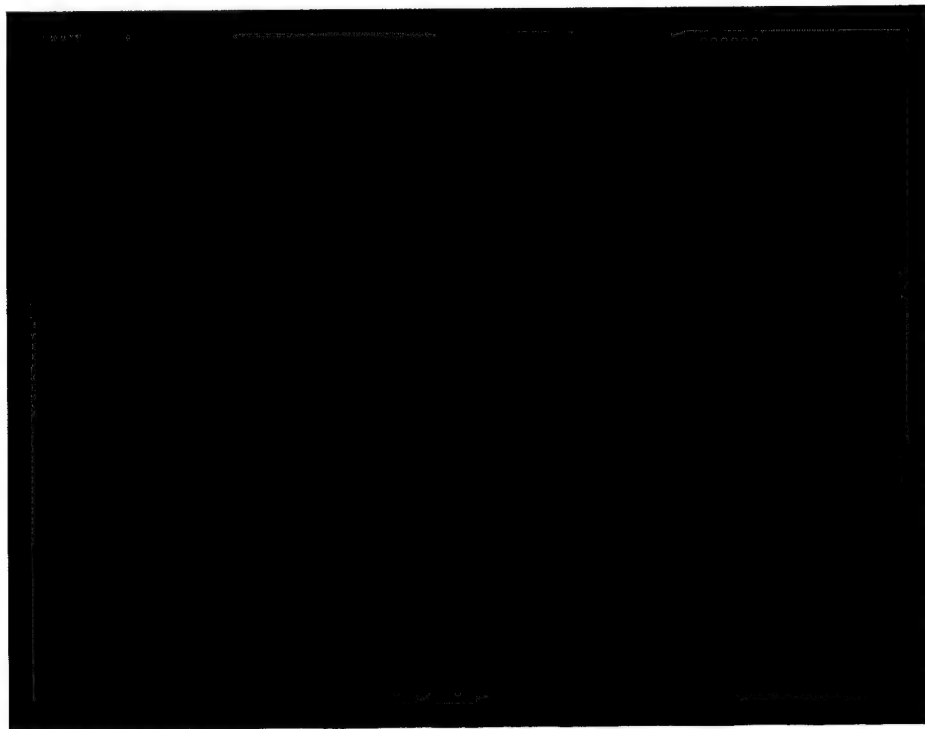


Figure 4-40. Digitally enhanced image of backlit on-pixels. The real image was too dim to illustrate due to the high magnification. The color of the pixels was altered as a result of the enhancement.

Our measurements likely have accuracy within $\pm 0.2 \mu\text{m}$. As can be seen in Figure 4-39, the edges of the pixels are blurred and therefore made measurements of fill factor less accurate. The lower fill factor leads to an improved MTF and CTF.

Pixel defects. Due to the physical configuration of the display and drive electronics, we were unable to use photomicroscopy to document pixel defects. However, while viewing the source under 10X and 25X photometric magnification, several pixels were noted to be continuously "on". Display # 1 which showed signs of pixel clearing was unfortunately destroyed prior to any conclusive evaluation. While no major pixel defects were noted, it is our opinion that the number of stuck-on pixels is greater than that normally observed in large LCD panels.

Maximum luminance. To determine the maximum display luminance, a 100 by 100 pixel square centrally located and set to maximum luminance (digital level = 63) was measured with a calibrated Pritchard 1080A photometer. All other pixels were set to zero. The LCD was backlit by a Kaiser provided arc lamp brought to the display by a fiber optic bundle which provided a moderately spatially-uniform backlight (see luminance uniformity below). Maximum luminance was 167 fL for source number 1. Using a 25 square pattern, source number 9 achieved a 236 fL peak luminance in the middle of the display.

Luminance uniformity. To determine on-axis luminance uniformity, a 25 window pattern was used with each window being 80 horizontal by 64 vertical pixels in size. The windows were centered at the 10, 30, 50, 70, and 90 percentile locations. Each rectangular block of pixels was set to a maximum gray level of 255. The background was set to a gray level of 0. For off-axis uniformity, a 100 by 100 pixel square in the middle of the display was set to 255 while all remaining pixels were set to off. The on-axis luminance values for the 25 window pattern are presented in Table 4-8. Off-axis luminance uniformity is shown in Figure 4-41 for the 100 pixel square target.

Table 4-8.
On-axis luminance (fL) for each of the windows.

193	210	222	240	230
220	225	235	246	245
218	224	236	247	245
222	233	237	249	240
230	235	237	250	240

As shown in Table 4-8, the on-axis luminance did not deviate from the mean by more than $\pm 20\%$. Although the luminance uniformity meets Comanche requirements, it should be remembered that the uniformity is largely the result of the backlight and this backlight is not intended for final use in the HIDSS. For off-axis luminance, luminance falls off with angular distance as expected for a LCD.

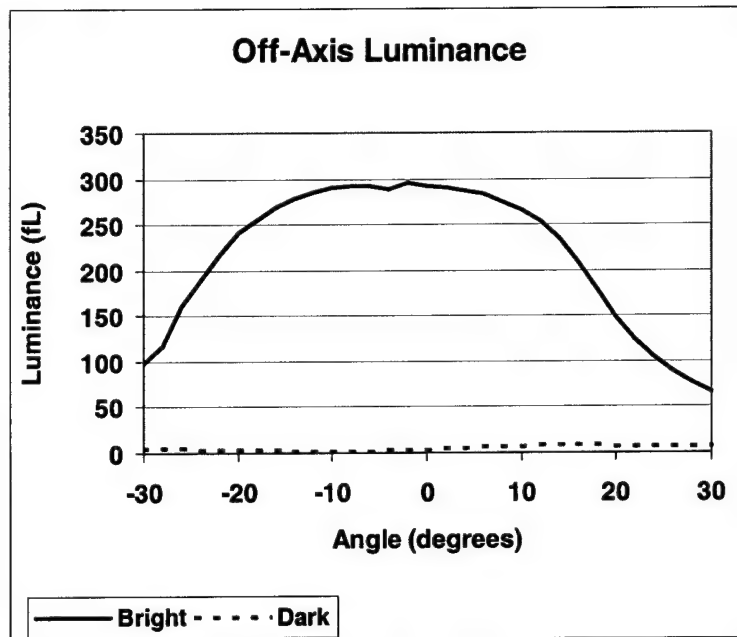


Figure 4-41. Off-axis luminance as a function of angular orientation. Luminance is reportedly higher here owing to the numerical aperture of the standard lens and measurement distance used to collect these data. The lens used here was selected in order to collect data with a smaller angle of regard.

Contrast uniformity. For on-axis contrast, the 25-window pattern (discussed above) was used. For off-axis contrast, the single 100 pixel square window in the middle of the display was used. See luminance uniformity for further explanation of the display patterns. Luminance measurements were taken for each of the 25 windows and at locations to the right of each window and beneath each window. For the measurements to the right, the photometer measured a dark area 80 pixels away from the center of the window. For the measurements below each window, the photometer measured an area 64 pixels directly below the center of each window. Measured contrasts for the on-axis condition are shown in Table 4-9 and 4-10.

Table 4-9.
Lateral contrast ratios

26.67	27.41	27.86	28.64	36.00
26.72	26.33	26.19	27.03	40.95
23.54	24.63	24.41	25.22	35.83
22.94	23.43	21.41	22.44	37.56
27.00	23.57	29.30	32.00	43.33

Table 4-10.
Vertical Contrast ratios

24.29	26.91	26.90	27.70	30.00
25.41	26.78	27.05	27.03	31.85
20.68	21.30	23.06	24.51	29.66
21.67	20.00	24.20	25.00	28.64
31.76	28.95	29.30	29.83	30.73

Luminance response curve. To determine the luminance response function of the display, a 40 by 40 pixel square was centrally located and set to a range of gray levels from 0 to 255. All other pixels were set to zero. The plane of the display was aligned with the photometer focal plane. We centered the 40 pixel square target with the center of the viewing photometer aperture. Luminance readings were made for each of the 256 gray levels.

As can be seen in Figure 4-42, the Gamma was essentially monotonic up to a gray level of about 160. From a gray level of 160 on, the curve saturates and then rescinds. If this drop-off was due to a bit map problem, we would expect to see a break in the curve and a portion of the monotonic curve repeated.

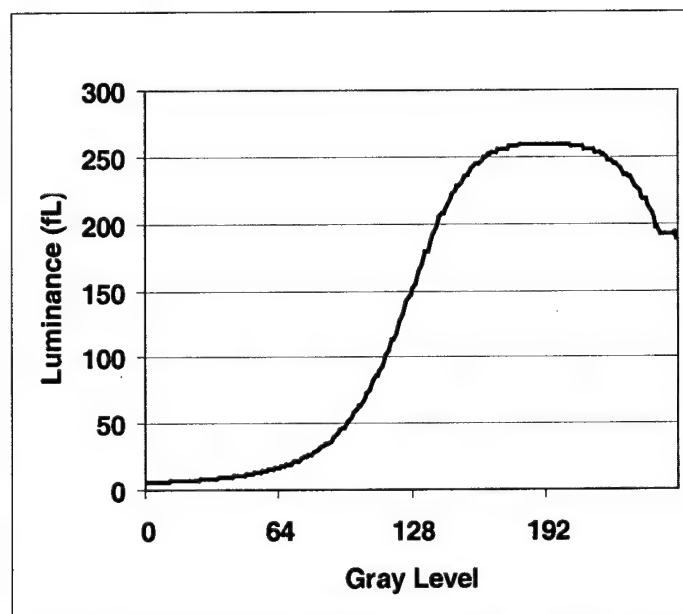


Figure 4-42. Luminance response curve for the Kaiser Electronics LCD.

CTF. The CTF was determined for a series of grill patterns. A horizontal grill with the peaks equal to 255 and the valleys equal to 0. The grill patterns covered a spatial frequency range of 16, 32, 64, 128, 256 and 512 cycles per display width. Figure 4-43 shows the CTF. The curve is expressed in cycles per millimeter calculated using a nominal pixel pitch of 12 μm . The highest frequency tested, the Nyquist frequency that was 512 vertical cycles per display width, equals 41.67 cycles/mm. Note at this frequency, the contrast was 0.85. Only minimal fall-off was observed.

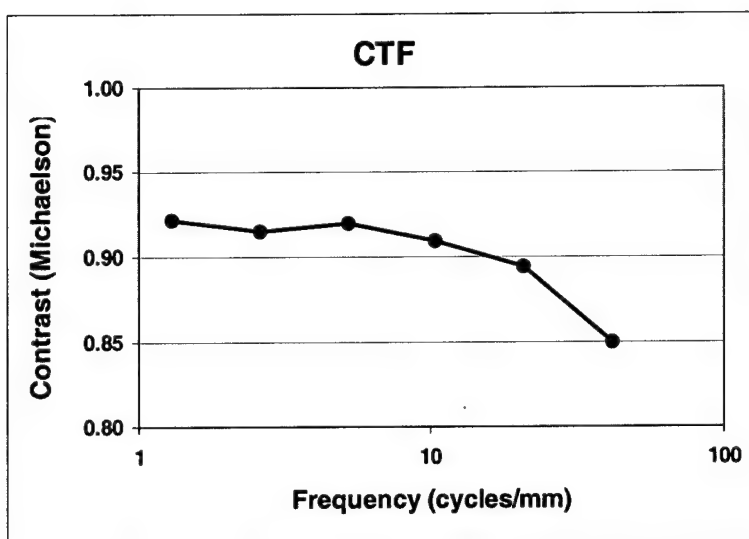


Figure 4-43. Vertical CTF for the Kaiser LCD.

MTF. To determine the horizontal and vertical modulation transfer function (MTF) for the LCD, a single horizontal pixel column or row, respectively, was turned on while all remaining pixels were turned off. Using alignment techniques mentioned above for the Honeywell display, 128-point line profile was captured for the single column and row of pixels. The complex conjugates of the FFT of the line-spreads yielded to the two MTFs. The vertical MTF can be seen in Figure 4-44.

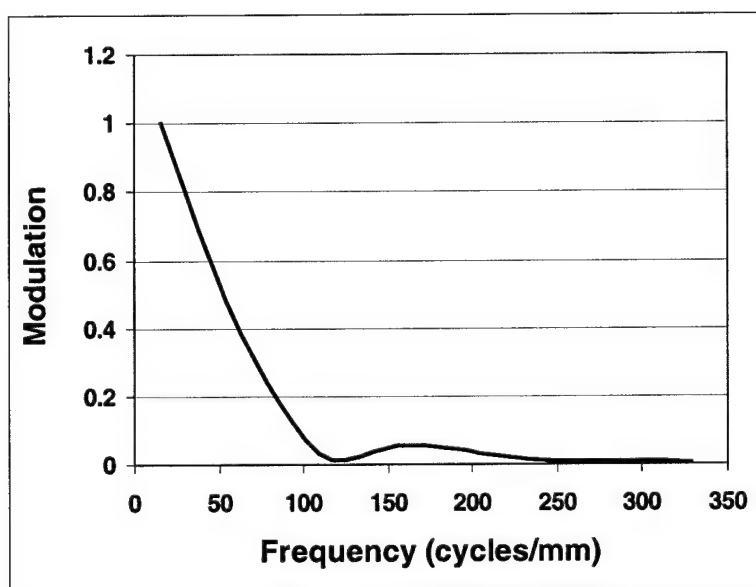


Figure 4-44. The Vertical MTF for the Kaiser 12μm LCD.

Spectral characteristics. To determine the spectral distribution of the display's transmitted light, a 100 by 100 pixel window was centrally located and set to a gray level of 63. All other pixels set equal to 0. A Photo Research PR704 Spectrascan was used to measure the

color spectrum. The spectral distribution peaked at 548/550nm and had a bandwidth at half height of about 46nm.

Perceptible gray levels. To determine the number of perceptible gray levels, a 16 panel gray level pattern (80 pixel/column) was used. The observers were instructed not to count each bar where a border was observed but rather to judge the number of separable gray levels. The six observers had scattered estimates of the number of gray levels. The estimates average 7.7 gray levels with a standard deviation of 2.4 gray levels.

Comparative test summary and discussion

The Honeywell 24+m EL display provided a luminance level of over 600 fL consistently, with excellent contrast ratios of 100 to 200 over most of the display area. This luminance level bodes well for EL technology with expectations of someday soon providing the luminance levels required by Comanche. Luminance uniformity was also excellent and was well within the plus or minus 20 percent deviation requirement. The CTF provided adequate contrast out to the Nyquist frequency. The gamma curve showed good linearity, although a probable bit mapping problem existed in the display we tested. This should be repairable with an improved manufacturing technique. Based upon Honeywell testing, the display had a reasonable temporal response.

Only two major shortcomings were noted. First, and the most damaging, the display suffers from "burn-in" of previously displayed imagery. This causes a reduction in contrast and provides for increased noise in the display's imagery. Second, the display had some pixel defects including whole columns of pixels which were steadily on. A sprinkling of single pixels were also steadily on. With the exception of the "burn-in" problem, most defects could be corrected with further advances in manufacturing. The Kaiser Electronics 12-urn LCD appeared to be a more advanced technology. However, our tests were conducted using a backlight which may or may not reflect future performance using another backlight. First and foremost, a much brighter backlight is required to achieve Comanche specifications. The highest luminance was about 250 fL with contrast ratios of around 30. On-axis luminance uniformity was good but is dependent upon the uniformity of the backlight source. Off-axis uniformity was typical of an LCD with luminance fall off with increasing off-axis angles. No major pixel defects were noted, although clearing was observed in one of the tested displays. The CTF was excellent, which is typical of a display with a low fill factor number. The temporal response was reasonable, although we were unable to perform a detailed analysis of temporal response characteristics.

The major shortcoming of the display was not having a suitable backlight to test. Given the characteristics of the HIDSS, a backlight of around 55,000 fL is required to produce comparative results with the CRT based system. Perhaps this luminance is achievable utilizing a display heater coupled with a high output arc lamp, however the logistics of an arc lamp in a confined cockpit are questionable. Of the two technologies, the LCD appears to be the most advanced; however, we are concerned by the high luminance requirements of the backlight if it is to achieve operational capability.

The Honeywell High Pass HMD

UES evaluated the Honeywell, Inc., Minneapolis, MN, high-pass helmet mounted display (hp-HMD) as a result of a request received from the Program Manager for Air Crew Integrated Systems (PM-ACIS). The hp-HMD can be seen in Figure 4-45. The HMD can be worn as a bi-ocular or monocular display or both displays can be raised for non-HMD viewing. The system received included an optical source, a single optical assembly (Figure 4-46), and driver electronics.

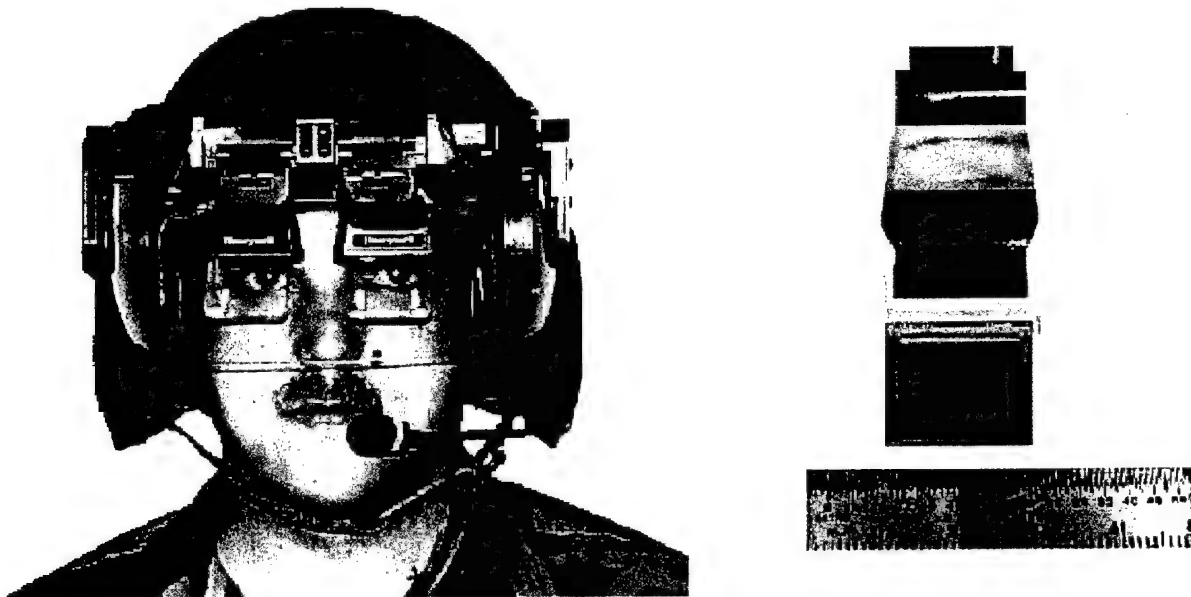


Figure 4-45. The hp-HMD mounted to a HGU-56p helmet in a bi-ocular arrangement. Please note that the HMD was not adjusted properly for this subject. On the right is shown a photograph of the hp-HMD source, a miniature electro-luminescent flat panel display.

The image source that accompanied the hp-HMD was a 12 μm , 1280 by 1024 resolution, electro-luminescent (EL) display manufactured by Planar Systems, Inc., Beaverton, Oregon. Two test sources were provided and all of the tests performed in this study used the display identified as 12SX00026 (Planar 12S1280). Figure 4-46 shows a photograph of the display. USAARL tested an earlier developmental version of this display (see above). That display showed considerable retention problems and several pixels were set permanently on (see Figure 4-32). The display presented here showed no signs of the problems that were encountered earlier.

The hp-HMD does not have a viewable exit pupil position like that of the IHADSS. The position of the exit pupil can only be found by backwards ray tracing. We did not attempt to determine the position of the exit pupil, but instead used data provided from Honeywell to position our measuring instruments in the exit pupil position. The hp-HMD shows considerable aberrations and excessive repositioning of our instruments showed only modest improvement in our measurements.



Figure 4-46. The hp-HMD mounted to a bar used for testing the device. Please note that the optic is composed of fused optical lenses. The lenses were glued to each other in order to make a single optical device.

Pixel geometry. Figure 4-47 is a photomicrograph of a pixel patch on the EL source of about 8 by 6 pixels. The photomicrograph provides details of the microscopic structure not commonly seen under normal viewing conditions. Please note that the brighter smudges inside each pixel are areas of higher luminance. At higher luminance levels (pixel driving levels), the pixel luminance appears more uniform and full. However, it should be noted, that with a 50X objective lens, very little light is passed through the objective lens and that much of the structure observed here is reflected light from the microscope's source which is transmitted from the objective lens to the flat panel and reflected back into the objective.

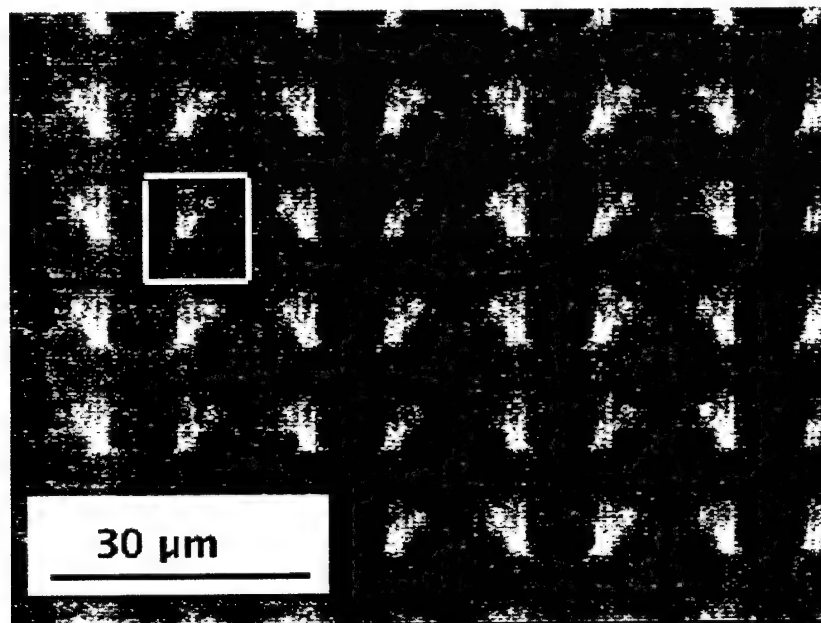


Figure 4-47. Photomicrograph of the EL sources pixel structure. The bright square outlines a single pixel.

Pixel pitch measured approximately $12.1\text{ }\mu\text{m}$. The ratio of the active pixel area to the pixel pitch squared is the fill factor. The active pixel area can be better seen in Figure 4-48. Here, every other row of pixels is turned on. The active area of the pixel was approximately square and was slightly smaller than the pixel pitch. We measured a fill factor of about 90%.

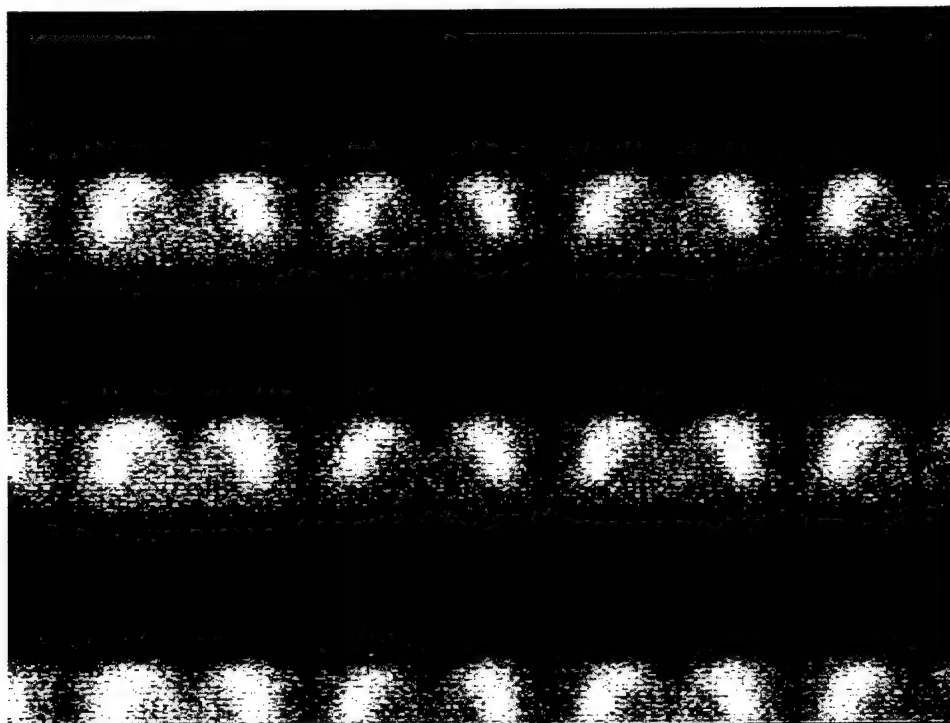


Figure 4-48. Photomicrograph of a small patch of pixels with every other row of pixels turned on. At the Nyquist frequency, it can clearly be seen that there is good contrast. This photomicrograph has been enhanced in Adobe Photoshop by adjusting the contrast curve to brighten the on-pixels, (a method similar to histogram equalization where the luminance range is stretched). The original photo would be difficult to discern any contrast when reproduced.

In comparing this display with the earlier Honeywell $24\text{ }\mu\text{m}$ EL display that was presented earlier, this display has a fill factor that is less than 1. The other display had an effective fill factor that was greater than 1 and was difficult to measure. Due to the large fill factor in the previous display, the MTF was less than expected from a flat panel display. For this display with a fill factor of 90 percent, the contrast at the Nyquist frequency should be quite high.

In addition to the improved fill factor, no obvious pixel defects were noted in this display. This is a major improvement over the earlier $24\text{ }\mu\text{m}$ version.

Maximum luminance and contrast. To determine the maximum luminance a 100 by 100 pixel square centrally located and set to maximum luminance (digital level = 63). All other pixels were set to zero. The plane of the display is aligned with the photometer focal plane. The 100 pixel square target was centered with the center of the viewing photometer aperture. To investigate maximum contrast for this condition, a luminance measurement was taken at a point

100 pixels to the right from the center of the square. The maximum luminance was 231.7 fL with a contrast of 51.1.

Luminance uniformity. To determine variation in luminance over the surface of the display, a pattern with every pixel turned on to 255 was displayed. The display was attached to a precision translator with the plane of the display orthogonal to the optical axis of the photometer. Using the smallest aperture as a sighting tool, we traversed the display to find the upper left and lower right corner which provided the coordinates for the four corners of the display. From this we calculated a scan path to obtain 63 measurements which sampled the luminance of the display. For each horizontal scan, nine equally spaced measurements were made. In all, seven equally spaced horizontal scans were made. The horizontal and vertical increments were 1.536 mm between measurements.

Table 4-11 shows the deviation from the average luminance for each of the 63 positions. Please note that the highest deviation was -4.62%. The luminance uniformity was quite good and most measurements were within less than one percent from the average luminance.

Table 4-11.

Deviations from the average luminance as a percent.

-1.83%	0.49%	0.03%	0.03%	0.49%	1.43%	0.03%	0.03%	0.03%
-0.90%	0.03%	0.96%	2.36%	1.43%	0.03%	0.49%	0.96%	1.43%
0.49%	0.03%	0.49%	2.36%	1.43%	0.03%	1.43%	2.36%	0.96%
-4.62%	-2.76%	-2.30%	-1.83%	-2.30%	-0.44%	0.49%	0.96%	0.03%
-0.90%	0.49%	1.43%	1.43%	-0.44%	0.96%	-0.44%	1.89%	0.96%
-1.83%	-0.44%	0.03%	-0.44%	-0.44%	0.03%	0.49%	1.43%	1.43%
-3.23%	-1.83%	-1.37%	0.03%	0.03%	-0.90%	-0.90%	-0.90%	-0.90%

Contrast uniformity. To determine contrast uniformity over a large area of the display, a 25-window pattern was used. Each rectangular block of pixels (80 by 64) was set to a maximum gray level of 255. The background was set to a gray level of 0. Luminance measurements were taken for each of the 25 windows and at locations to the right of each window that was 80 pixels away from the center of the window. Deviations from the average contrast for each position are given in Table 4-12. Since luminance uniformity was quite good, any differences here can be attributed to the value obtained from the darkened area. As can be seen in Table 4-12, the right side of the display had much higher contrast.

Table 4-12.

Deviations from the average contrast.

4.63%	-1.55%	-2.94%	-1.28%	52.24%
-9.83%	-15.01%	-15.34%	-13.69%	32.72%
-12.13%	-16.85%	-18.83%	-15.99%	28.55%
-10.44%	-14.63%	-16.43%	-14.61%	31.08%
0.34%	-4.31%	-6.46%	-4.16%	44.93%

Luminance response curve. To determine the luminance response function for the display, a 40 by 40 pixel square was centrally located and set to a range of gray levels from 0 to 63. All other pixels were set to zero. Figure 4-49 shows the relative luminance response curve for the display. The curve was monotonic and showed only slight non-linearity.

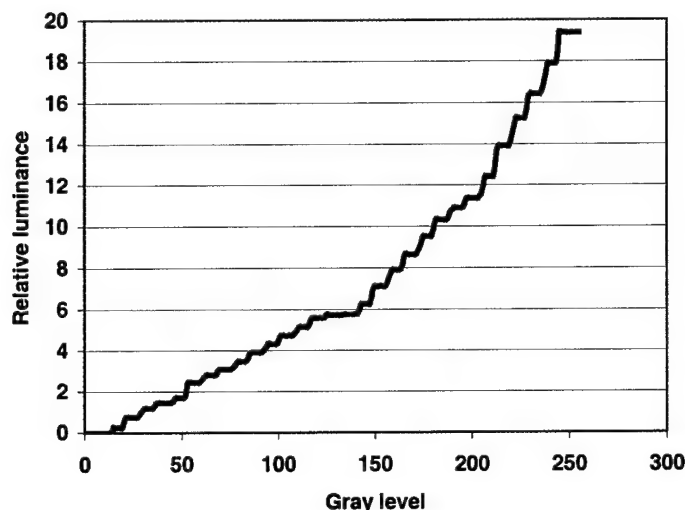


Figure 4-49. Luminance response function showing relative luminance over better than a 10,000 to 1 range.

CTF. To determine the Michaelson contrast for a series of grill patterns, a grill pattern composed of gray-levels of 0 for the valleys and 255 for the peaks was displayed in the middle of the display. The photometer's slit aperture was aligned near the middle of the display and with the center of the darkened half of the frequency pair and recorded the luminance. Luminance readings were then made for 47 other positions that covered two complete cycles of the square wave pattern. This procedure was repeated for each spatial frequency (20, 40, 80, 160, 320, 640 cycles per display width). Testing was performed with the 10X and the 25X lenses.

Figure 4-50 shows the measured CTF using the maximum and minimum luminance levels for each scan. The CTF was typical of a flat panel display showing considerable contrast at the Nyquist frequency (640 cycles/display width).

MTF. To determine the horizontal and vertical MTF for the display, the photometer slit aperture was aligned with the middle of the lighted pixel column. The slit was positioned approximately 128 μm to the side of vertical line. The line was then scanned in 2 μm increments for a total of 128 points. The measured line spread function is shown in Figure 4-51. The half-height width of the curve is a little less than 12 μm which corresponds to the pixel pitch. The horizontal MTF was calculated from the linespread function by normalizing the complex conjugate of the FFT of the line spread. The MTF is shown in Figure 4-52.

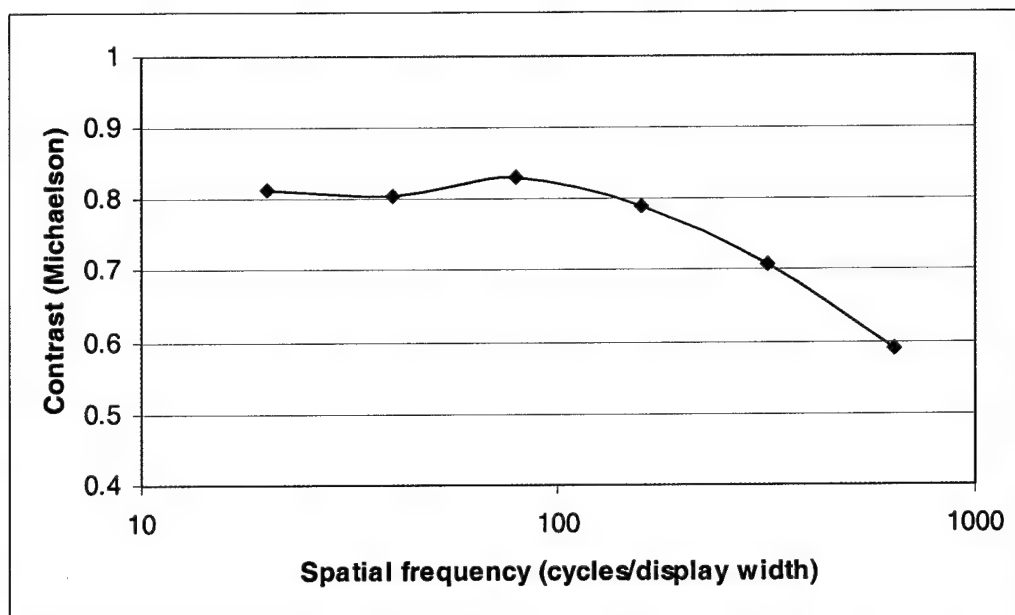


Figure 4-50. Michaelson contrast at six different spatial frequencies representing 32 on - 32 off, 16 on - 16 off, 8 on - 8 off, 4 on - 4 off, 2 on - 2 off, and 1 on - 1 off.

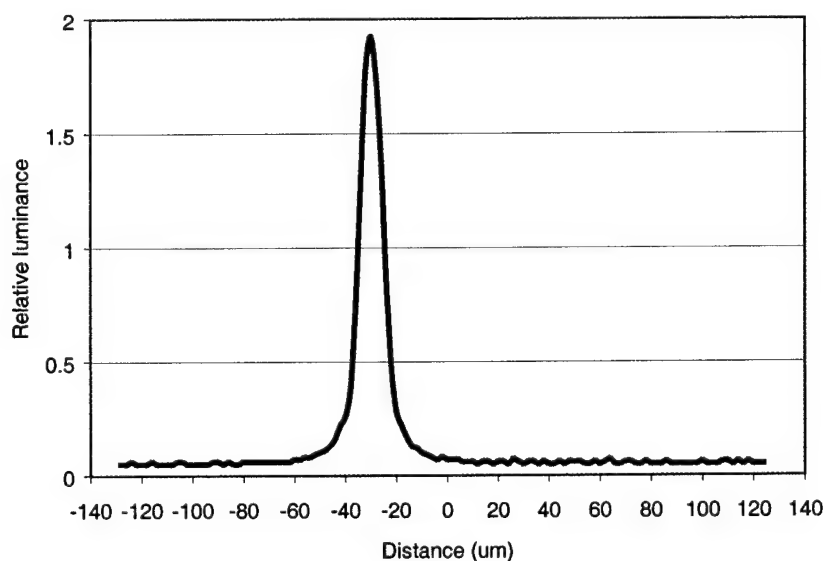


Figure 4-51. Line spread function measured for the single vertical column.

The linespread was well distributed and showed keen symmetry. The MTF was typical and showed an orderly progression from low to high frequency. The curve was slightly below expectation at the Nyquist showing only a 0.42 modulation (our prediction was closer to 0.60 modulation). Perhaps another sample may have shown improved results.

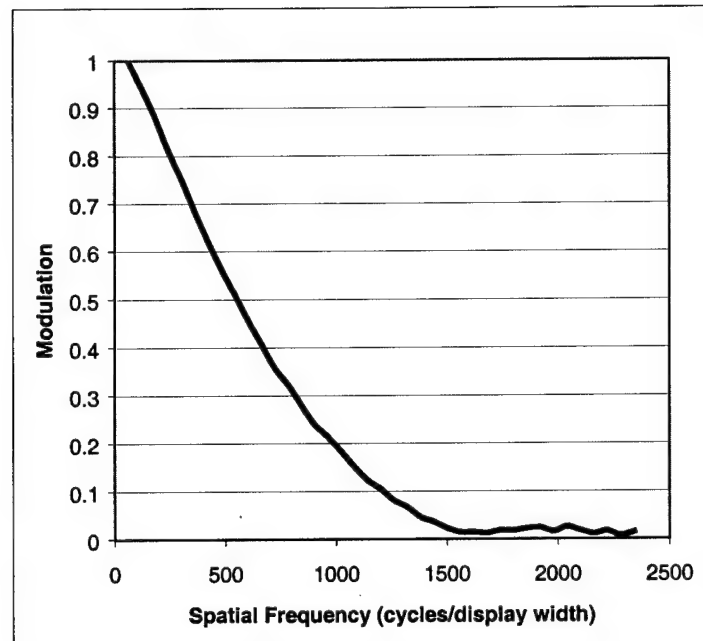


Figure 4-52. Horizontal MTF calculated from the line spread shown in Figure 4-50.

Spectral characteristics. To determine the spectral distribution and chromaticity of the display's emitted light a scan was made of 100 by 100 pixel window centrally located and set to a gray level of 255. All other pixels set equal to 0. The spectral output of the display can be seen in Figure 4-53. The peak was at 580nm and the bandwidth was about 54 nm at half amplitude. 1931 CIE chromaticity: $x = 0.5212$, $y = 0.4760$.

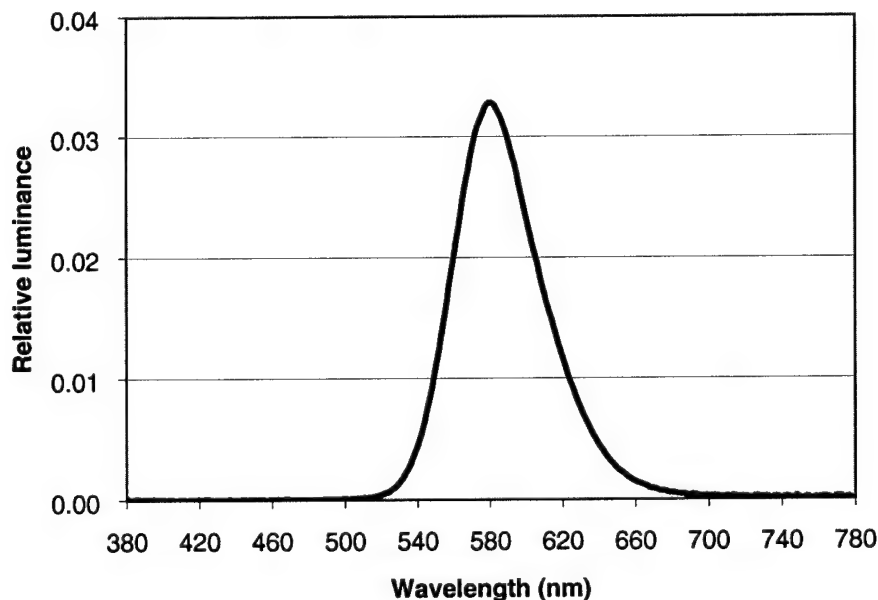


Figure 4-53. Spectral distribution of the display source.

System Tests

The source showed considerable improvement over the one measured earlier (see page 4-33). The HMD on the other hand, had several severe shortcomings. The imagery appeared out of focus and the optical aberrations seemed excessive. Further our measurements of system efficiency revealed only about a 58% efficiency compared to the 80% efficiency measured by Honeywell engineers. Details of these tests will be given below.

Exit pupil. The Honeywell system does not form a viewable exit pupil. To find the exit pupil requires mapping the light from the image source through the HMD and for various parts of the field-of-view. As Honeywell had previously mapped the system, we used their calculated position for the system measurements. In practice we made repeat measurements at a various positions in order to locate the desired exit pupil. In general, we did not locate an area where measurements were significantly improved. Over the areas we tested, there were considerable optical aberrations that were present over the entire field-of-view. Further, the optics themselves contained areas that blurred the image from that region. These areas were characterized by patches of glue between the lenses that caused considerable blurring. However, these patches could not explain the aberrations that were noted.

System efficiency. To determine the system transmission efficiency of the HMD, measurement of luminance from the source and from the HMD must be made and the ratios calculated. Two methods were used to measure efficiency.

In the first technique, the luminance of the 12 μm EL display was measured by focusing on the center of a 100 pixel square target in the middle of the display. All pixels were set on to their highest gray level. Relative measurements were made, since the system and the panel have to be focused at different points. Imagery in the HMD must be focused at infinity and the panel at some finite distance (about 1 meter). It is important to maintain the numerical aperture of the photometer fixed as changes in focus changes the relative position of the 5mm iris to the photometer's collecting aperture. Thus to focus on the HMD, we had to use a supplemental lens to focus the photometer on the 100 pixel square image plane. Again we took a relative measurement. We measured the transmittance loss of the supplemental lens (about 10.3%) and then calculated the system throughput.

In the second technique, the luminance of the 12 μm EL display 100 pixel square target was measured using two separate lens: the 1980a photometer with an OL-7 lens and no iris and the 10X lens and no iris. The luminance from the HMD was measured using the 1980a photometer with the OL7 lens with the 5mm iris. The effect of the iris was calculated by focusing the photometer on a standard lamp at about 31 feet away to simulate an object at infinity focus. The 31 feet was the furthest distance allowable in the laboratory. With the photometer's focus set to infinity, the effect of the 5mm iris was calculated by taking measurements with the iris in place and removed.

Using the relative measurements in the first technique, the EL display measured 6.797 and the HMD display 3.59. Calculating system output

$$(3.59 \times 1.103) / 6.797 = 0.5826$$

gives a system efficiency of 58.26%.

Using the absolute luminance measurements of the second technique, the EL display measured 253 fL with the OL7 lens and 253 fL with the 10X lens. The HMD measured 3.04 using the OL7 lens with the 5mm iris. The calibration factor for the iris was 43.599 for the 31 feet distance. Calculating system output

$$(3.04 \times 43.599) / 253 = 52.38\% \quad (\text{OL7 lens for both measurements})$$

$$(3.04 \times 43.599) / 233 = 56.88\% \quad (\text{OL7 and 10X lens})$$

The three measurements obtained from the two techniques were fairly close and yielded an average of 55.84% efficiency. This number is considerably lower than the numbers obtained by Honeywell engineers that averaged about 80%. The techniques discussed above are necessary to eliminate errors produced by using an iris with a photometer whose numerical aperture will change as a function of focus. Honeywell engineers were very cooperative and revealed that they did not account for this change. Not controlling for this effect we measured erroneous efficiencies of 85.0% and 78.5% that replicated Honeywell's results. These numbers will change depending on the calibration distance to the standard lamp (when calibrating the effects of the 5mm iris), therefore it is important always to calibrate the effects of the iris at the distance needed for the actual measurement.

FOV. To assess the FOV of the system, a pattern that clearly marked the periphery of the display was imaged on the display. A tangent screen was placed 55.19 inches in front of the exit pupil. While an observer looked through the optic, pins were placed on the tangent screen so that the top, bottom and side positions of the FOV were marked on the screen. Using a measuring tape, the separation of the pins was measured and converted to angular measurements using simple trigonometry.

The horizontal FOV was 37.76 degrees and the vertical FOV was 29.08 degrees. The FOV was smaller than the 40 by 30 degrees required by Comanche.

Aberrations. Field curvature was measured for four lateral transactions through the display as well as one vertical trans-section through the middle of the display. Field curvature was measured using a grid pattern with vertical and horizontal lines. Figure 4-54 shows field curvature for the five transactions showing best focus for the vertical lines only. Note the diversity in focus over the display.

Indications of astigmatic error were calculated by measuring the difference in focus to the horizontal and vertical lines. Errors higher than 3 diopters were observed in the periphery.

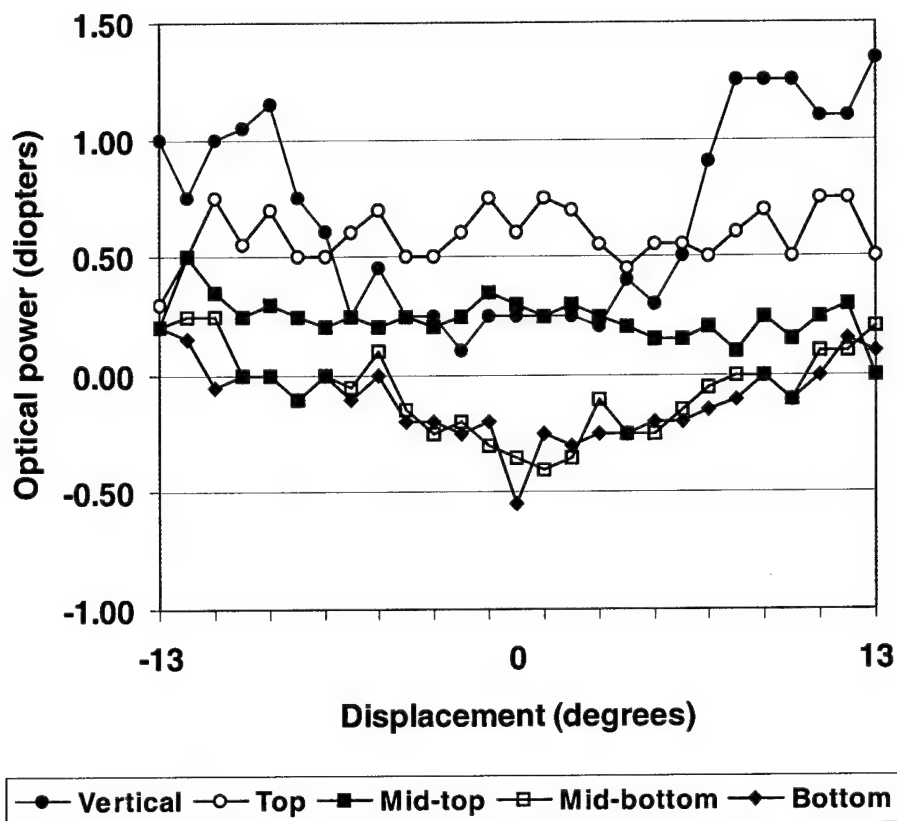


Figure 4-54. Measurement of field curvature for the four horizontal trans-sections and the one vertical trans-section.

Perceptual tests. Color tests D-15 hue test and the isochromatic plates were completed with no errors. We did find about a 1 line of resolution loss on and acuity chart. This was repeated with 2 observers as with the color discrimination tests. The loss of acuity was attributed to the optical errors in the display and with a problem in the HMD where two optical elements were glued together to form the HMD combiner lens. The poor gluing job created a haze appearance when viewing through the eyepiece, but this was essentially constrained to the lateral area of the display.

THE DEVELOPMENT OF HMD EVALUATION SYSTEMS

Over this contract period, UES scientists have been directly involved in developing measuring techniques that may adequately describe image quality in CRTs, flat panel displays, HMDs and night vision goggles (NVGs). Of particular note are two optical measuring devices that have been designed and co-developed by UES scientists and engineers. The first is a prototype of a ruggedized, mobile system for measuring image quality in the Apache's (AH-64) HMD (patent application filed). The Apache HMD, the Integrated Helmet and Display Sighting System (IHADSS), uses a miniature CRT as a source. As with all CRTs, image quality deteriorates over time. Along with USAARL technicians and Dr. Sheng-Jen Hsieh of Texas A&M University, we co-developed a mobile IHADSS image quality tester that automatically evaluates a built-in test image. Parameters evaluated include contrast, resolution, and field-of-view (FOV). Once fielded, this system would allow crew chiefs and/or maintenance personnel to rapidly evaluate IHADSS units in the field. Details of this system can be found in USAARL laboratory reports number 2000-08 and 2000-26. In addition UES designed and developed a laboratory HMD tester that allows technicians to control and to precisely position a range of measurement devices within the FOV of HMDs. The system shortens the amount of time required to evaluate HMDs by about 50%.

The Mobile IHADSS Tester

The IHADSS Tester is composed of a custom-built enclosure, a lap top computer with digital I/O and image-capture capabilities. The Apache IHADSS electronics has a built-in test image that was developed by Honeywell, Inc. The one test image is composed of gray shade variations and horizontal and vertical lines. Therefore, we developed the system around this one test image (see Figure 4-55). Software was developed to analyze this particular image.

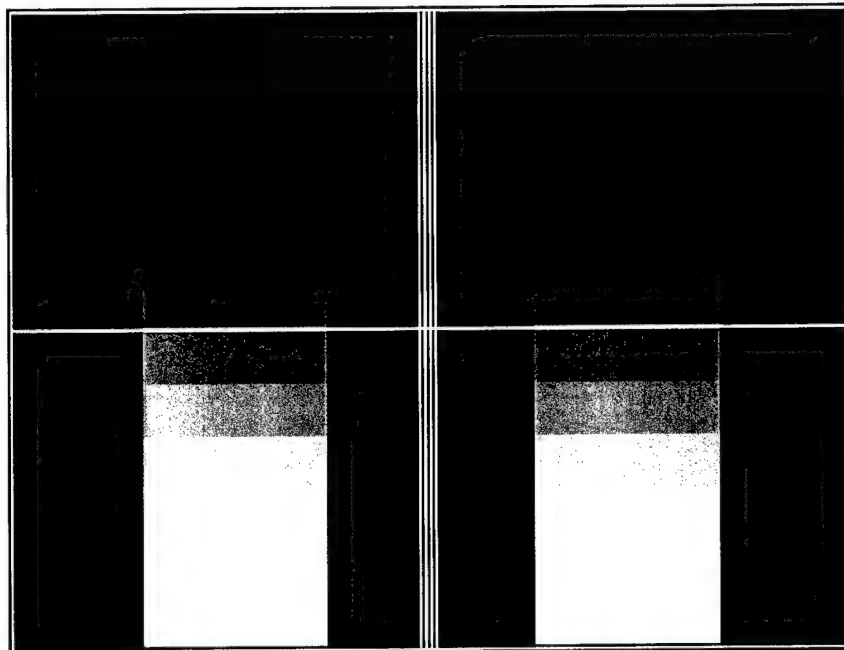


Figure 4-55. Computer rendition of the IHADSS test image.

To capture the images, a two CCD camera configuration was developed. One of the cameras was fitted with a wide-angle lens that is used for FOV measurements and gray-shade measurements. The other camera was fitted with a telephoto lens that is used for determining display resolution, contrast and orientation of the image (see Figure 4-56).

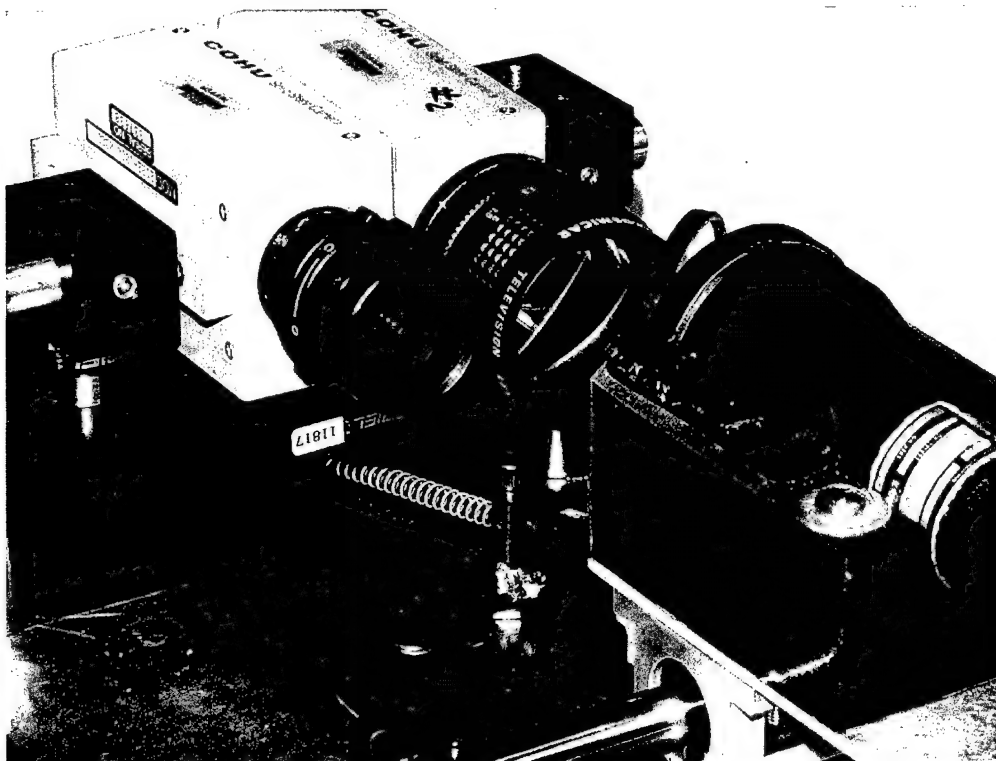


Figure 4-56. Photograph showing relationship between the two cameras and the IHADSS HMD. Please note that in this arrangement, the image is evaluated after passing through the combiner lens (as opposed to evaluating the test image following its reflection off of the combiner lens).

In Figure 4-56, a spring can be seen. This spring controls a switch that switches between the two cameras. The position in Figure 4-56 shows the alignment between the camera with the telephoto lens and the HMD. By sliding the HMD to the left, camera output is automatically switched to the camera with the wide-angle lens. The single spring technique for switching between cameras was developed by Mr. Ronnie Reynolds of USAARL. Micro-switches seated in the IHADSS holder and on the slide guarantee recognition of proper seating and positioning of the IHADSS unit. The slide that the IHADSS holder is mounted was purchased from McMaster Carr, Inc.

Figure 4-57 shows the complete system with the computer and power center along with the cameras and IHADSS unit. Battery power has been added to the system to allow for a complete self-contained mobile unit (Figure 4-58). A charging circuit charges the batteries and the computer battery can be charged either off of the main batteries or during system recharging.

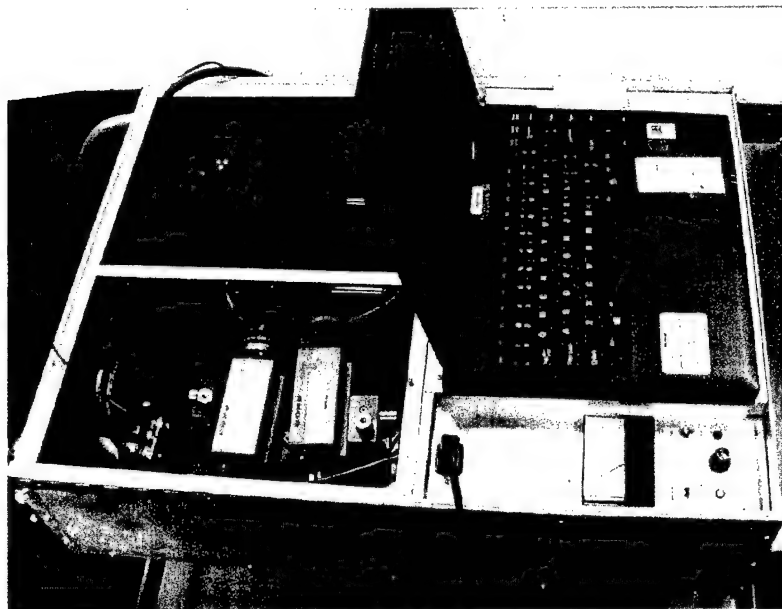


Figure 4-57. IHADSS mobile tester.

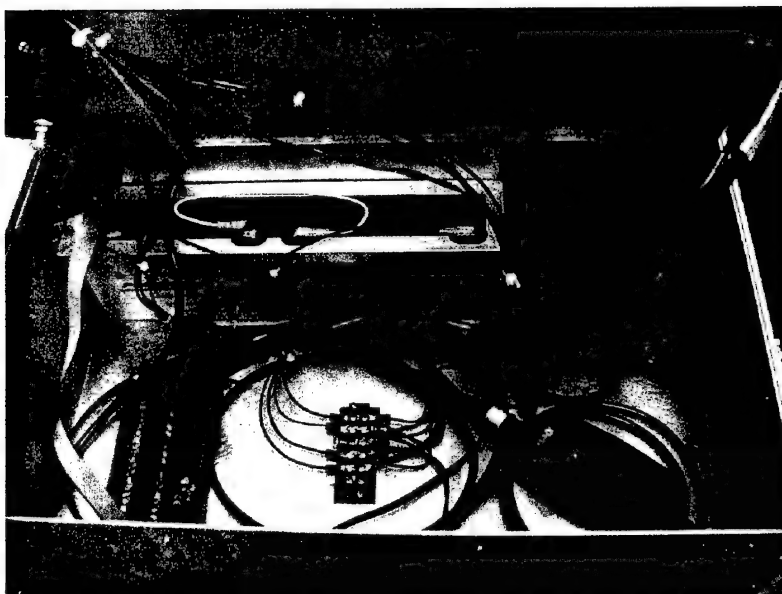


Figure 4-58. Battery and charging compartment mounted underneath the computer and switching platform.

Custom software analyses the captured images and provides a performance report to the user. The system analyzes FOV, contrast, luminance and resolution in the imagery. The algorithms developed are so sensitive that they can detect a change in focus of only 0.125 diopters. This level of blurring is very small and Army aviators should be able to easily accommodate this amount of defocus. The system will now have to be used to evaluate a small population of fielded IHADSS units in order to better clarify performance metrics for the system. Once variables in the software are set based upon population statistics, the system could be used as an effective tool for monitoring and maintaining IHADSS in the field.

Laboratory HMD Tester

UES designed and developed a laboratory HMD tester. Mr. Ronnie Reynolds of USAARL fabricated the system in the USAARL machine shop and also assisted in the design phase. The system is composed of vertical and horizontal translators that allow optical test devices to move around within the FOV of HMDs (Figure 4-59). The benefit of this tester is that the camera or other test instruments can be positioned anywhere within the FOV of the HMD while still maintaining proper alignment. This is achieved by the ability to position the instrument through precise rotation and elevation while keeping the instrument's entrance pupil co-located with the HMD's exit pupil. In other words, the center of rotation in both axes is around the center of the exit pupil (see Figure 4-60).

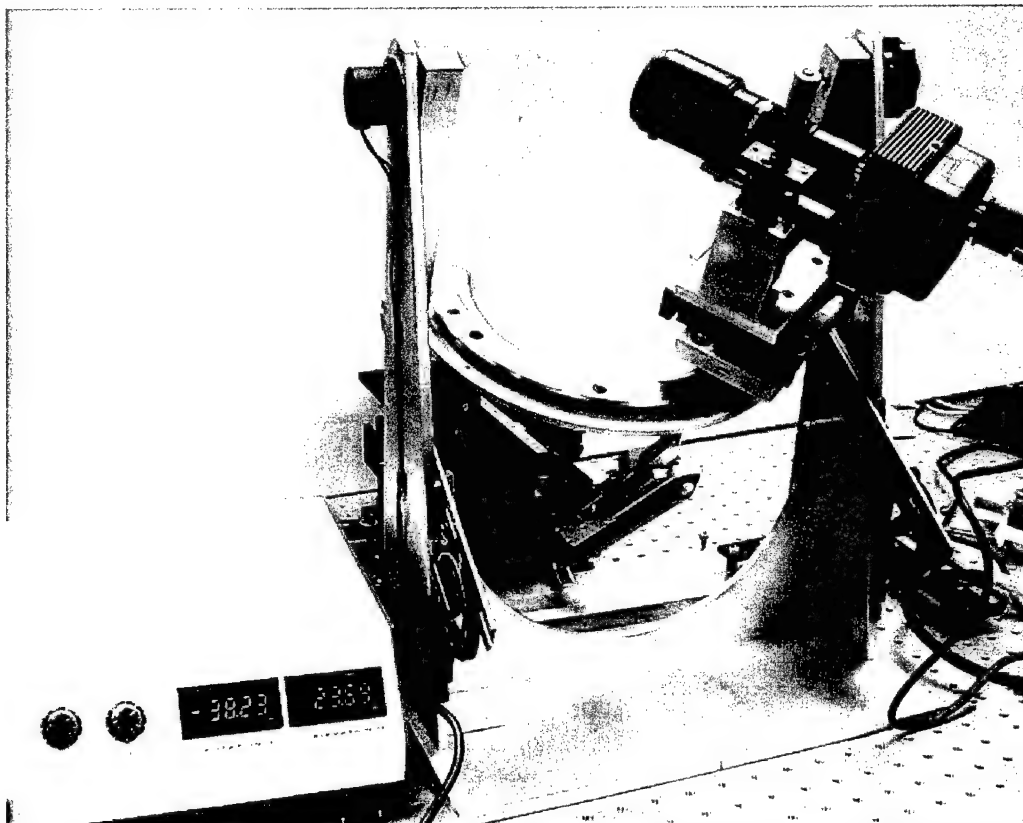


Figure 4-59. UES designed and developed laboratory HMD tester. The test system allows positioning of an optical test device anywhere within the FOV of an HMD. Here the photograph shows a high-resolution camera system mounted to an XYZ linear positioning stage. The stage in turn is mounted to a curved rail, which allows the system to rotate laterally within the FOV. The curved rail is mounted to a swing that allows vertical positioning within the FOV. The position of the camera is monitored by digital readouts of lateral and vertical degrees (measured to the nearest 1/100 of a degree).

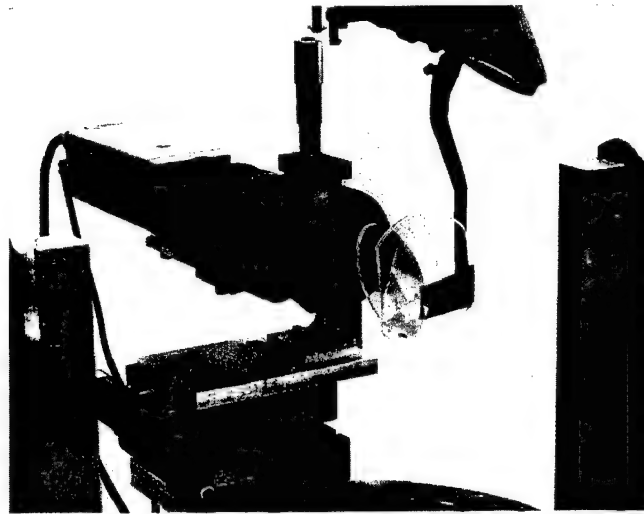


Figure 4-60. In the this photograph, one side of the Microvision phase II HMD is mounted and the formed exit pupil is formed in the center of a 3mm camera iris. The exit pupil is seen as a focused light-green circular spot of light.

To monitor angular position, two precision potentiometers monitor the horizontal and vertical position (Figure 4-61). The vertical position potentiometer is mounted to the left swing arm. The center shaft of the potentiometer is attached to the exact center of rotation position for the swing. The horizontal position potentiometer is chain linked to the stage mounted to the curve track. As the stage is moved, the spring-loaded potentiometer rotates one direction or the other as the chain is pulled or released depending on the direction of the movement.

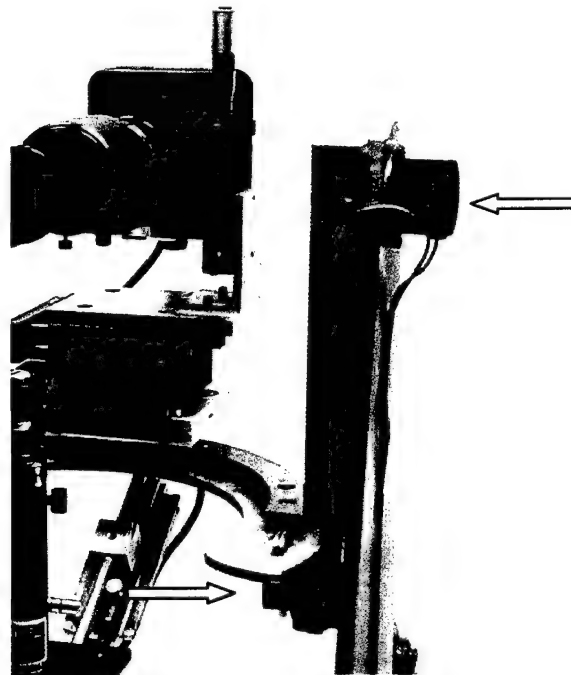


Figure 4-61. The arrows show the position of the two precision potentiometers.

Figure 4-62 shows the electronic circuit designed to linearly track horizontal and vertical position. The system is accurate to within 0.05 degrees over a 40 degree range. All components of the circuit were individually tested and modeled in order to maintain this level of accuracy.

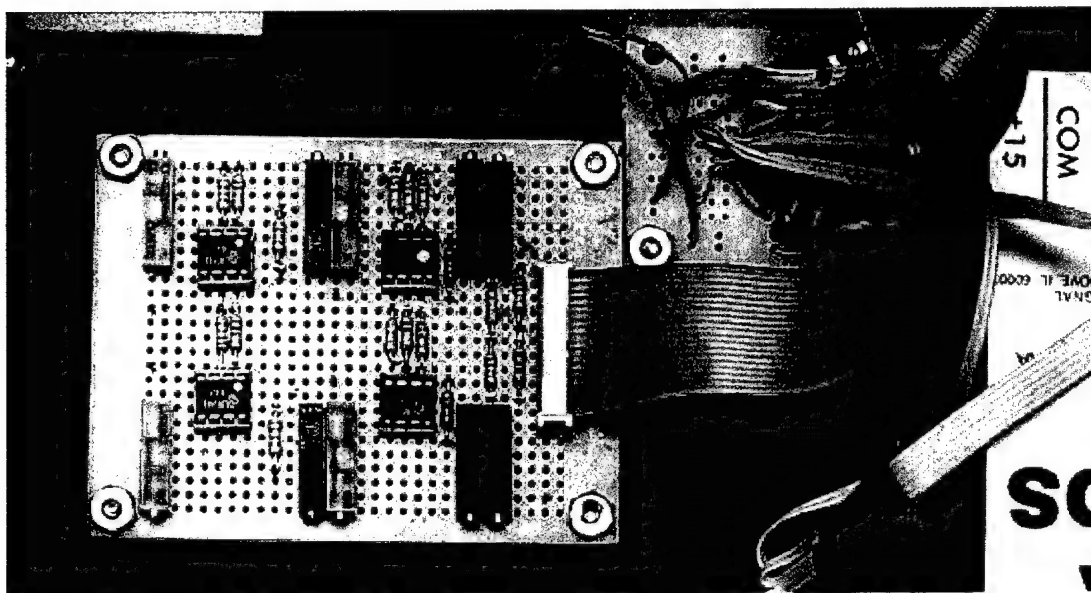


Figure 4-62. Control electronics for the laboratory HMD tester. The main parts include 4 analog operational amplifiers and gain control potentiometers along with a voltage zeroing circuit.

The tester enhances our ability to evaluate HMDs by eliminating many of the alignment procedures typically required to evaluate the optical and system performance of an HMD. The tester allows for different test devices to be attached to the XYZ stage. Currently we have configured the system for a high definition camera, and video photometer and a dioptometer. The XYZ stage allows us to evaluate aberrations as a function of decentration. To co-locate the center of horizontal and vertical rotation with the center of camera lens iris, a mechanical device was created to exactly position the camera lens (see Figure 4-63).

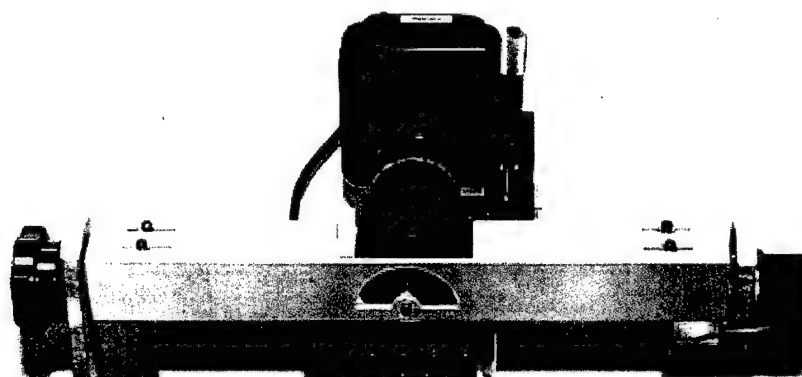


Figure 4-63. Mechanical device for positioning the camera lens' iris.

FIGURES OF MERIT

It is important that displays present information in an accurate and easily perceived manner. Ensuring operational efficiency and safety in informationally intensive environments, such as military cockpits, requires measures of the capacity of displays to transfer visual information to the human observer. Also, physical criteria evaluating the merits of old and new display technologies are needed in cost effectiveness analyses, system development, and procurement decision making. For the purpose of allowing consistent comparisons between displays, FOMs have been developed as criteria in order to objectively quantify various aspects of the image quality of displays.

A number of image quality metrics, or FOMs, have been developed to quantify the “goodness” of an image presented on a display. These FOMs have been used to quantify the quality of images displayed by cathode ray tubes (CRTs), a mature and ubiquitous technology, which, until recently, was the primary display technology. Newer technologies, known collectively as flat panel displays (FPDs), have been, and are being, developed to overcome some of the limitations of CRTs, such as the CRT’s physical depth, weight, power consumption, and electromagnetic interference. FOMs are being both borrowed and newly developed to meet the need to assess these newer technologies. Here, we are concerned with the visually relevant FOMs, and not with other physical aspects of the display, such as power consumption, weight, etc.

An example of an image quality metric is one which concerns the range of luminances that can be presented simultaneously in an image. This range, described by the concept of contrast, defines the relationship between the minimum and maximum possible luminance values. There are various ways to formulate and define contrast for different purposes, such as contrast ratio, modulation contrast, etc. (Klymenko et al., 1997). Additional FOMs concern other aspects of displays such as its color, spatial, or temporal properties. Table 4-13 gives a list of common FOMs for CRTs classified into the spatial, temporal, luminance and spectral domains. As alternative display technologies emerge, different image quality metrics may need to be developed to capture new variables affecting the image.

The displays based on the new flat panel technologies use different physical principles to present the image, and often introduce new variables that can affect the perception of the image. These new technologies include liquid crystal displays (LCDs), electroluminescent (EL) displays, plasma display panels (PDPs), light emitting diode (LED) displays and field emission displays to name a few (Harding et al., 1996; Castellano, 1992; and Tannas, 1995). If new variables are introduced, they need to be assessed. For example, the luminance and contrast of images on many LCDs vary as a function of viewing angle, where there is a reduction in off-axis luminance. Therefore, when evaluating these LCDs, the reduction in luminance as a function of viewing angle needs to be specified. The FOM quantifying luminance as a function of viewing angle is somewhat unique to this technology (Harding et al., 1996; Dragon, 1993) and was not a consideration in the traditional, more familiar, CRT displays (which are Lambertian sources). A totally new FOM was designed involving, among other things, measuring contrast as a function of spherical coordinates. Table 4-14 gives a list of common FOMs for FPDs.

Table 4-13.
Common CRT FOMs classified into four categories.

Spatial	Spectral	Luminance	Temporal
Viewing distance Resolution Spot size and shape Modulation transfer function Luminance Uniformity Signal/noise ratio Display size Aspect ratio Number of scan lines Interlace ratio Scan line spacing Linearity Focus	Color gamut Color purity	Luminance Gray shades Contrast ratio Halation Ambient illuminance Gamma Dynamic range	Frame rate Field rate Bandwidth

Table 4-14.
Common FPD FOMs classified into four categories.

Spatial	Spectral	Luminance	Temporal
Pixel resolution (H x V) Pixel size Pixel shape Pixel pitch Subpixel configuration Number of defective (sub)pixels	Spectral distribution Color gamut Chromaticity	Peak luminance Luminance range Gray levels Contrast (ratio) Uniformity Viewing angle Reflectance ratio Halation	Refresh rate Update rate Pixel rise/fall times

The number of defective pixels is also a new FOM in FPDs because of the difficulties in manufacturing totally defect-free displays. This FOM will be standardized by the International Standards Organization (ISO) sometime in 1998 and will likely include a number of allowable defective pixels, and how they are clustered on the display. The proposed North Atlantic Treaty Organization (NATO) Standardization Agreement (STANAG) (Study# 7095), for example, requires no more than 0.01 percent pixel defects, and the ratio of display pixels in square centimeters to number of cluster defects (two or more adjacent defective pixels) to be not less than 16 to 1. Also, defective rows or columns are unacceptable, and cluster defects where critical information is presented are unacceptable. FOMs are being developed based on what is visually important, and potential problems with a new technology, which can be anything from its method of image generation to the quality control of its manufacturing process.

The development of new image quality FOMs is a complex theoretical issue involving a number of measurement questions: What is the nature of the image quality being measured, and what are the most appropriate metrical units to quantify it? Do the units capture relevant variations in image quality? And, finally, is the FOM comprehensible in terms of the human user?

What FOMs measure

A number of different image quality aspects need to be measured. For each, one needs to consider the nature of the image quality being measured, and the most appropriate metric to quantify it. As an example, we would use a luminance measure (e.g., foot-lamberts), not a radiance measure, to quantify the "brightness" of a display, since it is intended for human observers (not sensors). Consider how one would quantify the number of distinct luminances, or gray levels, between the maximum and minimum luminances of the display. This is an important factor in characterizing the quality of images a display can generate. This quantity describes how realistic and how informative the images can be. By tradition, this quantity has been approximated as the number of square root of two increments in luminance between minimum and maximum luminance. This quantity, known as the shades of gray (SOG) FOM, reflects a compromise between engineering requirements (for simplicity) and psychophysical data. The SOG FOM is derived from the luminance range, or contrast, FOM of the display, by formula. The formula assumes the luminance range can be continuously sampled. This is reasonable and appropriate for analog CRTs, which can present any incremental gray level between the luminance extremes, (i.e., the luminance can take on any value over a continuous range). However, the use of the SOG FOM to characterize the new digital FPDs is misinformative because the continuous sampling assumption does not apply to FPDs, where gray scales are generated differently. FPD gray scales are discrete in that the luminance values are limited to specific values in the luminance range, (i.e., the range is digitally sampled). As a result, any computed SOG value, would be totally misleading as a descriptor of the display's grey scale capacity. What the display's capacity actually is, as we shall discuss later, depends on the placement of the discrete samples within the luminance range. [See Klymenko et al., (1997) for an extensive discussion.]

Another example of a descriptor of image quality, which when first used misled the general public and professionals alike, is the advertisement tactic of many computer graphic workstation manufacturers describing their displays as capable of producing millions of colors, all at once. Although these numbers are derived simply by multiplying the numbers of red, green and blue driving levels controllable by software, it implied, in the minds of many buyers, enormous new vistas of color sensation. In fact, in terms of human vision, this number is of no consequence whatsoever. The display might generate all these colors, but how large is the range (or gamut) of these colors in terms of human color space, and how many different colors can we actually see. A million levels of indistinguishable cyans are just that. Failure to consider the observer can be very misleading.

Many of the different FOMs quantify display variables in one or more of three ways: Range, resolution, and (form of) sampling. Range is the maximum extent of a variable. For

example, the maximum contrast of a display, or luminance range, represents the full range over which the luminance can vary. Resolution is how finely the range of the variable is divided. This includes spatial and temporal resolution, and for luminance, the number of gray levels available in the luminance range, e.g., 16 or 256. Sampling is the placement of the levels within a range. For example, where in the luminance range are those 16 or 256 gray levels? In analog CRTs, this can appropriately be specified by the gamma curve. A gamma curve can be misleading in digital displays with few grey levels. Which of these three ways---range, resolution, or sampling---is the basis of a particular FOM parameter should be kept clearly in mind.

For example, the previously mentioned SOG FOM has been inappropriately used to characterize digital FPDs. This should have been avoided by a consideration of the units of the FOM variables. Converting from physical contrast, a physical range FOM, to SOG, a (visual) brightness resolution FOM, was natural for analog CRTs, given the assumption of continuous (physical) sampling, the virtually unlimited resolution of the luminance levels of the CRT's video signal. But, because digital CRTs and FPDs use discrete numbers of driving levels (dls) to code luminance, the SOG FOM is not directly applicable. The luminance range, without the continuous sampling assumption, does not imply the SOG formulated number of (visually) available brightness levels. Another example is the millions of colors advertisement tactic noted above, which is based on quantifying physical color resolution (number of dls), but misleads the public into assuming it is somehow related to the perceptual color range seen by the observer.

As we have seen, we need to explicitly consider what a metric means in terms of the human observer. The SOG FOM incorporates the fact that the human brightness scale is not linearly related to the physical luminance scale. (The square root of two rule reflects the fact that greater luminance steps are required to noticeably increase the brightness of brighter objects than dimmer objects.) When assessing the image quality of different technology displays, metrics of image quality should be either formulated, or, at least comprehensible, in terms of their value to the human user. This means its value should be relevant in terms of human vision per se (the ability to see it) and/or in terms of human performance (the human's capacity to respond to it appropriately and efficiently). The ultimate goal of displays is the useful conveyance of visual information to the human observer. For our purposes, image quality metrics should be considered primarily in terms of visual information, with special attention to the difference between the potential informational capacity of the displayed image and the actual visual information that the image can convey to the human observer. This is based on how well the properties of the display match the visual requirements of the observer.

How much information does a displayed image present, and, how much of that information is conveyed to the observer? First, let us consider what constitutes visual information. Basically, visual information is patterned spatial information conveyed (primarily) by differences in luminance, known as contrast. The potential information content within a single displayed image can be (loosely) defined as the product of the following factors: number of gray (luminance) levels, number of different colors for polychrome displays, and the number of picture elements, or pixels. This result multiplied by the update rate of the display (how fast the image can change) gives the informational flow rate of the display (Biberman and Tsou, 1991). This defines abstractly how many different patterns the device can present. However, this abstract description of potential visual information does not take into account the magnitude or

type of information that human observers can usefully receive. The human observer's visual/cognitive system has specific visual (and cognitive) capacities and limitations. Human characteristics include, for example, the human's capacity for global pattern perception and insensitivity to minute local differences, the human's differential sensitivity across the spatial frequency spectrum, and the human's threshold limitations in distinguishing luminance levels (as compared to a photometer).

For a display to be useful in transferring information, there must be a match between the capacity for visual information presentation by the display and the capacity for visual information reception by the observer. FOMs are most useful in quantifying and distinguishing displays when they reflect this match.

As an example of the need to incorporate the match between display and human, consider the case of a monochrome matrix display, where each pixel can be either black or white. In terms of information, we would give the factor, the number of gray levels, a value of two, because this image, known as a binary image, has two luminances, or gray levels. It is, therefore, limited in the quality of the real imagery it can present because every pixel in the picture is either black or white. Many things that normally are distinguishable with unaided vision, such as the difference between a black circle and a shaded sphere, are, with only two gray levels, two indistinguishable black circles. Many items would become completely unidentifiable, that is many of the subtle pattern differences used by human observers would be lost. This is especially crucial in difficult tasks such as distinguishing and identifying small targets. Now consider, displaying the same image with 256, rather than two, gray levels. The image, with near photographic realism, becomes almost as salient as the real world, where targets are easier to see.

But, now, consider the case where a poor quality display device presents the same image, also with 256 gray levels, but the human user can not discern the difference between the lowest 251 levels, which all look equally black. Physically, as measured with a photometer, the image presents 256 distinct gray levels, but, visually, as seen by the user, the image is only conveying six discernibly different gray levels to the human visual system, what we define as perceivable gray levels (PGLs). Therefore, to the human visual system, the image is indistinguishable from an image containing much less information because the sampling of the gray scale is a suboptimal match to human requirements for receiving visual information. In the conveyance of information, there needs to be a match between the presentation of image information and the reception of visual information. (Here, we focus on the perceptual aspects of the reception of visual information, although we note there are cognitive aspects concerning the requirements of human attention and memory.)

In the different FOMs developed for characterizing the image quality of CRTs, this match between the display and the observer is sometimes explicit, as in the SOG FOM, and sometimes implicit and/or undefined, as in the display descriptions claiming millions of colors. Often additional data need to be incorporated in order to understand what the FOM means in terms of the human observer. This is perhaps the most difficult and controversial part in the development of image quality FOMs. One needs to understand how to interpret often esoteric and difficult psychophysical research when incorporating the requirements of the human user. Below, as an illustration, we discuss the development of spatial resolution FOMs. As we shall see, spatial

resolution FOMs used to characterize CRT displays (the standard display technology throughout most of this century) are still, even now, controversial in the ways in which they incorporate the requirements of the human observer. In many cases, what the value of a particular FOM means in terms of the observer is not known, or only known over a limited range or a limited set of experiments. As an example of this, refer to the Design Handbook for Imagery Interpretation (Farrell and Booth, 1984), the best compendium of display requirements when it was published, where innumerable relevant psychophysical experiments are described, but where caveats limit the findings to the specific experimental conditions.

As we have seen, the different types of image display FOMs, the spatial, spectral, geometric, temporal, and luminance FOMs for CRTs and FPDs, have implications for visual performance based on the match between the characteristics of the image and the requirements of the user. The requirements of the user encompass more than just the accommodation of the display to the visual capacity of the user. It also means taking into account the visual task required of the observer. In other words, taking into account the purpose for which the display is used by the observer.

The purposes for which a display is used will determine the most crucial FOMs for characterizing the image quality of a particular technology. Consider some examples. For the purpose of medical diagnosis in radiology, where image quality is tied to the user's ability to detect subtle targets, Roehrig et al., (1990) consider the most essential parameters, FOMs, for describing CRT display quality to be spatial resolution, noise, characteristic curve, and absolute luminance, with the additional parameters of brightness uniformity, veiling glare and distortion also being important. For the purpose of computer graphics, where subjective aesthetic quality and realism are of paramount importance, Oakley (1984) states that the image quality of CRTs is most usefully described by the parameters of size, resolution, contrast ratio, geometric distortion, flicker, video bandwidth, and shades of gray (and chromaticity and convergence for color displays). Oakley (1984), also, states that additional important variables are the spot size and shape, which are determined by how well the beam is controlled and focused, and the physical characteristics of the phosphors including their luminance efficiency, spectral responses, and temporal response properties, such as luminance rise time and decay rate. For the purposes of U.S. Navy display systems, Meister (1984) has compiled a database on operator performance in using electronic displays, particularly CRTs, to serve as a guide for their design. There he states that the eight most critically important factors affecting operator performance with CRTs are frame rate, contrast ratio, ambient illumination, target/symbol size, resolution, bandwidth, registration, and phosphor type. For use in Army aviation, Rash and Becher (1982) consider the most important factors bearing on CRT image quality as luminance, contrast, frame and field rate, resolution, spot size and shape, and modulation transfer function (MTF).

Images convey pattern information to users. A basic measure of the capacity of displays to generate patterned images is spatial resolution. To illustrate the issues we have introduced, we discuss next the example of the development of spatial resolution FOMs.

Examples

First, let us consider an aspect of the spatial domain, the size of a display's pixels in terms of visual angle. It takes about 3000 pixels per square degree of visual angle for a displayed image to be indistinguishable from reality, because of the limited resolving power of the human visual system (Silverstein et al., 1990). Complex images will look more realistic as they approach this; however, realism is a subjective quality and is not of paramount importance for most visual tasks in terms of the usable information generated. More important in terms of reliably conveying visual information, and probably the most important parameter, is the spatial resolution of the display, which is the ability of the display to generate finely detailed patterns.

Displays based on CRT technology operate on the principle of sweeping an electron beam across a phosphor screen, where the image on the display is the result of light being emitted from the phosphors when excited by the electrons. Spatial patterns, made up of luminance differences within the image, are accomplished by the modulation of the electron beam which results in a modulation of the luminance. Because of the nature of CRT technology, smaller details become increasingly difficult to display at a given contrast, because of the physical limitations of modulating the beam amplitude. The smaller the detail, the faster the beam needs to be modulated as it sweeps across the monitor at a constant rate. Increasing power is required to make equivalent amplitude changes more rapidly as the beam sweeps at its constant rate.

Physically, the maximum power output is set, that is, it will be independent of the frequency of modulation in a frame (i.e., independent of the spatial frequency). Therefore, more rapid modulations (higher spatial frequency) will have lower maximum amplitudes, which means that smaller details will have lower maximum contrast. This is problematic and a major factor in CRT quality control because those small details are where the human visual system requires greater contrast. A number of measures have been developed to quantify this spatial resolution.

Historically, the most commonly used FOMs for CRT spatial resolution have been the shrinking raster resolution, the television resolution (TV limiting response), and the MTF (Biberman, 1973).

To determine the shrinking raster resolution of a monitor, a raster of equally spaced lines are written on the display. The line spacing is reduced or shrunk until the lines almost blend together to form an indistinguishable blur. This flat field condition occurs, for an experienced observer, when the line spacing is approximately two standard deviations, where one standard deviation is the spot radius at the 60 percent amplitude of the spot intensity distribution, which has a Gaussian profile.

To determine the TV limiting response, a television wedge pattern is displayed and the spot size is measured by observing the point at which the lines of the wedge are just detectable. This is equivalent to the square wave modulation function and is often referred to as the limiting square wave response. The point at which the wedge is just detectable, given in terms of the number of TV lines per unit distance, is the measure of the limiting resolution.

These first two techniques, and other similar techniques, described in Biberman and Tsou (1991) and Verona (1992) have the disadvantage of being subjective and therefore subject to observer error as described in Verona (1992). And they do not allow one to predict observer performance (Biberman and Tsou, 1991). The MTF, therefore, came into use.

The MTF

The MTF does not suffer from the mentioned disadvantages in that it is objective and it has a natural interpretation in terms of human vision. The MTF is an FOM which characterizes the efficiency of a CRT display device in converting voltage (scene contrast data) into displayed image contrast over a range of spatial frequencies, where spatial frequency refers to the number of modulations per unit length. Also known as the sine wave response (SWR) curve, when each spatial frequency is measured individually, this FOM uses maximum modulation contrast sine wave gratings of different sizes as input data (Figure 4-64). Loosely speaking, the different spatial frequencies of the sine wave grating test the device's efficiency at different scales, or sizes. The measure of the input/output efficiency for each frequency is given by the magnitude of the reduction in contrast of each of the different sized sine waves in the displayed image. And the overall plot of the reduction in contrast (that is amplitude) as a function of frequency is the MTF.

A CRT display's MTF curve typically is a monotonic function, maximum at the lowest spatial frequency available (determined by the display width) and decreasing to the limiting highest spatial frequency of the display (known as the Nyquist limit). This means that smaller scales, representing smaller details and objects, can not be displayed with the same high contrast as larger ones. Figure 4-65 shows a representative measured MTF of a CRT.

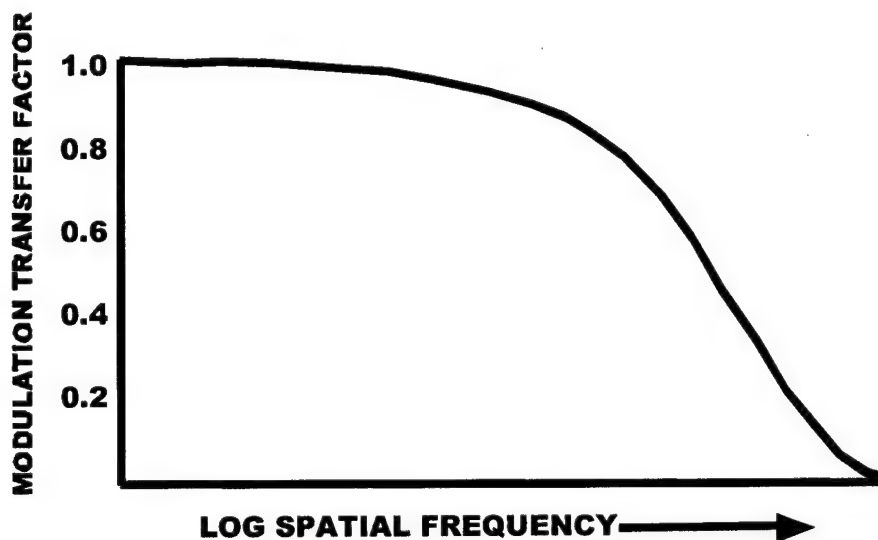


Figure 4-64. Typical modulation transfer function curve.

The Observer's CSF

Similar to the physical MTF for display devices, there are psychophysical functions for humans, which characterize the visual system's efficiency in transmitting contrast, in this case a physical stimulus contrast into a perception of that contrast. For humans, this curve is (typically) obtained by measuring the contrast detection thresholds of sine wave gratings over a range of spatial frequencies, i.e., the minimum contrast required to see the grating at each of the different spatial frequencies. The result is the contrast sensitivity function (CSF), sometimes referred to as the contrast transfer function, which can be considered as a (rough) psychophysical analogue of the MTF. (Whereas the MTF depicts the contrast output for different spatial frequencies when full contrast is input, the CSF depicts the minimum contrast required to see different spatial frequency sine waves.) Unlike the typical monotonic MTF for CRTs, which show maximal efficiency at the lowest spatial frequencies, the CSF shows that the human visual system is maximally efficient at intermediate spatial frequencies, of around 4 cycles per degree of visual angle, and drops off in efficiency at higher and lower frequencies, where greater contrast is required to see the grating. Figure 4-66 shows a typical CSF.

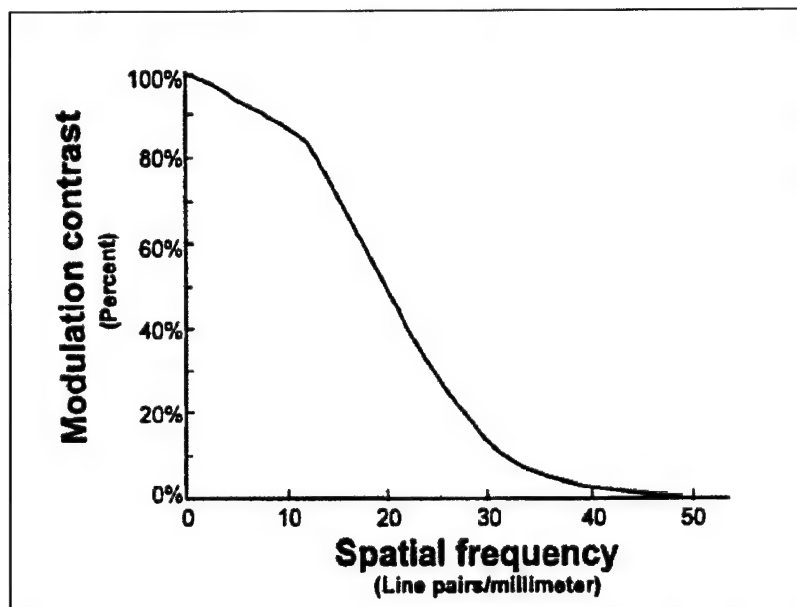


Figure 4-65. A representative measured modulation transfer function for a CRT.

Combining the MTF and CSF into an FOM to quantify conveyable information

Sine wave gratings are a convenient stimulus in generating both human and CRT efficiency functions because the mathematical tools available (Fourier analysis and linear systems theory) allow one to generalize the results to a wide range of stimuli and imaging conditions, (for example, the optical transfer function is an analogue of the MTF for characterizing the imaging quality of lenses). The mathematics of linear systems allow one, also, to cascade the transfer functions of various components of a complex optical system, such as a helmet mounted display, and to integrate the final component, the human perceiver, into a description of the total imaging context.

This last point---integrating the human perceiver--- is a complex issue: How does one combine the CSF of the human visual system with the MTF (or sine wave response curve) of a display device to derive an image quality metric based on units directly interpretable in terms of observer perception. That is, how do we obtain an overall FOM for the efficiency of a display-human system which starts by converting voltage, or scene contrast data, into a displayed image, which conveys a perceived image. Both functions are based on the contrast response of the respective systems, human and display, to sine wave gratings of a range of spatial frequencies. This question of how to combine them, not as straightforward as it may appear at first glance, has generated additional issues and some theoretical debate and visual experiments.

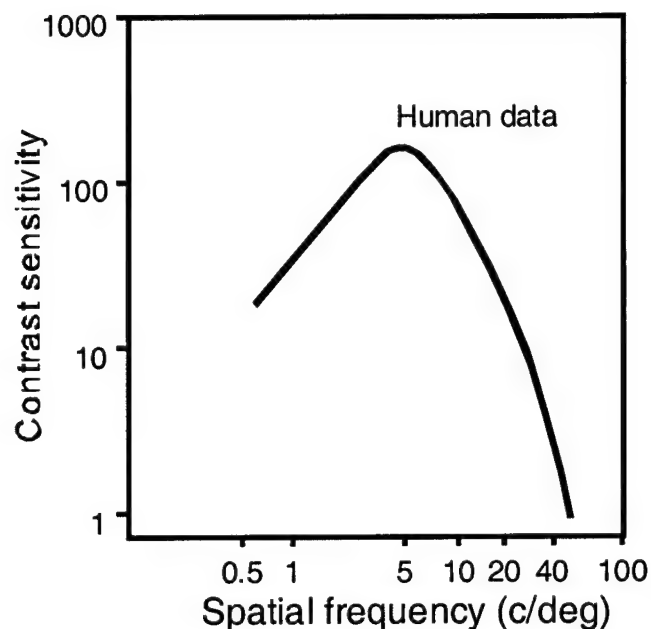


Figure 4-66. The contrast sensitivity function.

The most straightforward means of combining the human CSF and the display device MTFs is the image quality metric known as the modulation transfer function area (MTFA), shown in Figure 4-67, advocated by Synder (1973, 1980). Here the two curves are simply plotted and superimposed on the same spatial frequency scale. The point of intersection of the two curves is the upper spatial frequency limit, the point at which the device can no longer generate the contrast required for the human visual system to see the modulation. The human visual system can see the contrast generated by the device for the spatial frequencies to the left of this point. The MTFA metric, measuring the overall image quality of the device for spatial resolution, is quantified as the area between these two curves. This is the area that the device can display contrast which the human eye can see. This area, bounded on the bottom by the lowest contrasts the eye can see, and on the top by the highest contrasts the display can present, is taken to represent the integrated sum (over spatial frequency) of the amount of spatially resolvable information potentially available to the observer. The original assumption being that the greater area represented greater distance above threshold vision and hence better image quality. However, it is not obvious how the two axes of the MTFA graph should be scaled.

Task and Verona (1976) have argued that since human vision is not linearly related to the modulation axis in the MTF, it should be transformed into more visually relevant units. They transformed the contrast axis into square root of two incremented gray shades. The resulting Gray Shade Response (GSR), indicates how many gray shades are visible as a function of spatial frequency. This scale is more in keeping with the human's visual limitations in distinguishing gray levels. The new metric, defined as the area between the visual threshold curve and the GSR (instead of the MTF) is referred to as the Gray Shade Frequency Product (GFP).

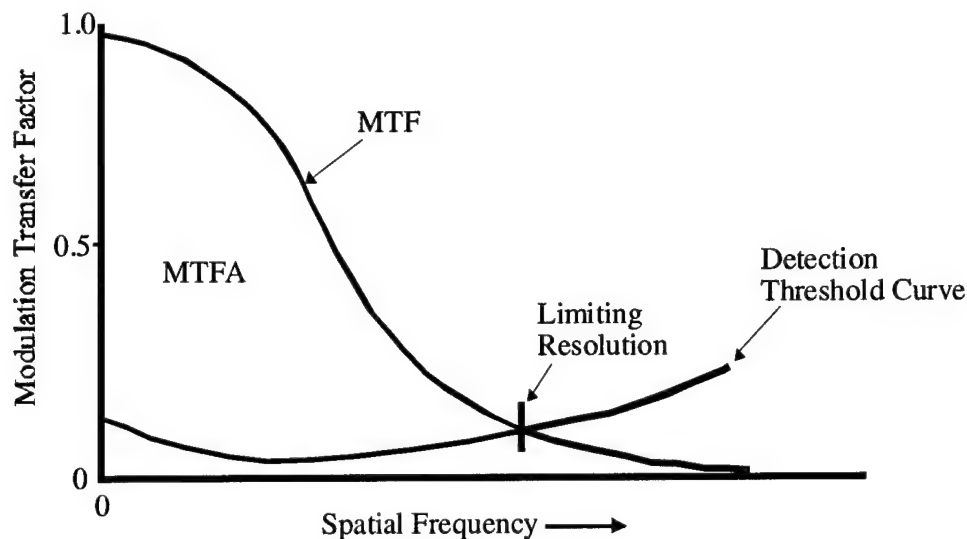


Figure 4-67. The modulation transfer function area.

To determine which FOM was more appropriate for describing image quality, Task and Verona (1976) performed a visual experiment to compare the predictions of the two metrics. The visual task was to increase the size of a target on the monitor until the subject could identify it. They used two versions of both the MTFA and the GFP. The two versions consisted of using linear and log scales for the spatial frequency axis in computing the values of the FOMs resulting in a total of four FOMs. In total, there were two scale conversions of each axis of the original MTF graph. The experiment ran as follows: Physically manipulating image quality by changing the electron beam to generate three spot sizes on the monitor, then computing the resulting indices for the four FOMs, and then visually testing the monitor with the three spot sizes to see which FOM best predicted the visual performance results. They conservatively reported that the visual performance results indicated that the (log scaled) GFP was at least as good a measure as the (log scaled) MTFA (Task and Verona, 1976). As opposed to analytically defining an FOM in advance, this is the empirical way to determine the value of an FOM; one derives the correlation between the value of the FOM for a number of image display conditions and the results of human visual performance.

In addition to the GSR, a number of other modifications of the MTF have been proposed. Based on a series of visual experiments, Barten (1990), for example, advocates his Square Root Integral (SQRI) Method as an improvement over the MTFA. His modification is essentially a different computational formula for deriving the FOM value based on certain assumptions about what is important to vision. For example, the MTFA weights changes in all

the spatial frequencies equally when computing the metric--a change in one spatial frequency will be the same as in another--, while the SQRI method uses a nonlinear scaling across spatial frequencies to weigh the scale according to visual importance (Barten, 1990). The Integrated Contrast Sensitivity (ICS) metric, another computational variation of the MTF, has been suggested (Van Meeteren, 1973) when one needs to take into account changes in human sensitivity, which vary with viewing condition. It is claimed that changes in the human contrast transfer function, such as occurs for adaptation level, are not accounted for in the MTF, but are in the ICS. Beaton and Farley (1991) discuss the relative advantages and disadvantages of the MTF, the ICS and the SQRI metrics. The research controversy with spatial resolution FOMs chiefly concerns how well behaved they are in tracking the effect of changes in the display conditions on visual perception. Barten (1990) claims the SQRI FOM tracks changes in a large number of viewing and image parameters.

Olson and Balram (1996), in their discussion of image quality metrics for display resolution, suggest that the limiting resolution and the MTF, because they both emphasize high spatial frequency performance, are more appropriate for evaluating military displays, while the SQRI, which was designed to heavily emphasize low spatial frequencies that play a major role in subjective quality, is primarily suited for evaluation of consumer displays. The SQRI de-emphasizes the higher spatial frequency information, which is of great importance in military tasks such as target detection and recognition.

Task (1979) tested a number of these metrics to determine how well they predicted visual performance. He correlated the metric values of images with observer performance in three detection/recognition studies in which image quality was varied by changing the system MTF. Of the FOMs he tested, he found that the MTF appeared to be the best predictor of visual performance. Many of these spatial resolution measures differ in the underlying assumptions as to the most important factors, and many of these methods differ simply in the computation of the FOM. The American National Standards Institute and the Human Factors Society, who have developed standards for monochrome displays published as the American National Standard for Human Factors Engineering of Visual Display Terminal Workstations in 1988 have adopted the MTF as the standard measure for spatial resolution.

The effect of visual tasks on spatial resolution requirements

Whatever the particular spatial resolution metric, observer performance dependent on spatial resolution will increase with increases in display resolution to some upper limit, where observer performance will reach an asymptote, caused by either a ceiling effect of the performance variable or by the display resolution exceeding the spatial sensitivity of the observer (Snyder, 1980). There is a task dependency, in that, in general, the simpler the task, the lower the resolution at which the asymptote is reached. For example, if the task is an alphanumeric character recognition task, a minimum of 12 television lines per symbol height is necessary for high recognition. Character recognition accuracy increases as TV lines increase from 8 to 16 lines per symbol. Also, for silhouette recognition, as raster lines per symbol height increase, so does identification accuracy (Baker and Nicholson, 1967).

Because of the complexity of the human visual system (including the visual cognitive system), which is not completely understood, it is not possible to make many unqualified general statements about the display's physical image quality requirements. Human factors psychologists have developed a body of sophisticated psychophysical techniques ranging from simple detection tasks, requiring no expertise, to more sophisticated techniques, which measure performance by experts in a particular visual task. An example is a spatial resolution study by Seeley et al. (1987) to determine the display requirements for making accurate medical diagnoses of a particular class of medical images on CRT monitors. This is a specific visual/cognitive task performed by highly trained experts. The accuracy of expert radiologists making patient diagnoses by viewing digital CRT images of chest X-rays was measured by receiver operating characteristic (ROC) analysis. In this task, where the spatial resolution of the displayed image was varied, they found that radiologists' performance peaked at a spatial resolution of 1.25 line pairs per millimeter (lp/mm). Therefore, 1.25 lp/mm was the minimum resolution standard they recommended for radiologists viewing chest films on a CRT.

As we have seen, the image quality requirements for even simple parameters such as spatial resolution can be very task specific. And, which FOM more accurately reflects the quality of a display will depend on how the display is to be used. For example, some consider the SQRI FOM as a better metric for commercial purposes, and the MTFA FOM a better metric for military purposes.

The effect of technology on spatial resolution FOMs

Originally, the MTF, and FOMs based on it, were developed for analog displays. Feltz (1990) and Moon (1986) have claimed that the MTF, originally developed for analog CRTs, can be applied to discrete matrix displays, including FPDs, by mathematical modifications in the way the MTF is calculated (see Beaton and Farley, 1991). They assume that despite the many differences between the analog quality of CRTs (such as the Gaussian luminance profile of its image spots) and the digital pixel structure of FPDs (including the variations in pixel geometry), the resulting MTF adequately can serve to predict visual utility of all display technologies. This is a controversial position. For example, Balram and Olson (1996) disagree and advocate the use of a new metric, the multivalued MTF or MMTF, which incorporates spatial phase as well as frequency, which is claimed to be necessary for a full characterization of matrix displays.

If we know a display's image quality in terms of its MTF, can we assume that in any visual performance task relying on spatial resolution (ranging from simple detection to more complex identification), the metric will be equally predictive of the visual performance results for the analog as well as for the digital display. The hidden assumption here is that all the different subjective quality aspects and the physical differences between displays that are not captured by the MTF are not as relevant or important in spatial resolution-limited tasks. This is currently a hotly debated assumption. Given the difficulties in arriving at new standards, an important question is whether or not FOMs previously developed for CRT displays can be applied to FPDs.

FOMs for CRTs and FPDs

We have seen the list of common FOMs used for CRTs and FPDs listed in Tables 4-14 and 4-15, and, using the example of spatial resolution, the issues involved in the development of FOMs including the issue of new digital technologies. Here, we look at which CRT FOMs can be directly applied to the newer FPD technologies, and we point out data voids, where new FOMs need to be developed for FPDs.

Differences of FPD technology

CRTs are a technology based around the modulation of a sweeping electron beam as described above. FPDs are electro-optical displays that derive their name from the flatness of the viewing surface and the reduced depth behind the surface. Unlike electron beam CRT technology, FPDs are based on a number of different technologies using varying physical mechanisms to produce the displayed image. This has consequences for visual perception and for what FOMs should be used to characterize them. The most prevalent current FPD technologies are LCDs, EL displays, plasma display panels, LED displays and field emission displays (FEDS). Each of these display types generally consists of a rectangular spatial array of picture elements (pixels) known as a matrix (Figure 4-68). Each pixel is independently controlled by electronic drivers. FPDs differ from CRTs, and each other, essentially in the physics of how each pixel generates or modulates light energy (Tannas, 1985). Independently of the physics associated with these technologies, FPDs may differ in the way the pixels are electronically addressed. Different addressing schemes will primarily affect the temporal parameters of the image and the type of noise likely to be encountered in the image. [In the context of military display updates, a recent survey of flat panel technologies can be found in Harding et al., (1996).]

Flat panels differ from CRTs and from each other in a number of significant ways that have been shown to have consequences for vision. As discussed, some have argued that the spatial resolution FOMs developed for CRTs can be used for FPDs, when modified for discrete matrix displays. The MTF of FPDs can be predicted based upon pixel density, spacing, and pixel geometry (Barten, 1991, 1993; Infante, 1993). However, in addition to the resolution of the pixels, their geometric arrangement, as well as pixel shape and pitch (distance between them), need to be specified in new FOMs, as these all have visual consequences. For example, Silverstein et al. (1990) have shown how these factors can introduce spatial artifacts, and affect display resolution and visual performance. Harding et al., (1997), controlling for visual angle, luminance, and contrast, have shown that the various pixel characteristics of FPDs can effect visual performance. They found that visual legibility was affected by pixel geometry, pixel noise, and screen filter characteristics. Another pixel characteristic, pixel fill factor, defined as the area of the active pixel divided by the total pixel area, also is important. Infante (1993) has shown that pixel fill factor affects screen resolution, where displays with smaller fill factors have a higher resolution as measured by the MTF. Also, the number of defective pixels, as mentioned, is a new variable needing particular attention because of the current quality control difficulties in manufacturing totally defect-free FRDs.

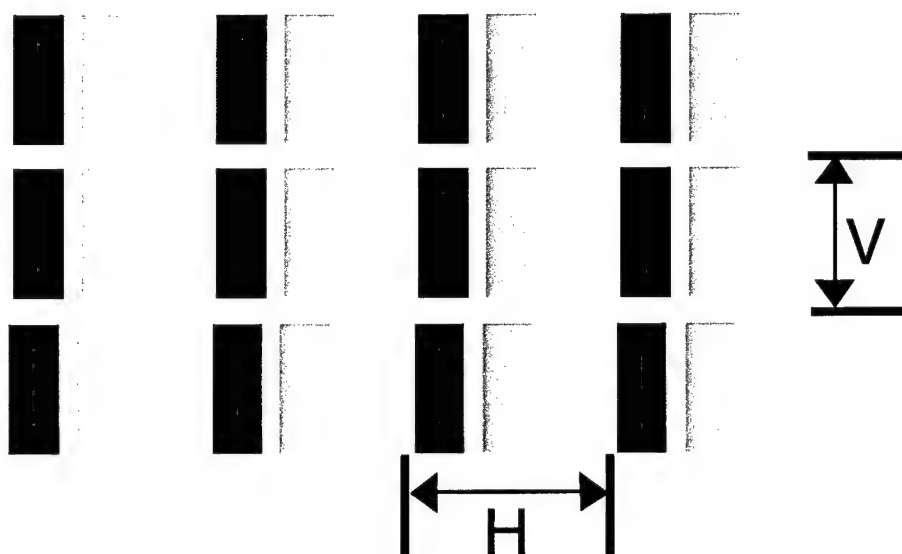


Figure 4-68. A rectangular spatial matrix of triad color (RGB) picture elements (pixels).

Which CRT FOMs apply to FPDs?

A number of variables effect CRT image quality as discussed above. They have been classified according to one tripartite scheme (Task, 1979) as follows: (1) Geometric variables such as display size and aspect ratio, number of scan lines and interlace ratio, illuminance, scan line spacing, and linearity; (2) electronic variables such as bandwidth, dynamic range and contrast ratio, signal/noise ratio, frame rate and field rate; and (3) photometric variables such as luminance and contrast ratio, gray shades, halation, MTF, color, resolution, spot size and shape, and luminance uniformity. Another four-part scheme was shown in Table 4-15. Many of these variables are tied to the specifics of the CRT's electron beam technology.

According to Curtin and Infante (1996), the most important factors affecting CRT image quality is listed in Table 4-15. Most have a relatively straightforward application to FPDs. Since pixel positions are fixed in FPDs, without the CRT variable of beam control, the issues concerning factors 4 (linearity) and 7 (convergence) do not apply to FPDs. Geometric distortion does not apply to FPDs which have fixed pixel positions, nor does convergence of colors, although the pixel packing geometry of FPDs will affect perception due to color fringes and spatial artifacts. [Note: these effects can be of concern at the highest resolutions (Silverstein et al., 1990).]

Factors 1 and 2, luminance and contrast FOMs, are directly applicable to FPDs, with the caveat that the ambient luminance must be taken into account. In general, brighter is better, with the required luminance of the display dependent on the environment, e.g., typical office displays require a luminance of 50 to 100 candelas per meter squared to achieve sufficient brightness. Brighter displays are needed for viewing in direct sunlight. Reflective and transreflective LCDs, which will compensate for increased light levels, need backlighting for low ambient light levels.

Whether the FPD display is emissive or passive will also determine how ambient light affects the contrast. For both luminance (display brightness) and contrast FOMs, the measures are the same for CRTs and FPDs, although differences in the effect of ambient lighting should be noted. In some FPDs, particularly LCDs, these measures need to be given as a function of viewing angle. Luminance uniformity across the display is an image quality issue with CRTs, but is less of a concern in most FPDs because of the nature of the addressing, by rows and columns, and the uniformity of the pixel activation.

Table 4-15.

Most important variables affecting CRT image quality (adapted from Curtin and Infante, 1996).

Factor	Perceptual Parameter	Physical parameter	Relevant for FPD
1	Brightness	Luminance	Yes
2	Contrast	Contrast	Yes
3	Sharpness, crispness	Resolution, addressability	Yes
4	Geometry, linearity	Linearity, straightness of lines	No
5	Vividness of colors	Color saturation, color contrast	Yes
6	Fidelity of colors	Color accuracy	Yes
7	Convergence	Convergence	No
8	Freedom from flicker	Refresh rate	Yes

Factor 3, resolution, as discussed above, is typically characterized by MTF-based FOMs. These translate in a relatively straightforward way from CRTs to FPDs. In the case of matrix displays, attention must be given to the pixel geometry which can cause visual artifacts and may effect perception at the highest resolutions. Resolution metrics, such as the MTF, will be similar for CRTs and FPDs, with modifications in the calculations due to the pixel matrix structure. Although as noted, the details here are controversial.

Metrics describing factors 5 and 6, concerning colors, should be the same for CRTs and FPDs. Color quality measurements, characterizing color saturation (purity of color) and chromaticity (color coordinates), and color gamut (range of colors) present no new conceptual issues for FPDs. Although, color fringing may be introduced at the highest resolutions with some subpixel patterns (Silverstein et al., 1990). Color anisotropy stands for the change in color as a function of viewing angle. In FPDs, if luminance and contrast FOMs need to incorporate viewing angle, so will color FOMs. Color uniformity across the display may need to be a concern to the degree that luminance uniformity is. Color tracking, the chromaticity changes as a function of luminance, may need to be specified to ensure color accuracy throughout the luminance range.

For factor 8, the conventional standard is that the display should be flicker free for direct viewing for 90 percent of the population. This should be true of CRTs and FPDs. This factor is a function of refresh rate, update rate and other (technology) specific temporal variables such as phosphor persistence. Of more concern, which we discuss below, is how these temporal variables contribute to the quality of dynamic imagery.

Another issue we have not touched on is the visual noise in the display (Biberman, 1973). Where the noise is in the signal source, the issue does not concern us here; where it is display technology dependent (e.g., "snow" or white noise produced by analogue circuits in CRTs, cross

talk in some flat panel displays, or defective pixels), separate technology-specific FOMs may need to be used to quantify the visual effects of the noise. Recent texts which cover many technology-based measurement issues include Holst (1995), Karim (1992), Keller (1997), and MacDonald and Lowe (1997). However, adequate FOMs to quantify and predict the visual consequences resulting from the temporal aspects of different displays are lacking.

The importance of measuring certain temporal aspects of displays such as phosphor persistence, pixel rise time, and so on, are recognized (Keller, 1997). Caveats on the need to be aware of dynamic image quality differences due to technology have been expressed (Parker, 1997; MacDonald and Lowe, 1997; Rabin and Wiley, 1995; Bitzakidis, 1995). And, dynamic imagery perception has been theoretically analyzed in the abstract (e.g., Lindholm, 1992). However, what is lacking are measures of dynamic image quality which can rationally characterize the visual consequences with dynamic imagery that result from the specific variations in the temporal parameters of different technology displays. FOMs need to be developed which can clearly delineate the visual quality of the dynamic imagery produced by different technologies. To do this, we need to consider what aspects of dynamic imagery are most important? Spatial resolution and gray scale, and how effectively these are matched to the observer, are the aspects of most importance in terms of visual information. How are these affected by dynamic imagery?

The differences in the quality of dynamic imagery is the most important new factor of concern with FPDs. When image motion is displayed on FPDs, the spatial resolution and the gray scale are affected, sometimes severely. (Whatever affects the gray scale also generally effects aspects of the color.) Exactly how they are affected needs to be quantified in a way that is comprehensible in terms of visual perception. This currently is the major data void in FPD FOMs.

Even with the long dominant CRT technology, the quality of dynamic imagery in certain applications has been a concern. Rash and Verona (1987) discuss the need to consider the display system's time constants because of its critical effect in pilotage and target acquisition. When modulation contrast degrades below a certain threshold level, targets begin to blend with the background and the user loses the ability to discriminate targets from their background. In dynamic images, pilots may fail to see tree branches and gunners mistake tanks for trucks. They suggest indexing image quality by dynamic MTFs, with modulation contrast reduction as a function of spatial frequency and drift rate. In order to predict the utility of CRTs for moving target detection and recognition, Rash and Becher (1982) have analyzed how various parameters of CRT technology contribute to the quality or degradation of dynamic images. The temporal parameters of the CRT, such as the phosphor characteristics (luminance rise and decay time, and phosphor persistence) and certain electronic variables (bandwidth, scan rate, frame rate, and field rate), contribute to image degradation of moving targets by blurring and smearing. Rash and Becher (1982) have developed equations modeling how target velocity, scan rate and phosphor persistence affect the MTF of the display.

How the phosphor persistence factor affects the MTF of CRTs can be seen by comparing Figures 4-69 and 4-70. In general, for relatively fast phosphors, such as P43, the MTF for static images on a CRT display describes the spatial resolution of static images as well as the spatial

resolution of dynamic images (Figure 4-69). In CRTs with slow phosphors, such as P1, the dynamic spatial resolution diverges from the static spatial resolution as shown in Figure 4-70.

The many novel factors involved in the generation of FPD images, each with their own novel time constants, will affect the dynamic MTFs. For example, Figure 4-71 shows how even a small ambient temperature change can induce large changes in the temporal response of an LCD display.

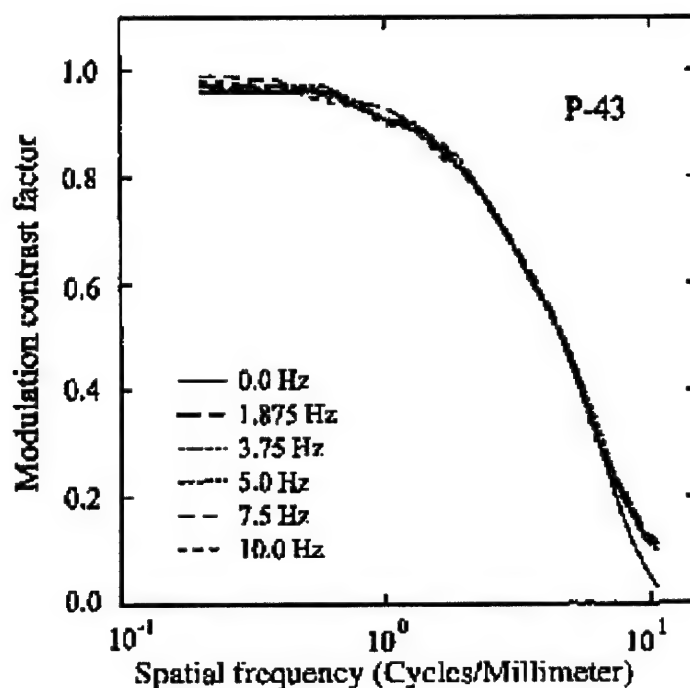


Figure 4-69. MTF curves for P43 phosphor (Beasley et al., 1995).

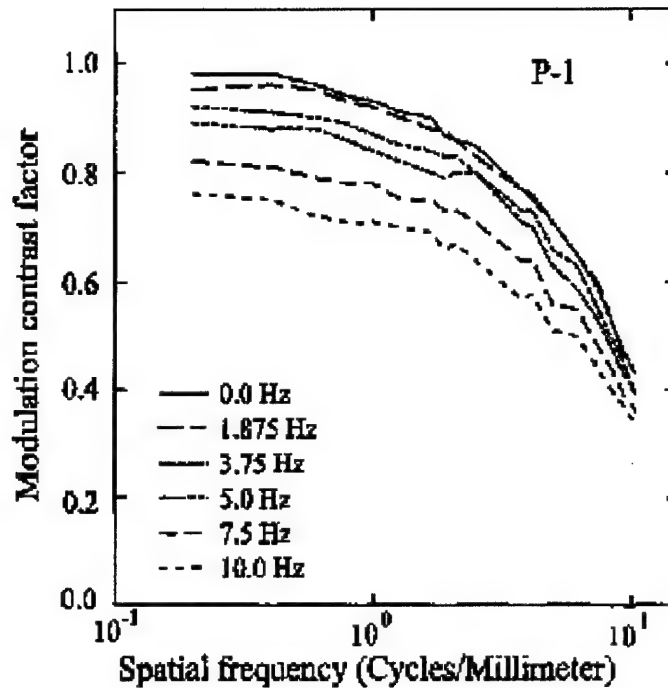


Figure 4-70. MTF curves for P1 phosphor (Beasley et al., 1995).

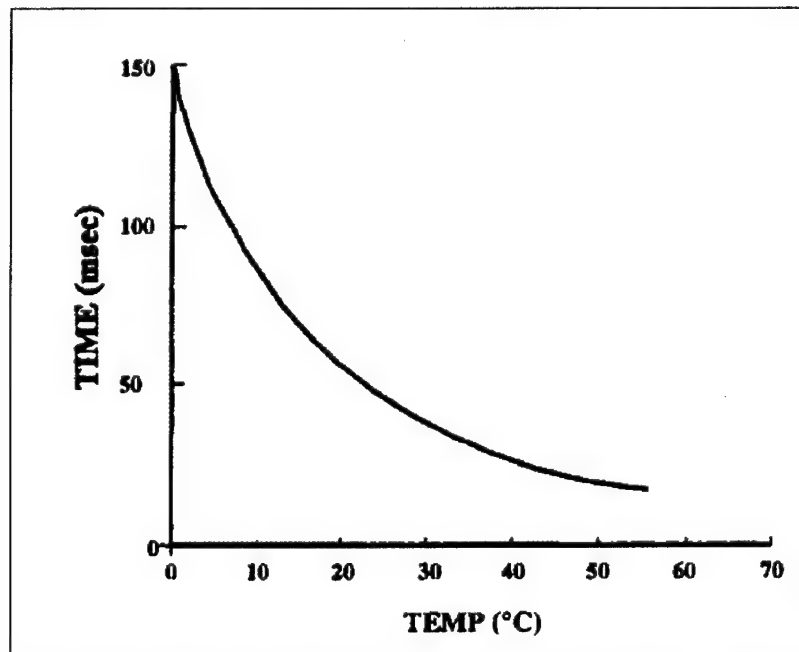


Figure 4-71. Temperature response of a liquid crystal display (Rash and Verona, 1987).

In order to clarify the issues of dynamic imagery on FPDs, we next delve into the essential factors at the root of a display's temporal parameters, which (along with the pixel factors discussed above) constitute the fundamental technology differences between CRTs and FPDs. These include methods of addressing, updating and gray scale generation.

Differences in image addressing and updating in CRTs and FPDs

A basic difference between the CRT and FPDs is the way displayed images are addressed and updated. Addressing refers to how an image location is coded and accessed in order to display a gray level (and color). Since the CRT uses periodic beam sweeps over a phosphor screen to generate the image, addressing is transparently accomplished by the simple association of a spatial location with the beam at a certain time in its cycle.

Updating the image in the CRT is equally transparent as the electron beam has a fixed rate of cycling through a complete image. The rate at which a complete CRT image is drawn, the time for the electron beam to complete a sweep to draw one frame, is known as the frame rate. The frame rate determines how smooth motion on the display will appear. CRTs are typically interlaced, where two fields are drawn for each frame, first the odd lines, and then the even lines. This allows the motion to appear smoother at a lower frame rate than if the images were non-interlaced, and this avoids flicker of the monitor. Thus, important parameters for CRTs are the frame rate, typically 30 Hz, as well as, the field rate, typically 60 Hz.

How fast the image is updated to change the image (the CRT's frame rate), and refreshed to avoid flicker (the CRT's field rate), is important to observer performance. Refresh rates should be over the critical flicker fusion (CFF) rate, when succeeding frames fuse together so that the image appears flicker free, but often it can not be much higher, because of the necessary increase in bandwidth. Additional contributing temporal characteristics of CRTs include phosphor persistence, horizontal scan rate, vertical refresh rate, and amplifiers' bandwidths. Rash and Becher (1982) have analyzed how these characteristics contribute to image smear with moving targets on CRTs.

In FRDs, addressing is done by a number of different electronic methods, usually involving some form of cycling through the column and row leads to the matrix array of individual pixels. While some older flat panels have inherent memory, where pixels remain on or off until addressed, most FPD technologies use periodic refreshing to avoid the perception of flicker. The required refresh rate to avoid flicker is based on the rise and decay rates of the pixels. If the pixel rise time and/or decay rate is too long, smearing may occur in dynamic images, as occurs in many LCDs. If too short, the refresh rate needs to be correspondingly faster to avoid flicker, particularly in those flat panel technologies which, like CRTs, use phosphors. These temporal characteristics of FPDs are pertinent when considering the conveyance of dynamic visual information, such as moving targets and changing imagery (Toms and Cone, 1995; Toms, Cone and Cavallaro, 1995; Rabin and Wiley, 1995). FOMs that are important here are the pixel rise and fall times for achieving a full luminance value, and the update and refresh rates.

Differences in image gray scales and contrast in CRTs and FPDs

As discussed, gray scales in CRTs are generated by modulating the amplitude of the electron beam. The resulting gray level corresponds to the amplitude of the transient voltage of the electron beam. Some of the older flat panel designs have used spatial aspects to generate gray

scales by trading spatial resolution for gray scale (e.g., by partitioning pixels into subpixels, where luminance equals the subpixel area turned on, or by dithering, which involves turning on random pixels in small unit areas to control the overall luminance of each unit area). These methods are not used in the newer displays where spatial resolution is important. Instead, many FPDs generate gray scales by using temporal aspects of the display, therefore, potentially trading temporal, rather than spatial, resolution for gray scale.

Each of these FPD methods rely on electronic controllers to translate gray level data to the form used by the display's circuitry. In pulse-amplitude modulation, transient voltage levels directly control luminance at each pixel. Instead of voltage, a number of methods use timing. The luminance is controlled by the amount of time a pixel is turned off versus turned on. In pulse-width modulation, the variation in the width of the pulse to a pixel during an addressing cycle determines the pixel's luminance. Other methods use different variations of the timing method such as duty cycle modulation, multiple pulse widths per frame, or combinations of pulse-width and pulse-amplitude modulation. All these methods interact with the physics of luminance generation and, each trades temporal resolution for gray scale. This can become a problem if the duration of the timing intervals needed to generate the gray scale become too large. This occurs in some LCDs that use this technique over multiple frames to control the luminance, which results in severe image smearing during image motion.

CRT technology has a known and consistent reduction in the available contrast for the smallest targets. This can be seen in the shape of a typical CRT MTF, in which there is a drop off at the highest display spatial frequencies (Figure 4-64). But, because the rate of the beam sweep in CRTs is a constant, moving that target across frames in dynamic imagery will not greatly effect the contrast already available at a particular spatial frequency (unless the phosphor is inordinately slow as shown in Figure 4-70). This was demonstrated in a study by Verona et al (1994) using temporally modulated sine waves as generic dynamic imagery (undergoing sinusoidal counterphase modulation). They tested two CRTs, with a slow phosphor (P-1) and a fast phosphor (P-44), and found the expected spatial MTF curve, which is the reduction in contrast for higher spatial frequencies. Only at the highest temporal frequencies (7.5 and 10 Hz) for the slow phosphor was there any effect of temporal frequency, where there was a slight reduction in contrast. Except for very slow phosphors, the MTF does not change shape appreciably as a function of temporal frequency.

However, the (relative) invariance of the shape of the MTF curve (quantifying spatial resolution) for image motion found in CRTs can not be taken for granted in FPDs due to the differences in technology. In the different types of flat panels, gray scales and contrast are generated in a number of different ways, often by pulse-width modulation alone, or in combination with amplitude modulation, or some variation of duty cycle modulation (Sobel, 1992; Klymenko et al., 1997). These methods may be completely adequate for static imagery. However, because of the timing requirements inherent in these methods, the gray scale and contrast available for dynamic imagery most likely will be affected. Thus, a problem in CRTs is that small targets have lower contrast and compressed grey scales. But, in many FPDs, this problem occurs for moving targets instead of small targets. This, combined with the smearing effect due to pixel persistence, may have disastrous consequences for perceiving dynamic visual information on some flat panels. That this is indeed the case has been shown by Rabin and Wiley

(1995), who found that visual performance with dynamic imagery was degraded with LCDs compared to CRTs, more so for higher velocity targets. They concluded that the differences between CRTs and LCDs were due not to differences in luminance, color, or spatial resolution, but to the poorer capacity of the flat panels to generate sufficient contrast for the dynamic imagery.

To summarize, in CRTs the small size of targets (indexed by the high spatial frequency response of the display) reduces contrast, while the high velocity of targets (indexed by the high temporal frequency response) does not. Conversely, in some of the matrix addressed FPDs, there is a problem of reduced contrast for high velocity targets, but not for small sized targets. Velocity, not size, is the main concern. [This is perceptually unusual in that in the real world the physical contrast of an object does not change based on its velocity.] Therefore, there is a need for a more inclusive FOM, reflecting the effects of motion as well as size.

New FOMs needed for dynamic imagery on FPDs

A number of commercial and government standards for CRTs, based more or less on psychophysical and human factors testing, have evolved to meet the requirements of the display community, including Underwriters Laboratories, Verband Deutscher Electrotechniken, the Federal Communications Commission, International Standards Organization (ISO), American National Standards Institute (ANSI), the Human Factors Engineering Society, National Information Display Laboratory, Society for Imaging Science and Technology, Society for Information Display, Society for Motion Picture and Television Engineers, Institute of Electrical and Electronic Engineers, and the National Institute of Standards and Technology's Flat Panel Display Laboratory. However, at the present time, there are no universal standards specifically for FPDs. Standards are being developed and proposed by the ISO (Greeson, 1996), but, because of the number of FPD technologies, and the continuing current development of the various technologies, it will still be some time before FPD standards are universally agreed upon in the same manner available for the mature CRT technology.

The standards of any new FOM need to mesh with the other display requirements. For example, it is mandatory for many military applications, particularly for displays that operate in day and night ambient lighting, that the display maintain its gray scale when dimmed over a 10 to 1 range, while maintaining an acceptable contrast ratio of 20 to 1 (Tannas, 1985). This is considered acceptable with the luminance either continuously variable, or controllable into at least 16 logarithmically spaced steps (64 for real world imagery to be aesthetically pleasing) Tannas (1985). Most flat panel displays do not use analog control for gray scale, but instead use temporal aspects of the image generation process such as pulse-width modulation, changing the element's duty factor on a frame time basis, etc. There are great demands on the contrast ratio and switching speeds already. Therefore, as we have indicated, there is a definite need to clearly assess the affect of temporal parameters on the spatial resolution and gray scale of dynamic imagery.

As we have seen, the influence of temporal factors would appear to be at the top of our list of concerns with the differences in FPD image quality that are not easily captured by any

standardized metric. There are definite differences in the properties of dynamic images between CRTs and FPDs (and, of course, among FPDs). These differences are based on the ways the images are generated by the different technologies, and FOMs are needed to quantify this in order to evaluate the new technologies. Before the insertion of FPDs, to replace CRTs, these new FOMs need to be implemented for image quality control assessments. This is especially crucial in areas such as medical imaging involving motion (e.g., dynamic cardiac imaging), and military applications (e.g., detection, discrimination and identification of moving targets), and aviation, or piloting, (where, often, the entire scene may be moving). The way dynamic imagery affects spatial resolution and the gray scale of the display, are the key variables of concern we turn to next.

Gray scale and spatial resolution of dynamic imagery on FPDs

The capacity of new display technologies to present dynamic visual information, such as moving letters across a monitor, or moving targets, or a moving background landscape seen by a pilot wearing a helmet mounted display (HMD), can not be fully defined by the old FOMs. As seen in Tables 4-14 and 4-15, where the common FOMs are divided into standard categories, there are FOMs for measuring temporal and other properties independently, but no FOMs for assessing variables in other categories under dynamic conditions, for example, what happens to a display's luminance range with dynamic as opposed to static stimuli. In as recent a source on display measurement as Keller's (1997) text, temporal measurements are considered only independently, as a separate category from other measurements.

As we have seen, in some FPDs the shape of the MTF of the display changes based on the temporal characteristics of the image. Velocity in the image is likely to be the important variable, where higher rates produce more of a reduction in image quality. Also, as we have noted, in certain FPDs, especially some LCDs where the gray scale is generated by pulse-width modulation over multiple frames, the gray scale will be greatly impoverished for moving images, and the impoverishment will also likely be a function of velocity--a more degraded gray scale for faster moving objects. The quality of spatial resolution (measured by the MTF), and the quality of the gray scale (luminance range and/or resolution, possibly sampling) are affected by temporal factors. How should one quantify this?

First let us reiterate, the basic function of displays is to present patterned visual information as static and as dynamic images. Image quality FOMs for spatial resolution, such as the static MTF, inform us as to the fineness of the details in the patterns that the device can present. These, though not without controversy, appear to be, more or less, sufficient for their intended purposes for static images. FOMs quantifying contrast and grey scale inform us as to the range, and/or number, of luminance levels that make up the spatial patterns, in essence, the number of potentially different patterns that can be presented at each resolution. (These contrast FOMs are discussed in detail in Klymenko et al., 1997.) Generally these FOMs are adequate as far as they go, the quantification of the maximum static contrast of a display and the number of SOGs in static images of analog CRTs.

In dynamic images on FPDs, the spatial resolution and the gray scale of the display will often be degraded. This change in image quality with dynamic imagery needs to be specified

precisely in a way that can be generalized over many imagery conditions, and be useful in assessing the relative merits of different displays for observers. What we need are FOMs to quantify the change in image quality, specifically the changes in the spatial resolution and gray scale of the device, as a function of the dynamic nature of the image. A further question concerns how to integrate the observer into these FOMs for dynamic imagery. In the case of gray scales, this may entail quantifying dynamic gray scale in terms of number of PGLs, and in the case of spatial resolution this may entail combining dynamic MTFs with dynamic CSFs.

Considerations in developing the new FOMs

One useful characteristic of many FOMs is that the FOM is a summary, or condensation, of information. For example, the MTFA FOM for spatial resolution, discussed above, gives a single number, which represents weighed averages of more information. How one assigns weights may be based on research, as in the example of Task and Verona's (1976) research which compared log and linear weighing of spatial frequencies; or, it may be based on what one considers important. The SQRI more heavily weighs low spatial frequencies, considered important for commercial viewing, while the MTFA is more biased toward high spatial frequencies, considered important for military applications. Reducing data this way, for the purpose of putting the various displays on a unidimensional scale so that they can be easily compared, has a drawback. While it reduces the need to consider the original data and many variables, it does lose information.

The new FOMs that need to be developed to quantify the way dynamic imagery affects FPDs will need to summarize the image quality effects of a large number of temporal conditions of a number of parameters. What happens to the MTF under different dynamic conditions? What happens to the gray scale of a standard target moving at various velocities? The maximum contrast, or luminance range of a gray scale, needs to be specified for dynamic conditions, in addition to the baseline static case. Is anything else going on when a gray scale is compressed; i.e., is there a change in the shape of the sampling distribution within the luminance range, in addition to the reduction in the luminance resolution?

For these data, one might parametrize the dynamic aspect of the imagery in terms of temporal frequency, or in terms of velocity. In FOMs for dynamic image quality, temporal frequency, defined as cycles per second of a periodic stimulus modulated over time (moving or flickering), may be useful analytically in the way spatial frequency is useful. Here, the FOM might use moving or flickering sine wave gratings as a stimulus. Alternatively, velocity (defined as either distance per second, or degrees of visual angle per second) might be more useful in terms of directly understanding real images moving on the display.

How should the observer be modeled? For example, how is the number of perceptual units between the maximum and minimum luminance, PGLs, determined? Should previously published data, or a standard assumption similar to the square root of two SOG rule, be used to model this, or are new psychophysical data required? How does the number of PGLs in the luminance range depend on velocity? Also, how would these FOMs incorporate visual tasks? A dynamic FOM is likely to give very different results if it is based on a task such as identifying a target that is being tracked versus a task such as identifying a target that streaks by.

What is the relevance of perceptual units, whether spatial resolution or gray scale PGLs, under different dynamic and task conditions? Consider the gray scale. If less PGLs, are available for moving targets, then less visual information can be generated, and conveyed, about that target when it is moving. In terms of information, the number of PGLs determines the number of potential targets that can be discriminated by the observer. This is important to know, particularly for many military applications, where rapid identification of small, high velocity targets is crucial. A gray scale FOM for dynamic imagery should inform one as to how many gray levels, and how many PGLs, are available for targets moving at different rates.

Consider spatial resolution, a more complicated topic. Should one simply generalize previous FOMs such as the MTF for static displays, to now include data for different temporal frequencies and/or velocities of the standard stimuli, as Verona et al. (1994) and Beasley et al. (1995) have done for CRTs. If done for new technologies, this might produce a great deal of data, and some means of rationally reducing the data might be necessary. Issues on incorporating the observer, as has been done in the MTFA, would be far more complicated, as humans have their own quite complicated contrast sensitivity function, which changes based on temporal frequency and velocity. The human visual response depends on both the spatial and temporal properties of the stimulus, so the CSF is now a two dimensional spatio-temporal response surface. Incorporating the data modeling the observer into an FOM is, as we have seen, a non-trivial exercise. The question of how to combine physical MTFs (measured with moving stimuli and parametrized in terms of spatial and temporal frequencies) with human CSF responses is likely to generate at least as many controversial ways as has the purely static case discussed earlier.

In summary, the overall question is how will these data be weighed and reduced to create simple, reliable and useful standard FOMs quantifying the quality of dynamic imagery on FPDs?

CONCLUSIONS

The functions and development of FOMs for visual displays have been discussed with spatial resolution FOMs serving as an illustrative example of the issues involved. These issues include what aspects of the image are measured and in what units, how FOMs are often technology-specific, and how FOMs may incorporate the user, and the purpose of the display, and the particular visual task. Visual information on displays was defined and the concept of conveyable information was discussed in terms of the need for some FOMs to indicate how well the properties of the display match the requirements of the observer.

Various new technologies under the general rubric of FPDs are competing with the old mainstay, the CRT, in display applications in the private, commercial, entertainment, aviation, military, medical and other arenas where displays are used. In some cases, FOMs used for CRTs can be applied to FPDs, and in other cases, the new FOM needed is rather straightforward, such as the defective pixel count FOM for FPDs, and the off-axis viewing contrast reduction FOM for LCDs.

FPDs have introduced a number of new parameters such as different methods of image addressing and updating, and image gray scale generation. Many of these affect temporal characteristics of displayed images in ways not encountered with CRTs. These temporal aspects play a large role in the new FPD technologies, and directly affect the quality of the imagery, particularly dynamic imagery.

There are no well-developed FOMs to assess and quantify the resulting quality of dynamic imagery on FPDs. New FOMs need to be developed to fill this data void. We have discussed various issues which need to be considered when designing these new FOMs, including the specific needs for assessing gray scale and spatial resolution with dynamic imagery. We have suggested that these new FOMs should be developed to quantify gray scale and spatial resolution as a function of temporal frequency or velocity.

We have identified a crucial need for new FOMs to characterize the quality of dynamic imagery on FPDs. As we have seen, there are many complex considerations in the development of new FOMs. However, this data void needs to be addressed before the insertion of FPDs in critical areas such as medical and military applications.

VISUAL EVALUATION OF LEGIBILITY WITH LCD FLAT PANEL DISPLAYS

INTRODUCTION

The introduction of flat panel displays into U.S. Army military aircraft is in progress. Flat panel displays offer several advantages over the older CRT technology. Flat panels are lighter in weight, lower in cost, lower in power consumption, and smaller in size.

In this study, the United States Army Aeromedical Research Laboratory (USAARL) evaluated five color liquid-crystal displays (LCDs) on the basis of their pixel structure. Four of the displays were active matrix while the other one was passive matrix. The evaluation consisted of equating the five displays for background and target luminance and viewing distance, so as to assess visual acuity as a function of pixel and target geometry. A physical evaluation of each display was completed in which pixel geometries, display resolution, luminance response, luminance uniformity, contrast, and viewing angle were examined. Some of these data are presented elsewhere (Harding, Martin, Beasley, and Rash, 1997).

METHODS

Displays. Five color LCDs were used in this study. Table 4-16 provides a listing of these displays along with some of their characteristics. In the body of the paper we will identify the particular panel by its ID.

Table 4-16.
Listing of the five active matrix displays and their particulars.

ID	Model #	Manufacturer	Matrix Type	Format (pixels)	Active Area (mm)
CP-1	PV440	PixelVision	Active	640 X 480	210.82 X 157.48
CP-2	LQ9D161	Sharp	Active	640 X 480	170.9 X 129.6
CP-3	LQ10DH15	Sharp	Active	640 X 480	211.2 X 158.4
CP-4	LM64C35P	Sharp	Passive	640 X 480	214.2 X 158.4
CP-5	LM64C21P	Sharp	Active	640 X 480	173.0 X 132.4

Psychophysical Stimuli. We developed two sets of visual stimuli. Each set consisted of one each of the 26 capitalized letters of the Roman alphabet. The two sets differed by their pixel matrices, one was a 5X5 and the other was a 7X7 matrix. The geometry of each letter is shown in Figure 4-72. In the 5X5 set, each letter was five pixels wide and five pixels high, and likewise in the 7X7 set, each letter was seven pixels wide and seven pixels high. In the 5X5 set, some letters differed by only one pixel (e.g., the letters 'C' and 'O'). The minimum difference increased to two pixels in the 7X7 set as with the letters 'D' and 'O'.

Stimulus duration ended when a keyboard response was made. Faster keyboard responses resulted in shorter durations of letters. For each letter, about 5 seconds were allowed for a response. If a response was not made, the letter was turned off and the screen was blanked for a timeout period that lasted about 2 seconds. A tone signaled the end of the timeout and a new letter was then presented.

Subjects. Five observers (two males and three females) with normal vision were used in this study. The ages of the subjects ranged from 25 to 31 years. To assure that each observer was well practiced with the task and was familiar with the letter geometries, each observer, prior to the experiment, was given a copy of the experimental software so that they could run simulations of the experiment on their own personal computers. Each observer was allowed to participate when they achieved a perfect score on three consecutive trials at a normal computer monitor viewing distance.

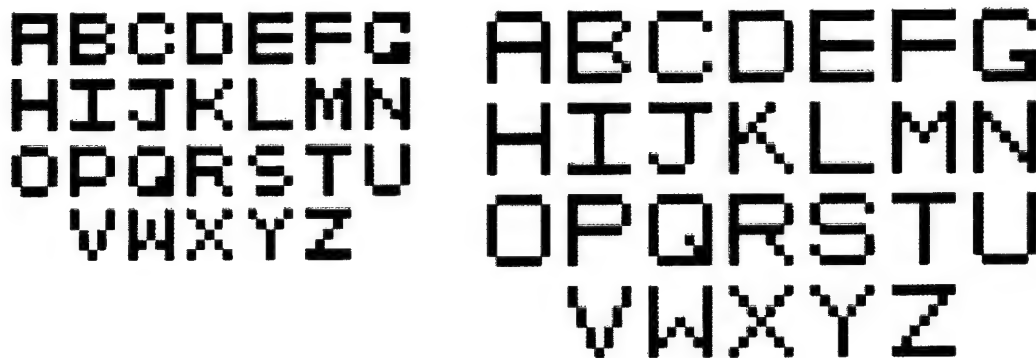


Figure 4-72. Alphabetical letters created for the psychophysical experiment. Alphabet on left is composed of 5X5 pixels and alphabet on right is composed of 7X7 pixels.

In order to obtain a comfortable typing position, the subjects' chair and keyboard position were adjusted to mimic their typical typing posture. While in the typing position, a chin rest was positioned under their chin to maintain head position. The chin rest was attached to an optical bench upon which the displays were mounted. The height of each display was adjusted to coincide eye level with the center of the display.

Pixel pitch and viewing distance. Three viewing distances were used in this study (near, medium, and far). In order to equate displays for target size, we measured each display's pixel pitch and calculated the required distances for the three viewing distances. Table 4-17 shows the viewing distances and pixel pitch for each of the displays. The distances for the 5X5 and 7X7 letters were chosen so that the letters subtended the same visual angle. For example, letters in the 5X5 near and 7X7 near subtended the same visual angle. (Please note that the flat panel used in CP-1 is the same flat panel used in CP-3, except for the presence of the diffusing screen. The differences in pixel pitch can be attributed to measurement error and to blurring caused by CP-1's diffusing screen).

Table 4-17.
Viewing distances for the five flat panel displays (given in centimeters).

ID	Pixel Pitch	5X5 Letter Matrix			7X7 Letter Matrix		
		Near	Medium	Far	Near	Medium	Far
CP-1	0.3291 mm	90.0	112.5	135.0	126.0	157.5	189.0
CP-2	0.2681 mm	73.3	91.6	110.0	102.6	128.3	154.0
CP-3	0.3296 mm	90.1	112.7	135.2	126.2	157.7	189.3
CP-4	0.3250 mm	88.9	111.1	133.3	124.4	155.5	186.7
CP-5	0.2550 mm	69.7	87.2	104.6	97.6	122.0	146.4

Test design. To counter learning and like variables that could affect our results, a counter balanced design was developed. The design (Table 4-18) called for each subject to start their testing with a different display. Also, on all subsequent days of testing, no two subjects tested on the same display.

Table 4-18.
Counter-balanced design for subject-display-day interaction.

	Day 1	Day 2	Day 3	Day 4	Day 5	Day 6	Day 7	Day 8	Day 9
Subject 1	CP-1	CP-2	CP-3	CP-4	CP-5				
Subject 2		CP-2	CP-3	CP-4	CP-5	CP-1			
Subject 3			CP-3	CP-4	CP-5	CP-1	CP-2		
Subject 4				CP-4	CP-5	CP-1	CP-2	CP-3	
Subject 5					CP-5	CP-1	CP-2	CP-3	CP-4

A subject viewed only one display during each day's session. At each of the 5X5 and 7X7 distances, three trial sessions were conducted. Each trial consisted of a pseudo-random presentation of each of the 26 letters of the alphabet and then a second presentation of each of the 26 letters of the alphabet. Thus 52 observations per trial and 3 trials per distance for a total of 18 trials per subject-day were completed. Since subjects continued at their own pace, with the exception of required rest periods between conditions, most sessions lasted approximately one hour or less. In all, 23,400 observations were recorded (52 observations per trial x 3 trials per conditions x 3 distances x 2 letter sizes x 5 displays x 5 subjects).

Equating contrast and luminance of display targets. To control for luminance and contrast of target letters across displays, we measured the luminance response functions for a target letter as a function of gray level. Our gray level range was from 0 to 255 in 16 incremental steps. Figure 4-73 shows a plot of luminance response functions for each of the five

displays. Please note that the luminance response function for CP-3 was multi-valued and as CP-1 and CP-3 use identical displays (with the exception of the passive diffusion screen), there is no plausible explanation for the discrepancy. Since the luminances at only two points were used in these experiments (i.e., target and background luminances), the response behavior of CP-3 did not affect the outcome of these experiments.

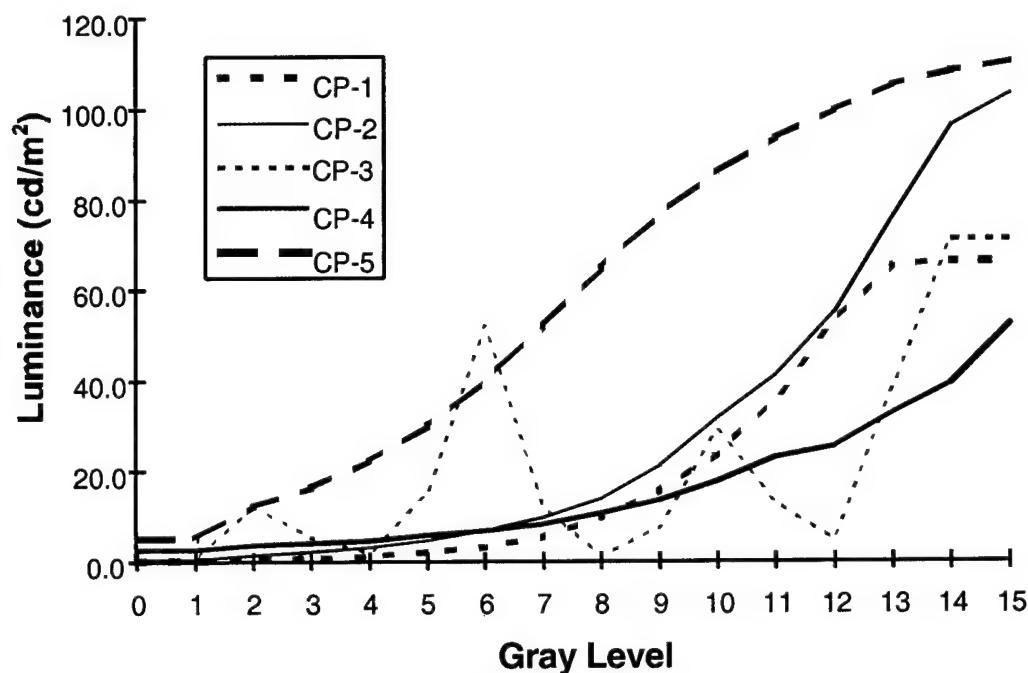


Figure 4-73. Luminance response as a function of computer gray level for the five flat panel displays.

Table 4-19 provides a summary of the luminance values and contrast ratios achieved with the five displays. Although equality was not achieved, a fairly reasonable luminance and contrast match was achieved in order to compare display pixel features. Figure 4-74 provides a graphical representation of each display's target and background luminances.

Table 4-19.

Summary of target and background luminances used in the acuity study.
Target and background luminances are given in cd/m^2 .

Displays ID	Target Gray Level	Background Gray Level	Target Luminance	Background Luminance	Contrast Ratio
CP-1	12	7	52.6	5.2	10.1
CP-2	12	5	55.0	4.6	12.0
CP-3	6	3	51.8	5.2	10.0
CP-4	15	5	52.2	5.8	9.0
CP-5	7	1	51.8	5.1	10.2

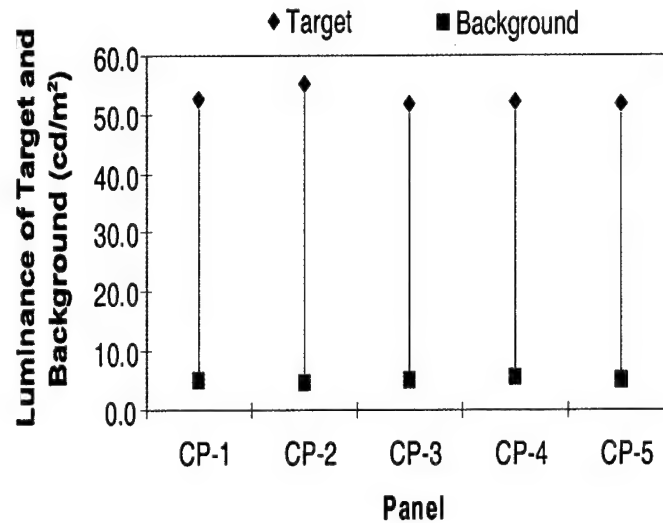


Figure 4-74. Target and background luminances for five flat panel displays.

Image size, pixel geometry, diffusion and fill factor. The viewing distances described in Table 4-17 for each of the displays provide for a constant image size across all of the displays. In the psychophysical experiments, an effort was made to maintain equal viewing conditions among the displays with the only differences relating to display pixel geometry and the clarity of pixels. Figure 4-75 shows a rendition of the 5X5 letter 'E' with nominal color pixel geometry. Distance G is equal to pixel pitch and distance S equals five times the pixel pitch. Table 4-20 provides the accompanying measurement data for Figure 4-75.

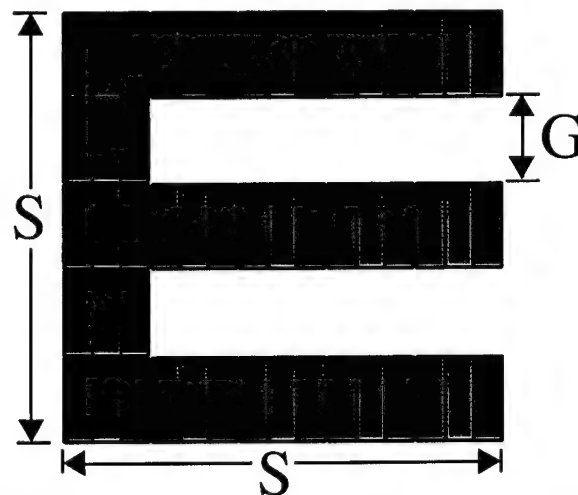


Figure 4-75. Nominal geometry of the 5X5 letter E. The distance G equals the pixel pitch and the distance S equals five times the pixel pitch. For the purpose of this illustration, the fill factor is 1; i.e., the illumination of the subpixels occupy all of the allotted space.

Table 4-20.
Visual angle of distances S and G in Figure 4-75 measured in degrees.

Distance	Near 5X5	Mid 5X5	Far 5X5	Near 7X7	Mid 7X7	Far 7X7
S	0.1048	0.0838	0.0698	0.1048	0.0838	0.0698
G	0.0210	0.0168	0.0140	0.0299	0.0239	0.0200

With certain liberties, the letter stimuli can be related to Snellen letters using the measurement for the pixel pitch as the acuity gap. In this fashion, an approximate Snellen letter size can be established for the three distances and two letter sizes. Figure 4-76 shows the Snellen equivalent line for each of the stimulus conditions. Although the 5X5 and the 7X7 letters subtend the same visual angle, their gaps are significantly different and ease of viewing should be considerably less with the 7X7 letter sizes.

Color Plate 1 in the Appendix of USAARL report number 97-XX shows photographs taken of the 5X5 and 7X7 letter 'E' for each of the displays. From the photographs, the differences in pixel geometry and clarity are readily apparent. In essence, there are two distinct pixel geometries: the pixel geometry observed in CP-1 and CP-3 (with identical flat panels), and the pixel geometry observed in CP-2, CP-4 and CP-5. The obvious difference between CP-1 and CP-3 is that the pixels in CP-1 are blurred intentionally by the manufacturer using a diffusing screen placed over the panel itself. Likewise, CP-2 is blurred using a diffusing screen.

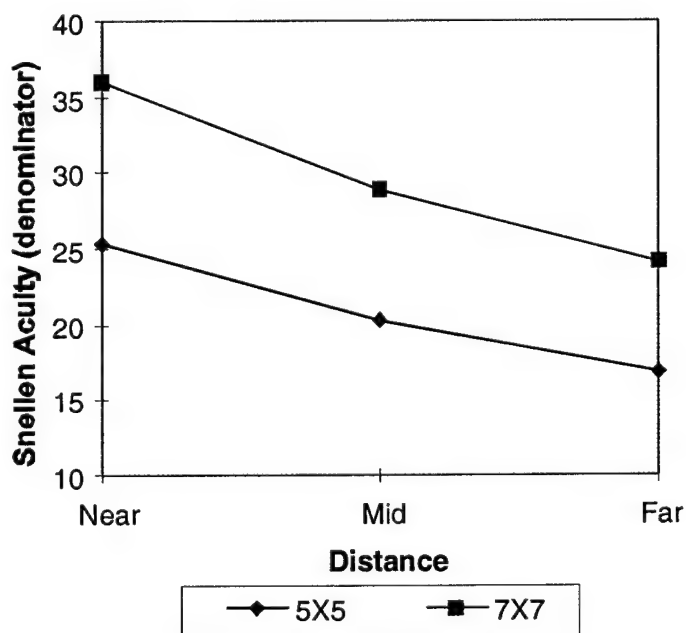


Figure 4-76. Equivalent Snellen acuity line for the three stimulus conditions.

The fill factor for each of the flat panels was measured using photomicrographs like those shown in the aforementioned Color Plate 1. Fill factor is a measure of the area of the active pixels or subpixels to the total area. It is a factor that affects the overall resolution of flat panel

displays (Infante, 1993). Displays with smaller fill factors provide for a higher resolution as measured by the display modulation transfer function (MTF). Mathematically, the fill factor is the active pixel area divided by the total area. Table 4-21 shows the fill factors measured for each of the displays. CP-2 was considerably difficult to measure due to its blur and, therefore, the accuracy of this measurement is highly suspect.

Table 4-21.
Measured fill factors for each of the flat panel displays.

Flat Panel	CP-1	CP-2	CP-3	CP-4	CP-5
Fill Factor	0.61	0.70	0.61	0.80	0.74

Visual acuity of test observers. To compare experimental results with known behavior, visual acuity was assessed at three viewing distances using the Graham-Field acuity chart. At each distance, the observer was asked to read the smallest letter sized paragraph that they could read. Through a series of approximations, we chose the paragraph (acuity level) where few mistakes were made in their reading, and the subject appeared to be able to read the paragraph with slight effort. In Figure 4-77 we plot the acuity values obtained for each subject.

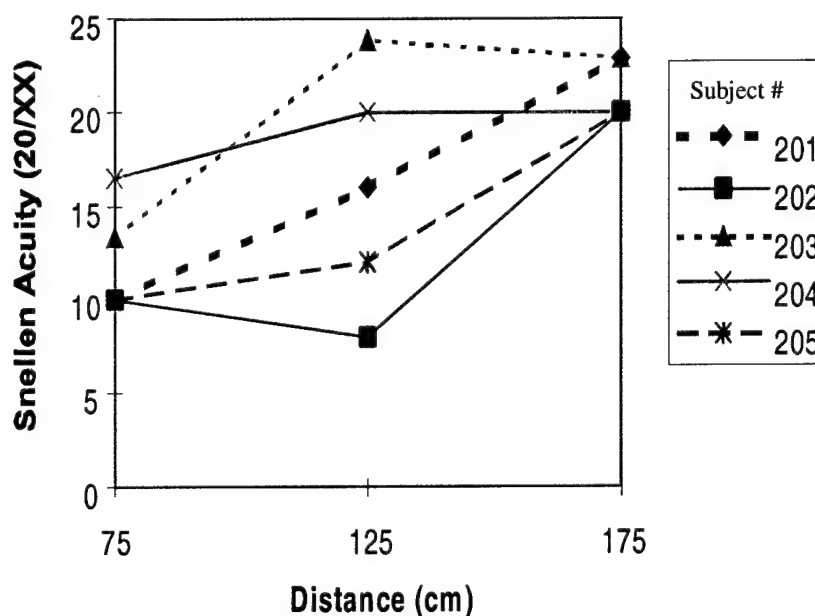


Figure 4-77. Subject acuity as a function of viewing distance.

RESULTS

From a cursory viewing of the data, it may be said that the majority of errors made in letter recognition were made due to a failure to clearly recognize the letter, as opposed to errors made in typing. We believe this since, for the easiest condition, subjects made very few mistakes. For example, the average recognition performance for the 7X7 letters at the nearest viewing distance was 98.31 percent. This error rate equates to less than one error for every trial (i.e., for every 52 observations). In addition, for entry into this study, each subject had to

complete three trials, at a comfortable viewing distance, without a single mistake. Thus we can be confident that typing errors were minimal and accounted for less than 2 percent of the total error rate.

Each condition can be ranked by perceptual difficulty by averaging recognition performance across subjects and across displays. Figure 4-78 shows average scores collected for each of the conditions.

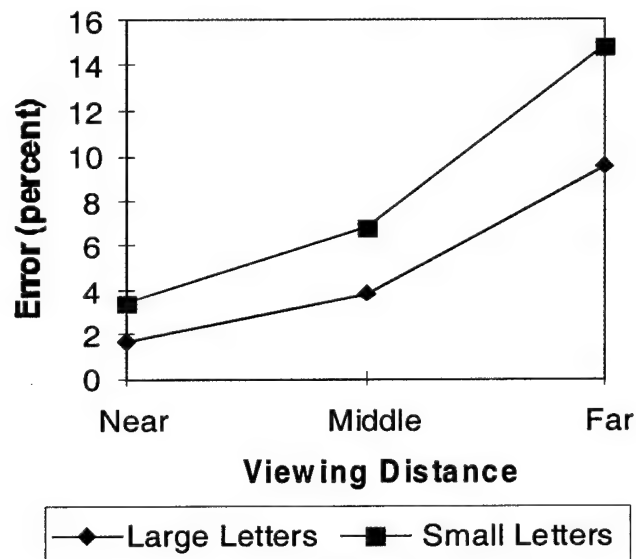


Figure 4-78. Average error rate for each of the stimulus conditions. Data are averaged across displays and across subjects.

We immediately see that the error rate, as expected, increases with increases in distance. Also, it was observed that the small letters with the minimum of one pixel gap were harder to identify correctly than the large letters with the minimum of two-pixel gap, even though at each distance, the large and small letters subtended the same visual angle. The reason for the difference lies in the ratio of the letters' gap width to its stroke width. Stroke width in this case is the diameter of the liquid crystal (i.e., subpixel arrangement). This particular issue will be discussed further below.

Acuity considerations. In Figure 4-76, the predicted equivalent Snellen acuity line is shown for each stimulus condition. These curves are based on the nominal measurements shown in Table 4-20. These figures assume that the fill factor of each display is 1.0. From our measurements of fill factor, we know that each of the five displays had a fill factor considerably less than 1.0 (Table 4-21). However, from Figure 4-76 an ordered arrangement is seen with the 7X7 near condition being the simplest task and the 5X5 far condition being the hardest task. As observed in Figure 4-78, these two expectations were met. However, expectations for the other data points did not fare as well. The reason for this failure lies with two main factors. First, a Snellen eye chart does not present all letters of the alphabet, but rather presents those letters that have more or less equal legibility. That is to say, each letter has a gap which is critical for recognition, and these gaps are the same size. To better test natural viewing conditions and to

use the data for predictive models, we used all 26 capital letters and obviously letters with different legibilities. The question of letter legibility is addressed in a companion paper (Harding, et al. 1997). As an example, we can clearly see that the letter 'L,' which doesn't contain a small gap as does the letter 'C,' must be easier to recognize. Secondly, each letter in a Snellen line has equal stroke width. In our study we have grouped data from five displays which have a range of fill factors which can be likened to stroke width and gap width. Since the data plotted in Figure 4-76 are based upon nominal data instead of measured data, the predictions may be in error (see MTF factor effects below). Another consideration is the contrast provided by a Snellen eye chart which consists of crisp black letters on a solid white chart. LCDs modulate light by changing the conformity of their crystals. The conformation has a polarizing effect and the modulation can be likened to crossed polarizers. In the closed position, some light escapes which reduces the overall contrast of the image.

Display performance. In general, psychophysical performance across the five displays was quite good. However, it might be beneficial to rank order each display to see if there are certain physical characteristics that could account for subtle perceptual differences. Figure 4-79 shows overall psychophysical performance with each of the displays. The data represent averages obtained across all three viewing distances and all five subjects for each of the two letter sizes. It is interesting to note that two of the three best displays are displays CP-1 and CP-2. As shown in the color plate in Appendix A, the photomicrographs for these two displays are blurred. The reason for this is that the manufacturer placed a diffusion screen directly over the display. This diffusion causes a general blurring of the image which may cause similar perceptual benefits as those seen with the Gaussian phosphor blur observed in CRT displays. This technique limits perceptual aliasing from unwanted higher spatial harmonics. It is also interesting to note that the two worst displays, CP-4 and CP-5, had similar pixel geometry, and these displays also had significant noise levels not apparent in the other displays. In addition, the pixel geometry of these two displays had the highest fill factor (see Table 4-21) of any of the other displays. As we know from the work of Infante (1993), a high fill factor causes a more rapid fall-off of the display's MTF. Noise is apparent in the photomicrographs of CP-4 and CP-5 and is in the form of light bleed-through from adjacent off pixels. After a careful examination, it was observed that the noise level in CP-5 was obviously greater than that in CP-4 and may have contributed to that display's poorer performance.

It would be beneficial to examine overall display performance at the furthest viewing distances to investigate display quality under demanding visual requirements. Figure 4-80 shows data obtained for only the furthest viewing distance. The same general trend remains as observed in Figure 4-79, although two observations are clear. First, CP-2 was clearly the best display in the test, and secondly, CP-5 was clearly the worst display in the test. It is also interesting to compare CP-1 and CP-3, since the only difference between the two is the diffusion screen placed over CP-1. From Figures 4-79 and 4-80, we see that CP-1 was better in the large letter condition and CP-3 was better in the small letter condition. Although the differences could be due to the randomness of the data, it is interesting to speculate that the blur of CP-1 may improve large object resolution (if one could argue that a 7X7 pixel character is large) and degrade finer object resolution. This point must, however, await further analysis.

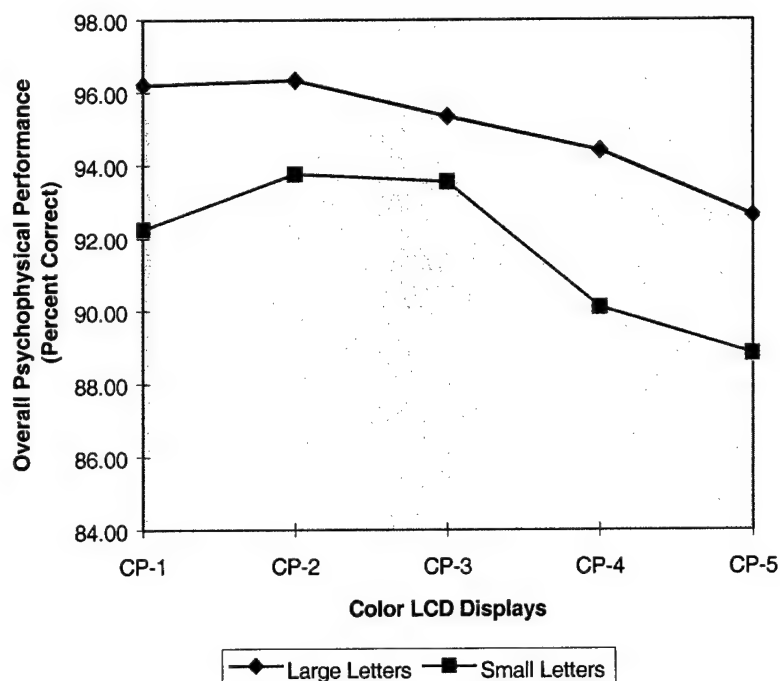


Figure 4-79. Overall psychophysical performance on each of the color displays. Each data point represents the average performance scored across all three viewing distances and all five subjects.

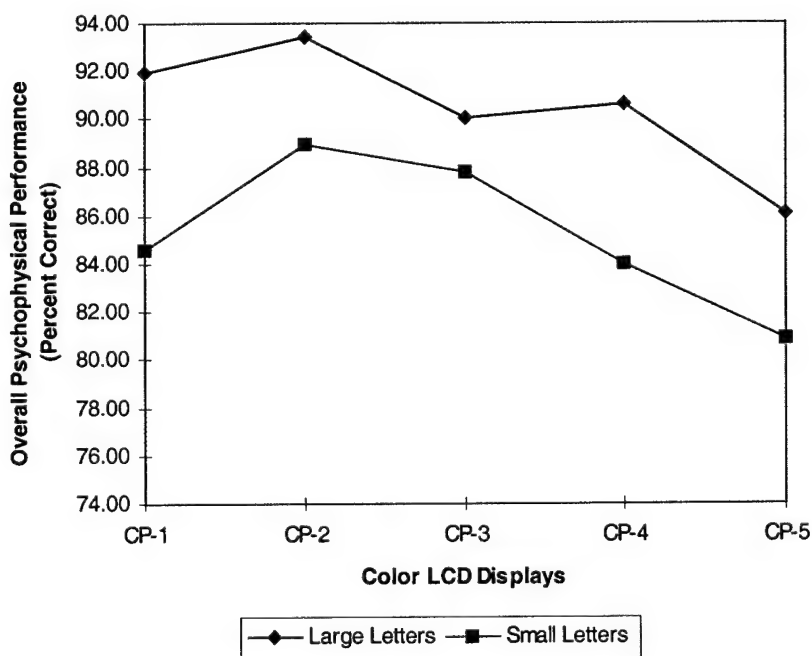


Figure 4-80. Overall psychophysical performance at the furthest viewing distance for each of the displays. The data were averaged across all five subjects.

Fill factor effects. The role of fill factor in display resolution can best be expressed by the MTF. The MTF of flat panel displays can be predicted based upon pixel density, spacing, and geometry (Barten, 1991, 1993; Infante, 1993). The MTF takes the form of a sinc function and is expressed as:

$$\text{MTF}(\mu) = \left| \sin(\pi\sqrt{F_f}x_p\mu) / (\pi\sqrt{F_f}x_p\mu) \right| = \left| \sin(\pi x_a\mu) / (\pi x_a\mu) \right|$$

$$\text{Where } x_a = \sqrt{F_f}x_p$$

and μ is spatial frequency, F_f is fill factor, and x_p is the pixel pitch.

The MTFs show very little variation and, even at the Nyquist frequency, the modulation range is less than 10 percent. Nevertheless, the curves agree to a certain extent with the results of this paper, in that CP-4 and CP-5 had the poorer MTFs while the other three displays fared slightly better.

These MTFs, however, should be viewed with some skepticism for a variety of reasons. First, the MTF equation that was used was developed for monochrome flat panel displays and not color displays with their subpixel elements and different geometries. Secondly, two of the displays, CP-1 and CP-2, were intentionally blurred by the manufacturers by placing a diffusion screen over the pixel array. This diffusion causes a slight blurring of the and this blurring may cause similar perceptual benefits to the Gaussian blur caused by CRT phosphor burn. In any case, the blur will surely influence the MTFs for these two panels, and therefore, the MTFs would show a faster fall-off in the high frequency range.

DISCUSSION

Here, we evaluated five LCDs in a letter recognition task. The five displays were balanced for luminance, contrast and target size. Five touch typists with excellent vision took part in this study. Their response data is the subject of two papers, with this paper being the first of the sequence. We found several display factors that may influence recognition.

Certain facts begin to fall-out from only a tertiary examination of the data. The five subjects were visually challenged by the furthest viewing distances and misidentified the 5X5 letters more often than the 7X7 letters even though the letters subtended the same visual angle. There are several reasons for this. Acuity has a relatively steep fall-off near the threshold. We attempted to challenge the subjects while still maintaining a high performance level and the data confirm this approach. For letters well above threshold, they can be clearly seen regardless of their size. Near the resolution threshold, visual performance begins to fall-off rather rapidly. Only a small decrease in letter size can produce large changes in performance. Using the letter stimuli at a viewing distance equivalent to about a Snellen 20/17 line, an approximate 14% error rate was found. If the study had extended to a distance equivalent to the 20/10 mark, for example, it would be expected that most observers would approach chance performance. Given 26 letters in the alphabet, chance performance is only about 4 percent or a 96 percent error rate.

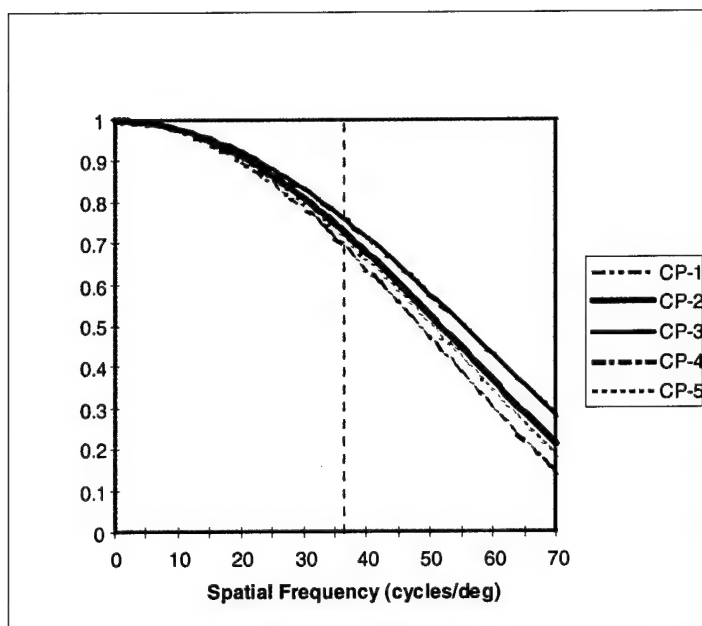


Figure 4-81. Predicted MTF for the 5 flat panel displays.

However, we are not as interested in the distance that produces mere chance behavior but are instead interested in conditions that produce unreliable behavior. The smaller letters were harder to distinguish mainly because of their smaller gap widths since the matrices had the same stroke width (width of one pixel).

Two of the displays tested in this study (CP-1 and CP-2) had a diffusion screen placed over the display by the manufacturer. As seen in the color plate in Appendix A, the pixels appeared blurred and the subpixel borders were harder to accurately characterize. It was therefore somewhat of a surprise that display CP-2 ranked as overall best of group in this study. Further, CP-1 tied for second along with CP-3. The two displays were identical with the exception of the diffusion filter placed over CP-1. Display CP-1 had higher scores with the 7X7 letter matrix and CP-3 had higher scores with the 5X5 matrix. We are not certain whether anything should be made of these results. We can say that the that the diffusion screens did not hinder recognition and even may have helped by filtering out unwanted higher frequency noise.

Displays CP-5 and CP-4 ranked poorer than the other three displays. Both displays had similar pixel geometry and had the highest fill factor. In addition, both displays suffered from noise arising from light leakage from off pixels.

In conclusion, we tested displays at their resolution limit (small characters) under conditions that would generally not arise during the course of routine observation. Given the normal scatter inherent in psychophysical data of this kind, the data variability reported here relate almost entirely to display parameters such as pixel geometry, pixel noise (mainly CP-5 and CP-4) and screen filter characteristics (display CP-1 and CP-2 only), since we controlled for image size, contrast and luminance of targets.

VISUAL EVALUATIONS OF PERFORMANCE METRICS
AS A FUNCTION OF HELMET MOUNTED DISPLAY
FOV CONFIGURATION

Monocular helmet-mounted displays (HMDs) currently are used in the Army's AH-64 Apache helicopter. A partial binocular overlap HMD is slated for use with the Army's new RAH-66 Comanche helicopter. The size of the binocular HMD's field-of-view (FOV) is the size of the visual world available to the Army helicopter pilot via an imaging sensor. The Comanche HMD presents the FOV in a partial binocular overlap configuration rather than a full binocular overlap configuration. In this latter configuration, the images presented to both eyes, the monocular fields, present identical views of the visual world where the FOV consists of a single binocular region. In the partial binocular overlap configuration, the FOV consists of a central binocular overlap region seen by both eyes, and two flanking monocular regions, each seen by one eye. What is the operational effectiveness of this new visual interface? First, we briefly describe the relevant differences between normal unaided vision and vision with a binocular HMD. Then, we cover our recent empirical findings on the sensory and perceptual effects of this type of display and how visual performance might be affected. Any deficits in performance need to be quantified before they are manifested on the battlefield. This study investigates how target acquisition is affected by implementing various configurations of the HMD's binocular display.

Normal unaided human vision consists of an overlapped divergent binocular FOV where the overall horizontal FOV is approximately 200 degrees of visual angle (when viewed straight ahead), with each eye's monocular field around 120 degrees of visual angle. The two partially overlapping monocular fields produce an FOV consisting of three regions. The central binocular region, which both eyes can see, is approximately 120 degrees, and the two lateral monocular regions, seen exclusively by each eye, are each approximately 40 degrees. The FOV is divergent because the right eye sees the monocular region to the right of the overlap region, and the left eye sees the monocular region to the left of the overlap region (Figures 4-82 and 4-83).

Current technology limits the size of the monocular fields an HMD can present to each eye due to the weight and size of the HMD oculars and the need for adequate eye clearance. Small FOVs can be detrimental to the visual tasks required of military pilots (Kenyon and Kneller, 1993; Osgood and Wells, 1991; Wells, Venturino, and Osgood, 1989; Wolpert, 1990). Relative to full overlap (FO), the horizontal FOV of HMDs can be increased, without increasing the size of the monocular fields, by partially overlapping the HMD's FOV (Melzer and Moffitt, 1989, 1991). The partial overlap (PO) configuration can be either divergent or convergent. The HMD's monocular fields can be overlapped in the divergent configuration as in normal vision. The resulting visual regions will be smaller than for normal vision because the HMD's monocular fields are smaller than each eye's normal view. Alternatively, the HMD can be overlapped in the convergent partial overlap (CPO) configuration, where contrary to the divergent partial overlap (DPO) configuration, the right eye instead will see the monocular region to the left of the binocular overlap region, and the left eye will see the monocular region to the right. If the monocular regions are in the FO configuration, the FOV will be one binocular region limited to the size of a monocular field (Figure 4-83).

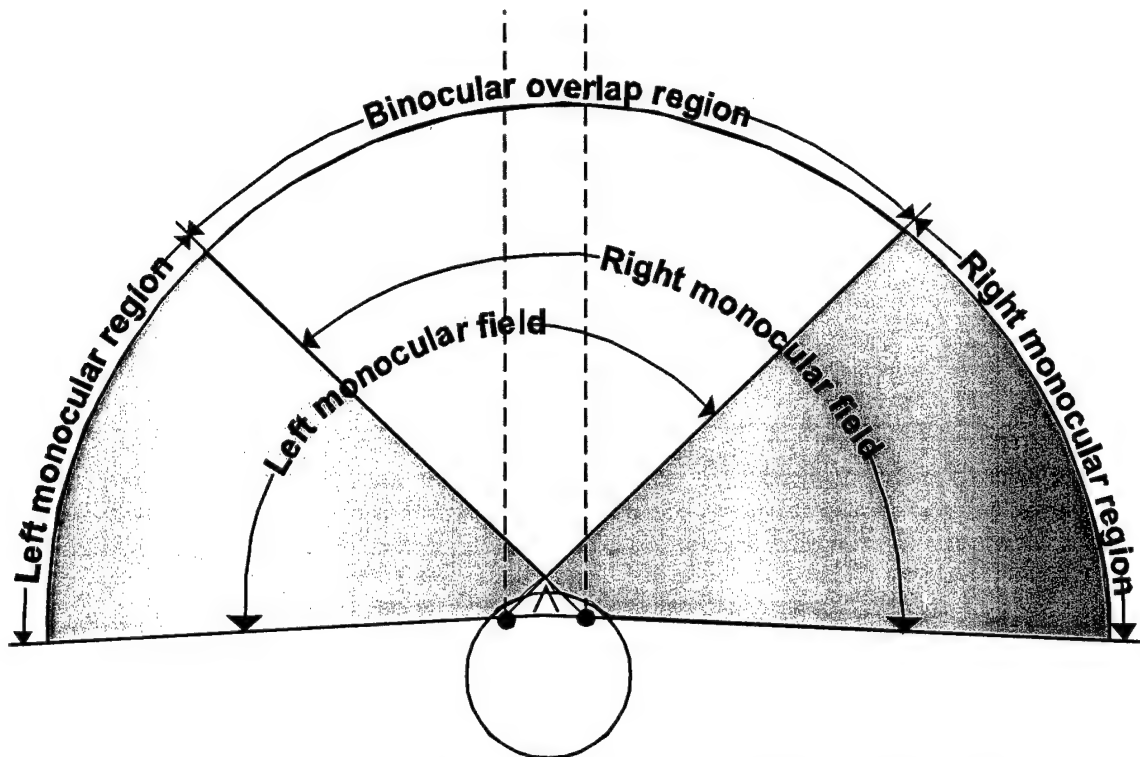


Figure 4-82. In normal unaided vision the two monocular fields are partially overlapped producing a divergent FOV consisting of three regions, the central binocular overlap region and two lateral monocular regions.

The PO method was designed to increase the limited FOV available in the HMD without incurring unacceptable increases in the size and weight of the HMD or losses in central resolution. However, increasing the FOV by this method has been a concern (Alam et al., 1992; Edgar et al., 1991; Kruk and Longridge, 1984; Landau, 1990; Moffitt, 1989; Moffitt, 1991; and Moffitt and Melzer, 1991). One detrimental consequence of the partial binocular overlap display configuration is the perceptual effect known as luning (Figure 4-83), which is a subjective darkening of the monocular regions near the binocular overlap border (Moffitt, 1989; Klymenko et al., 1994b).

Luning can lower the visibility of stimuli as well as distract the pilot using the HMD. Fragmentation can also occur in partial overlap displays. This refers to the segmented phenomenal appearance of the display as three distinct regions instead of the perceptually unitary FOV normally seen (Klymenko et al., 1994a). The detrimental visual effects of luning and visual fragmentation tend to be greater in divergent than in convergent displays (Klymenko et al., 1994a,b). The most likely reason for this is as follows. The partially overlapped FOV of the HMD, which is smaller than the FOV in normal vision, results in the display's central binocular region and two flanking monocular regions falling in a visual area that is normally completely binocular. Visual processes such as binocular rivalry and dichoptic competition become visually pronounced and are experienced as luning and fragmentation in the FOV. (See extensive discussions in Klymenko et al., 1994a,b,c.) Also, there is an effect on the visibility of targets in the monocular regions of partially overlapped FOVs.

The visibility of targets, and the visual world in general, seen in the HMD's FOV is of paramount importance to military aviators. In a target detection task, where the contrast needed to see a target was compared across display configurations, Moffitt (1989) found no significant effects of partially overlapping the displays. Target visibility, as measured by the degree of contrast needed to simply detect the presence of a target in a blank field, was unaffected by the method of overlap. Klymenko et al., (1994c), however, did find a difference in target visibility as measured by the degree of contrast needed to determine the orientation of a target. The results showed that targets were most visible in the FO FOV display, least visible in the DPO FOV, and intermediately visible in the CPO FOV. Other display factors were also found to effect target visibility. Targets in the binocular region were, as expected, more visible than targets in the monocular region. Also, targets in the monocular region adjacent to the binocular overlap border were less visible than more displaced targets. The target visibility effects were relatively small in terms of contrast, but were clear cut and systematic.

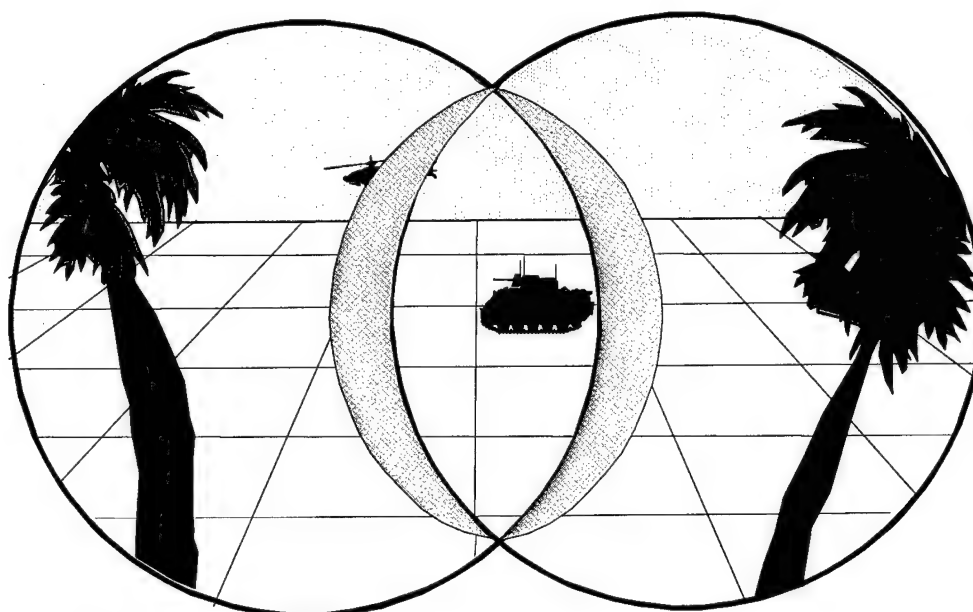


Figure 4-83. Pilot's view of visual world in an HMD with a partially binocular overlapped FOV. Each eye sees a circular monocular field against a black background. The real world image to each eye matches in the binocular region, but in the monocular regions, the real world image of each eye is matched to the black background of the other eye leading to visual effects such as binocular combination and binocular rivalry. Luning, the temporally varying subjective darkening near binocular overlap borders, can result. Also, fragmentation of the FOV into three phenomenally distinct regions and reduced target visibility in monocular regions can occur.

The reason for the reduced target visibility in PO FOVs is the dichoptic competition between the two eyes due to conflicting visual information. This includes a general visual system effect of binocular rivalry (and alternating monocular dominance) between the two eyes, and a specific stimulus effect due to the binocular overlap border in the display. For more extended discussions see Klymenko et al., (1994a,b,c).

Klymenko et al., (1994) used the threshold contrast for orientation determination as a measure of target visibility. Are these reduced target visibility effects likely to affect general visual performance? The increase in target thresholds in the DPO FOV display compared to the CPO FOV and the increase in both of these compared to the FO FOV were small and might arguably be a negligible effect. The contrast thresholds differed usually by only a few percent in modulation contrast (Klymenko et al., 1994). Those findings were from a psychophysical study concerned with the effect on the visual system response and not with the effect on visual performance under realistic operational conditions. Therefore, the viewing procedure had been optimized in a number of ways. Subjects always knew the location of the target and fixated it during the contrast threshold setting procedure. They had unlimited time to view each target and to set the threshold, and the target remained in one location throughout an experimental session. Also, there were no additional demands on the subject; that is, the mental workload, the drain on attentional capacity, was nil. What would happen to the small differences in human responses to different FOV configurations if these factors were less optimal? Will the small differences disappear or be magnified under non-optimal, more operationally realistic, viewing conditions?

It is possible that the optimization of viewing conditions for contrast threshold in Klymenko et al., (1994) may have alleviated the deleterious effects of partial binocular overlap displays. If so, these effects may be more serious than the small thresholds seem to imply. For example, the lack of time constraints in our previous experiment may have reduced the effect of binocular rivalry because the subject had time to voluntarily shift attention between the two eyes, or to simply wait for an optimal phase in the temporal progression of binocular rivalry. Also, direct fixation and knowledge of location may help lower contrast threshold by reducing uncertainty. In short, the differential effects we found may have been minimized by the optimal viewing conditions by pushing all the results towards a common floor (the lowest possible thresholds). Normal viewing in the real world is seldom so optimal, especially in a military aviation environment. Therefore, the effect of the HMD display configuration on visual performance under realistic viewing conditions remains an open question.

In short, previously, we have found differences in human vision due to the different display configurations. Those results showed less visual impairment in FO FOVs than in PO FOVs, and between the PO FOVs, there was less impairment under the CPO FOV than under DPO FOV. How important are these psychophysical differences in practical terms? The current study was designed to gain more understanding of the real world impact of these HMD designs on general visual performance by using a target acquisition task under the more realistic psychological constraints experienced in aviation. This included time pressure, uncertainty of target location and orientation, multiple possible targets and nontargets, nonstationary targets, a randomly cluttered background, and a requirement for scanning eye movements across the FOV. This was a higher mental workload task demanding more attentional capacity. Would this difficult task alleviate or exacerbate the differences between the display configurations? In other words, would the small, yet systematic, perceptual differences induced by the different FOV configurations be mirrored in visual performance under more realistic and demanding viewing conditions, or will they disappear? Aviation is an attention-demanding (high mental workload) environment with a high rate of visual information throughput where visual inspection time is limited. Often the eyes need to continually scan an FOV with a moving visual scene and moving targets. This is a stimulus environment that often taxes the visual performance of the human

perceiver, who has been described as a limited capacity processor of visual information. Under operational conditions, human performance may be compromised by the PO FOV design. The performance decrements with these HMDs may become critical in attention demanding environments such as military aviation. This study assesses the effects of these FOV configurations on visual performance under more demanding viewing conditions.

THE EFFECT OF FOV ON TARGET ACQUISITION

Our first investigation was designed to determine how display configurations affect visual performance in a target acquisition task under demanding viewing conditions. The purpose was to measure the effect of partial binocular overlap on visual performance. The viewing conditions are designed to simulate the high visual information throughput an aviator might experience under operational conditions. Performance in three different FOV configurations was measured by response time (RT) and error rate. The three configurations were the FO, the CPO, and the DPO FOV. The task required subjects to visually scan for and identify the target's position in a randomly cluttered FOV as quickly as possible while minimizing errors. The target could be in any one of nine locations and could be any member of a subset of a larger total set of similar objects, all of which were visually degraded. Monocular field size was controlled across display configurations, meaning that the same sized monocular fields were used in the FO and the two PO FOVs.

Except for orientation contrast threshold and perception of lining and fragmentation (Klymenko et al., 1994a,b,c), we do not currently know which factors, and their relative importance, might be influenced by the type of FOV configuration. We therefore implemented a number of factors likely to reveal differences. These included the physical characteristics of the targets, and the target positions. For dichoptic stimulation, figures with sharp edges and sharp temporal onsets and offsets tend to be better dichoptic competitors, and so more visible in the fused binocular percept than figures with smooth edges and smooth temporal offsets and onsets. Therefore, the targets used in the experiment were spatially blurred and presented with smooth temporal onsets and offsets. In PO displays, targets are likely to be least visible in the monocular regions adjacent to the binocular borders (Kaufman, 1963,1964; Klymenko et al., 1994c); therefore, positions located there were included among the scanned positions.

In this preliminary study, a number of factors were psychophysically designed to induce differences between FOV configurations in order to determine the practical relevance of the FOV configuration in terms of visual performance. The displays and task were unique to the experiment, so prior experience with particular HMDs and symbology would not be a factor.

Methods

Subjects. Fifteen Army aviators, 13 males and 2 females, voluntarily took part in the experiment. This population had passed class II flight physical vision tests. All had 20/20 unaided or better Snellen acuity. Mean age was 31.8 (SD = 6.3), ranging from 24 to 42.

Equipment. The equipment consisted of three major components: A Hewlett-Packard HP-9873 1 Turbo-SRX computer graphics workstation used to generate the visual stimuli, a custom optical table configuration used to optically direct the visual stimuli from the workstation monitor to a pair of viewing binoculars, and a subject booth. The booth was a light-proof enclosure behind the binoculars where the subject viewed the stimuli via the binoculars and responded via an HP response keypad, the "buttonbox". The HP-98731 Turbo-SRX computer graphics workstation consisted of a 19-inch color Trinitron monitor (1280 x 1024 pixels) for presenting visual stimuli and a computer for generating the stimuli, recording the responses, and analyzing the data. Connected to the workstation was a terminal to allow the experimenter to run the experimental programs and monitor the progress of each experimental session, and a button-box to allow the subject to respond to the visual stimulus presentations.

An optical table configuration consisted of a 4-foot x 6-foot optical table, with the workstation monitor mounted at one wide end of the table, and eight front-surfaced mirrors mounted on the table to direct the visual image--the optical train--to a pair of viewing binoculars mounted on the other wide end of the table (Figure 4-84). The mirrors allowed the independent presentation of two channels, one to each ocular of the binoculars, from the same monitor. Through the binoculars, the image on the top half of the monitor was seen by the left eye and the image on the bottom half of the monitor was seen by the right eye.

The 7x50 binoculars were mounted within a fixture that allowed the inter-pupillary distance (IPD) to be adjusted for each subject. Affixed on the front of the binoculars were auxiliary focusing lenses to focus the magnified image for the optical train viewing distance. A light baffle in front of the monitor between the two optical paths was positioned to prevent cross talk between the two image channels. The two mirrors, L.4 and R.4 in Figure 4-84, mounted directly in front of the binoculars, were movable to allow adjustments corresponding to the IPD settings of the binoculars.

The images seen through each ocular of the binoculars were 50 degrees of visual angle corresponding to 1280 pixels. The spatial resolution of the display was 25.6 pixels per degree of visual angle as seen through the binoculars. The temporal resolution, or frame rate of the monitor, was 60 Hz non-interlaced. The luminance resolution was 256 driving levels. The driving level to luminance conversions are given below. The 7x50 binoculars have a vertex distance of 27 mm and an exit pupil diameter of 7.14 mm. The subject, within reach of the buttonbox, was seated at a chin rest in the light-proof subject booth in front of the binoculars. Except for the stimuli viewed through the binoculars, the subject was in darkness.

Stimuli. The stimuli consisted of a series of computer generated displays, where each display contained one of three FOV configurations. Each FOV contained a 3 by 3 array of blurred and flickering alphanumeric symbols, eight of which were random letters and one a random numerical digit, which was the target. Also, described below, each FOV contained 6 small crosses for fusion locks and 30 random ellipses for background clutter. Stimulus details are given below and examples are shown in Figures 4-85 to 4-87.

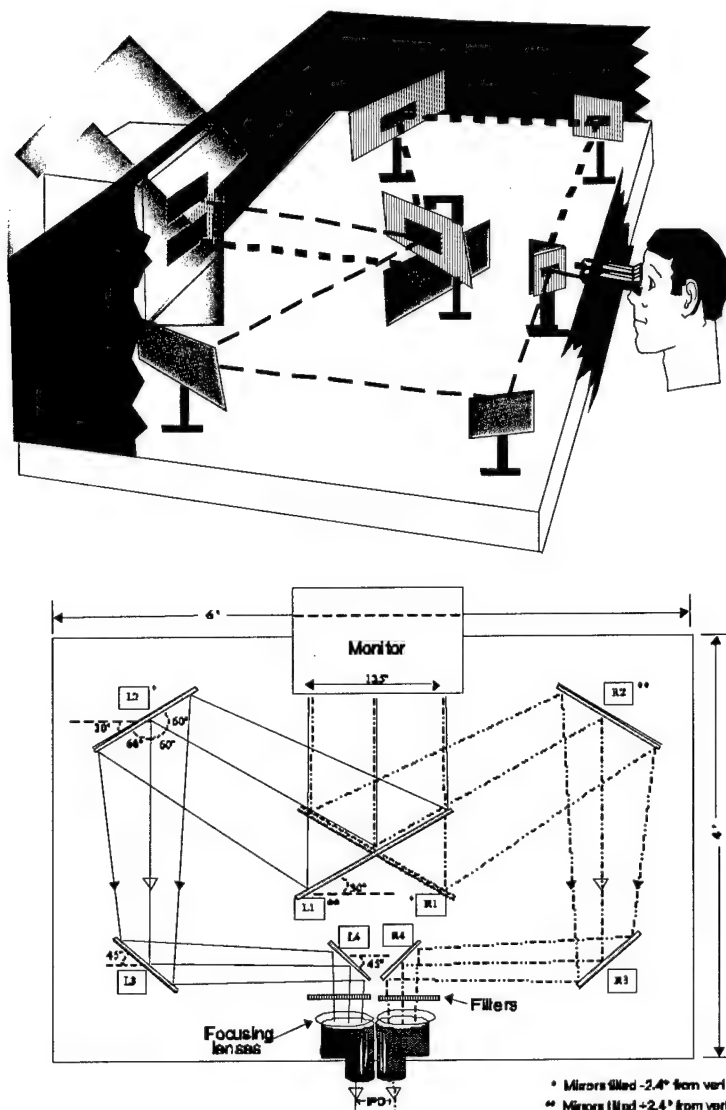


Figure 4-84. Perspective and schematic illustrations of the optical table configuration consisting of the monitor, eight mirrors, focusing lenses, and binoculars. Top image of monitor is directed to left eye, and bottom image is directed to right eye.

Stimulus luminance values, in terms of computer driving levels, ranged from 0 (black, 0.01 fL) to 255 (white, 31.67 fL), with intermediate values of 64 (dark grey, 1.33 fL), 128 (neutral grey, 6.65 fL) and 192 driving levels, (light grey, 16.81 fL). Half of the ellipses were light grey and half were dark grey, and the FOV background was neutral grey. The area outside the FOV was black, as were the fusion locks and the alphanumeric symbols (before blurring). Before display, the symbols were blurred. Blurring causes the luminance of a symbol's pixels (and neighboring pixels) to vary in a complex way with different pixels taking on different values. The values were between the symbol's original pre-blurred value (black) and the values of the symbol's local surround, which could be light, dark and/or neutral grey. The displayed driving levels were computed from the pre-blurred driving levels, and then the blurred symbol was temporally modulated for display as described below.

FOV. The total FOV was a rectangular area, 32.8 degrees of visual angle horizontal (840 pixels) by 10 degrees of visual angle vertical (256 pixels) (Figure 4-85). Subjects saw parts of the total FOV by the monocular fields presented to each eye. The monocular fields were each 23.4 horizontal degrees of visual angle, 600 pixels, by the full vertical extent. The FOV display configurations differed in the portions of the total FOV presented to the monocular fields of each eye. In the FO FOV configuration, each eye's monocular field displayed the same central portion of the total FOV, so that the FOV seen by the subject was binocular. In the DPO configuration, the right eye's monocular region was the rightmost 9.4 degrees of the potential FOV, and the left eye's monocular region was the leftmost 9.4 degrees of the potential FOV. Conversely, in the CPO configuration the right eye's monocular region was the leftmost 9.4 degrees of the total FOV, and the left eye's monocular region was the rightmost 9.4 degrees of the FOV (Figure 4-86).

In both PO conditions, the FOV seen by the subject was the full 32.8 degrees of the total FOV. This FOV consisted of a 14.1 degree central binocular region, and two flanking 9.4 degree monocular regions, with each eye seeing the monocular regions as described. In the FO condition, the FOV seen by the subject was the central 23.4 degree portion of the total FOV. In the FO condition, the binocular region was larger than in the PO conditions, while in the PO conditions an enlarged FOV is seen with a smaller binocular region.

These FOVs were presented by displaying each eye's monocular field separately on the top and bottom halves of the monitor (Figure 4-87). Imagery was directed to each eye's view through the binoculars via the optical table configuration (Figure 4-84).

Optical convergence, accommodation and fusion locks. Optical convergence and accommodation were both set for 2 meters. Optical convergence here refers to the angle between the optical axes of the eyes and should not be confused with the CO FOV configuration. Since the centers of both the right eye and the left eye images were focused to 2 meters (-0.50 diopter) through the binoculars, the right and left images also were positioned so that the eyes converged to 2 meters. This was done by shifting each eye's image on the monitor 0.86 degree of visual angle (22 pixels) in the nasal direction.

Subjects require similar stimuli common to both eyes to prevent disjunctive eye movements in order to binocularly fuse images properly and to avoid image slippage, which leads to the binocular overlap of inappropriate regions of the two monocular images. To ensure binocular locking of the appropriate areas of the monocular fields, and to provide a way to monitor binocular fusion, fusion locks were present in each display. These were six crosses, three in the upper center of the total FOV and three in the lower center. Subjects were told that they should see three crosses above and below the center of each display. If they saw more, then the images were not properly fused, and they should tell the experimenter. This did not occur. With the background clutter described below, there were ample binocular stimuli to prevent slippage.

The bottom shows the location of the monocular field borders, which in the FOV become binocular borders, separating the three regions of the PO FOV. The right monocular field contains the center and right regions, and the left monocular field contains the center and left

regions. In a DPO FOV, the right monocular field is presented to the right eye and the left field to the left eye, whereas in the CPO FOV, this is reversed. In FO FOVs, a smaller portion of the total FOV is seen as shown in Figure 4-86.

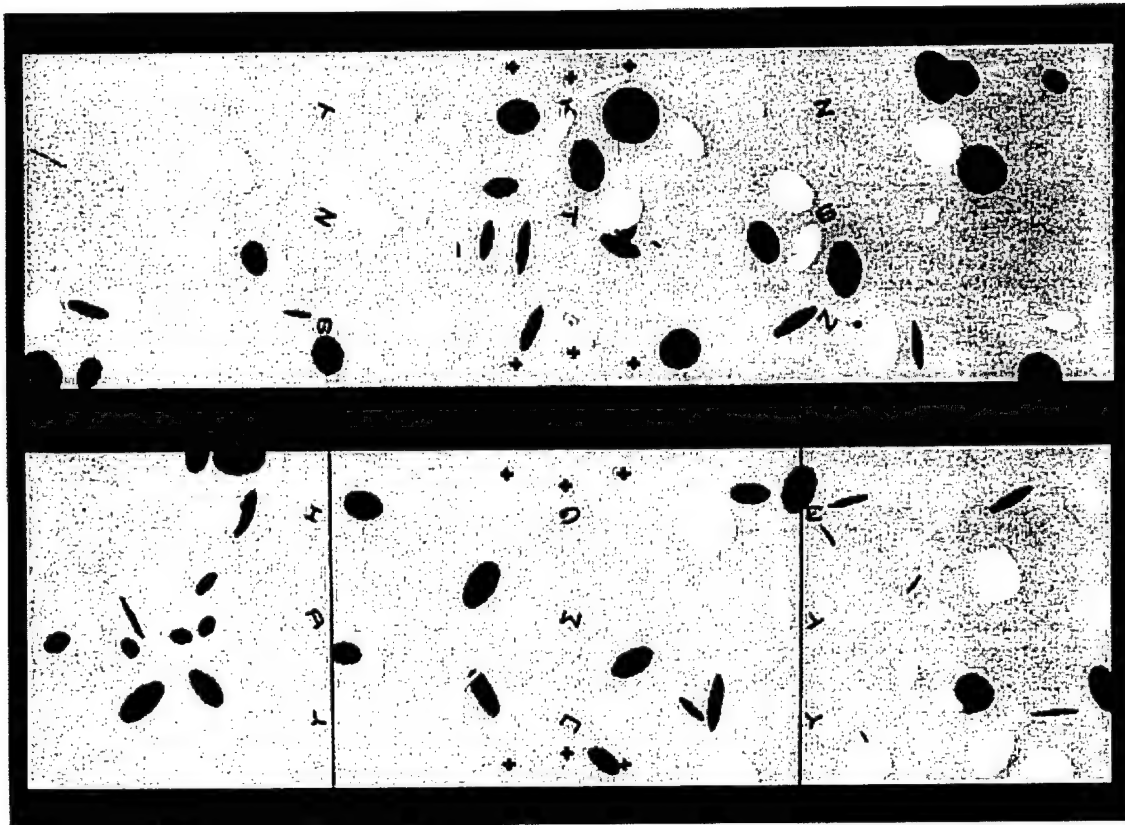


Figure 4-85. Examples of the total FOV with targets and clutter. The top shows the total FOV with nine alphanumeric symbols, six fusion locks (crosses), and random clutter (ellipses). Target is the "6" in the left bottom position. The horizontal extent is 32.8 degrees of visual angle, and the vertical extent is 10 degrees of visual angle. In the PO FOV configurations, this is presented to the subject via two monocular fields, each 23.4 degrees of visual angle in horizontal extent.

Each shaft of the crosses was 8 pixels long by 2 pixels wide. Center crosses were 25 pixels from the top and bottom of the FOV and flanking crosses were located 44 pixels to the right and left of the center and 16 pixels from the top and bottom of the FOV.

Background clutter. For clutter, each display contained 30 ellipses, randomly oriented, randomly sized, and randomly positioned. The center of each ellipse could, with equal probability, be located on any pixel within the total FOV. The orientation of each ellipse could, with equal probability, be anywhere from 0 to 180 degrees. Ellipse size was randomized by sizing each of the two axes of each ellipse with equal probability anywhere from 1 to 44 pixels in length. Of course, only the portion of each ellipse falling in the monocular fields were displayed in the FOV. Ellipses were alternatively light and dark grey, with later ellipses drawn over former ellipses and the alphanumeric symbols drawn last.

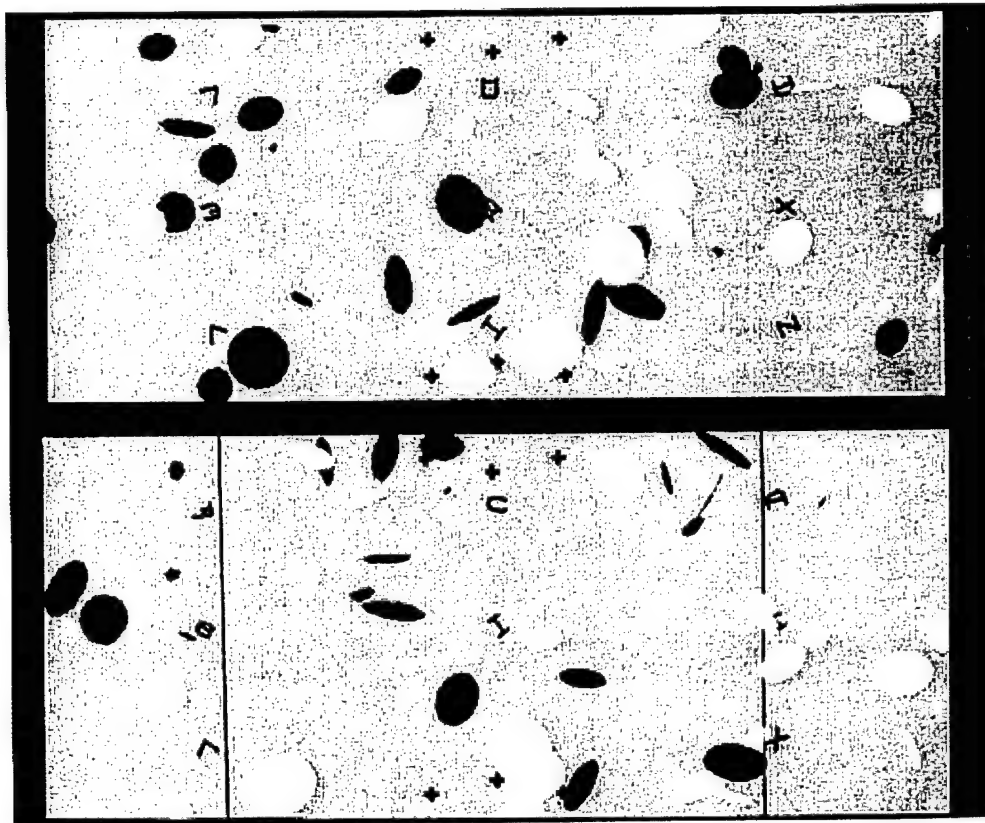


Figure 4-86. Examples of reduced FOV seen in FO FOVs. The top shows the FO FOV, where both monocular fields present the same center region (23.4 degrees of visual angle in the horizontal extent) to each eye. The bottom shows how much the binocular portion of the FOV is shrunk in the PO FOVs. Figure 4-85 shows how the FOV is enlarged by PO.

Alphanumeric symbols. In each display, one of nine alphanumeric symbols was the target number and the remaining eight were nontarget letters. Alphanumeric symbols were all in "stick figure" font, or font number 1, predefined in the Hewlett-Packard Starbase computer graphics language. Letters were all capitals, and all alphanumeric symbols were defined within a 16 by 16 pixel symbol square (1.6 by 1.6 degrees of visual angle). Alphanumerics were initially 0 driving levels, the background of the FOV was 128, and the light and dark ellipses were 192 and 64 driving levels, respectively. Before display, each symbol was preprocessed by rotating and blurring. The orientation of each symbol was randomized by rotating the symbol randomly from 0 to 360 degrees.

Spatial blurring of the symbol was implemented as follows. The original 16 by symbol square consisted of symbol pixels and non-symbol pixels. The symbol pixels and adjacent non-symbol pixels were defined as the blur zone. This blur zone included any symbol pixel, that is a pixel that contained part of the alphanumeric symbol, and any non-symbol pixel that was adjacent to a symbol pixel, adjacency defined as the eight contact pixels. The pixels in the blur zone were then filtered by a 3 by 3 Gaussian kernel. This means, that for each blur zone pixel, the old driving level was replaced by a new driving level, which was the weighed average of the

old value and the driving levels of the eight pixels around it. The kernel weights were as follows where the central 12 represents the weight of the old driving level:

$$\begin{array}{ccc} 1 & 4 & 1 \\ 4 & 12 & 4 \\ 1 & 4 & 1 \end{array}$$

Therefore, symbols were blurred into the background, which included the FOV background and any ellipse adjacent to the symbol. The new blurred symbol thus contained more pixels with smoother transitions between symbol and background.

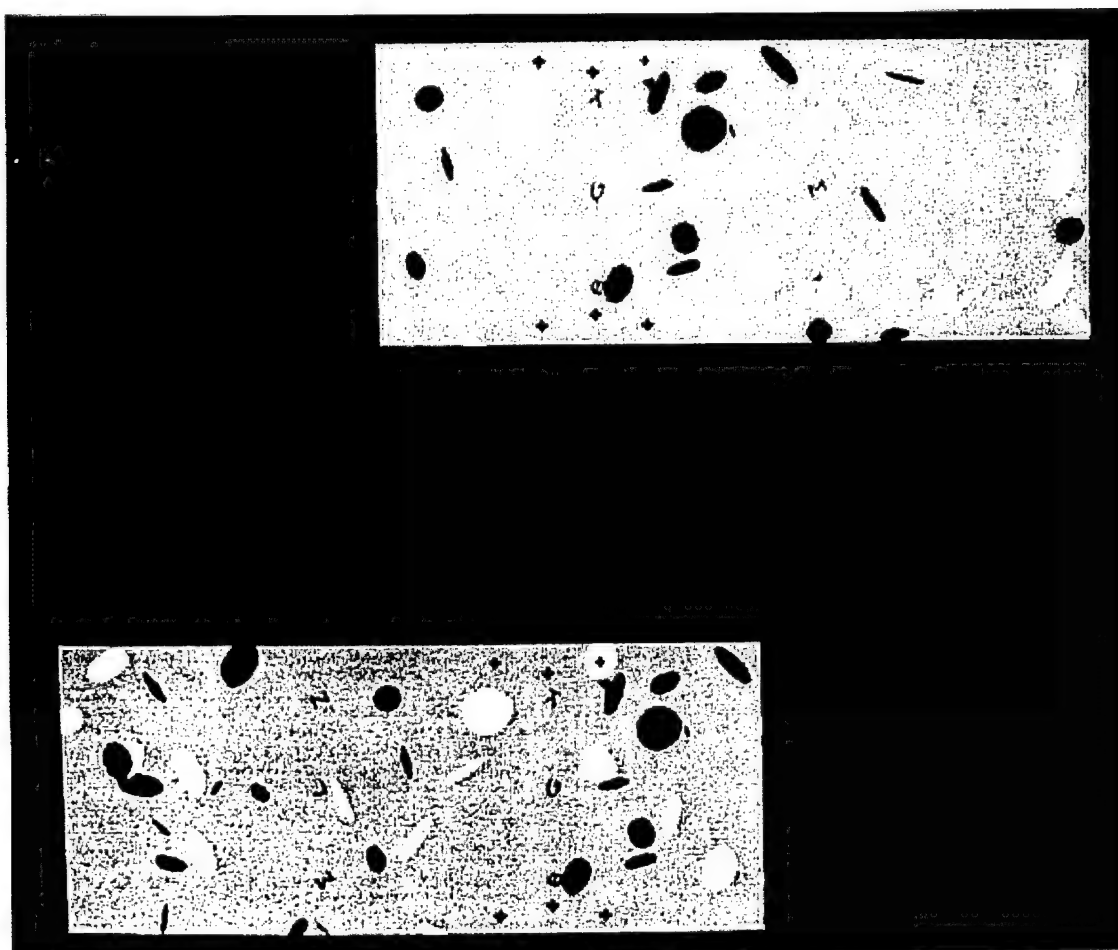


Figure 4-87. The two monocular fields on the monitor are each optically directed to an ocular of the binoculars for viewing by the subject.

Temporal modulation was implemented by passing the blurred symbol through a series of lookup table functions, one function for each frame of the temporal sequence. In the lookup table function, each original input driving level in the blurred symbol was changed to an output displayed driving level. Cycling through the set of functions caused the original stimulus's luminance to change smoothly from identity at one extreme, where the original blurred symbol

was displayed, to invisibility at the other extreme, where all the pixels were equal to the background of the FOV (128). This was done by the following lookup table equation:

$$y = x * \tan(\text{angle}) - (128 * \tan(\text{angle})) + 128,$$

where x = input pixel driving level; y = output pixel driving level; and angle = 0 to 45 degrees in steps of 2.5 degrees.

Angle represents the slope of the input-output lookup table function which was changed for each frame of the temporal modulation sequence. At one extreme, the angle equaled 45 degrees, causing all displayed driving levels (y) to equal all original input driving levels (x), that is, the original blurred image was displayed. At the other extreme, where the angle equaled 0 degrees, all output driving levels (y) equaled 128, where the entire blurred symbol was the same driving level as the background of the FOV and therefore invisible with respect to it. Between 0 and 45 degrees, each of the symbol's driving levels was intermediate between 128 and the original value.

Eighteen frames were created by incrementing the angle from 0 to 45 degrees in steps of 2.5 degrees. The frames were displayed in the sequence 1 - 19, 18 - 2 for a full modulation cycle of 36 frames, with cycles repeating until the subject responded correctly. Frames were presented at the rate of 30 per second, with a frame duration of 33.3 msec. With 36 frames in a full modulation cycle, the flicker rate was 0.83 cycles per second, or 1.2 seconds per cycle. The flicker cycle smoothly varied the symbol contrast between maximum visibility, the original blurred symbol, and invisibility (i.e., invisible with respect to the background of the FOV). All symbols slowly faded into and emerged from the background by appearing and disappearing. When the angle was 0, a symbol may have still been visible if it was on or near an ellipse, because the symbol's driving level of 128 was distinguishable from the ellipse driving level of 64 or 192. All nine flickering symbols were in phase. Stimulus onset started at invisible/

The nine symbol positions were in three columns and three rows. Defined from the center of the symbol, one column was 2 pixels to the right of the FOV center. The left column was 195 pixels to the left, 7.5 degrees of visual angle to the left of center. The right column was 189 pixels to the right of center, 7.4 degrees of visual angle to the right of center. When in the PO FOVs, the left column was two pixels away from the edge of the monocular field border, and the right column was adjacent to the monocular field border. This is in terms of the 22 x 22 pixel square of the potential occupied region of each letter after blurring and rotation (Figures 4-85 to 4-87). One row was centered in the middle of the FOV, and the other two were 80 pixels, or 3.1 degrees, above and below the middle row (center to center). Column positions are referred to as Right (R), Center (C), and Left (L); and row positions are referred to as top (t), middle (m), and bottom (b), generating the nine designations: Rt, Rm, Rb, Ct, Cm, Cb, Lt, Lm, and Lb. For the DPO and CPO FOVs, the right and left columns of symbols outside the overlap border were monocular stimuli, as opposed to the center column of symbols which were binocular. Under the FO FOV configuration all the symbols were binocular.

Design. Each trial consisted of a unique display to which the subject responded. In the experiment, there were 216 trials presented in 6 blocks, where each block contained 3 FOV configurations, FO, DPO, and CPO, presented in random order. For each FOV configuration, there were 12 trials. Unknown to the subject, the first 3 of these 12 were considered practice to allow the subject to acclimate to the FOV, and the data were not recorded. From the subject's point of view, which of the nine positions the target occupied, and which number symbol was used for the target, was random on each trial. In fact, the position of the target was random with replacement for the first three trials in each FOV, and random without replacement for the final nine trials for which the data were recorded. Across displays, the number that was the target was randomized with replacement from the following seven numbers: 2, 3, 4, 5, 6, 8, and 9. Within displays, and across displays, each of the eight nontarget letters was randomized with replacement from a set of 23 letters (alphabet minus the letters O, Q and L). The experiment was a 6 (block) x 3 (FOV configuration) x 9 (position) design.

Procedure. The subject's interpupillary distance was measured and the equipment adjusted accordingly. The mean interpupillary distance for the 15 subjects was 61.3 (SD = 1.8). Subjects were given instructions and assurances of anonymity, and signed the consent form. Then subjects adjusted the chin rest, keypad, and height of the seat for comfortable viewing of the display through the binoculars.

To ensure there was no visual clipping of the FOV, or vignetting, for the area which would contain the experimental stimuli, a binocular display containing three widely spaced circles was shown. It contained the same optical convergence as the stimulus displays. The three circles were superimposed over a purple background with a white grid. There was a black circle in the center of the display, a blue circle to the right of center, and a yellow circle to the left of center. The black circle was 24 pixels in diameter and the outer two circles were 34 pixels in diameter. The outer edges of the outer circles were 668 pixels (26.1 degrees) distance from each other. The subjects were asked if they could see, without moving their head position, the entire yellow circle, the entire blue circle, and the grid surrounding each circle clearly and without vignetting when they visually scanned across the display.

In the experiment, subjects viewed a series of stimulus displays, each with nine alphanumeric symbols in nine standard positions. One symbol was always a number, and the remaining eight were always letters. The subjects were told the following: There would be nine symbols in each display, one of which was the target number. The symbols would be blurred, randomly oriented and flickered. Their task for each display was to identify the position of the number as quickly as possible by hitting the appropriate key on the keypad, and to avoid misses; that is, avoid hitting non-targets. The nine keys in the keypad were configured in a 3 by 3 array corresponding to the nine potential positions of the target. To induce the need for rapid response, as well as the need to maintain accuracy, subjects were told to imagine that the target number symbol was the enemy which would shoot them if they did not shoot it first, and the non-target letter symbols were friendlies. The computer calculated the percentage of targets, including the practice trials, over each block that were acquired on the first try without misses. At the end of every block, this percentage appeared on the screen to motivate the subject to maintain accuracy and avoid random guessing.

To accomplish the task, the subject needed to scan the entire display, compensating for the symbol rotations and blurring, and catching the symbols when they were visible and quickly deciding which symbol in the display was the number. The subjects were told to respond as quickly as possible while maintaining accuracy. For every change of FOV, the letters "OK" appeared in the center of the first display of the new FOV without the targets. Subjects were told that for these displays they could pause if they wanted, and then initiate the next series by hitting a start key.

Once the series of displays started, for each display, the image would remain on until the target was hit. If an error was made, a transient asterisk appeared in the location of the letter to indicate that it was not the target. When the key was released, the letter returned. When the target number was identified by hitting the correct key, the screen went blank and 2.5 seconds later a new FOV appeared.

To familiarize themselves with the task and targets, the subjects first ran one block with a practice program, where each of the three FOVs contained six displays, with random target position without replacement, and no clutter ellipses in the FOV. Then they practiced with the same program with the clutter ellipses for from one to three FOVs, as determined by when they felt comfortable with the task. Then four minutes later, they ran the experiment.

Data analysis. The data were analyzed in a three-way repeated measures analysis of variance (ANOVA) where the 162 treatments consisted of 6 Blocks times 3 FOV configurations times 9 Positions. Four types of data were collected. These included RT, the time to indicate the correct target; and logRT, which is the log of RT. The log of response time is typically used as a check in reaction time and response time data analysis to remove the undue influence of outliers. As a further check on the data, the number of misses before acquiring the correct target was recorded for each trial. The percent of first scores, that is the percent of no-miss target acquisitions, was also recorded. The number of misses meant the number of wrongly acquired targets on each trial; which, as there were nine symbols, could be a maximum of eight for each trial, and a minimum of zero if the first target acquired was the correct one. The percent of first scores was calculated as follows: A condition was scored as one for each trial in which the target was hit on the first guess, and zero if the first guess was incorrect, that is a miss. The RT (and logRT) measures performance speed, and the number of misses and the percent of first scores measure performance accuracy.

Results and Discussion

For RTs, the three-way Blocks x FOV x Position interaction was not significant, $F(80,1120) = 1.02$, $p = .43$. The two-way Block x FOV interaction was not significant, $F(10,140) = 0.32$, $p = .97$ (as shown by the rough parallelism between FOV configurations in Figure 4-88), and the two-way Block x Position interaction was not significant, $F(40,560) = 1.38$, $p = .06$. The two-way FOV x Position interaction was significant, $F(16,224) = 4.11$, $p = .000001$ (indicated by the overlapping FOV lines in Figure 4-89). The focus of this study, the effect of FOV on RT, is examined below for each position.

For RTs, there was no interaction between the Blocks factor and either, or both, of the other two factors. The main effect of Blocks on RT was significant, $F(5,70) = 6.55$, $p = .000047$. There is a general decline in RT over blocks which can be seen in Figure 4-88, where each of the three FOV configurations are plotted separately. This general improvement in performance continues through the sixth block for the FO FOV and through the fifth block for the CPO and DPO FOVs.

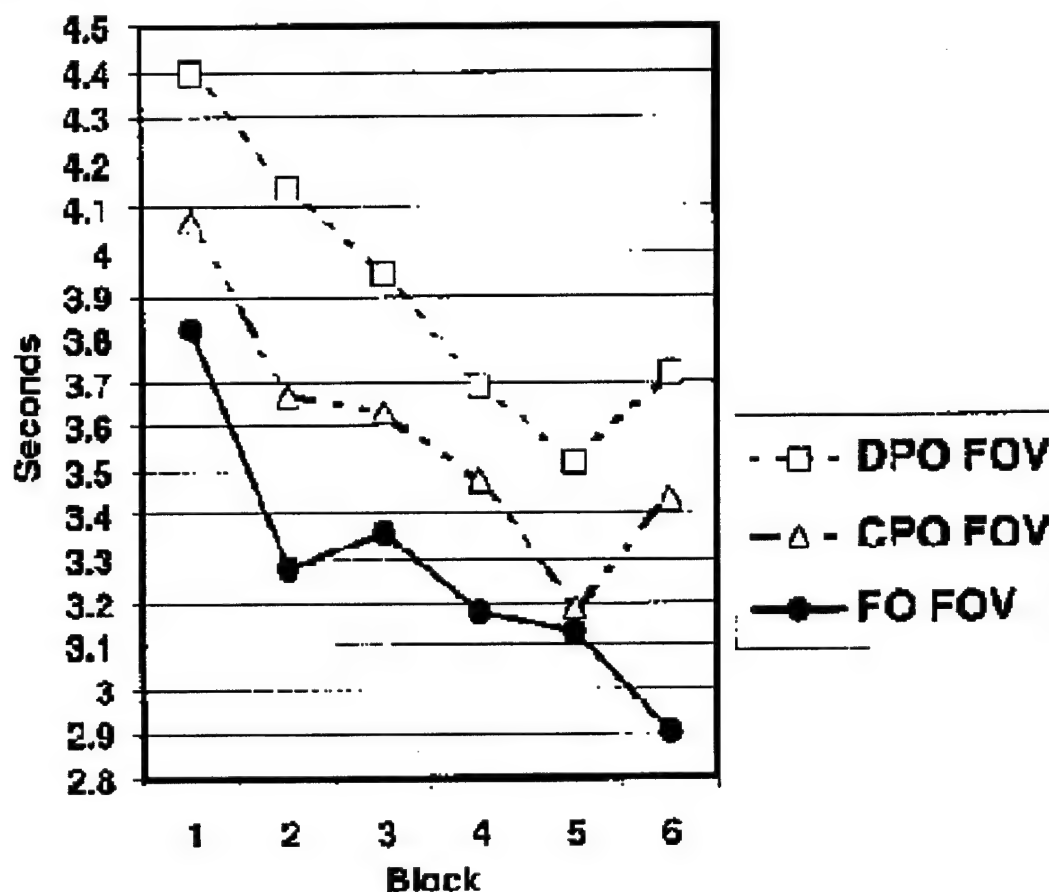


Figure 4-88. Mean response time to acquire target (FOV x Block).

The significant FOV x position two-way interaction on RT can be seen in Figure 4-89, where each of the three FOVs, again plotted separately, are not parallel. There was also a significant main effect of FOV on RT, $F(2,28) = 12.48$, $p = .000133$, as well as a significant main effect of position on RT, $F(8,112) = 8.97$, $p < .000001$. The position main effect per se is not of special interest here as there are many possible confounding factors that can affect RTs to position, such as the preferred scan patterns of observers, or the time to respond with a particular keystroke position. It was not unexpected that the RTs to centrally located and binocular positions would be faster than RTs to lateral and/or monocular targets. Observers in this study were free to use any scan pattern and were not instructed on how to search. While not the focus of our study, it is interesting to note that the bottom positions in each of the three columns of targets have the longest RTs for their respective columns. This would seem to indicate that observers tended to search the top half of the FOV first, although we can not rule out confounding effects of keypad position and so on.

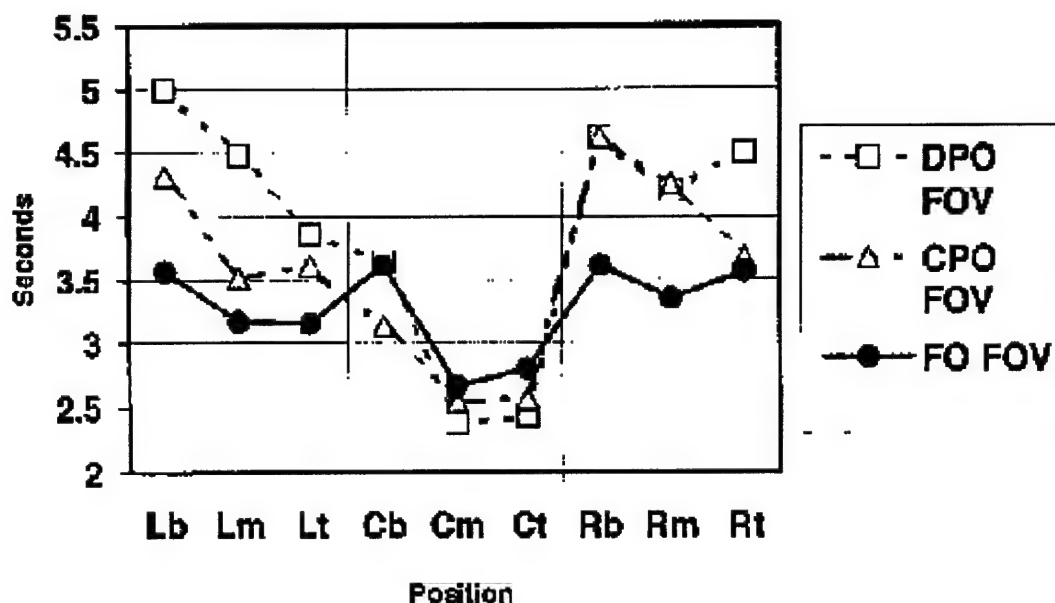


Figure 4-89. Mean response time to acquire target (FOV x Position).

The focus of this study was the effect of FOV configuration on performance. A series of planned comparisons examined the effect of FOV configuration on RT for each of the nine positions. Of these positions, the three center positions, Cb, Cm, and Ct, are binocular under all three FOV configurations, and the lateral positions, Lb, Lm, Lt, Rb, Rm, and Rt, are monocular in the two PO FOVs and binocular in the FO FOV. For each position, our planned comparisons consisted of first, comparing the RTs of the two PO FOVs, the CPO and the DPO, with the RTs of the FO FOV; and second, comparing the RTs of the DPO FOV with the RTs of the CPO FOV.

The mean RTs in seconds (collapsed over blocks) are shown in Table 4-22, where rows represent the FOVs and columns represent the positions. These are plotted in Figure 4-89. The means represent the time to respond to the target when the target was in each of the nine positions. The next row gives the results of the planned comparisons testing for a difference between the two PO FOVs and the FO FOV, and the row below it gives the significance level. With $p < .05$ as our criterion for significance, the results show that there were no significant differences for the three centrally located positions where the targets were binocular in all three FOV configurations. The partial overlapping of the FOV caused a significant increase in RT to locate the target for all the lateral positions where the target was monocular. The target was monocular in the two PO FOVs and binocular in the FO FOV.

How much the CPO and DPO FOVs increased the RT over the FO FOV in percentage terms is shown in Table 4-23. Partially overlapping the FOV caused the RT to lateral targets to increase an average of from 3 to 42 percent. For all positions, the DPO FOV increased RTs an average of 18 percent, and the CPO FOV increased it an average of 9 percent, but for lateral targets in particular, the average increase was 31 and 18 percent, respectively.

Table 4-22.

Mean response times in seconds, collapsed over blocks, and planned comparisons.

Position	Left			Center			Right		
	bottom	middle	top	bottom	middle	top	bottom	middle	top
DPO FOV	4.99	4.49	3.87	3.66	2.38	2.44	4.61	4.21	4.50
CPO FOV	4.32	3.52	3.61	3.14	2.55	2.57	4.61	4.25	3.68
FO FOV	3.56	3.17	3.16	3.62	2.67	2.80	3.62	3.35	3.56
CPO, DPO FOVs vs FO FOV. F (1,14) =	26.15	363.5	19.34	1.80	0.90	2.17	18.73	18.21	6.31
P=	.0002 **	.0000 **	.0006 **	.201	.359	.162	.0007 **	.0008 **	.025 *
DPO FOV vs CP FOV, F (1,14) =	3.39	7.48	0.71	3.46	0.55	0.24	0.00006	0.01	5.11
P=	.086	.016	.414	.084	.469	.630	.994	.923	.040 *

Note: * = $p < .05$, ** = $p < .01$, Data graphed in Figure 4-89.**Table 4-23.**

Mean percentage increase in response time, collapsed over blocks.

Position	Left			Center			Right			Row Mean
	bottom	middle	top	bottom	middle	top	bottom	middle	top	
DPO / FOV	40	42	23	0.9	-11	-13	28	25	26	18
CPO / FO	21	11	15	-13	-4	-8	28	27	3	9
CPO / DPO	16	27	7	16	-7	-5	-0.7	-1	22	8

The next to the last row in Table 4-22 gives the results of the planned comparisons testing for a difference between the CPO FOV and the DPO FOV, and the last row gives the significance levels. With $p < .05$ as our criterion for significance, the results show that there were two significant differences, the Lm and the Rt positions, both lateral positions. The Lb and Cb positions approached significance. In half of the lateral positions, the RT to a target in a DPO FOV was significantly, or close to significantly, longer than to a target in the CPO FOV. The Cb RT were close to significantly longer. How much the DPO FOV increased RT over the CPO FOVs in terms of percentage is shown in the last row of Table 4-23. Overall, for these lateral positions, the DPO FOV increased RTs an average of 11 percent over the CPO FOV.

As a check on the RT data, the log of each RT was used as the input data for statistical analysis. This was to remove the potentially distorting effect that outliers can have on the means in RT data. The following results of the analysis of the logRTs were essentially the same as the analysis of the RTs, with minor differences in significance. Again, the three-way Blocks x FOV x Position interaction was not significant, $F(80,1120) = 1.10$, $p = .27$. Again, the two-way Block x FOV interaction was not significant, $F(10,140) = 0.66$, $p = .76$, but this time, the two-way Block x Position interaction marginally reached significance, $F(40,560) = 1.42$, $p = .05$. The two-way FOV x Position interaction was highly significant, $F(16,224) = 5.19$, $p < .000001$.

The three main effects were each highly significant: Blocks, $F(5,70) = 7.49$, $p = .000012$; FOV, $F(2,28) = 14.69$, $p = .00043$; and Position, $F(8,112) = 13.80$, $p < .000001$.

Table 4-24 gives the mean logRTs to locate the target, where the rows and columns correspond to those of Table 4-22. Below the data rows are the results of the planned comparison testing for a difference between the two PO FOVs and the FO FOV, and below that the significance level. With $p < .05$ as our criterion for significance, the results for the logRTs again show that the partial overlapping of the FOV causes a highly significant increase for all of the lateral positions. In addition, this time, the Cm position marginally reached significance in the reverse direction. The next to the last row gives the results of the planned comparisons testing for a difference between the CPO FOV and the DPO FOV, and the last row gives the significance levels. With $p < .05$ as our criterion for significance, the results again show that identifying the target was significantly longer in the DPO than in the CPO for the Rt and Lm positions. Additionally, the Lb and the Cb positions also reached significance. In half of the lateral positions, the mean logRTs to a target in a DPO FOV was significantly longer than to a target in the CPO FOV. The overall results of the analyses examining the logRTs were essentially similar to the results for the raw RTs, with minor differences in significance levels.

Figure 4-90 graphs the mean number of misses before acquiring the target, collapsed over blocks, and Table 4-25 lists the means. The numbers are very low, ranging from 0.03 to 0.26, out of a possible range of 0 to 8, which indicates that subjects followed instructions and generally did not guess the target until they were reasonably sure. These data, when subjected to the same 3-way ANOVA as the RT data, show all nonsignificant effects except for a slightly significant main effect of FOV on number of misses, $F(2,28) = 3.62$, $p = .04$. The average was 0.13 for the DPOs, 0.13 for the CPOs and 0.09 for the FOs. This supports the RT data in that there were a higher number of misses for the PO FOVs, which had longer RTs compared to the FO FOV. which had shorter RTs.

Table 4-24.

Mean log of response times (in seconds), collapsed over blocks, and planned comparisons.

Position	Left			Center			Right		
	bottom	middle	top	bottom	middle	top	bottom	middle	top
DPO FOV	0.666	0.600	0.532	0.505	0.277	0.304	0.620	0.570	0.570
CPO FOV	0.583	0.496	0.481	0.441	0.303	0.330	0.613	0.555	0.503
FO FOV	0.522	0.458	0.448	0.498	0.348	0.358	0.533	0.482	0.494
CPO, DPO FOVs vs FO FOV . $F(1,14) =$	24.22	14.77	31.30	2.54	5.00	2.23	21.95	15.78	5.41
P=	.0002 **	.002 **	.00007 **	.133	.042 *	.157	.0004 **	.001 **	.035 *
DPO FOV vs CP FOV, $F(1,14) =$	7.87	10.47	2.21	6.15	0.53	0.50	0.11	0.26	10.05
P=	0.14 *	.006 **	.159	.027 *	.477	.489	.743	.621	.007 **

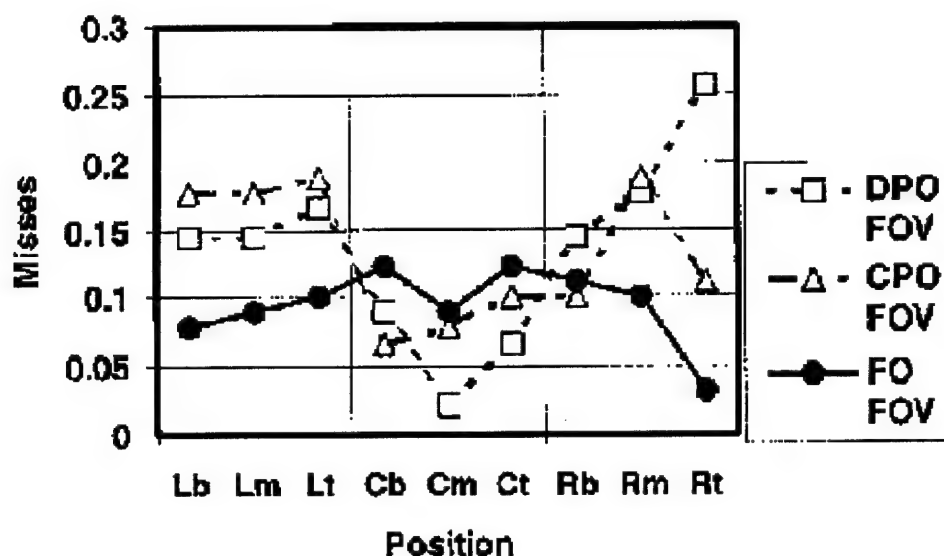


Figure 4-90. Mean number of misses before target acquisition (FOV x Position).

Table 4-25.

Mean number of misses (out of a maximum of 5), collapsed over blocks.

Position	Left			Center			Right			Row Mean
	bottom	middle	top	bottom	middle	top	bottom	middle	top	
DPO FOV	0.14	0.14	0.17	0.08	0.02	0.07	0.14	0.18	0.26	0.13
CPO FOV	0.18	0.18	0.19	0.07	0.08	0.10	0.10	0.19	0.11	0.13
FO FOV	0.08	0.09	0.10	0.12	0.09	0.12	0.11	0.10	0.03	0.09

Figure 4-91 graphs the mean percent first scores, the percentage of times the target was acquired on the first guess; that is, the targets that were acquired without misses. Improving performance or increasing percentage increases down the ordinate to bring the graph into conformity with the other graphs. Table 4-26 lists the mean percent first scores (collapsed over blocks). These data when subjected to the same 3-way ANOVA as the RT data showed all non-significant effects except for a marginally significant main effect of FOV on percent first scores, $F(2,28) = 3.35$, $p = .05$. The average was 88.3 for the DPOs, 89.1 percent for the CPOs, and 91.4 percent for the FOs. There were lower percent first scores for conditions that had longer RTs and for conditions that had a higher number of misses.

Table 4-26.

Mean percent of first scores, collapsed over blocks.

Position	Left			Center			Right			Row Mean
	bottom	middle	top	bottom	middle	top	bottom	middle	top	
DPO FOV	87	87	86	91	98	93	88	86	79	88
CPO FOV	84	87	84	94	93	96	90	84	90	89
FO FOV	92	92	92	88	91	90	91	90	97	91

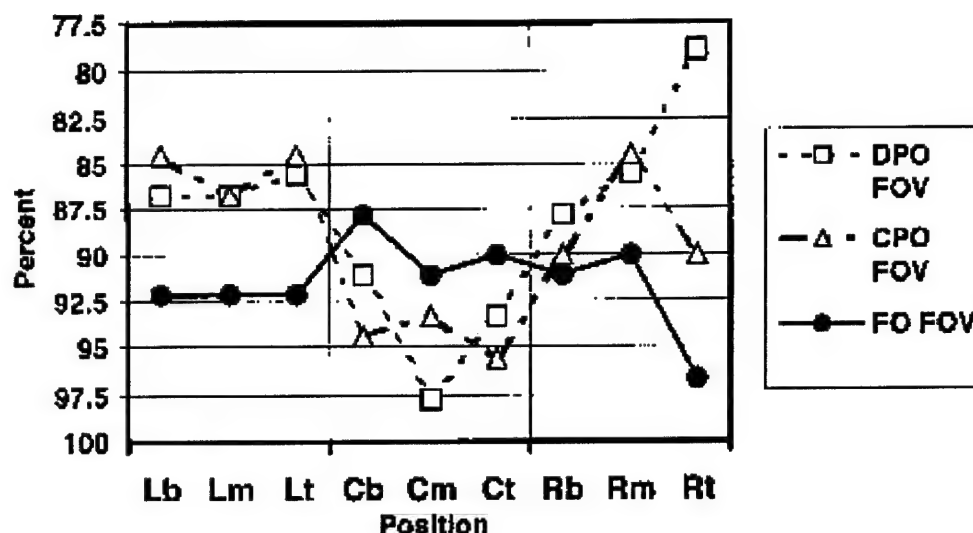


Figure 4-91. Mean percent of first scores (FOV x Position).

The mean number of misses are relatively small compared to a possible maximum of eight, with four the chance response; and the mean percent first scores are within three percentage points of each other, which indicates there is unlikely to be any speed accuracy tradeoff in these data. A speed accuracy tradeoff would be suspected if the conditions with the faster RTs had lower accuracies, and the conditions with the slower RTs had higher accuracies. If there had been large differences in the number of misses, and large percent first score differences in the opposite direction to the RT data (i.e., relative performance was better by one measure and poorer by another), then there would have been a concern with the interpretation of the data because of the need to determine the function of the speed accuracy tradeoff. However, the number of misses and percent first scores data are in the same direction as the RT data, and so, if anything confirm, rather than mitigate the conclusions one draws from the RT data concerning which are the easier or harder conditions in terms of overall performance. Compare the similar patterns of Figures 4-90 and 4-91 with Figure 4-89. It is interesting to note that, for the center positions, performance with the CPO and DPO FOVs is slightly better, though not significantly better, than in the FO FOV. It is possible that in the PO conditions, the center region tends to draw the observer's attention to the detriment of the lateral regions, while in the FO FOV, the subject tends to more evenly spread attention over the entire FOV. Though this cannot be determined from these data, the slight performance improvements for the POs over the FO to targets in the central region of the FOV may be due in large part to the smaller relative area of the binocular portion of the FOV where subjects tend to focus attention.

In summary, on average, performance was best in the FO FOV, where RTs were fastest, and worst in the DPO FOV, where RTs were slowest. These performance differences tended to be confirmed by the number of misses and the percent first score data. The differences between FOV configurations tended to be most pronounced for lateral targets, which were in monocular regions in the PO FOVs.

Conclusion

Moffitt (1989) suggested that the contours that occur in an FOV displaying a natural scene should eliminate the luning, and presumably, the other detrimental effects such as reduced visibility of targets that occur in partial binocular overlap displays. One might assume that the added contours would bias the binocular rivalry to the monocular image that contains the contours, the real world scene and the targets, as opposed to the opposing image which only contains a black background and one contour, the binocular border. Our displays were highly cluttered with background contours from the randomly placed ellipses, and yet, the RT results reflect the results found in the previous luning, fragmentation, and target visibility studies: Performance is highly significantly affected by PO FOVs, more so in the DPO FOV than in the CPO FOV. This was true even though our targets were well above threshold for most of their flicker cycle. Also, any stimulus that moves or flickers is known to bias binocular rivalry to the benefit of the moving or flickering target (Arditi, 1986; Fox, 1991; Fox and Check, 1968, 1972), but the added clutter contours and flickering suprathreshold targets did not remove the detrimental effects on performance of partially overlapping the FOV.

There is a tradeoff in enlarging the FOV by the partial overlap method. The FOV is larger, but as this study shows, PO can have significant human performance consequences. In our experiment, average time to find a target increased by as much as 31 percent for divergent and 18 percent for convergent FOVs. This preliminary study found that performance decrements due to FOV configurations parallel the previously found psychophysical decrements. The relative contributions of different factors to the performance decrements with PO configurations and possible ways to alleviate it need to be further investigated.

VISUAL SEARCH IN HMDS WITH PARTIAL OVERLAPPED BINOCULAR FOV

In the first study (above), we found that visual performance, as measured by response time to target acquisition, and accuracy of target acquisition is, in general, poorer in the monocular regions of partial overlap FOVs, more so in the divergent than the convergent partial overlap FOV. In that study, target positions were constant. The current study, incorporating a number of methodological changes, is an investigation of visual search performance where target locations are variable and the observer must scan the display to find the target. The study was designed to gain more understanding of the real world impact of FOV designs on general visual performance by using a visual search task under the psychological constraints experienced in aviation. These include time pressure, uncertainty of the specific target and of its location, and a randomly cluttered background. Observers needed to visually scan the FOV to search for the target. Aviation is an attention-demanding (high mental workload) environment with a high rate of visual information throughput where visual inspection time is often limited and the eyes need to continually scan an FOV. This is a stimulus environment that often taxes the visual performance of the human perceiver. Under operational conditions, human performance may be compromised by the partial overlap FOV design. The performance decrements with these HMDS may become critical in attention demanding environments such as military aviation. This study assesses the effects of these FOV configurations on visual performance under demanding viewing conditions.

Visual search experiment

In this exploratory study, the task was to search through a group of randomly located alphanumeric symbols and identify the target (one of five possible numbers) from among similar distractors (letters) in each trial display as quickly as possible. Response time and accuracy were the measures of visual performance. The target could be any one of several numbers, and the distractors could each be any one of several letters. The task was to identify which number was present in each display. To make the task more difficult, the target number and distractor letters (collectively, the alphanumeric symbols), were randomly oriented, and unlike the previous study (Klymenko et al., 1999), their locations were randomized, rather than being in an array of fixed positions. Also, on half the trials, the alphanumerics were spatially blurred to test the effect of this factor. Each display contained random clutter in the form of randomly located ellipses of random size and orientation. Automated feedback was given to motivate subjects to perform at maximum capacity. Also, we used smooth temporal onsets for the symbols, as abrupt onsets make stimuli strong dichoptic competitors (Kaufman, 1963; 1964) and therefore could mask relevant differences among conditions.

We had four general hypotheses: One, the FOV factor would effect target acquisition, with subjects exhibiting better performance in full overlap than in partial overlap FOVs and better performance in convergent partial overlap than divergent partial overlap FOVs. Two, performance would depend on the target position in the FOV. It was expected that performance would be worst in the monocular regions of partial overlap FOVs. Because of the change from the previous study, we eliminated response bias as a factor, therefore performance at different positions is now directly comparable. Three, we conjectured that blurred targets might cause poorer performance in monocular regions because blurring reduces a stimulus' strength in dichoptic competition (Kaufman, 1963, 1964). Four, we assumed performance would improve over time.

In this study, we looked at how the type of FOV, the position of a stimulus in the FOV and the spatial blurring of the stimulus affected visual performance, and how visual performance is maintained over time. The task was to visually search the FOV for a series of displays, and in each display, identify the target as quickly as possible without making errors.

Methods

Subjects. Twenty-one student army aviators, 20 males and 1 female, voluntarily took part in the experiment. This population had passed Class II flight physical vision tests. All had 20/20 unaided or better Snellen acuity. The mean age was 26.5 (SD =2.8), ranging from 21 to 30. Two additional subjects were not included in these data because the testing was interrupted due to computer and equipment problems.

Equipment. The equipment used were essentially the same as the equipment used in the first study discussed above. The equipment consisted of three major components: a Hewlett-Packard HP-98731 Turbo-SRX computer graphics workstation used to generate the visual stimuli, a custom optical table configuration (see Figure 4-84) used to optically direct the visual stimuli from the workstation monitor to a pair of viewing binoculars, and a subject booth. The

booth was a lightproof enclosure behind the binoculars where the subject viewed the stimuli via the binoculars and responded via an HP response keypad, the "buttonbox". The HP-98731 Turbo-SRX computer graphics workstation consisted of a 19-inch color Trinitron monitor (1280 x 1024 pixels) for presenting visual stimuli and a computer for generating the stimuli and recording the responses.

Stimuli. The stimuli consisted of a series of computer-generated displays, where each display was in one of three FOV configurations. Each FOV contained eight alphanumeric symbols, all sharp or all blurred, seven of which were letters and one a numerical digit, which was the target. The particular letters and the particular number, the position of the target, the vertical location of all symbols, and each symbol's orientation were randomized. Also, each FOV contained 6 small crosses for fusion locks and 60 randomly-sized and randomly-positioned ellipses (half light grey and half dark grey) for background clutter. For each trial, two seconds after the FOV appeared, the eight symbols slowly appeared, taking an additional 0.8 seconds to go from invisible to maximum visibility. Stimulus details are given below, and shown in Figures 4-92. Stimulus luminance values displayed on the screen, in terms of the 0-255 digital driving levels, took on values between 0 (black, 0.01 fL) through 64 (dark grey, 1.33 fL), 128 (neutral grey, 6.65 fL) to 192, (light grey, 16.81 fL). Half of the ellipses were light grey and half were dark grey. The FOV background was neutral grey. The area outside the FOV was black, as were the fusion locks.

The original sharp symbols were predefined as black, and the blurred symbols were sharp symbols modified by the blurring algorithm which causes the luminance of a symbol's pixels (and neighboring pixels) to vary in a complex way with different pixels taking on different values. The resulting values were between the pixel's original pre-blurred (black) value and the values of the pixel's local surround---some combination of black and neutral grey pixels. Then the symbol values were modified by lookup tables before display in order to present a smooth temporal onset. In essence, what this did was to start off the symbols as invisible and then smoothly increase the contrast by making the symbol darker to a value where they were clearly visible. This is described in detail below.

FOV. The total FOV was a rectangular area, 32.8 degrees of visual angle horizontal (840 pixels) by 10 degrees of visual angle vertical (256 pixels) (Figures 4-92 to 4-95). The subjects saw the total FOV via the monocular fields presented to each eye. The monocular fields were each 23.4 degrees of visual angle horizontal (600 pixels) by the full vertical extent. The FOV configurations differed in how the two monocular fields overlapped, and consequently the total FOV presented to both eyes. In the full overlap FOV configuration, each eye's monocular field displayed the same central portion of the total FOV, so that the FOV seen by the subject was binocular and consisted of the central 23.4 degrees of the total FOV. In the divergent partial overlap FOV, the right eye's monocular field was the right-most 23.4 degrees and the left eye's monocular field was the left-most 23.4 degrees of the total FOV; therefore, the FOV seen by the subject consisted of a central binocular overlap region of 14.1 degrees and two flanking monocular regions, each of 9.4 degrees. In the convergent partial overlap FOV, the right eye's monocular field was instead the left-most 23.4 degrees and the left eye's monocular field was the right-most 23.4 degrees of the total FOV. Again, the FOV seen by the subject consisted of a central binocular overlap region of 14.1 degrees and two flanking monocular regions, each of 9.4

degrees. In the divergent case, the right eye saw the flanking monocular region to the right and the left eye saw the flanking monocular region to the left, while in the convergent case these were reversed, that is, the left eye saw the right monocular region and the right eye saw the left region (Figure 4-92).

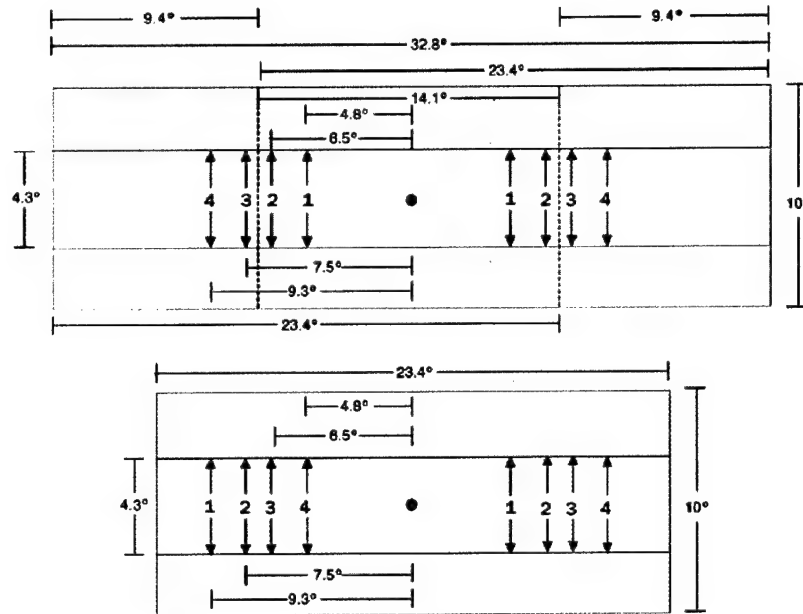


Figure 4-92. FOV dimensions. Four target positions in degrees of visual angle from the center are shown on the right and four symmetrical positions are shown on the left. The top shows a partial overlap FOV and the bottom shows a full overlap FOV.

In both partial overlap conditions, the FOV seen by the subject was the full 32.8 degrees of the total FOV. This FOV consisted of a 14.1 degree central binocular region and two flanking 9.4 degree monocular regions, with each eye seeing the monocular regions as described. In the full overlap condition, the FOV seen by the subject was the central 23.4 degree portion of the total FOV. In the full overlap condition, the binocular region was larger than in the partial overlap conditions, while in the partial overlap conditions, an enlarged FOV is seen with a smaller binocular region. In all the conditions, the monocular fields were the same size.

The subjects require similar stimuli common to both eyes to prevent disjunctive eye movements in order to binocularly fuse images properly and to avoid the image slippage which leads to the binocular overlap of inappropriate regions. To ensure proper binocular locking of the monocular fields and to provide a way to monitor binocular fusion, fusion locks were present in each display. These were six crosses, three in the upper center of the total FOV and three in the lower center. Subjects were told that they should see three crosses above and below the center of each display. If they saw more, then the images were not properly fused and they should tell the experimenter. This did not occur. With the background clutter described below, there were ample binocular stimuli to prevent slippage. Each shaft of the crosses was 8 pixels long by 2 pixels wide. Center crosses were 25 pixels from the top and bottom of the FOV, and flanking crosses

were located 44 pixels to the right and left of the center and 16 pixels from the top and bottom of the FOV (Figures 4-93 to 4-95).

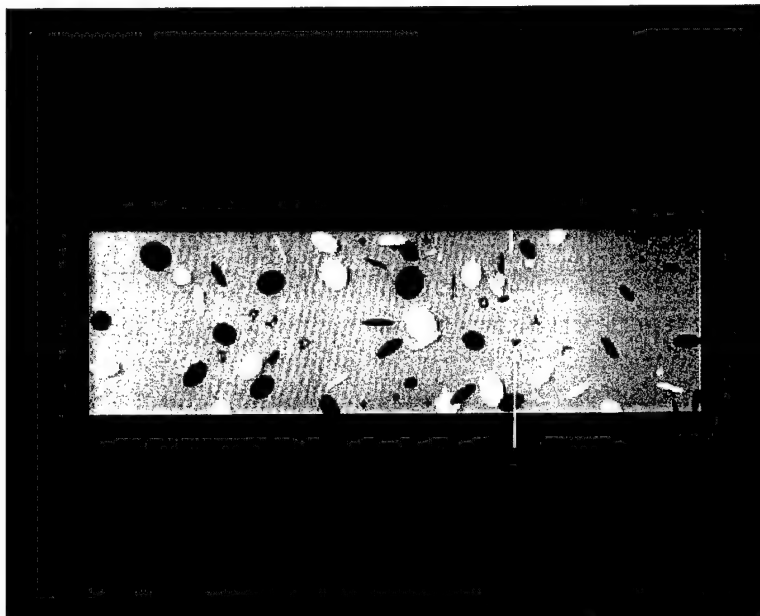


Figure 4-93. Example of a total FOV with blurred symbols. Target is the numeral "4" indicated by an arrow.

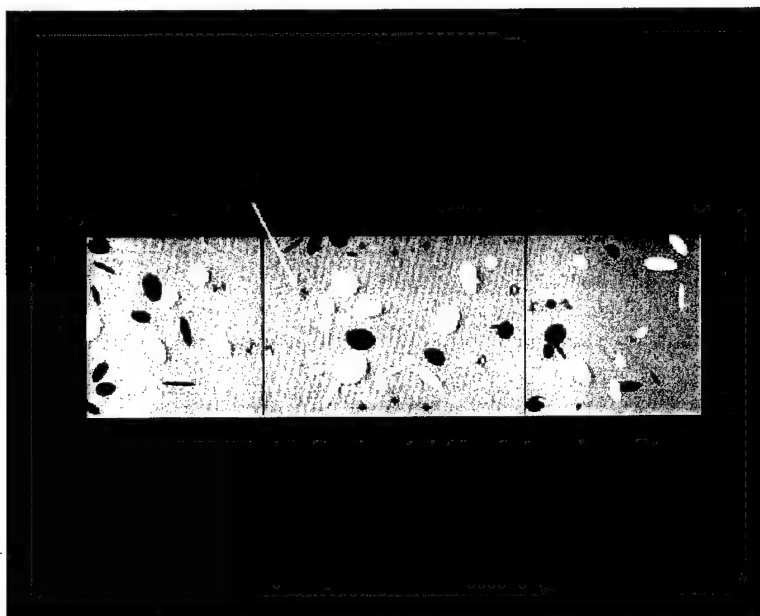


Figure 4-94. The total FOV divided into the three regions seen in the partial overlap displays, the central binocular overlap region and the two flanking monocular regions. The vertical lines were not present in the displays. The left monocular field consists of the left and central regions, and the right monocular field consists of the central and right regions. In the divergent FOVs, the left eye saw the left monocular field, and the right eye saw the right monocular field. In the convergent FOVs, the left eye instead saw the right monocular field, and the right eye saw the left monocular field.

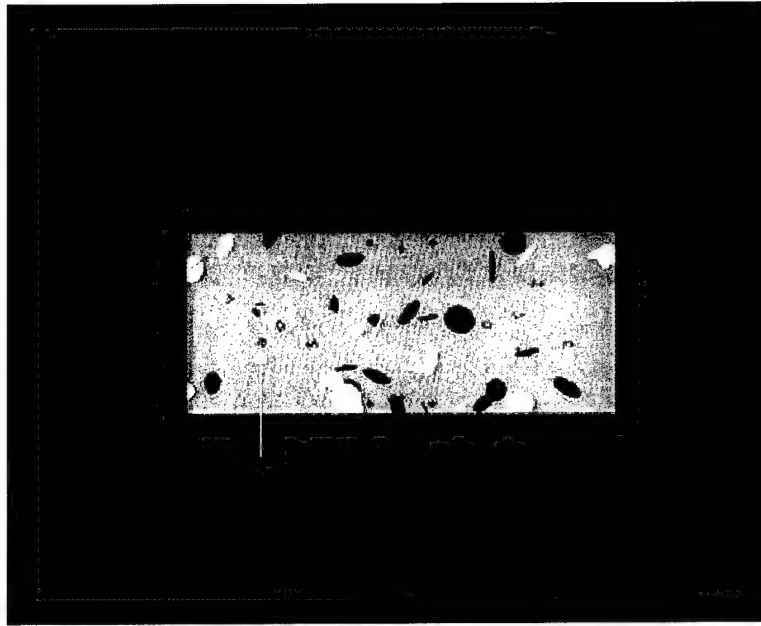


Figure 4-95. A full overlap FOV where both monocular fields consist of the same central portion of the total FOV. The symbols are sharp. Target is the numeral "2" indicated by the arrow.

Alphanumeric symbols and targets. In each display, one of eight alphanumeric symbols was the target number, and the remaining seven were nontarget letters. Alphanumeric symbols were all in "stick figure" font, or font number 1, predefined in the Hewlett-Packard Starbase computer graphics language. Letters were all capitals, and all alphanumeric symbols were originally defined within a 16 by 16 pixel symbol square (0.6 by 0.6 degrees of visual angle). Alphanumerics were initially defined as 0 driving levels (black). The orientation of each symbol was randomized by rotating the symbol randomly from 0 to 360 degrees. The blurred symbols were spatially blurred as follows. The original symbol square consisted of black symbol pixels and non-symbol pixels. The symbol pixels and adjacent non-symbol pixels were defined as the blur zone. This blur zone included any symbol pixel, that is a pixel that contained part of the alphanumeric symbol, and any non-symbol pixel that was adjacent to a symbol pixel, adjacency defined as the eight contact pixels. The pixels in the blur zone were then filtered by a 3 by 3 Gaussian kernel. This means that for each blur zone pixel, the old driving level was replaced by a new driving level, which was the weighed average of the old value and the driving levels of the eight pixels around it. The kernel weights were as follows where the central "12" represents the weight of the old driving level:

1	4	1
4	12	4
1	4	1

The symbol edges were softened by blurring the symbol into the FOV. The blurred symbols contained more pixels with smoother transitions between symbol and background.

All symbols, sharp and blurred, gradually appeared in the FOV to avoid sharp temporal onsets. This was implemented by passing the symbol (blurred or sharp) through a series of lookup table functions, one function for each frame of the temporal sequence. In the lookup table function, each original input driving level in the symbol was changed to an output displayed driving level. Cycling through the set of functions caused the original symbol's luminance to change smoothly from invisible, where all the pixels were equal to the background of the FOV (128 driving levels) to clearly visible, which was 45 driving levels in the sharp symbols, and in the blurred symbols, the pixel values were based on the pixel values resulting from the original blurring. The temporal onset was done by the following lookup table equation:

$$y = x * \tan(\text{angle}) - (128 * \tan(\text{angle})) + 128,$$

where x = input pixel driving level; y = output pixel driving level; and angle = 0 to 30 degrees in steps of 1.25 degrees.

Angle represents the slope of the input-output lookup table function which changed every two frames. At 45 degrees, all displayed driving levels (y) would be equal to original input driving levels (x), zero in the case of the sharp symbols and the original blurred values in the case of the blurred symbols. At 0 degrees, all output driving levels (y) equaled 128, where the entire symbol was the same driving level as the FOV background and therefore invisible. Forty-eight frames, taking 0.8 seconds, presented the transition from invisible (0 degrees) to fully visible (30 degrees) by incrementing from 0 to 30 degrees in steps of 1.25 degrees with 2 frames per step.

The symbol positions in terms of degrees of visual angle from the center of the symbol to the center of the FOV were located as shown in Figure 4-96. Four positions were to the right of center, and four symmetrical positions were to the left of center. Horizontally, the symbols were located as follows. The positions numbered 1 were 123 pixels (4.8 degrees of visual angle) to the right and left of center. The positions numbered 2 were 167 pixels (6.5 degrees of visual angle) to the right and left of center. Positions numbered 3 were 193 pixels (7.5 degrees of visual angle) to the right and left of center, and positions numbered 4 were 237 pixels (9.3 degrees of visual angle) to the left and right of center. The edge of the symbols in positions 2 and 3 were two pixels away from the adjacent binocular overlap border. The position of each individual symbol was vertically randomized; it could be located with equal probability vertically anywhere within the central 110 pixels high region (4.3 degrees of visual angle).

Background clutter. For clutter, each display contained 30 dark grey and 30 light grey ellipses, each randomly oriented, randomly sized, and randomly located within the total FOV. The center of each ellipse could, with equal probability, be located on any pixel within the total FOV with the following stipulation. If the random placement procedure located the ellipse on or near a symbol, that is if they overlapped, then the ellipse was instead placed in a new random location. For this purpose, the symbol was defined as the original 16 x 16 pixel square and the ellipse region was defined as a square around the ellipse center with sides equal to the major axis of the ellipse. This was to avoid contaminating the results with extremely difficult to see alphanumeric on top of ellipses. The orientation of each ellipse could, with equal probability, be anywhere from 0 to 180 degrees. Ellipse size was randomized by sizing each of the two axes of

each ellipse with equal probability anywhere from 1 to 44 pixels in length. Ellipses were alternatively light and dark grey, with later ellipses drawn over former ellipses.

Design and data analysis. Each trial consisted of a unique display to which the subject responded. In the experiment, 378 trials were presented in 7 blocks, where each block contained 3 FOVs, presented in random order. There were 18 trials in each FOV, where unknown to the subject, the first two of these were merely to allow the subject to acclimate to the FOV and the responses not recorded. The acclimation trial displays were random with respect to target type (sharp or blurred), target position and target number. The remaining 16 trials consisted of each of the two target types, once in each of the eight positions presented in random order. For each display, the number of the target symbol was randomly 1, 2, 3, 4 or 5, and each of the seven non-target letters was randomly one of twenty-two letters (the alphabet minus the letters B, E, I and S). The experimental design for analysis was a 6 (block) x 3 (FOV) x 2 (target type) x 4 (position) repeated measures analysis of variance (ANOVA) with 144 data points for each subject for each of three response measures. The first of the seven blocks was considered practice and not included in the data analysis. Also, only the four positions to the right of center were included in the data analysis. Originally, we had intended to include all eight positions; however, we found that with some slight movement of the head for some IPDs, it was possible in some cases for the far left symbol to fall out of the left ocular's sweet spot, i.e., become slightly blurred.

In a visual search experiment subjects might inadvertently move their heads when scanning the visual field, so we eliminated some possible confounding effects of this blurring by limiting the data analysis to the four right-most positions. The three response measures were response time (RT), number of errors, and percent errorless target acquisition. RT measures the time to hit the correct key indicating the correct target, irrespective of the number of errors. The alphanumerics appeared gradually in each FOV, taking 0.8 seconds to go from completely invisible to fully visible. The response times were measured from the halfway point, 0.4 seconds, in terms of the number of frames, which were updated every sixtieth of a second. The number of errors measures the number of wrongly acquired targets on each trial before acquiring the correct target, and it could vary from a minimum of zero to a maximum of four, as there were five possible answers. Percent errorless target acquisition measures the percentage of times subjects made no errors before target acquisition.

Procedure. Subjects were given instructions and gave informed consent for participation in the study. Each subject's interpupillary distance was measured and the equipment adjusted accordingly. The mean interpupillary distance for the 21 subjects was 61.3 mm (SD = 3.9). Subjects adjusted the chin-rest, keypad, and height of the seat for comfortable viewing of the display through the binoculars. To ensure there was no visual clipping of the FOV, or vignetting, for the area which would contain the experimental stimuli, a binocular display containing three widely spaced circles was shown. It contained the same optical convergence as the stimulus displays. The three circles were superimposed over a purple background with a white grid. There was a black circle in the center of the display, a blue circle to the right of center, and a yellow circle to the left of center. The black circle was 24 pixels in diameter and the outer two circles were 34 pixels in diameter. The outer edges of the outer circles were 668 pixels (26.1 degrees) distance from each other. The subjects were asked if they could see, without moving their head

position, the entire yellow circle, the entire blue circle, and the grid surrounding each circle clearly and without vignetting when they visually scanned across the display.

In the experiment, subjects viewed a series of stimulus displays, each with eight alphanumeric symbols. The subjects were told the following: There would be eight symbols in each display, one of which was the target number. The symbols could be blurred or sharp and would be randomly oriented and randomly located. Their task for each display was to identify the number of the target, one to five, as quickly as possible, hit the appropriate key on the keypad, and avoid mistakes. Subjects could pause only during the feedback displays or "continue" displays. Five response keys in a row were assigned to each number. The middle key had a bump, so subjects could feel them in the dark.

The row of four keys above the response keys were the "next" keys, which were for continuing past the feedback displays, or the displays with the word "continue." A display with the word "continue" preceded each new FOV. To induce the need for rapid response, as well as the need to maintain accuracy, subjects were told to imagine that the target, the number, was the enemy which would shoot them if they did not shoot it first, and the nontargets, the letters, were friendlies. Feedback displays were presented throughout the experiment to reinforce the subject's motivation to maintain maximum performance.

There were two types of feedback displays. First, seven times during the experiment, at the end of each block of trials (with three FOVs), a percentage display came on. This display showed a number with a percent sign representing the percentage of trials of the fifty-four trials of the block that were acquired on the first try without any errors. This percentage appeared on the screen to motivate the subject to maintain accuracy and avoid random guessing. Second, after every seven trials, two numbers appeared in a feedback display. The top number, followed by the word 'sec.', was the average response time in seconds to the third decimal place that the target was acquired for the last seven trials, and the bottom number, followed by an 'X,' was the number of targets out of the last seven where there were errors before target acquisition. If there were no errors in the preceding seven trials, the word "OK" appeared instead. Seven displays was used as the average because it is not evenly divisible into the number of trials per FOV, so subjects would not be inclined to monitor their performance with respect to FOV type. The continue and the feedback displays remained on until a next key was hit. Subjects were told that for these displays they could pause if they wanted to and then initiate the next series by hitting a next key when they were ready.

Once the series of displays started, for each display, the image would remain on until the target was hit. If an error was made, a transient asterisk appeared in the center of the display and remained on as long as a wrong key was depressed. When the target number was identified by hitting the correct key, a cross appeared on the target, then the screen went blank and 1 second later a new FOV appeared, and 2 seconds later the targets began increasing contrast, reaching full visibility 0.8 seconds later.

In the experimental session, two display programs were run; one for the training and one for the experimental phase. The first ran the training phase to familiarize the subject with the task. It had FOVs with fewer trials (6 per FOV instead of 18) and, unlike the experimental phase,

the symbol factors of blur and position of target were totally random, that is, random with replacement. No data were recorded. Subjects ran at least one block, and as many additional trials as they thought they needed, to fully familiarize themselves with the task and stimuli. All subjects ran between one and two blocks in this phase. Three minutes later, in the experimental phase, the second program ran seven blocks where the first block was considered practice. The blur and position factors of the acclimation trials, unlike the remaining 16 trials, were totally random. In the remaining 16 trials for which the data were recorded, the blur and position factors were random without replacement, that is, each target type-position combination appeared once. The number of the target in each trial was totally random. Subjects were not told these details; to them, all the trials were equally important and all stimulus factors were random. There were 378 trials for each subject. The 144 non-acclimation trials of the right-most four positions of the last six blocks were included in the analysis and results reported here.

Results

Table 4-27 shows the ANOVA tests for RTs. None of the interactions were significant. Three of the four main effects were significant. There was a significant block effect with RTs tending to get faster over time as shown in Figure 4-97, which gives the RTs over blocks for the practice block and the six test blocks for each of the three FOVs. There is some improvement over time, as one might expect, and, there is no interaction between the block factor and any other factor. The noninteraction between the block and the FOV factor is indicated by the rough parallelism of the three lines.

There was a significant main effect for FOV. Mean RT to targets in the three FOVs were as follows: divergent overlap FOV, 1.97 seconds; convergent overlap FOV, 1.93 seconds; and full overlap FOV, 1.74 seconds. The divergent FOV RT was significantly slower than the full overlap FOV, $F(1,20) = 25.03$, $p < .00007$; and the convergent FOV was significantly slower than the full overlap FOV, $F(1,20) = 20.18$, $p < .0002$; but the divergent FOV was not significantly slower than the convergent FOV, $F(1,20) = 0.77$, $p < .39$.

There was no significant main effect of target blurring. The means for blurred and non-blurred targets, respectively, were 1.88 and 1.87 seconds. Although the differing appearances of the two types of targets were apparent, the measured responses to them were virtually indistinguishable.

There was a significant main effect for position with slower RTs for targets farther away from the center. The means for positions 1 through 4, respectively, were as follows: 1.71, 1.73, 1.88 and 2.19 seconds. Figure 4-97 shows the RTs for each position for each of the three FOVs. Table 4-28 shows the ANOVA tests for number of errors. None of the statistical tests were significant. The three FOVs over position are graphed in Figure 4-99.

Table 4-29 shows the ANOVA tests for percent errorless target acquisition. None of the tests were significant. The three FOVs over position are graphed in Figure 4-99. Here the perfect score of 100 percent is at the bottom of the graph to keep it in line with the other graphs where performance decrements are higher on the graph.

The two accuracy measures, in conjunction with the RT measure, show that there was no systematic speed-accuracy tradeoff, that is, no pattern of substituting speed for accuracy, or accuracy for speed, differentially across conditions.

Table 4-27.
RT ANOVAs

Effect	Test	F	p-level
1. Block	F (5,100)	4.58	.0008**
2. FOV	F (2,40)	14.34	.00002 **
3. Target	F (1,20)	0.07	.80
4. Position	F (3,60)	31.64	< .000001 **
5. Block x FOV	F (10,200)	0.93	.51
6. Block x Target	F (5,100)	1.17	.33
7. FOV x Target	F (2,40)	1.58	.22
8. Block x Position	F (15,300)	0.64	.84
9. FOV x Position	F (6,120)	1.92	.08
10. Target x Position	F (3,60)	0.05	.98
11. Block x FOV x Target	F (10,200)	1.13	.34
12. Block x FOV x Position	F (30,600)	1.12	.31
13. Block x Target x Position	F (15,300)	1.51	.10
14. FOV x Target x Position	F (6,120)	1.01	.42
15. Block x FOV x Target x Position	F (30,600)	0.98	.50

** = $p < .01$.

In the first study, using response time and accuracy of target acquisition under different FOVs in a different design, position was confounded with keystroke movements; i.e., subjects responded to the position of the target with a key associated with that position. In the current study, each key was associated with a particular target number, rather than position, thereby eliminating response bias as a factor. Differences between positions here can therefore be attributed solely to the stimulus (visual) differences between positions.

One can see that, overall, target acquisition is fastest in the full overlap FOV, and slower in the two partial overlap FOV conditions.

As described previously, the positions differ categorically from each other in that positions 3 and 4 are monocular in the convergent and divergent FOVs and binocular in the full overlap FOV, and positions 1 and 2 binocular in all cases. The graphed data in Figures 4-97 to 4-99 do not show any clear (statistically significant) pattern of changes across the boundary between positions 2 and 3 for the overlap FOVs. Distance appears to be the important factor with these supra-threshold stimuli. Separating distance and the effect of the overlap border requires additional research and more statistical power. Because the severest luning in the monocular border regions is just outside the binocular border, one might have expected peaks in the RTs for position 3. This may not have occurred here, possibly due to the attenuating effect on luning of the background clutter.

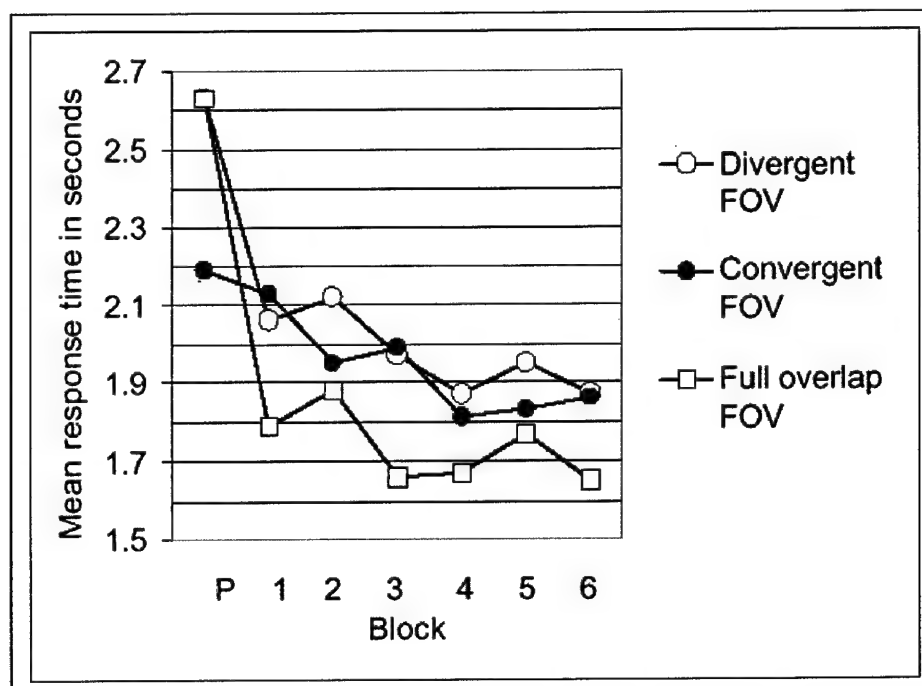


Figure 4-96. Mean RT to acquire target (FOV x Block). P is the practice block.

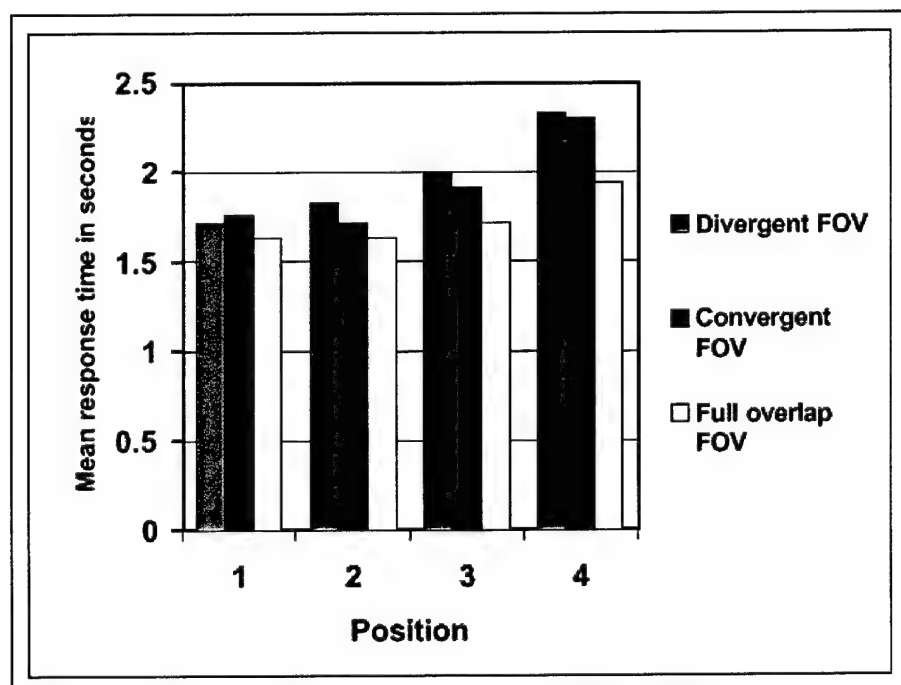


Figure 4-97. Mean RT to acquire target (FOV x Position).

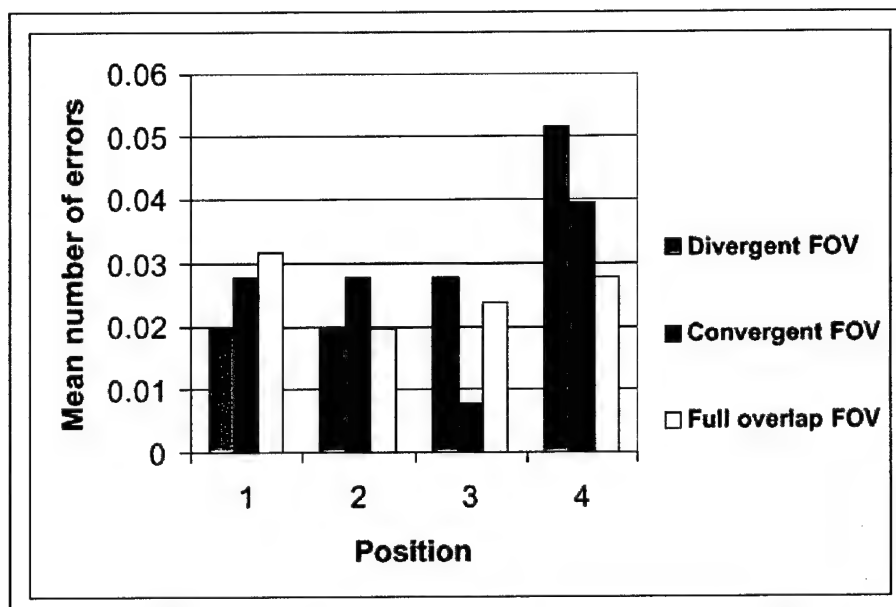


Figure 4-98. Mean number of errors per target acquired (FOV x Position).

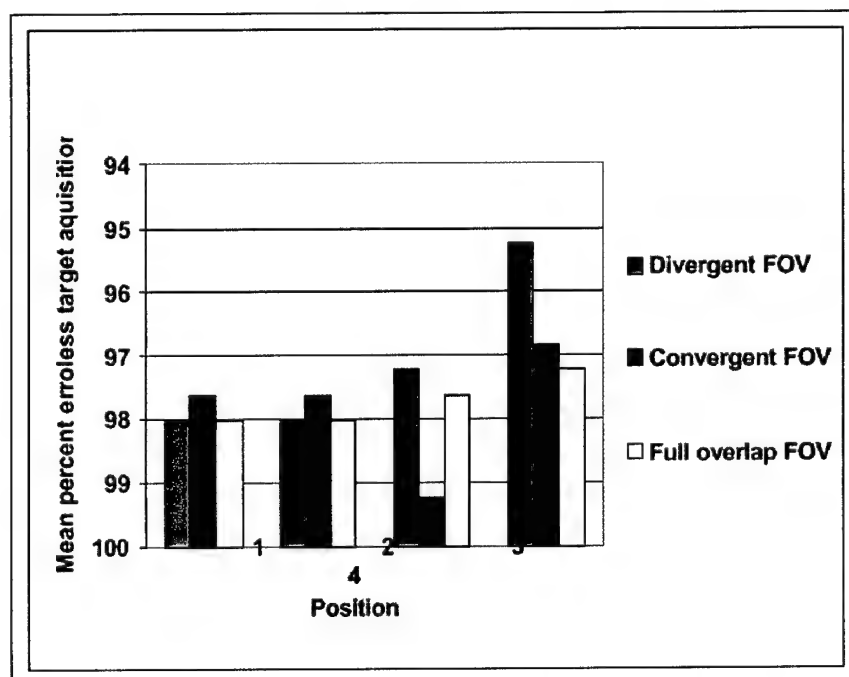


Figure 4-99. Mean percent errorless target acquisition (FOV x Position).

Table 4-28.
Number or Errors ANOVAs

Effect	Test	F	p-level
1. Block	F (5,100)	0.18	.97
2. FOV	F (2,40)	0.15	.86
3. Target	F (1,20)	3.49	.08
4. Position	F (3,60)	1.25	.30

5. Block x FOV	F (10,200)	0.73	.69
6. Block x Target	F (5,100)	0.73	.60
7. FOV x Target	F (2,40)	0.03	.97
8. Block x Position	F (15,300)	1.03	.42
9. FOV x Position	F (6,120)	0.74	.62
10. Target x Position	F (3,60)	0.85	.47
11. Block x FOV x Target	F (10,200)	0.49	.90
12. Block x FOV x Position	F (30,600)	1.34	.11
13. Block x Target x Position	F (15,300)	0.98	.48
14. FOV x Target x Position	F (6,120)	0.60	.73
15. Block x FOV x Target x Position	F (30,600)	0.92	.60

Table 4-29.
Percent errorless target acquisition ANOVAs

Effect	Test	F	p-level
1. Block	F (5,100)	0.17	.97
2. FOV	F (2,40)	0.65	.53
3. Target	F (1,20)	1.61	.22
4. Position	F (3,60)	1.39	.25
5. Block x FOV	F (10,200)	0.70	.72
6. Block x Target	F (5,100)	1.11	.36
7. FOV x Target	F (2,40)	0.39	.68
8. Block x Position	F (15,300)	0.80	.67
9. FOV x Position	F (6,120)	0.61	.73
10. Target x Position	F (3,60)	0.81	.50
11. Block x FOV x Target	F (10,200)	0.67	.75
12. Block x FOV x Position	F (30,600)	1.19	.23
13. Block x Target x Position	F (15,300)	1.42	.14
14. FOV x Target x Position	F (6,120)	0.86	.53
15. Block x FOV x Target x Position	F (30,600)	0.88	.65

Discussion

Although not all the differences were significant, overall performance as measured by RT and accuracy tended to be best in the full overlap FOVs and worst in the partial overlap FOVs. There was no effect of target type. We had expected that since sharp targets are better dichoptic competitors, they would have shown superior performance. However, it may be that the clutter in our displays outweighed this factor. That is, FOV articulation caused by the contours from the clutter serves to lock in the correct competing image, and lock out the dark competing image from the incorrect eye, so that it does not come through in the binocular percept of the total FOV. Moffitt (1989) suggested that contours that occur in an FOV displaying a natural scene might eliminate luning and, presumably, the other detrimental effects such as the reduced visibility of targets that occur in partial binocular overlap displays. This occurs because the added contours bias the binocular rivalry in favor of the monocular image that contains the contours as opposed to the incorrect image which only contains a black featureless background and one contour, the

binocular border (e.g., see Arditi, 1986; Anderson and Nakayama, 1994; Fox and Check, 1968, 1972; Fox, 1991; and Norman, Norman and Biotta, 2000). One would need to test visual search of targets in a clear uncluttered FOV to determine this. Performance, as expected, tends to get better over time as indicated by the block main effect and be better for positions closer to the center of the FOV as indicated by the position main effect. How much of an effect is due to the binocular border per se remains to be seen. Further research is needed to clarify these issues. In summary, on average, performance tended to be best in the full overlap FOV and poorest in the partial overlap FOVs, and the RT performance data were not disconfirmed by the two accuracy measures (number of errors and percent errorless target acquisition).

AN OPERATIONAL GRAYSHADES AND SEE-THROUGH COLOR MODEL

Program managers and combat developers must determine the performance specification of a helmet-mounted display (HMD) in order to meet mission requirements. Specifications are often based upon simplifying approximations regarding optical performance. These specifications may lack operational validity.

To assist the program manager and developer in understanding the HMD requirements and to allow modeling of hardware, this preliminary model handles specific hardware to include transmission spectra for windscreens, visors, protective masks, laser protection devices and personal eyewear. The model includes emission spectra for cockpit instrumentation, lasers, and for several HMDs. The user interface includes provisions for modeling user specified data. Daylight spectra are calculated from color temperature specifications. Also included in the model are target/background spectra that allow contrast prediction based upon hardware configuration. To simplify the process of variable selection and to provide an intuitive feel, a complete graphical user interface has been developed which allows for complete user specification of modeled variables. Given these conditions, it is possible to model HMD imagery in a simulated operational environment. Table 4-30 includes a list of the hardware currently included in the non-classified model.

The selections in Table 4-30 will likely be expanded in future versions of the model. As the model was developed specifically for HMDs, the "Null HMD" condition (Table 4-30) allows for modeling other hardware alone or in combination without the influences of an HMD. As shown in the table, users can specify their own spectra for each hardware device. The model allows up to 50 separate user specified spectra for each hardware condition. Users can also specify daylight conditions (luminance and color temperature of skylight), lasers, instrument emission spectra, target/background imagery, and HMD emission and transmission spectra. This flexibility is one of the model's strong points. The model currently encompasses a light spectrum from 450 to 750 nanometers (nm) in 2-nm increments. This spectrum was chosen due to spectral limitations in some of the previously captured data. An improvement is underway to increase the spectrum from 380 to 780 nm to more accurately describe the bandwidth of visual sensitivity.

To better understand the quality of the see-through imagery and overlaid HMD symbology, a color model was added to the grayshades model. The purpose of the model is to simulate real world viewing of images through the hardware. Of course, no model can accurately simulate real world conditions. This is an extremely complex issue and is beyond the realm of this paper. A major problem is that the eye can see contrast over a several-log-unit range of ambient luminance. Most computers can only address a maximum of 256 gray levels, and actual displayed gray levels (on the monitor) are considerably less than 256. Another problem lies in using transmissivity spectra to filter RGB imagery. The model currently translates the transmissivity curves to the 1964 CIE Colorimetric system and calculates the x-y chromaticity coordinates. Likewise the x-y coordinates are calculated for the monitor's RGB spectra. Given these coordinates, the model solves for the RGB coefficients representing the transmissivity curve. Given these coefficients, each image pixel is then scaled accordingly.

Even though tri-stimulus matching curves are normalized, the model's current limit in the blue end of the spectrum may limit the model's usefulness until the model is expanded to the larger bandwidth.

Table 4-30.
Hardware variables included in current model.

HMDs	Windscreens	Visors	Protective Masks	Personal Wear
H-64 IHADSS	AH-1 Cobra	Comanche Clear	M-45	Spectacles
Microvision AIHS	AH-64 Apache	Comanche Tinted	M-48/M-49	Contact Lens
Kaiser CRT HIDSS	CH-47 Chinook	Gentex Tinted	User Specified	AOtech Laser
Null HMD	OH-58 A&D Models	Gentex Laser Prot.	None	User Specified
User Specified	OH-58 C Model	User Specified		None
	TH-67 Creek	None		
	UH-1 Iroquois			
	UH-60 Blackhawk			
	User Specified			
	None			

Model Implementation

The majority of the model was implemented in Microsoft's Excel 2000. Excel offers a tremendous advantage when working with arrays and implementing formulas quickly. Its database capabilities provide easy access to data, while its charting and graphing support make most tasks required of the model routine. A graphical user interface was developed in the main Excel spreadsheet and this can be seen in Figure 4-100. Pull down menus can be accessed to view charts, modify variable properties, maintain files, check for software updates, view results, and edit user data. A separate Excel spreadsheet is used for maintaining and modifying user data. Once user data have been entered into this spreadsheet, their data can be selected from the main menu like any other variable. To make the program secure, all files have routine security protection applied and the Excel files cannot be accessed or modified except through the constraints of the program. By using executable linking files and controlled access, the use of Microsoft Excel is rather transparent to the user. Much of the programming in Excel was done in Microsoft Visual Basic for Applications. For the user to run the model, Excel must be enabled to execute macros. Thus, on most computers, virus protection for Excel must be temporarily relaxed.

The Basic Model

The basic model is outlined in Figures 4-101 and 4-102. In Figure 4-101, outside imagery is filtered first by the aircraft windscreen or canopy. Other filtering also may occur. The windscreen-filtered image can be filtered in turn by a visor, an HMD combiner lens, a protective mask, and eyewear. This progression of filters results in an image of the outside world that can be greatly altered in color appearance and in luminance. Figure 4-102 depicts the filtering process of cockpit imagery such as the emission spectra of multifunction displays, reflective spectra of cockpit instruments, etc. The transmittance spectra of windscreens, visors, and protective masks, as well as items of personal eyewear, are fairly flat except for items where laser protective coatings or dye have been used. As a general rule, the major alterations to the color of outside and inside imagery occurs as a result of filtering by the HMD, where the HMD's combiner lens has coatings to maximally reflect the HMD source emission spectra.

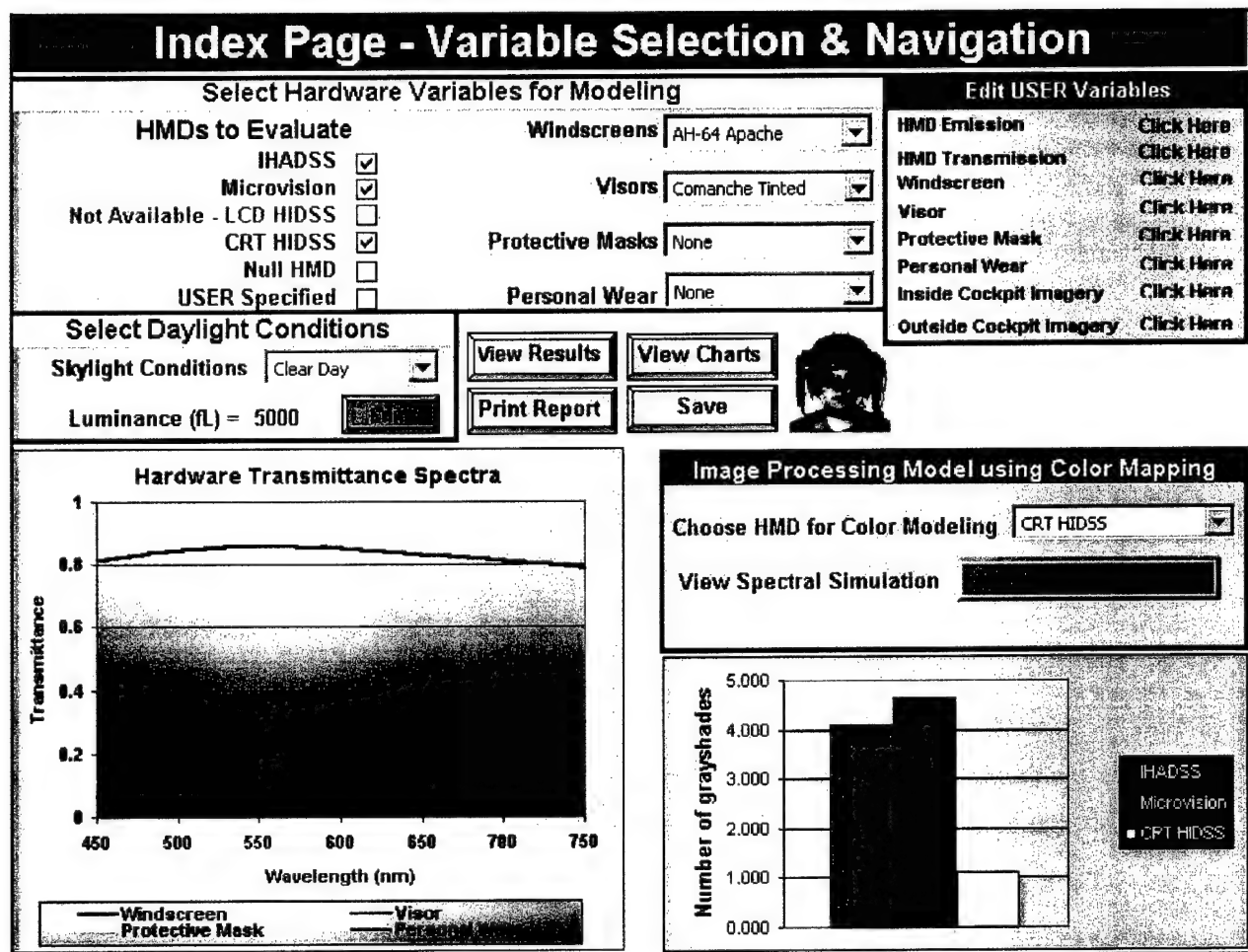


Figure 4-100. Main index page for the model. From here, the user can quickly navigate the model and select variables.

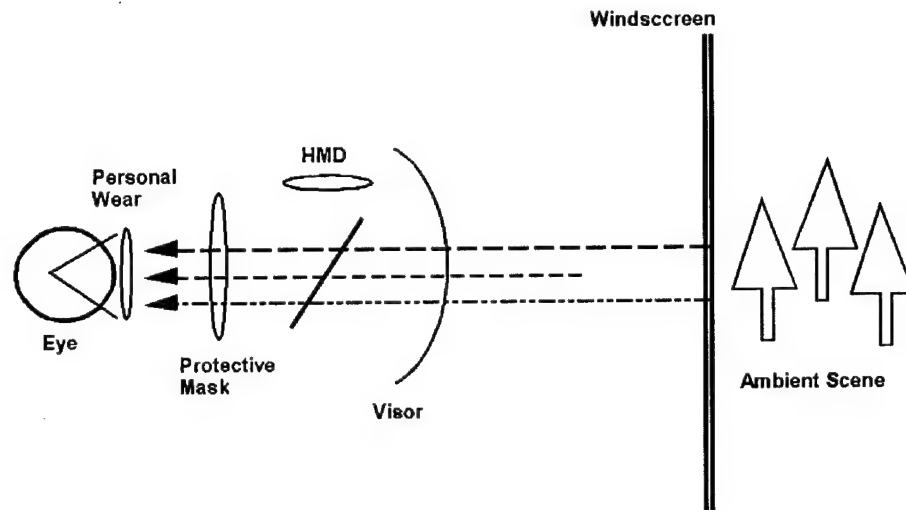


Figure 4-101. Basic scenario for outside the cockpit imagery.

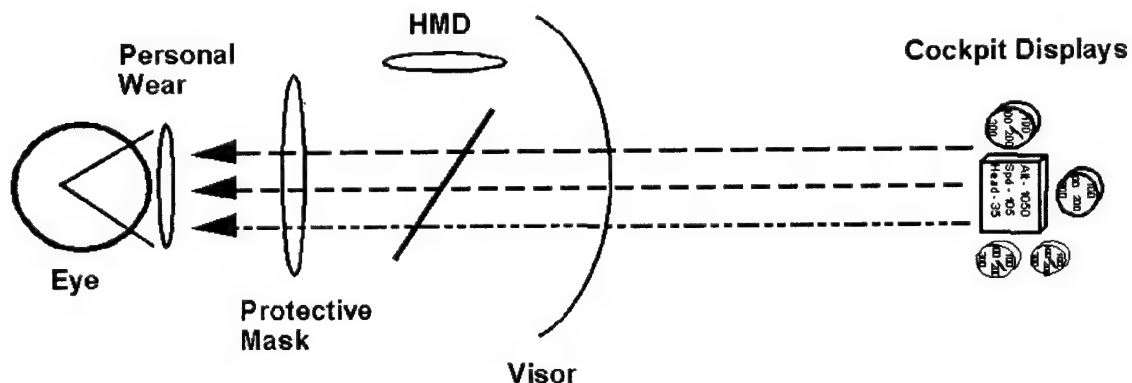


Figure 4-102. Basic scenario for inside the cockpit imagery.

Grayshades

Most developers are interested in the number of grayshades of symbology that are visible against the ambient scene. For ease of calculation, grayshades are defined as the number of one-half octave increments in luminance that are available above the background. The following formula is used to calculate available grayshades:

$$\text{Number of Grayshades} = 1 + (\log(L_{DF}/L_B)/\log(2^{0.5}))$$

Where L_{DF} is display foreground (luminance of symbology) and L_B is the ambient background luminance plus the display noise. Note that this formula ignores color and only considers luminance. Color contrast is an important consideration in describing HMD performance, but regrettably, this topic has largely been absent in HMD requirement documents. To illustrate the point, when the background luminance exceeds the foreground luminance (i.e.,

the grayshades number is negative), symbology may still be visible particularly if there is good color contrast between the symbology and the background imagery.

The RAH-66 Comanche HIDSS (Helmet Integrated Display Sighting System) has a daytime requirement to display symbology. For illustrative purposes, let us assume the following:

Daylight:	5000 fL
HMD:	Microvision AIHS (Aircrew Integrated Helmet System) with a peak luminance of 1485 fL and a contrast ratio of 20 and an average transmittance of 0.322.
Windscreen:	AH-64 Apache with an average transmittance of 0.82.
Visor:	Comanche tinted with an average transmittance of 0.17.

Using the grayshades formula from above and substituting in the sample numbers we obtain:

$$\text{Grayshades} = 1 + (\text{Log}(1485/((1485/20)+(5000*0.322*0.82*0.17)))) / \log(2^{0.5}))$$

$$\text{Grayshades} = 1 + (\text{Log}(1485/298.68) / \log(2^{0.5}))$$

$$\text{Grayshades} = 5.63$$

These calculations are based upon the assumptions of flat spectra and average transmittances. In contrast, the computer model calculates luminance grayshades based upon actual daylight and hardware spectra. In the example above, the model calculates the number of grayshades to be 5.22. This is a small difference, but the differences are important, and they are based upon actual spectra and transmittances. Using the above sample data, the actual model results are shown in Figure 4-103. (Please note that the model's graphics are in color and these black and white images are captured from the monitor.) The graph in the bottom left of the photograph represents the luminance of the skylight reaching the eye (the transmitted spectra of the skylight is convolved with the photopic curve). This provides an indication of the sky's color. This curve can be compared to the skylight spectrum shown in the upper right of Figure 4-103.

Skylight

Daylight spectra used by the model, for example see Figure 4-103, and were derived from the CIE S0, S1 and S2 to calculate daylight from 4000°K to 25,000°K. Separate S0, S1, and S2 values must be calculated for each wavelength. For color temperatures below 4000°K, other formulas must be used. Table 4-31 shows the default luminance and color temperature data for the various skylight conditions. A pop-up menu allows changes to any of these values by the user.

Table 4-31.

Skylight conditions with default luminance and color temperature specifications.

Skylight Conditions	Luminance (fL)	Color Temperature (°K)
Clear Day	3000	8500
Overcast Day	300	4500
Gray Day	30	4000
Dawn	3	4000
Dusk	3	3500
Night	0.01	3800

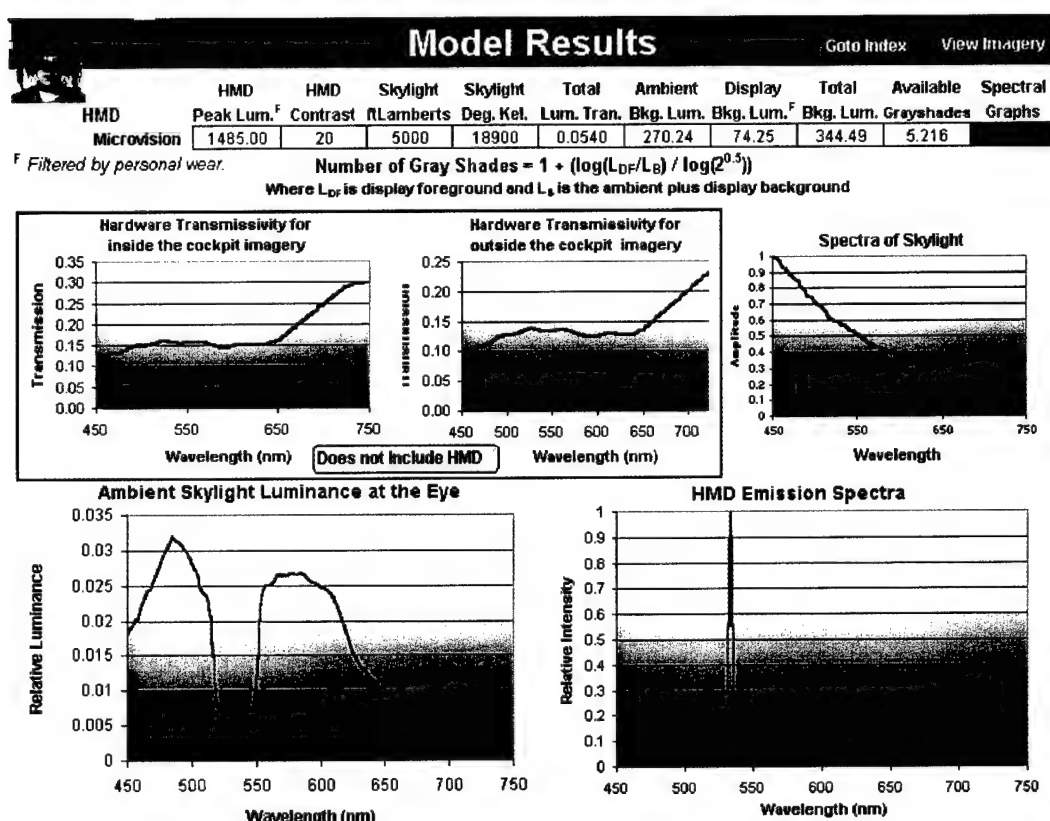


Figure 4-103. Actual model results for the sample conditions mentioned above.

Image and symbology simulation

The image processing simulation models the hardware selected on the index page in association with a single HMD (Figure 4-100). Most of the graphics processing for this simulation are performed in an executable program. Scalars are passed to the executable program from an Excel spreadsheet. As mentioned above, the transmission spectra and the

monitor's component spectra are translated into CIE x-y coordinates. The model then solves for the RGB coefficients. The coefficients are normalized such that the average coefficient equals 1.0. This normalization produces images whose luminance is approximately the same as the original image. For scalars greater than 1.0, it is highly probable that following the filtering some pixels will have component values greater than 255. In this case, the maximum component value would be scaled back to 255, and the same scaling applied to all pixels. All of the scaling assumes a linear Gamma. Non linear Gammas would affect the final image's color rendering in rather unpredictable fashion. Of course, a lookup table could be incorporated into the model to linearize the Gamma. Adding this feature would require each user to calibrate his own monitor. As most users would not likely have access to a photometer, a simpler solution should be sought.

As an example of the filtering process, consider the transmissivity spectra for the AH-64 Apache windscreen, a Comanche tinted visor, and the Microvision HMD. Figure 4-104 shows the component transmissivity curves and the resultant hardware transmissivity curve. The hardware curve is a notch filter with the green wavelengths greatly reduced while the red and blue wavelengths remain relatively unaffected. Figure 4-105 shows an image that has been filtered with this hardware transmissivity curve.

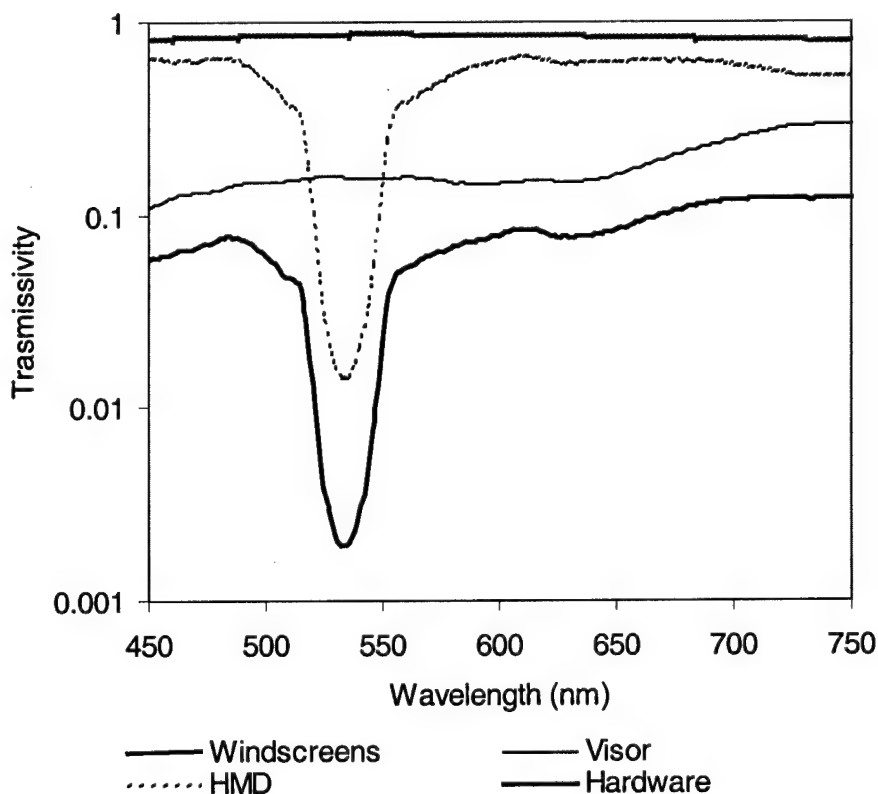


Figure 4-104. Transmissivity curves for the AH-64 windscreen, the Comanche tinted visor, the Microvision HMD, and the combined transmissivity curve.

To derive the filtering coefficients for the image in Figure 4-105, the transmissivity curve was convolved with the CIE color matching functions $x(\lambda)$, $y(\lambda)$, and $z(\lambda)$. These functions provide the relative contributions of light to the CIE tri-stimulus values X, Y and Z. The

matching functions were derived over λ from 380 to 780 nm. Due to our limited bandwidth, the curves were truncated to 450 and 750nm. Following the truncation, the resultant curves were normalized to have equal area. The hardware transmittance curve $T(\lambda)$ was convolved with the three normalized matching curves:

$$\begin{aligned} \lambda &= 750 \\ X &= \sum x(\lambda) \cdot T(\lambda) \\ \lambda &= 450 \end{aligned}$$

$$\begin{aligned} \lambda &= 750 \\ Y &= \sum y(\lambda) \cdot T(\lambda) \\ \lambda &= 450 \end{aligned}$$

$$\begin{aligned} \lambda &= 750 \\ Z &= \sum z(\lambda) \cdot T(\lambda) \\ \lambda &= 450 \end{aligned}$$

The convolved spectra have a resolution of 2 nm. The CIE color coordinates were derived using the following formula.

$$x = X/(X+Y+Z) \qquad y = Y/(X+Y+Z) \qquad z = Z/(X+Y+Z)$$

In similar fashion, the color coordinates were obtained for the monitor's red, green and blue spectra. Given these coordinates, it is then possible to determine the RGB primaries required to produce a color equivalent to the transmissivity curve (white light filtered by the curve). These primary coefficients were obtained for RGB space using the following calculations:

$$\begin{bmatrix} x_{red} & x_{green} & x_{blue} \\ y_{red} & y_{green} & y_{blue} \\ z_{red} & z_{green} & z_{blue} \end{bmatrix} \cdot \begin{bmatrix} C_R \\ C_G \\ C_B \end{bmatrix} = \begin{bmatrix} x \\ y \\ z \end{bmatrix}$$

Solving the above equation, the C component coefficients for RGB space were calculated. These coefficients were used to scale the photo shown in Figure 4-105.

Figures 4-106 and 4-107 depict the modeling of the IHADSS HMD. Here, a composite image is constructed based upon the relative contributions of the ambient scene, the HMD symbology and HMD noise. The relative contributions were calculated based upon the model's grayshade determination. For example, consider a grayshade of 1.0 where the peak luminance of the symbology and background scene are the same. To construct such an image, the symbology image and background image would be scaled to the peak pixel component of 127 and then added together. To maximize luminance, the composite image is linearly scaled so that the maximum pixel component is 255. The scaling of course would be different for other grayshade

values. HMD noise is added to the image based upon the HMD's contrast ratio. For a contrast ratio of 20, a five percent noise value is added to the composite image. To display symbology, RGB coefficients are determined for the HMD's emission spectra in the same fashion as the hardware transmissivity curve is converted to RGB values. A symbology image constructed of a black background and white symbology (an RGB of 255, 255, and 255) is multiplied by the RGB coefficients to simulate the emission spectra.

The composite images shown in Figures 4-106 and 4-107 should be considered a rough approximation of actual imagery reaching the eye. The utility here may be in the ability of the user to view the clarity of the symbology over a wide selection of different landscape images.

Conclusion

The preliminary model performs well when determining grayshades and the luminance and contrast of spectral images that reach the eye. Lasers, target spectra, skylight, and emission spectra can all be modeled fairly accurately. To assess the reliability of the color coefficients, an IHADSS combiner and six different color filters (Wratten) were evaluated using the following method: A CCD camera was used to photograph an outdoor scene with a good color mix. The camera captured multiple filtered and unfiltered images. The images were evaluated visually to select the images with the best visually correct color rendering. The selected images were analyzed by extracting the red, green and blue components and determining the mean pixel values. From these data, the color coefficients were determined empirically. These coefficients were then compared to the coefficients determined by the model. The model yielded results that were fairly consistent with the empirical data. For coefficients greater than 0.5, the largest discrepancy was 17%. For coefficients less than 0.5, the difference escalated especially for coefficients near zero (as expected). Since the color rendering largely depends on the higher coefficients, the color model appears to provide at least a first approximation to the actual HMD color filtering.

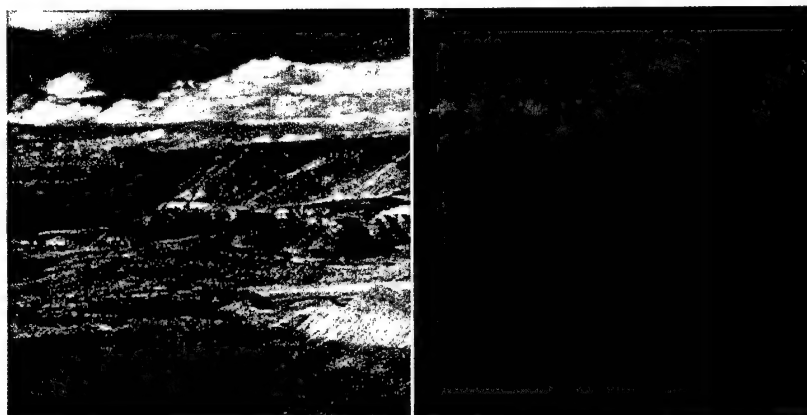
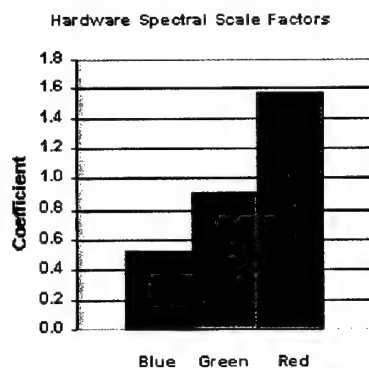


Figure 4-105. Spectral scale factors (left), original image (middle) and filtered image (left). Filtering was performed using the hardware transmissivity curve shown in Figure 4-104. The scale factors used to filter the image were Red = 1.57, Green = 0.91, and Blue = 0.52.

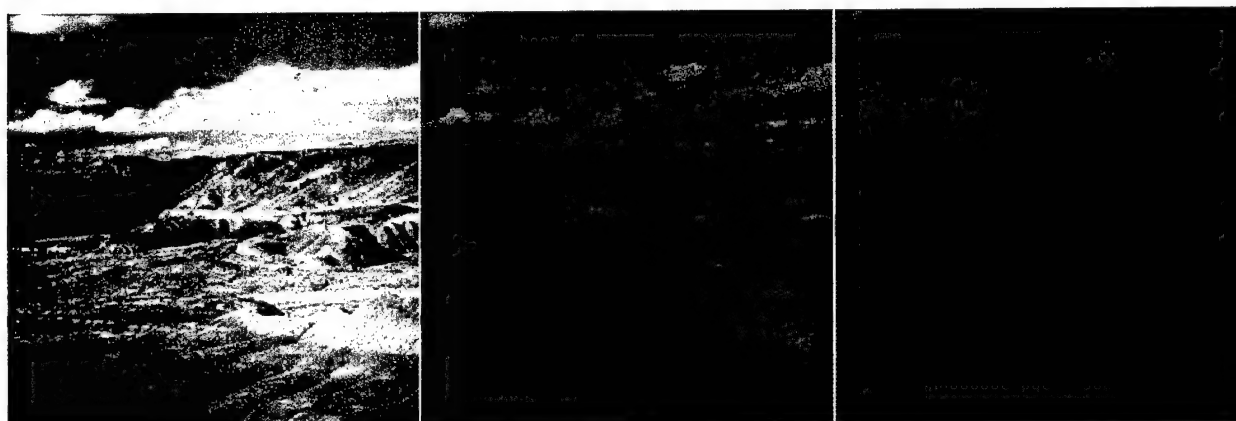


Figure 4-106. Original (left), filtered image (center) and composite image (right). Filtering was performed using an IHADSS HMD, an AH-64 Apache windscreen and a Comanche clear visor. Note the greenish tint and lack of red in the filtered image. The scale factors used to filter the image were Red = 0.70, Green = 1.37, and Blue = 0.93. The composite image represents HMD symbology against a see-through background. The composite resulted from 200 fL symbology against 5000fL peak ambient luminance. Under these conditions, the predicted HMD gray level is – (minus) 3.836. Please compare with Figure 4-107.

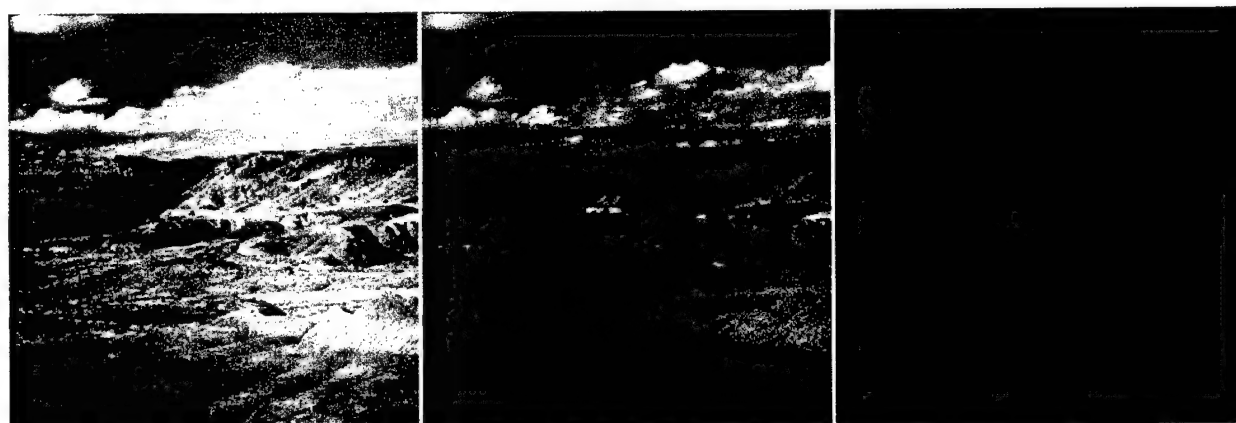


Figure 4-107. Same as in Figure 4-106, except that the Comanche tinted visor was used instead of the clear visor. The symbology is now discernable. Using the tinted visor, the HMD grayshades increased from –minus 3.836 to positive 1.187. Note the difference between the filtered image here and the filtered image in Figure 4-106. The only difference is the HMD. The scale factors used to filter the image were Red = 0.73, Green = 1.11, and Blue = 1.16.

References

- Alam, M. S., Zheng, S. H., Iftekharuddin, K. M., and Karim, M. A. 1992. Study of field-of-view overlap for night vision applications. Proceeding of the 1992 IEEE National Aerospace and Electronics Conference, NEACON Vol. 3, 1249-1255. Dayton, OH.
- American National Standard for Human Factors Engineering of Visual Display Terminal Workstations (ANSI/HFES 100-1988). 1988. Santa Monica, CA: Human Factors Society, Inc.
- Anderson, B. L., and Nakayama, K. 1994. Toward a general theory of stereopsis: Binocular matching, occluding contours, and fusion. *Psychological Review*, 101, No. 3, 414-445.
- Arditi, A. 1986. Binocular vision. In (K. R. Boff, L. Kaufman, and J. P. Thomas) *Handbook of perception and human performance*, Vol. 1, New York: John Wiley & Sons.
- Baker, C. H. and Nicholson, R. 1967. Raster scan parameters and target identification. Proceedings of the 19th Annual National Aerospace Electronics Conference (NAECON) pp. 285-290. Dayton, OH: Institute of Electrical and Electronic Engineers.
- Balram, N. and Olson, B. 1996. P-10: Multivalued modulation transfer function for flat-panel displays. Proceedings of Society for Information Display International Symposium Digest of Technical Papers, Vol. XXVII, pp. 429-432.
- Barten, P. G. H. 1990. Evaluation of subjective image quality with the SQRI method. Journal of the Optical Society of America, (A), Vol. 7, pp. 2024-2031.
- Barten, P. G. H. 1991. Resolution of liquid crystal displays. Proceedings of Society for Information Display International Symposium Digest of Technical Papers, Vol. XXII, pp. 772-775.
- Beasley, J. H., Martin, J. S., Klymenko, V., Harding, T. H., Verona, R.W., and Rash, C. E. 1995. A characterization of low luminance static and dynamic modulation transfer function curves for P-1, P-43, and P-53 phosphors. Fort Rucker, AL: U.S. Army Aeromedical Research Laboratory. USAARL Report No. 95-29.
- Biberman, L. M. (Ed.) 1973. *Perception of displayed information*. New York: Plenum Press.
- Biberman, L. M. and Tsou, B. 1991. Image display technology and problems, with emphasis on airborne systems. Institute for Defense Analysis, IDA paper P-2448.
- Billock, V., and Harding, T. H. 1988. Unpublished data on visual modeling. USAARL, Fort Rucker, AL.
- Bitzakidis, S. 1995. Moving image enhancement on AMLCDs. Journal of the Society for Information Display. Vol. 3, No 4, 249-255. (A).

Blackwell, H. R. 1946. Contrast thresholds of the human eye. *Journal of the Optical Society of America*, Vol. 36, p. 624-643.

Blackwell, O. M., and Blackwell, H. R. 1971. Visual performance data for 156 normal observers of various ages. *Journal of the Illuminating Engineering Society (IES) of North America*, October, p. 3-13.

Castellano, J. A. 1992. *Handbook of display technology*. Academic Press: San Diego, CA.

Calves, J. P., and Brun, J. 1978. Colour and brightness requirements for cockpit displays: proposal to evaluate their characteristics. Presented at the 29th AGARD Avionics Meeting, June 1978, Paris, France.

Crook, M. N., Hanson, J. A., and Weisz, A. 1954. Legibility of type as a function of stroke width, letter width, and letter spacing under low illumination. Dayton, Ohio: U.S. Air Force. WADC Technical Report 53-440.

Curtin, C., and Infante, C. 1996. *Fundamentals of Emissive Displays (short course s-3)*. Santa Ana, CA: Society for Information Display, p. 23.

Dragon, A. 1993. Sharp Application Note. Liquid Crystal Displays, Image quality: Measurements and definition.

Edgar, G. K., Carr, K. T., Williams, M., and Clark, A. L. 1991. The effect upon visual performance of varying binocular overlap. AGARD symposium on helmet-mounted displays and night vision goggles, Neuilly-sur-Seine, France, (AGARD Conference Proceedings 517), 8-1 to 8-15.

Farrell, R. J., and Booth, J. M. 1984. *Design handbook for imagery interpretation equipment*. Boeing Aerospace Company: Seattle, WA.

Feltz, J. C. 1990. Development of the modulation transfer function and contrast transfer function for discrete systems, particularly charge-coupled devices. *Optical Engineering*, Vol. 29, No. 8, pp. 893-904.

Fox, R. 1991. Binocular Rivalry. In (D. Regan) *Vision and visual dysfunction*, Vol. 9, 93-110.

Fox, R., and Check, R. 1968. Detection of motion during binocular rivalry suppression. *Journal of Experimental Psychology*, 78(3), 388-395.

Fox, R., and Check, R. 1972. Independence between binocular rivalry suppression duration and magnitude of suppression. *Journal of Experimental Psychology*, 93(2), 283-289.

Godfrey, G. W. 1982. *Principles of display illumination techniques for aerospace vehicle crew stations*. Aerospace Lighting Institute: Tampa, FL.

Greenson, J. C. Jr. 1996. International standards organization ergonomic standards for displays (seminar F-6). Society for Information Display Seminar Lecture Notes, Vol. II. Santa Ana, CA.

Harding, T. H., Martin, J. S., Beasley, H. H., Rash, C. E., Garrard, J. A. 1996. A survey of flat panel display technologies. Fort Rucker, AL: U.S. Army Aeromedical Research Laboratory. USAARL Report No. 96-19.

Harding, T. H., Martin, J. S., Beasley, H. H., Rash, C. E. 1997. A visual evaluation near the threshold of acuity of five color liquid-crystal flat-panel displays. Fort Rucker, AL: U.S. Army Aeromedical Research Laboratory. USAARL Report No. 97-29.

Harding, T. H., Martin, J. S., Beasley, H. H., Rash, C. E. 1996. Figures of merit and performance specifications for the IHADSS and ANVIS. Fort Rucker, AL: U.S. Army Aeromedical Research Laboratory. USAARL Report No. 96-13.

Harding, T. H., Beasley, H. H., Martin, J. S., Rash, C. E., McLean, W. E., Mora, J. C., McEntire, B. J., 1988. Optical and biodynamic evaluation of the helmet mounted integrated display sight system (HIDSS) for the RAH-66 Comanche development and validation program phase. Fort Rucker, AL: U.S. Army Aeromedical Research Laboratory. USAARL Report No. 98-22.

Holst, G. C. 1995. Electro-optical imaging system performance. Winter Park, FL: JCD Publishing and Bellingham, WA: SPIE Optical Engineering Press.

Human Factors Society, Inc. 1988. American National Standard for Human Factors Engineering of Visual Display Terminal Workstations. ANSI/HFS 100-1988. Santa Monica, CA: Human Factors Society, Inc.

Illuminating Engineering Society (IES) of North America. Kaufman, J. E., editor. 1984. IES Lighting handbook. Illuminating Engineering Society of North America: New York, NY.

Imbeau, D., Wierwille, W. W., Wolf, L. D., and Chun, G. A. 1989. Effects of instrument panel luminance and chromaticity on reading performance and preference in simulated driving. Human Factors, Vol. 31, No. 2, pp. 161-166.

Infante, C. 1993. On the modulation transfer function of matrix displays. Journal of the Society for Information Display, Vol. 1 No. 4, pp. 449-450.

Jennings, S., and Dion, M. 1997. An investigation of helmet-mounted display field-of-view and overlap tradeoffs. Proceedings of the Human Factors and Ergonomics, 41st Annual Meeting, 32-36.

Jennings, S., Dion, M., Srinivasan, R. and Baille S. 1997. An investigation of helmet-mounted display field-of-view and overlap tradeoff in rotorcraft handling qualities. 23rd European Rotorcraft Forum, 43.1-43.14.

- Kaiser, P. K., Herzberg, P. A., and Boynton, R. M. 1971. Chromatic border distinctness and its relation to saturation. *Vision Research*, Vol. 11, p. 953.
- Karim, M. A. (Ed.). 1992. *Electra-optical Displays*. New York: Marcel Dekker, Inc.
- Kaufman, L. 1963. On the spread of suppression and binocular rivalry. *Vision Research*, 3, 401 - 415.
- Kaufman, L. 1964. Suppression and fusion in viewing complex stereograms. *American Journal of Psychology*, 77, 193-205.
- Keller, P. A. 1997. *Electronic display measurement*. New York: John Wiley & Sons, Inc.
- Kenyon, R. V., and Kneller, E. W. 1993. The effects of field of view size on the control of roll motion. *IEEE transactions on systems, man, and cybernetics*, 23(1), 183-193.
- Klymenko, V., Harding, T. H., Beasley, H. H., Martin, J. S. and Rash, C. E. 1999. The effect of helmet mounted display field-of-view configurations on target acquisition. Fort Rucker, AL: U.S. Army Aeromedical Research Laboratory. USAARL Report 99-19.
- Klymenko, V., Harding, T. H., Martin, J. S., Beasley, H. H., Rash, C. E., and Rabin, J. C. 1997. Image quality figures of merit for contrast in CRT and flat panel displays. Fort Rucker, AL: U.S. Army Aeromedical Research Laboratory. USAARL Report No. 97-17.
- Klymenko, V., Verona, R. W., Beasley, H. H., Martin, J. S., and McLean W. E. 1994a. Factors affecting fragmentation of partial binocular overlap displays. Fort Rucker, AL: U.S. Army Aeromedical Research Laboratory. USAARL Report 94-29.
- Klymenko, V., Verona, R. W., Martin, J. S., Beasley, H. H., and McLean W. E. 1994b. Factors affecting the perception of luning in monocular regions of partial binocular overlap displays. Fort Rucker, AL: U.S. Army Aeromedical Research Laboratory. USAARL Report 94-47.
- Klymenko, V., Verona, R. W., Martin, J. S., Beasley, H. H., and McLean W. E. 1994c. The effect of binocular overlap mode on contrast thresholds across the field-of-view as a function of spatial and temporal frequency. Fort Rucker, AL: U.S. Army Aeromedical Research Laboratory. USAARL Report 94-49.
- Krim, M. A., Editor. 1992. *Electra-optical displays*. Marcel Dekker: New York.
- Kruk, R., and Longridge, T. M. 1984. Binocular overlap in a fiber optic helmet mounted display. The image 3 conference proceedings, 363, 363-377. Brooks Air Force Base, TX: Air Force Human Resources Laboratory, Air Force Systems Command. AFHRL-TR-84-36.
- Landau, F. 1990. The effect on visual recognition performance of misregistration and overlap for a biocular helmet mounted display. *SPIE proceedings*, Vol. 1290, helmet-mounted displays II, 173-184. San Jose, CA: SPIE-The International Society for Optical Engineering.

Lindholm, J. M. 1992. Perceptual effects of Spatiotemporal sampling. In (M. A. Karim-Ed.) *Electro-optical Displays*. (Chapter 19, pp 787-808). NY: Marcel Dekker, Inc.

Lippert, T. M. 1986. Color-difference predictions of legibility performance for CRT raster imagery. In *Society of Information Digest* (pp. 86-89). New York, NY: Palisades Institute for Research Services, Inc.

Lovasik, J. V., Matthews, M. L., and Kergoat, H. 1989. Neural, optical, and search performance in prolonged viewing of chromatic displays. *Human Factors*, Vol. 31, No. 3, pp. 273-289.

MacDonald, L. W., and Lowe, A. C. (Eds.) 1997. *Display Systems: Design and Applications*. New York: John Wiley & Sons, Inc.

Marr, D., Poggio, T., Hildreth, E. 1980. The smallest channel in human vision. *Journal of the Optical Society of America*, Vol. 70, p. 868-870.

Masterman, H., Johnson, C., Silverstein, M. F. 1990. *How to Select a CRT Monitor*. Medfield, MA: Beta Review, Inc.

Meister, D. 1984. Human engineering data base for design and selection of cathode ray tube and other display systems. San Diego, CA: Navy Personnel and Research Training Center. Report No. NPRDC TR 84-51.

Melzer, J. E., and Moffitt, K. 1989. Partial binocular overlap in helmet-mounted displays. *SPIE Proceedings*, Vol. 1117, display system optics II, 56-62. San Jose, CA: SPIE-The International Society for Optical Engineering.

Melzer, J. E., and Moffitt, K. 1991. An ecological approach to partial binocular-overlap. *SPIE proceedings*, Vol. 1456, large screen projection, ionic, and helmet-mounted displays, 175-191. San Jose, CA: SPIE-The International Society for Optical Engineering.

Moffitt, K. 1989. *Lining and target detection*. San Jose, CA: Kaiser Electronics.

Moffitt, K. 1991. *Partial binocular overlap: concepts, research, & systems*. San Jose, CA: Kaiser Electronics.

Moffitt, K., and Melzer, J. 1991. *Partial binocular overlap*. San Jose, CA: Kaiser Electronics.

Moon, D. 1986. *Image quality for electro-optical displays: variables, metrics, and measurements*. Ph.D. dissertation, University of Dayton, Ohio.

North Atlantic Treaty Organization. *Design criteria for flat panel technology displays. Study 7095 for proposed NATO Standardization Agreement (STANAG7095)*.

Norman, H. F., Norman, J. F., and Bilotta, J. 2000. The temporal course of suppression during binocular rivalry. *Perception*, 29(7), 831-841.

Oakley, D. 1984. Raster graphics display technology: A review. *Displays*, Oct., pp. 229-234.

Olson, B. and Balram, N. 1996. Video quality on AMLCD versus Shadow-Mask CRT Proceedings of SPJE: Cockpit Displays III. Aerosense' 96, Vol. 2734, pp. 12-22.

Osgood, R. K., and Wells, M. J. 1991. The effect of field-of-view size on performance of a simulated air-to-ground night attack. AGARD symposium on helmet-mounted displays and night vision goggles (AGARD Conference Proceedings 517), 10-1 to 10-7, Aerospace medical panel symposium, Pensacola, FL.

Parker, D. 1997. The dynamic performance of CRT and LC displays. In (L. W. MacDonald and A. C. Lowe-Eds.) *Display Systems: Design and Applications*. (Chapter 18, pp 353-364). New York: John Wiley & Sons, Inc.

Pastoor, S. 1990. Legibility and subjective preference for color combinations in text. *Human Factors*, Vol. 32, No. 2, pp. 157-171.

Peli, E. 1990 Contrast in complex images. *Journal of the Optical Society, A*, Vol. 7, No. 10, 2032-2040.

Post, D. L. 1983. Color contrast metrics for complex images. Doctoral dissertation, Virginia Polytechnic Institute and State University, Blacksburg, VA.

Rabin, J. and Wiley, R. 1995. Dynamic visual performance: Comparison between helmet-mounted CRTs and LCDs. Journal of the Society of Information Display, Vol. 3 No. 3, pp. 97-100.

Rash, C. E. and Becher, J. 1982. Analysis of image smear in CT displays due to scan rate and phosphor persistence. Fort Rucker, AL: U.S. Army Aeromedical Research Laboratory. USAARL Report No. 83-5.

Rash, C. E., Monroe, D. R., and Verona, R. W. 1981. Computer model for the evaluation of symbology contrast in the Integrated Helmet and Display Sighting System. Fort Rucker, AL: U.S. Army Aeromedical Research Laboratory. USAARL Report No. 81-6.

Rash, C. E., Beasley, H. H., Martin, J. S., and Harding, T. H., 1999. Alternate source evaluation for the aircrew integrated helmet system Comanche compatibility program phase IIB. Fort Rucker, AL: U.S. Army Aeromedical Research Laboratory. USAARL Report No. 99-06.

Rash, C. E., Harding, T. H., Martin, J. S., and Beasley, H. H., 1999. Concept phase evaluation of the Microvision, Inc., aircrew integrated helmet system HGU-56P virtual retinal display. Fort Rucker, AL: U.S. Army Aeromedical Research Laboratory. USAARL Report No. 99-18.

- Roehrig, H., Blume, H., Ji, T. and Browne, M. (1990). Performance tests and quality control of cathode ray tube displays. *Journal of Digital Imaging*, Vol. 3, No. 3, pp. 134-145.
- Schuchard, R. A. 1990 Evaluation of uniform CRT display scales with visual threshold data. *Applied Optics*, Vol.29, No.4, 570-578.
- Seeley, G. W., Fisher, H. D., Stempski, M. O., Borgstrom, M., Bjelland, J., and Capp, M. P. 1987. Total digital radiology department: spatial resolution requirements. *American Journal of Radiology*, Vol. 148 No. 2, pp.421-426.
- Shurtleff, D. A., and Wuersch, W. F. 1979. Legibility criteria in design and selection of data displays for group viewing. In *Proceedings of the Human Factors Society 23rd Annual Meeting* (p 411-414). Santa Monica, CA: Human Factors Society, Inc.
- Silverstein, M.F. 1989. How to Select a Flat Panel Display. Medfield, MA: Beta Review, Inc.
- Sobel, A. 1992. Flat panel displays. In (M.A. Karim, Ed.). *Electra-optical displays*, 121-185. Marcel Dekker: New York.
- Silverstein, L. D., Kranz, J. H., Gomer, F. E., Yeh, Y. and Monty, R. W. 1990. Effects of spatial sampling and luminance quantization on the image quality of color matrix displays. *Journal of the Optical Society of America, A*, Vol.7, No. 9, pp.1955-1968.
- Snyder, H. L. 1973. Image quality and observer performance. In (L. Biberman) Perception of Displayed Information. New York: Plenum Press, pp 87- 118.
- Snyder, H. L. 1980. Human visual performance and flat panel display image quality. Virginia Polytechnical Institute and State University Technical Report HFL-80-1.
- Sobel, A. 1992. Flat panel displays. In (M. A. Karim) *Electra-optical Displays*. NY: Marcel Dekker, Inc.
- Tannas, L. E., Editor. 1985. Flat-panel displays and CRTs. Van Nostrand Reinhold: New York.
- Task, H. L. 1979. An evaluation and comparison of several measures of image quality for television displays. Wright Patterson AFB, OH: Aerospace Medical Research laboratory. AMRL-TR-79-7.
- Task, H. L. and Verona, R. W. 1976. A new measure of television display quality relatable observer performance. AFAMRL-TR-76-73.
- Toms, M. L. and Cone, S.M. 1995. Subjective LCD-CRT comparison of USAF transport aircraft cockpit electronic display formats. *Proceedings of SPIE, Cockpit Displays II*, Vol.2462, pp. 36-46.

Toms, M. L., Cone, S. M., and Cavallaro, J. J. 1995. Subjective image quality comparisons of AMLCD and CRT implementations of electronic flight formats. Final Report (WL-TR-95-3074). Veda, Inc.

Travis, D. S., Bowles, S., Seton, J., and Peppe, R. Reading from color displays: A psychophysical model. Human Factors, Vol. 32, No. 2, pp. 147-156.

Van Meeteren, A. 1973. Visual aspects of image intensification. Ph.D. Dissertation, University of Utrecht. The Netherlands.

Verona, R.W. 1992. A Comparison of CRT Display Measurement Techniques. Proceedings of SPIE. Helmet Mounted Displays III, Vol. 1695, pp. 117-127.

Verona, R. W., Beasley, H. H., Martin, J. S., Klymenko, V. and Rash, C. E. 1994. Dynamic sine wave response measurements of CRT displays using sinusoidal counterphase modulation. Fort Rucker, AL: U.S. Army Aeromedical Research Laboratory. USAARL Report No. 94-22.

Wells, M. J., Venturino, M., and Osgood, R. K. 1989. The effect of field-of-view on performance at a simple simulated air-to-air mission. SPIE proceedings, Vol. 1116, helmet-mounted displays, 126-137. San Jose, CA: SPIE-The International Society for Optical Engineering.

Widdel, H., and Post, D. L. (Editors) 1992. Color in electronic displays. Plenum Press: New York.

Wilson, H. R., McFarlane, D. K., and Phillips, G. C. 1983. Spatial frequency tuning of orientation selective units estimated by oblique masking. Vision Research. 23, p. 873-882.

Wolpert, L. 1990. Field-of-view information for self-motion perception. In (R. Warren and A. H. Wertheim) Perception and control of self-motion. Hillsdale, NJ: Lawrence Earlbaum Associates.

TASK 5

Mathematical Modeling and Computer Simulation of Human Bio-Dynamics and Crash Environments

INTRODUCTION

The crashworthy design of modern Army helicopters has resulted in fewer injuries from the impact acceleration in survivable crashes. The injury reduction, primarily to the spinal column, may be attributed to the energy-absorbing seat design, which limits the forces transmitted to the seated pilot. Head and upper torso injuries also have been addressed with various design concepts to cockpit interior components, such as the breakaway optical relay tube used by the gunner in the AH-64 Apache helicopter. Following the introduction of these energy-absorbing devices into the U.S. Army Apache and Black Hawk helicopters, the injuries sustained in Army helicopter crashes between 1980 and 1985 due to excessive accelerations have dropped relative to other helicopters (Shanahan, 1989). Ten years later, the risk of injury to U.S. Army helicopters occupants during the 1990-94 period was reduced significantly, primarily due to a 40% drop in head injuries (Shannon, et. al., 1996). Despite the success of the crash-worthy design of modern helicopters, flail injuries continue to occur and, in fact, outnumber acceleration injuries. Contact or flail injuries are produced in secondary collisions which result from inadequate restraints, collapsing structure, or a combination of both.

The addition of HSDs has increased the risk of neck injury due to inertial loads generated during helicopter crashes. Furthermore, the emergence of new helmet design concepts has raised new design and safety questions. For these reasons, this study was undertaken to evaluate the relationship between HSD mass and center of mass (CM) placement for a number of different impact conditions and seat stroking distances.

A widely used tool for biodynamic simulation and accident reconstruction is the ATB simulation software. Given a number of body segments connected by mathematical models at common joints, ATB automatically formulates the differential equations that govern the motion of the body segments. Acceleration pulses that approximate crash profiles drive the model. ATB then integrates those equations to compute the kinematics of every body segment and to calculate the forces at all joints. The software can produce time histories of force and acceleration of body segments that are then used to predict injuries. Each simulation represents a unique combination of seat stroking distance, impact condition, head-supported mass, and CM position.

This task has four sub-sections:

- Mass and location criteria of Head-Supported devices using Articulated Total Body Simulations
- Effects of Seat Stroke Distance on the Allowable Mass of Head Supported Devices
- Influence of Airbags on Selection of Mass and CM placements of Head Supported Devices

- Effects of optical relay tube (ORT) display modifications on the risk of facial and neck injury

Study was conducted to understand the effects of seat stroke distance, head support devices (weight and location) on the inertial loads being exerted on the head and neck in typical crash environments. In the other section the focus of the investigation was to compare the risk of impact between occupant's head and both the standard display and the flat-panel display in the event of a helicopter mishap.

MASS AND LOCATION CRITERIA OF HEAD-SUPPORTED DEVICES USING ARTICULATED BODY SIMULATIONS

Introduction

During the evolution of Army rotary-wing aviation, the amount of head-borne mass has steadily increased. This is due in large part to the evolution of aircrew helmets. Prior to the 1950's, aircrew flight helmets were nothing more than leather or cloth caps. Beginning in the 1950's, hard shell helmets were introduced into service. These helmets provided a dramatic improvement in head impact protection and provided greater sound attenuation and integral communications equipment. These benefits came at the price of increased helmet mass – the mass of these hard shell helmets was three times that of their leather and cloth counterparts. Furthermore, with the advent of night vision systems during the 1980's, helmets began to serve as mounting platforms for numerous combat-essential devices. Among these devices are night vision goggles (NVGs) and the AH-64's integrated helmet and display sighting system (IHADSS) helmet display unit (HDU) which displays weapon targeting information, forward looking infrared (FLIR), and flight instrumentation symbology. With the addition of each of these systems, the amount of head-supported mass has steadily grown.

Biodynamic Simulations

The major simulation parameters would be discussed in this section.

Occupant model

The mid-size male Hybrid III manikin was used to represent the 50th percentile male aviator. The GEBOD program was used to generate the segment and joint data for a sitting Hybrid III dummy.

Energy-attenuating seat

The AH-64 crewseat was designed to attenuate energy in a vertical direction through use of a pair of inversion tubes. In the simulations, the energy attenuating mechanism was modeled using a spring/damper system. The spring was used to absorb the vertical component of impact energy while the viscous damper was used to limit seat travel and prevent the seat from rebounding.

The crewseat used in the co-pilot/gunner (CPG) station of the AH-64 is designed to stroke a maximum of 25.4 cm in the vertical direction. However, accident investigations performed by the U.S. Army Safety Center have shown that in many helicopter mishaps, the

travel of the seat can be hindered by obstructions resulting from fuselage deformation. Therefore, partial seat stroking distances of 2.54 centimeters (cm) and 15.24 cm were modeled in addition to the full stroking distance of 25.4 cm.

Restraint system

A five-point harness was included in the simulations. The harness included two waist belts, two shoulder belts, and a center tie-down strap. The inertia reels with which the shoulder belts are equipped were also modeled. Optimally functioning inertia reels were modeled by giving the shoulder belts an initial slack of 0.254 cm. This simulated the inertia reels locking within 9 milliseconds (msec) of impact.

Impact conditions

Impact conditions are dependent on variables such as helicopter velocity, attitude, and design. Due to their ability to fly vertically and horizontally, helicopters can impact terrain in a variety of attitudes. In addition, unlike older aircraft such as the UH-1, modern helicopters such as the UH-60 and AH-64 have been constructed with crashworthiness in mind. Energy-absorbing landing gear, fuselage structures, and seats have been designed with the intent to reduce the acceleration transferred to the occupants. Therefore, for identical impact orientations and velocities, the duration and shape of the acceleration profiles experienced by the occupants of a UH-60 would differ from those experienced by the occupants of a UH-1. For these reasons, there is no one typical impact condition from the occupant's perspective.

Five different impact conditions were considered in this investigation. The first three impact conditions modeled vertical impacts between the helicopter and a rigid horizontal surface. The last two conditions simulated the helicopter impacting horizontally with a rigid vertical surface. These impact acceleration profiles and subject orientations are presented in Figures 5-1 through 5-5.

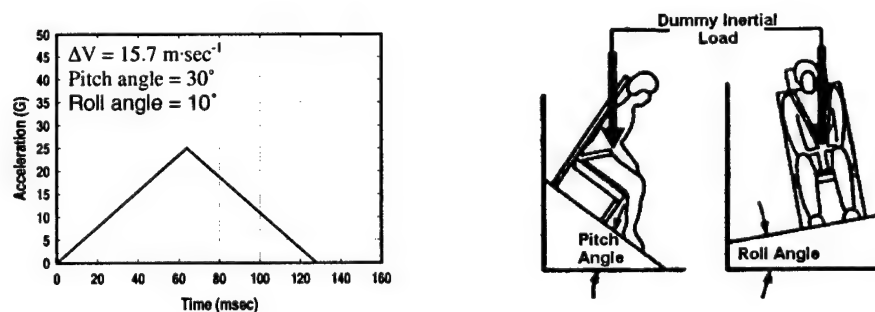


Figure 5-1. Acceleration pulse and subject orientation modeled in impact condition 1.

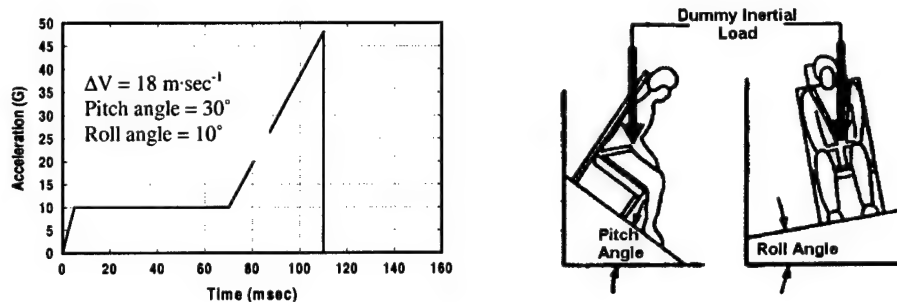


Figure 5-2. Acceleration pulse and subject orientation modeled in impact condition 2.

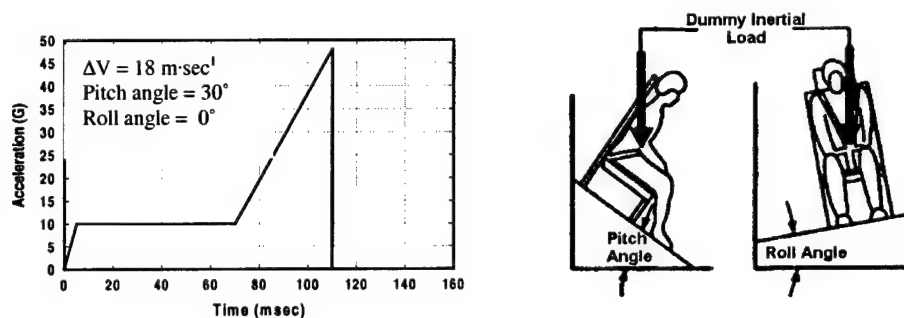


Figure 5-3. Acceleration pulse and subject orientation modeled in impact condition 3.

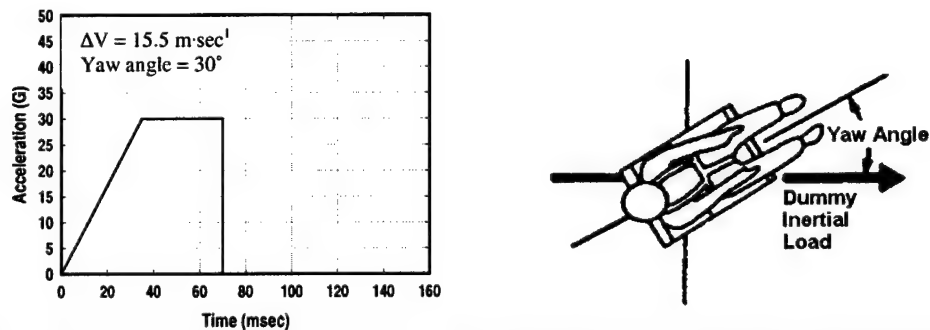


Figure 5-4. Acceleration pulse and subject orientation modeled in impact condition 4.

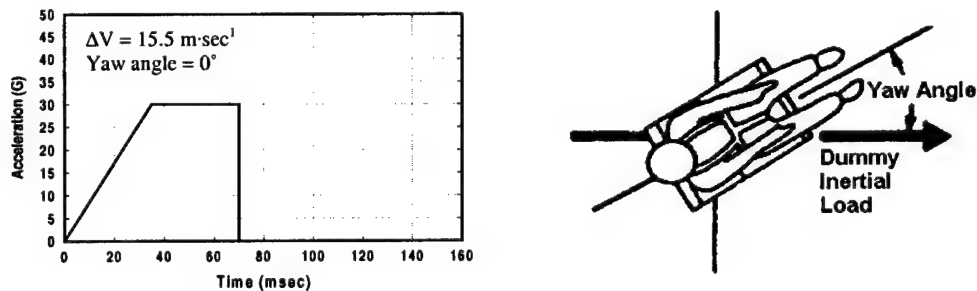


Figure 5-5. Acceleration pulse and subject orientation modeled in impact condition 5.

Head-supported mass

Three HSD masses were simulated in this investigation. These masses were 0.45 kilogram (kg), 1.35 kg, and 2.70 kg. The masses correspond to weights of 4.45 Newtons (N), or 1 pound (lb), 13.35 N (3 lbs), and 26.7 N (6 lbs), respectively. This range encompassed the masses associated with HSDs currently in the U.S. Army aviation inventory.

Center of mass position

At each combination of impact condition, helmet mass, and seat stroking distance, 147 HSD CM positions were simulated. The CM positions were grouped by lateral CM position into three sets of 49 discrete x-z pairs. The first group was located in a plane 3 cm to the left of the head CM ($y = -3$ cm). The second group was clustered in the mid-sagittal plane of the occupant's head ($y = 0$ cm). The final set of 49 x-z pairs was positioned in a plane 3 cm to the right of the head CM ($y = +3$ cm). In each of the three planes, the longitudinal coordinates (x positions) of the HSD CM positions were located at -6 cm, -4 cm, -2 cm, 0 cm, +2 cm, +4 cm, and +6 cm relative to the head CM. Likewise, the axial coordinates (z positions) were placed at -6 cm, -4 cm, -2 cm, 0 cm, +2 cm, +4 cm, and +6 cm. These CM positions resulted in 147 discrete combinations of longitudinal, lateral, and axial coordinates.

Discussion

Most aircrew helmets in the U.S. Army inventory have their CM positions within the mid-sagittal plane of the head. For this reason, discussions of the relationship between HSD mass and CM placement will be limited to results of simulations conducted within the mid-sagittal plane at a 2.54-cm seat stroking distance. Furthermore, the effect of placing lateral CM positions off the mid-sagittal plane will be presented for both symmetric and asymmetric impact conditions. In addition, the effects of seat stroking distance on both vertical and horizontal impact conditions will be discussed.

HSD mass and CM position

In the case of impact condition 1, acceptable x-z CM locations were determined for each of the three HSD masses. However, the number of acceptable x-z CM locations diminished from 49 at a HSD mass of 0.45 kg to 18 at a HSD mass of 2.70 kg. As for impact condition 2, only three acceptable x-z CM locations could be determined for a HSD mass of 0.45 kg. For the other two masses, the number of acceptable x-z CM locations diminished to zero. Similarly, for impact condition 3, no acceptable x-z CM positions were found for any of the HSD masses. Acceptable x-z CM locations were determined for HSD masses of 0.45 kg and 1.35 kg when impact conditions 4 and 5 were considered. As with the results of impact condition 1, the number of acceptable x-z CM positions was reduced with increasing HSD mass. Similar trends were found for the other combinations of lateral CM position and seat stroking distance.

It is also interesting to note that as HSD mass grows larger, acceptable x-z CM positions begin to cluster to the rear of and below the head CM. This trend is most obvious when impact conditions 1 and 4 are considered. For impact condition 1, when HSD mass was increased from 0.45 to 2.70 kg, the region of acceptable x-z CM positions reduced from one that encompassed all 49 CM positions to a trapezoidal shaped region spanning from $x = -6$ to -2 cm and from $z = +6$ to -4 cm. In impact condition 4, at an HSD mass of 0.45 kg, the region of acceptable x-z CM positions encompassed all 49 CM positions. When HSD mass was increased to 1.35 kg, most of the acceptable x-z CM positions became clustered in a region spanning from $x = -6$ to -2 cm and

from $z = +6$ to $+2$ cm. Three other acceptable x - z combinations occurred at a z position of $+2$ cm and x positions of 0, $+2$, and $+4$ cm. Again, similar trends were found for the other combinations of lateral CM position and seat stroking distance.

Effects of lateral CM position

Impact condition 4 is an asymmetric impact condition; i.e., the inertial load does not act strictly within the occupant's mid-sagittal plane. This is caused by the 30° yaw condition associated with this crash scenario. Impact condition 5 is symmetric, in that there are no yaw, pitch or roll conditions associated with this impact condition that would cause the load to be applied outside the mid-sagittal plane.

Lateral CM position has no effect on the acceptable HSD mass. In the case of impact condition 4, HSD masses of up to 1.35 kg could be worn no matter which lateral CM plane their longitudinal and axial CM positions are placed within. In addition, an acceptable HSD mass of up to 1.35 kg could be worn within each lateral CM plane. However, for both impact conditions, x - z CM placement is extremely limited for the 1.35-kg HSD mass.

Also, placing the HSD CM position off the mid-sagittal plane reduces the number of acceptable x - z CM positions for each HSD mass. Comparisons between the results of placing the lateral CM position at $+3$ cm and coincident with the mid-sagittal plane show that placing the lateral CM position at $+3$ cm reduces the number of acceptable x - z CM positions. Placing CM positions to either side of the mid-sagittal plane reduces the number of acceptable x - z CM positions when compared with results involving CM positions within the mid-sagittal plane.

There is an exception, however, in the case of impact condition 4 and an HSD mass of 1.35 kg. Placing the lateral CM position at -3 cm increases the number of acceptable x - z CM positions compared to a lateral CM coincident with the mid-sagittal plane. However, to date, no statistical analysis has been performed on these data. Therefore, it is unknown whether the increased number of acceptable x - z CM positions is statistically significant.

Effects of seat-stroking distance

In the case of a vertical impact condition, increased seat stroking distance allows for greater flexibility in the selection of HSD mass and x - z CM placement. At a seat stroking distance of 2.54 cm, the maximum HSD mass that could be worn by an aviator was 0.45 kg, but by increasing the distance that the seat is allowed to travel to 15.24 or 25.4 cm, the allowable HSD mass increases to 2.70 kg. Furthermore, acceptable regions of x - z CM position grow larger as seat stroking distance increases. Take, for example, an HSD mass of 1.35 kg. With the stroking distance limited to 2.54 cm, this HSD mass could not be positioned anywhere within the mid-sagittal plane without posing a serious risk of neck injury. However, the number of acceptable x - z CM positions grows to 15 with a stroking distance of 15.24 cm and to 49 when the seat is allowed to stroke 25.4 cm. The results of impact conditions 1 and 3 exhibit similar trends.

The results of impact condition 5 show that seat stroking distance has no effect on acceptable HSD mass and x - z CM placement when horizontal impact conditions are considered.

EFFECTS OF SEAT STROKE DISTANCE ON THE ALLOWABLE MASS OF HEAD SUPPORTED DEVICES

Introduction

Aircraft crew safety and crash survival has been the subject of considerable attention since the early days of aviation. In the evolution process of Army aircraft, numerous protective devices and systems have been introduced into the aircraft/aircrew. Some of these devices include helmet-mounted electronics, protective masks, body armor, advanced restraint systems, inflatable restraint devices and energy attenuating seats. Of the additional equipment carried by an Army aviator, few serve as many functions as the modern helmet. In addition to providing head impact protection, today's helmet is a mounting platform for many advanced devices such as night vision goggles (NVG) and integrated helmet and display sighting system (IHADSS).

The addition of head-supported devices (HSD) has increased the risk of neck injury due to inertial loads generated during helicopter crashes. Furthermore, it is hypothesized that the use of energy attenuating helicopter seats may influence helmet design. Therefore, the objective of this study is to investigate the effects of stroking distances on the inertial loads being exerted on the head and neck in five typical helicopter crash environments and four different head supported device masses.

Biodynamic simulations

A number of parameters were considered to determine head-borne mass criteria under various conditions. Using ATB simulations, biodynamic response to five different crash pulses, also referred to as impact conditions, were generated for the Hybrid III manikin. The GEBOD program (Kaleps, 1988; Gross, 1991) was used to generate the segment and joint data for a sitting Hybrid III dummy. For each of these five impact conditions, four different HSD masses and two different seat stroke distances were considered. Time histories for the transmitted head and neck forces and moments were recorded for each case. These time histories were used to determine a correlation between the HSD mass and transmitted force or moment levels for each allowable seat stroke distance. The following parameters were modeled in the simulations:

Impact conditions. The first condition was a 25 g vertical triangular pulse of 128 millisecond (msec) duration (velocity change of 15.7 m/s) with 30 deg pitch and 10 deg roll subject orientation. The second condition was a 30 g horizontal triangular pulse of 160 msec duration (velocity change of 23.5 m/s) with 30 deg yaw subject orientation. The third condition was an 18 g vertical triangular pulse of 148 msec duration (velocity change of 13.1 m/s) with 30 deg roll subject orientation. The fourth pulse was a 10-48 g vertical bi-level pulse of 110 msec total duration (velocity change of 18 m/s) with 30 deg pitch and 10 deg roll subject orientation. Finally, the fifth condition was a 30 g horizontal trapezoidal pulse of 70 msec duration (velocity change of 15.5 m/s) with 30 deg roll subject orientation.

Helmet mass. Four HSD masses of 0.45, 1.36, 2.72, and 4.09 kilograms were simulated. The effect of helmet mass was incorporated into the head segment by adding the mass of the helmet

to the mass of the head. Then, the mass moments of inertia of the head segment were altered to account for the additional mass.

CM location. One CM position was simulated in this study. The CM of the HSD mass coincided with the CM of the head. For the Hybrid III dummy, this location is 1.4 centimeters (cm) above and 5.08 cm to the front of the occipital condyles in the mid-sagittal plane.

Seat stroke. The effect of seat stroke was incorporated into the simulations (Beale, et al., 1996). Since the UH-60 and AH-64 helicopters are equipped with energy absorbing seats, the simulations were expanded to include the stroking of the seat. These simulations were confined to allowable seat stroke distances of 2.5 cm and 25 cm.

Restraint system. A standard four-point restraint system was used in the simulations. The harness system was modeled to simulate "no malfunctions" during the different crash scenarios, i.e. the inertia reels locked at the onset of each crash pulse.

Complete motion. The total duration of each simulation was confined to 400 msec. This was necessary to allow sufficient time for the head motion to develop. Response parameters were output at 1-msec intervals.

Inertial loading. Only the inertial loading exerted on the head-neck interface was considered. This was accomplished by determining the point in time, if any, at which the head contacted the seat's headrest. The analysis process was then carried out to that time point only. Beyond that point, the data was determined to be contaminated by contact forces and therefore, not representative of purely inertial loadings.

Injury assessment

Injury assessment generally requires the use of crash dummies in actual crash tests to determine the forces of impact. These forces are then used to assess the risk of injury to humans. The method of assessment is to compare the magnitudes and durations of individual force and acceleration pulses, measured at strategic locations in the dummy, to acceptable tolerance limits. Assessment methods and injury criteria are well defined for the Hybrid III type dummies (Mertz, 1993). In this study, the same assessment methods and injury criteria are applied to the time history generated by the ATB simulations. The main features of the analysis method used in this study to arrive at the injury assessment are explained in the following paragraphs.

Response parameters. Only the response parameters with published threshold values were considered in this analysis. These response parameters were the fore-aft shear forces ($\pm F_x$), compression ($-F_z$), tension ($+F_z$), extension ($-M_y$) and flexion ($+M_y$), measured at the occipital condyles. For the extension and flexion moments, the threshold values are constant at 57 N.m and 190 N.m, respectively. The published threshold values for compression-tension and fore-aft shear forces are shown in Figures 5-6 and 5-7, respectively (Mertz, 1993).

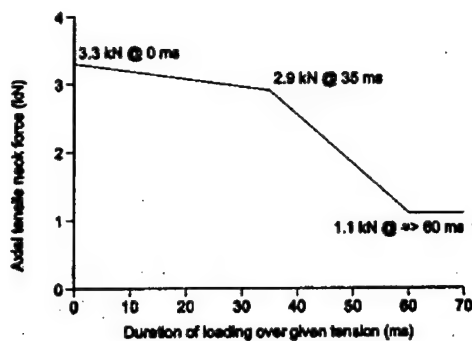


Figure 5-6. Axial tensile neck force.

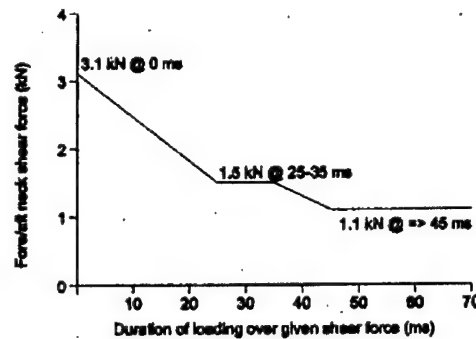


Figure 5-7. Fore/Aft neck shear force.

Results and discussions

Time history traces for the six response parameters were output from the simulations. From these time histories, evaluation of the effects of seat stroke was done using the injury assessment techniques described earlier. It should be noted that this assessment method is used as a comparative tool to allow evaluation of results of paired simulations without inferring any injury outcome.

The time history for neck compression-tension force is shown in Figure 5-8. In this case, the occupant (Hybrid III) is wearing a 1.4 kg helmet while subjected to impact condition four. In this example, the solid line represents the time history for the allowable 2.5 cm seat stroke distance. The results of the allowable 25 cm seat stroke are represented by the dotted line. From this figure it is evident that the peak values of the neck compression and tension forces reduce dramatically for the 25 cm seat stroke as compared to the 2.5 cm seat stroke.

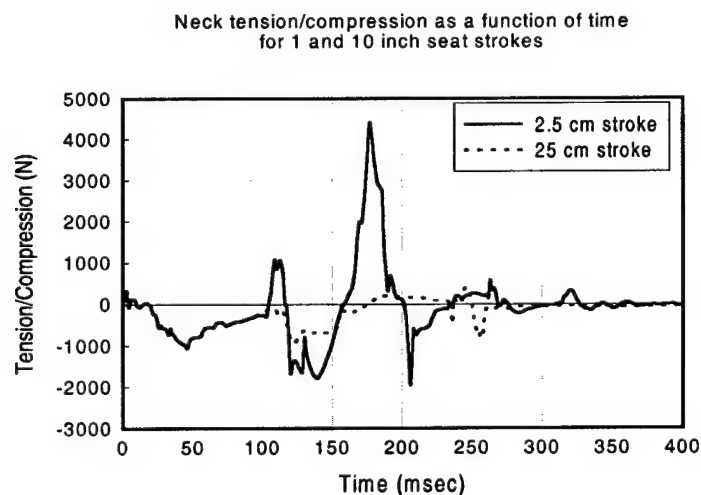


Figure 5-8. Time history for neck compression-tension force.

The corresponding load duration plots for these two response parameters are shown in Figure 5-9. Hollow bullets represent the loading levels for the 25 cm seat stroke. Examination of this figure reveals that increased seat stroke reduces the injury risk by placing the load exposures within the injury corridors.

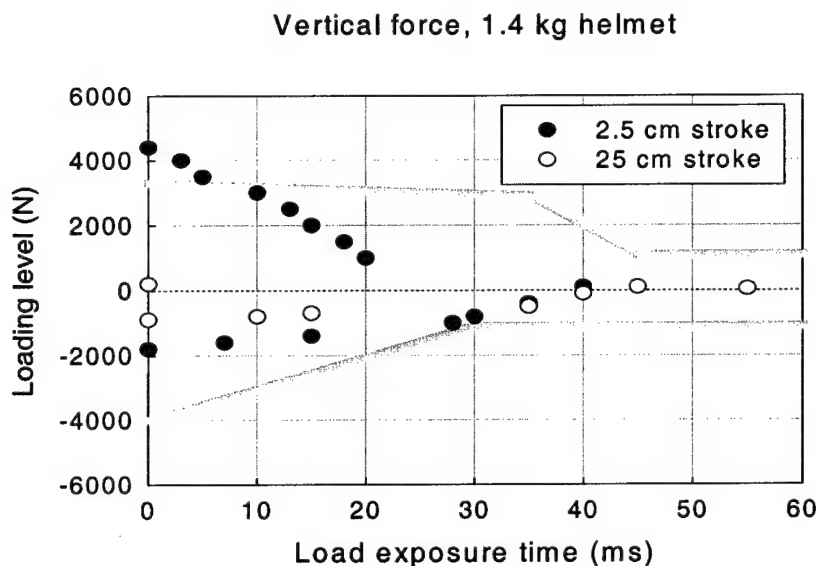


Figure 5-9. Neck load duration plots for 2.5 cm and 25 cm stroke distance.

The time histories of the six response parameters resulting from all the simulations were analyzed using the same method as depicted above. For comparison, the results of the simulations incorporating 2.5 cm and 25 cm seat stroking distances are paired together. Each entry in the table represents the number of response parameters (out of the six considered) which failed the time history analysis. A failure results when at least one of the data points within the LDP falls directly on or outside of the injury corridor boundaries. If one out of the six response parameters fails the time history analysis, no recommendation on allowable HSD mass can be made.

Consider Table 5-1 and the first impact condition. For this case, the effect of seat stroking is clearly evident. For an allowable 2.5 cm seat stroke, analysis shows that a high risk of injury is incurred when a 1.4 kg HSD is simulated. Hence, for this combination of impact condition and seat stroke distance, a HSD mass of no greater than 0.45 kg can be chosen. However, for an allowable seat stroke distance of 25 cm, a HSD mass of no greater than 1.4 kg can be selected.

Table 5-1.

Summary of response parameters which failed the injury test for the two stroking distance and the four helmet masses.

HSD mass (kg)		0.0		0.45		1.4		2.7		4.1	
Allowed stroking distance (cm)		2.5	25	2.5	25	2.5	25	2.5	25	2.5	25
Impact condition	1	0	0	0	0	1	0	1	1	3	1
	2	0	0	0	0	2	2	2	2	2	2
	3	0	0	0	0	0	0	0	0	0	0
	4	1	0	2	0	3	0	4	0	5	1
	5	1	1	1	1	2	2	2	2	2	2

Now, consider impact condition four. For the allowable 2.5 cm seat stroke, time history analysis shows that a risk of injury exists even for the lowest HSD masses. Therefore, no safe HSD mass can be predicted. However, for the allowable 25 cm seat stroke, low risks of injury exist up to an HSD masses of 2.7 kg. It must be noted that both impact conditions one and four are dominated by the vertical components of acceleration.

In impact conditions two and five, the stroking of the seat has no pronounced effect on the allowable HSD mass. These two conditions are principally longitudinal with 30 deg yaw. For these two impact conditions, the number of response parameters, which fail the time history analysis, is identical for each seat stroking distance. This is due to the fact that the seat stroking mechanism is designed to attenuate energy in the vertical direction only. However, some seats do exist which stroke in the horizontal direction. These seats were not considered in these simulations.

As in impact conditions one and four, impact condition three is also dominated by the vertical components of acceleration. However, no difference is observed in the injury assessments made on the results of both the allowable 2.5 cm and 25 cm seat strokes. Due to the nature of this impact condition, sufficient energy was not applied to cause the seat to stroke.

Consider, for example, impact condition one with an allowable 2.5 cm seat stroke. For this case, the peaks for fore-aft shear and tension fall below their respective thresholds for all four HSD masses. For compression, the peak coincides with its threshold at an HSD mass of 2.8 kg. For the extension moment, the peak reaches the threshold at 1.15 kg, and for the flexion moment, the peak reaches the threshold at 3.1 kg. The limit on HSD mass for impact condition one with an allowable 2.5 cm seat stroke is therefore 1.15 kg. That is, the minimum of 4.1 kg, 2.7 kg, 1.15 kg, and 3.1 kg. Using a similar approach, the limit on HSD mass for impact condition one with an allowable 25 cm seat stroke is calculated to be 2.57 kg. Table 5-2 summarizes the allowable HSD masses for each impact condition and seat stroke distance. As in the time history analysis, it is evident that for impact conditions of primarily vertical nature, higher HSD masses could be accommodated using a 25 cm seat stroke rather than a 2.5 cm seat stroke.

Table 5-2.

Comparison of HSD mass limits for the 2.5 cm and 25 cm seat stroking distances for each impact condition

		HSD mass limit (kg)	
Allowed stroking distance (cm)		2.5	25
Impact condition	1	1.15**	2.57**
	2	0.64**	0.64**
	3	4.10**	4.10**
	4	--*	2.91**
	5	--*	--*

** Extension moment was the governing factor in determining HSD mass limit.

* No limit on HSD mass can be determined

In all these discussions, keep in mind that only the 50th percentile male aviator was simulated. Results will be different for other aviator sizes, particularly for a small size female. It should also be stressed that these results are based a HSD CM coincident with the CM of the Hybrid III head. These results should not be interpreted to account for CM locations other than the one simulated.

Conclusions

In this study we examine the effect of seat stroking distance on reducing the severity of potential neck injury to the aircrew during a helicopter crash. For this purpose, we performed mathematical simulations of the pilot's biodynamics to examine the inertial loads at the head-neck interface. The simulations demonstrated that for impact conditions of primarily vertical nature, the peak magnitudes of neck loads were reduced significantly for a 25 cm seat stroke as compared with 2.5 cm seat stroke. This allowed higher HSD mass to be worn. In addition, the primary factor in determining HSD mass limit was the extension moment for both allowable seat stroke distances. No significant differences were observed for impact conditions which were not primarily vertical in nature.

INFLUENCE OF AIRBAGS ON SELECTION OF MASS AND CM PLACEMENTS OF HEAD SUPPORTED DEVICES

Introduction

The crashworthy design of modern Army helicopters has resulted in fewer injuries from the impact acceleration in survivable crashes. The injury reduction, primarily to the spinal column, may be attributed to the energy-absorbing seat design, which limits the forces transmitted to the seated pilot. Head and upper torso injuries also have been addressed with various design concepts to cockpit interior components, such as the breakaway optical relay tube used by the gunner in the AH-64 Apache helicopter. Following the introduction of these energy-absorbing devices into the U.S. Army Apache and Black Hawk helicopters, the injuries sustained in Army helicopter crashes between 1980 and 1985 due to excessive accelerations have dropped relative to other helicopters (Shanahan, 1989). Ten years later, the risk of injury to U.S. Army helicopter occupants during the 1990-94 period was reduced significantly, primarily due to a 40% drop in head injuries (Shannon, et. al., 1996). Despite the success of the crash-worthy design of modern helicopters, flail injuries continue to occur and, in fact, outnumber acceleration injuries. Contact or flail injuries are produced in secondary collisions which result from inadequate restraints, collapsing structure, or a combination of both.

Total delethalization of U.S. Army helicopter interior systems is impossible because of operational requirements and design constraints. Further, current restraints systems are unable to prevent secondary impacts (McEntire, 1992). The use of some airbag protection for the gunner has been suggested for many years (Loushine, 1975), but no acceptable system ever was introduced into Army helicopters. More recently, the U.S. Army Aeromedical Research Laboratory (USAARL), Fort Rucker, Alabama, has demonstrated the effectiveness of airbags in reducing the severity of head injury (Alem, et. al. 1992), and evaluated the projected effectiveness of airbag as supplemental restraint systems in Army helicopters (Shanahan, et. al., 1993). These studies and other factors convinced the Army of the need to introduce airbag technology as a method of delethalizing the cockpit interior of its helicopters. As part of a development program by the Aviation Applied Technology Directorate to reduce the likelihood that aviators will be injured seriously by cockpit strikes (Smith, 1993 and Greth, et. al., 1992), Simula, Inc., developed a multi-airbag system (Zimmerman, 1993) which will inflate during a crash to protect the aviator.

In this study, we attempt to further investigate the effectiveness of airbags in reducing the risk of serious neck injuries during helicopter mishaps.

Objectives

The objective of this study was to examine the limits of the head supported devices' mass and center of mass (CM) locations in various helicopter crash environments which include stroking of the seat, harness system and supplementary harness system (airbags).

Test matrix

The test matrix considered in this study was composed of three impact conditions, four different HSD masses, 49 CM placements and two cases where in the first the airbag was deployed and in the second the airbag was not deployed. Time histories for the transmitted head and neck forces and moments were recorded for each case. A more detailed description of each of the parameters considered in this study is described below:

Impact conditions. The first condition was a 25 g vertical triangular pulse of 128 millisecond (msec) duration (velocity change of 15.7 m/s) with 30 deg pitch and 10 deg roll subject orientation. The second condition was a 30 g horizontal triangular pulse of 160 msec duration (velocity change of 23.5 m/s) with 30 deg yaw subject orientation. Finally, the third pulse was a 10-48 g vertical bi-level pulse of 110 msec total duration (velocity change of 18 m/s) with 30 deg pitch and 10 deg roll subject orientation.

Helmet mass. Four HSD masses of 0.45, 1.36, 2.72, and 4.09 kilograms were simulated. The effect of helmet mass was incorporated into the head segment by adding the mass of the helmet to the mass of the head. Then, the mass moments of inertia of the head segment were altered to account for the additional mass.

CM location. Forty-nine CM positions (7 by 7 grid) were selected uniformly in the mid-sagittal plane. The 7 by 7 grid spanned the head CM ($x = 0$ cm, $y = 0$ cm, $z = 0$ cm) from -6 cm to 6 cm at 2 cm intervals along both the x and z axes.

Seat stroke. The effect of seat stroke was incorporated into the simulations (Beale, et al., 1996). Since the UH-60 and AH-64 helicopters are equipped with energy absorbing seats, the simulations were expanded to include the stroking of the seat. These simulations were confined to allowable seat stroke distance of 25 cm.

Airbag position. Airbag positions based on the geometry of the black hawk helicopter environment were simulated. Accurate measurements of the Black Hawk environment were made in the UH-60 simulator at USAARL and were incorporated in the simulations. In the case considered, one bag is placed to the front and a second bag is placed to the left of the co-pilot.

Restraint system. A standard four-point restraint system was used in the simulations. The harness system was modeled to simulate "no malfunctions" during the different crash scenarios, i.e. the inertia reels locked at the onset of each crash pulse.

Complete motio. The total duration of each simulation was confined to 300 msec. This was necessary to allow sufficient time for the head motion to develop. Response parameters were output at 1-msec intervals.

Inertial loading. Only the inertial loading exerted on the head-neck interface was considered. This was accomplished by determining the point in time, if any, at which the head contacted the seats headrest. The analysis process was then carried out to that time point only. Beyond that point, the data was determined to be contaminated by contact forces and therefore, not representative of purely inertial loadings.

Discussions

In this section we will examine in detail the parameters considered in this study and their relationships with each other.

Influence of impact condition. Examination of the output shows a definite change in the magnitude of the helmet mass limits obtained for each of the impact conditions considered. For all 49 CM positions in the test matrix, it is evident that the helmet mass limits decrease in the order of impact condition three, impact condition one and impact condition two. That means that of the three cases considered, impact condition two (primarily horizontal orientation) is the deciding factor in determination of the helmet mass limit. Keep in mind that the UH-60 Black Hawk is equipped with seats which attenuate energy along the vertical axis, a feature that was modeled in the simulations. With the use of energy absorbing seats, some of the energy that would have been transferred to the occupant is dissipated. This allows higher mass limits for the cases with vertical seat stroking.

CM dependenc. For the vertical impact conditions, the results reveal that the helmet mass limits increase as we move downward (from $z = -6$ cm to $z = +6$ cm) and backward ($x = +6$ cm to $x = -6$ cm). For the horizontal crash pulse (impact condition 2), it seems that the helmet mass limits also increase as we move downward; however along the axial direction, they have a parabolic nature, with the maximum mass limit centered in the neighborhood of $x = 0$ cm.

Influence of airbag. In all three cases, it is observed that the use of airbags allows higher mass limits and more versatility in selection of helmet mass and CM placement. Higher mass limits, in essence, translate into lower loads on the head-neck interface and consequently lower risk of spinal injury. This effect is more pronounced in impact conditions one and three (primarily vertical impacts with seat stroke capability) than it is with impact condition two (primarily horizontal impact without seat stroke capability).

For impact condition one - airbag active, the maximum HSD mass of 4.1 kg is obtained for z - elevations in the range of +6 cm (6 cm below the head CM) to -6 cm (6 cm above the head CM); however, when airbag is not active, z -elevation for the 4.1 kg HSD mass is limited to the range of (+6 cm to + 2 cm). By the same token, with the airbag active, the HSD mass limit of 4.1 kg could be obtained within the longitudinal range of -6 cm to +6 cm. While for the case in which the airbag is not active, the longitudinal range of CM placement is limited to - 6 cm to -2 cm.

In all these discussions, keep in mind that only the 50th percentile male aviator was simulated. Results will be different for other aviator sizes, particularly for a small size female.

Conclusions

In this study we examine the effect of airbags on reducing the severity of potential neck injury to the aircrew during a helicopter crash. For this purpose, we performed mathematical simulations of the pilot's biodynamics to examine the inertial loads at the head-neck interface. The simulations demonstrated that for the three impact conditions considered, the peak magnitudes of neck loads were reduced significantly when airbags were used. This allowed higher HSD mass to be worn. In addition, the primary factor in determining HSD mass limit was the extension moment. It was shown that selection of HSD mass and CM placement is pulse dependent. For impact conditions of primarily vertical nature, potential of head-neck injury reduced further due to presence of energy attenuating seats. This effect was less pronounced for the horizontal impact conditions.

EFFECTS OF OPTICAL RELAY TUBE (ORT) DISPLAY MODIFICATIONS ON THE RISK OF FACIAL AND NECK INJURY

Introduction

The U.S. Army, as well as all of America's other armed forces, is dealing with an ever-decreasing defense budget. Shrinking budgets are forcing military planners to think twice about where their limited funding should be spent. As a result, production and fielding of new weapons systems such as the Army's RAH-66 Comanche and the Air Force's F-22 Raptor have been slowed. In the interim, the military has embarked on a program to modernize existing equipment. This effort will enable the U.S. military to maintain its edge on the modern battlefield until these newer, more-advanced weapons systems can enter service.

The AH-64A Apache is to be the recipient of such modernization. The Apache was originally delivered to the U.S. Army in 1984, and has served as its premiere attack helicopter for more than a decade. Beginning in early 1997, the Army's entire fleet of AH-64A's is to be remanufactured into the AH-64D Apache Longbow. In addition to being lighter and able to carry more armament, this most advanced version of the Apache will be equipped with digital radar systems and cockpit instrumentation. The new digital cockpit will incorporate multifunctional flat-panel displays (FPD's) to provide battlefield information to the pilot and co-pilot/gunner (CPG). The use of these FPD's should provide the pilot and CPG with improved situational awareness during combat missions.

One such FPD will be used to augment the existing optical relay tube (ORT) display used by the CPG to acquire and engage targets. The ORT will stay in place, but the standard monocular display is to be replaced by the FPD. The FPD will be positioned further forward relative to the occupant's design eye-point (DEP) than the current display. In addition, the new FPD will be located slightly higher than the existing display.

With either display system, the possibility of secondary impacts between the occupant and display exists. The focus of this investigation was to compare the risk of impact between the occupant's head and both the standard display and the FPD in the event of helicopter mishaps.

In addition, the risk of facial and neck injury was assessed for both the standard display and the FPD. To these ends, two sets of simulations were performed. One set in which the existing display was modeled, and the other set in which the FPD was modeled. In addition to modeling different cockpit interiors, several impact conditions were simulated, as were inertial reels of varying effectiveness.

Biodynamic simulations

Using ATB simulations, biodynamic response to six different crash pulses, also referred to as impact conditions, were generated for the Hybrid III manikin. The GEBOD program (Kaleps, et. al., 1988; Gross, 1991) was used to generate the segment and joint data for a sitting Hybrid III dummy. For each of these six impact conditions, two different ORT displays and four different harness slack lengths were considered. Time histories of the head/display contact forces were recorded for each case, as were time histories of the position and velocity of the occupant's head, neck, and upper torso. In addition, time histories of the transmitted head and neck forces and moments were output from each simulation. Detailed descriptions of the major simulation parameters are given in the following sub-sections.

Modeling of the ORT displays

While ellipsoids are used to represent segments of the occupant's body, rectangular planes are used to define the environment surrounding the occupant. These planes are most commonly used to construct dashboards, instrument consoles, seats, or any other structures with which the occupant might come into contact. The user must anticipate which combinations of planes and segments will interact with one another and specify that contact forces be calculated when plane/segment interaction occurs. To calculate these contact forces, force-deflection functions are defined for each plane/segment combination. When a segment intersects the plane, the maximum distance of segment penetration is calculated. Using the predefined force-deflection function, the contact force experienced by the segment is then calculated as a function of this maximum penetration distance. In this manner, the interaction between the occupant and his surroundings is modeled.

Both the standard monocular display and the FPD were modeled using these rectangular planes. For the purposes of this investigation, contact between the head and the surface of each display was of interest. Therefore, only one plane was needed to model each of the displays, i.e. one plane to represent the face of the standard display and one to represent the surface of the FPD. These planes, as well as several others, can be seen in Figures 5-10 and 5-11. The additional planes shown in Figures 5-10 and 5-11 were included in the simulations to make the cockpit interior resemble more closely that of the Apache helicopter.

The dimensions of the planes used to represent the surfaces of each display are also shown in Figures 5-10 and 5-11. The dimensions shown for the standard monocular sight were measured directly from an available crash-damaged ORT. In reality, the surface of the display is a circular lens of approximately 6.53 centimeters (cm) in diameter. For these simulations, the surface of the lens was approximated by a panel measuring 6.53 cm square. Dimensions for the FPD were provided by its design contractor, Lockheed Martin. The surface of the FPD was

12.70 cm wide and 10.80 cm high. The angular orientations of each display were 57° and 65° relative to the horizontal plane for the standard display and FPD, respectively.

The positions of the displays were provided relative to the occupant's design eye-point (DEP). Since the occupant's head was modeled using an ellipsoid, no actual eyes existed. Thus, a point on the surface of the ellipsoid was chosen as the DEP. The point was chosen 7.62 cm forward, 3.81 cm to the right, and level with the center of the ellipsoid. The position of the DEP is shown in Figure 5-12.

In this modeling effort, the initial positions of the two displays were input relative to the occupant's DEP. From data provided by Lockheed Martin, the center of the standard display was determined to be approximately 25.4 cm forward and 25.4 cm below the DEP. Laterally speaking, the standard display was centered 0.625 cm left of the DEP. This placed the center of the standard display 3.175 cm to the right of the aircraft centerline. A diagram showing the position of the standard display is given in Figure 5-13. As for the FPD, its center was determined to be located 33.02 cm forward and 20.32 cm below the occupant's DEP. In addition, the FPD was centered 3.81 cm to the left of the DEP. This placed the center of the FPD directly on the centerline of the aircraft. Thus, the center of the FPD was located 7.62 cm forward, 5.08 cm above, and 3.175 cm to the left of the standard monocular display. The position of the FPD relative to the occupant's DEP is shown in Figures 5-14.

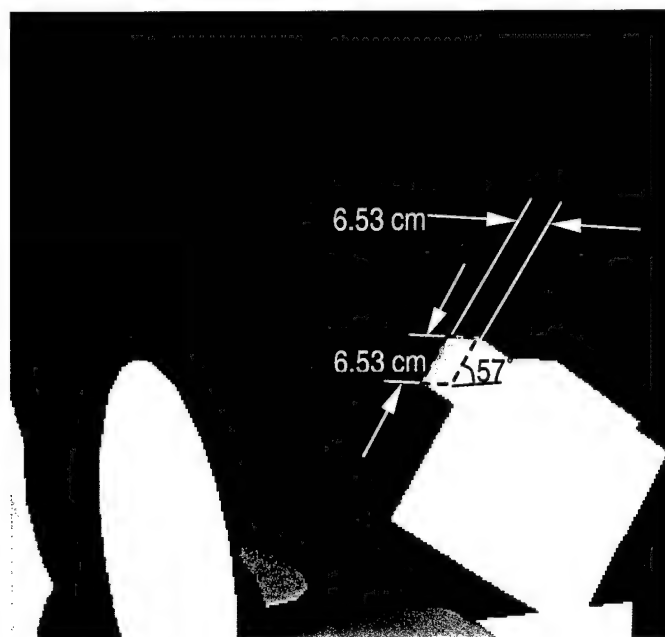


Figure 5-10. Dimensions of plane used to model standard monocular ORT display.
(Figure is not to scale.)

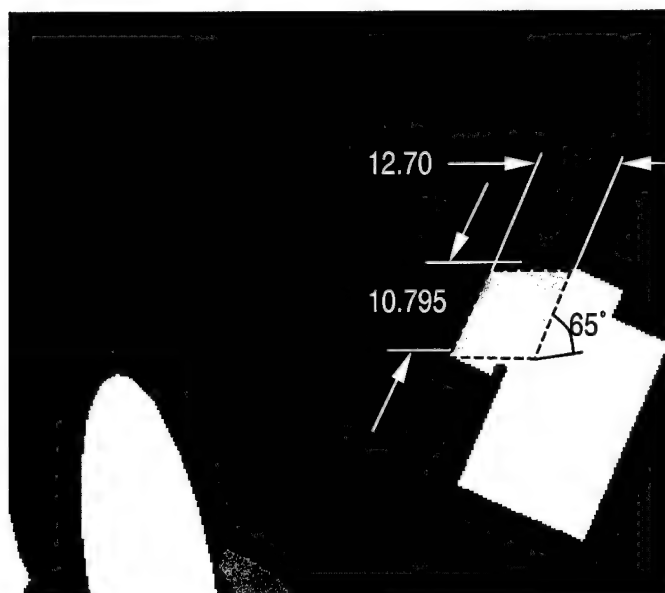


Figure 5-11. Dimensions of plane used to model proposed flat-panel ORT display.
(Figure is not to scale.)

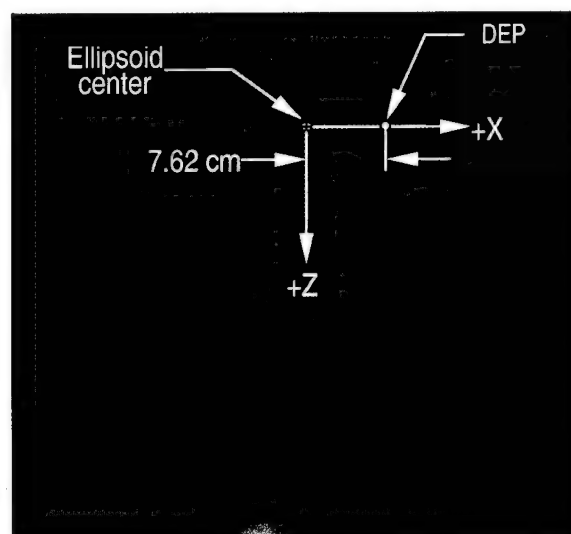
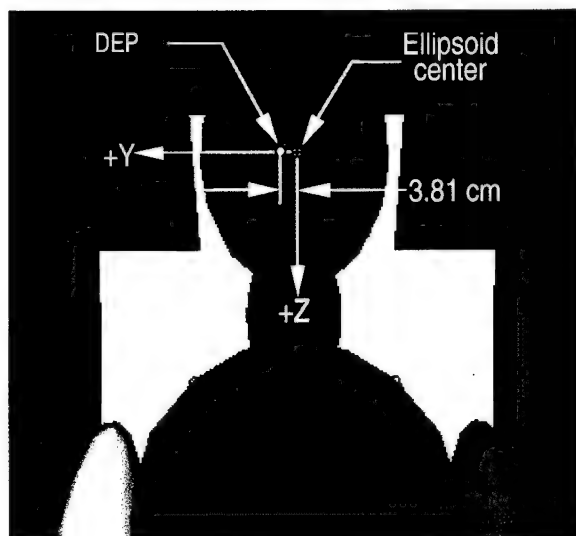


Figure 5-12. Position of design eye-point relative to the center of the ellipsoid used to model the occupant's head. Left: front view, right: side view. (Figures are not to scale).

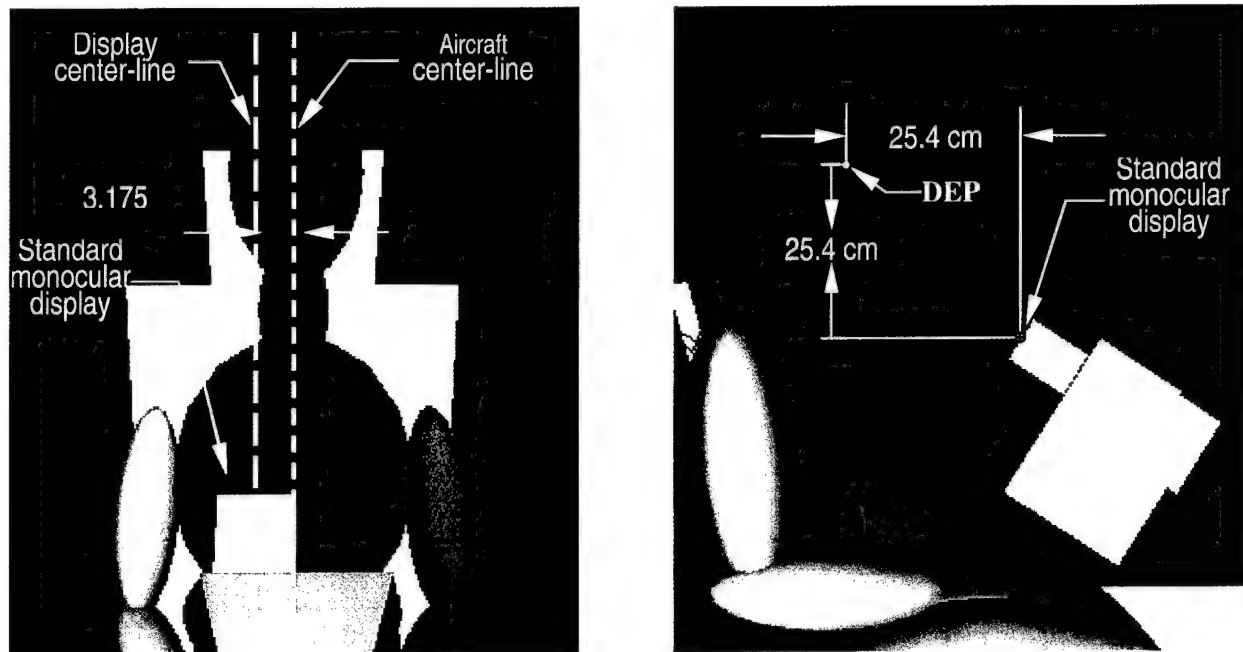


Figure 5-13. Diagram of standard monocular ORT display relative to the design eye-point of the co-pilot/gunner. (Figures are not to scale).

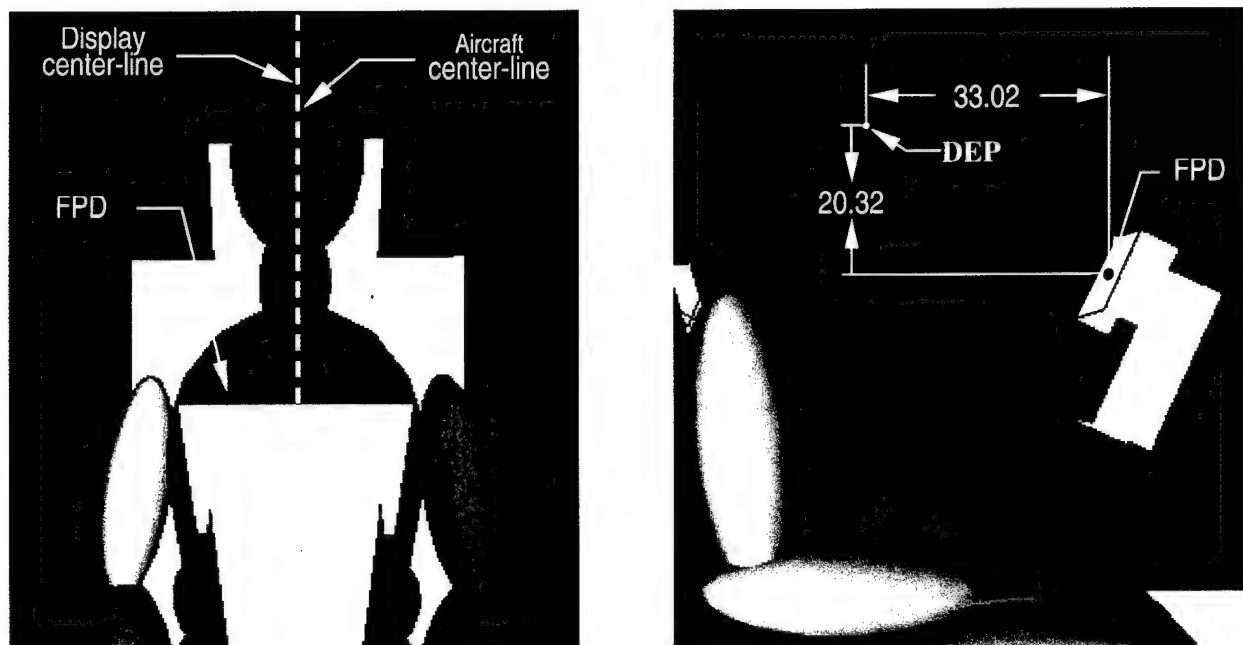


Figure 5-14. Diagram of flat-panel display relative to the design eye-point of the co-pilot/gunner. (Figures are not to scale).

Head-supported mass

To ensure biofidelity, the occupant was modeled wearing the standard Integrated Helmet and Display Sighting System (IHADSS). To do this, the mass and inertial properties of the head and helmet were lumped together into a combined head/helmet segment. The effect of helmet mass (1.47 kilograms) was modeled by adding the mass of the helmet to the mass of the head. In addition, to account for the extra mass, the mass moments of inertia of the head segment were altered.

Impact conditions

Six individual helicopter mishaps were modeled during this study. These six impact conditions were derived using combinations of the acceleration profiles and subject orientations shown in Figures 5-15 and 5-16, respectively. The major aspects of each impact condition are given in Table 5-3.

Table 5-3.
Impact Condition Summary

Impact condition	Acceleration profile	Impact direction	Subject orientation		
			Yaw (deg)	Pitch (deg)	Roll (deg)
1	Figure 5-15a	Horizontal	0	0	0
2	Figure 5-15b	Horizontal	0	0	0
3	Figure 5-15c	Vertical	0	30	0
4	Figure 5-15c	Vertical	0	30	10
5	Figure 5-15d	Vertical	0	30	0
6	Figure 5-15d	Vertical	0	30	10

As can be seen from Table 5-3, the first two impact conditions simulated were horizontal in nature. These impact conditions were used to simulate a head-on impact between a helicopter and a rigid vertical surface (Coltman, et. al., 1989; Desjardins, et. al., 1989). For impact condition 1, the acceleration profile was triangular with a peak acceleration of 30 G's and a total duration of 160 milliseconds (msec). The velocity change (ΔV) associated with this acceleration profile was $23.5 \text{ m}\cdot\text{sec}^{-1}$. As for impact condition 2, the acceleration profile was trapezoidal in shape. The shape of the acceleration profile simulated the limited energy-attenuation characteristics of the aircraft fuselage. The ΔV for the acceleration pulse was calculated to be $15.5 \text{ m}\cdot\text{sec}^{-1}$.

The final four impact conditions used in this study simulated vertical impacts. These impact conditions simulated a helicopter impacting vertically on a rigid horizontal surface in either a 30° nose-down attitude or a combined 30° nose-down and 10° right-roll attitude (Coltman, et. al., 1989; Desjardins, et. al., 1989). For impact conditions 3 and 4, the acceleration profile was triangular with a 25-G peak acceleration and a total duration of 128 msec. The ΔV produced by this acceleration profile was $15.7 \text{ m}\cdot\text{sec}^{-1}$. The acceleration profile used in impact conditions 5 and 6 was a modified version of the one used in the previous two impact conditions.

The acceleration pulse was modified to include the energy-attenuating characteristics of the helicopter's landing gear. The constant acceleration of 10 G's occurring between 5 and 70 msec represented the acceleration time history profile produced by stroking of the landing gear. The sudden rise in acceleration between 70 and 110 msec simulated fuselage impact (Desjardins, et. al., 1989). This acceleration profile resulted in a ΔV of $18.0 \text{ m}\cdot\text{sec}^{-1}$.

Energy-attenuating seat

The Apache is equipped with seats that attenuate energy in the vertical direction. In the actual aircraft, the energy is absorbed using a pair of inversion tubes (Desjardins, et. al., 1989). In the simulations, the energy attenuating mechanism was modeled using a spring/damper system. The spring was used to absorb the vertical component of impact energy. Since the seat used in the CPG station is designed to stroke 25.4 cm in the vertical direction, the viscous damper was used to limited seat travel to 25.4 cm and also prevented the seat from rebounding.

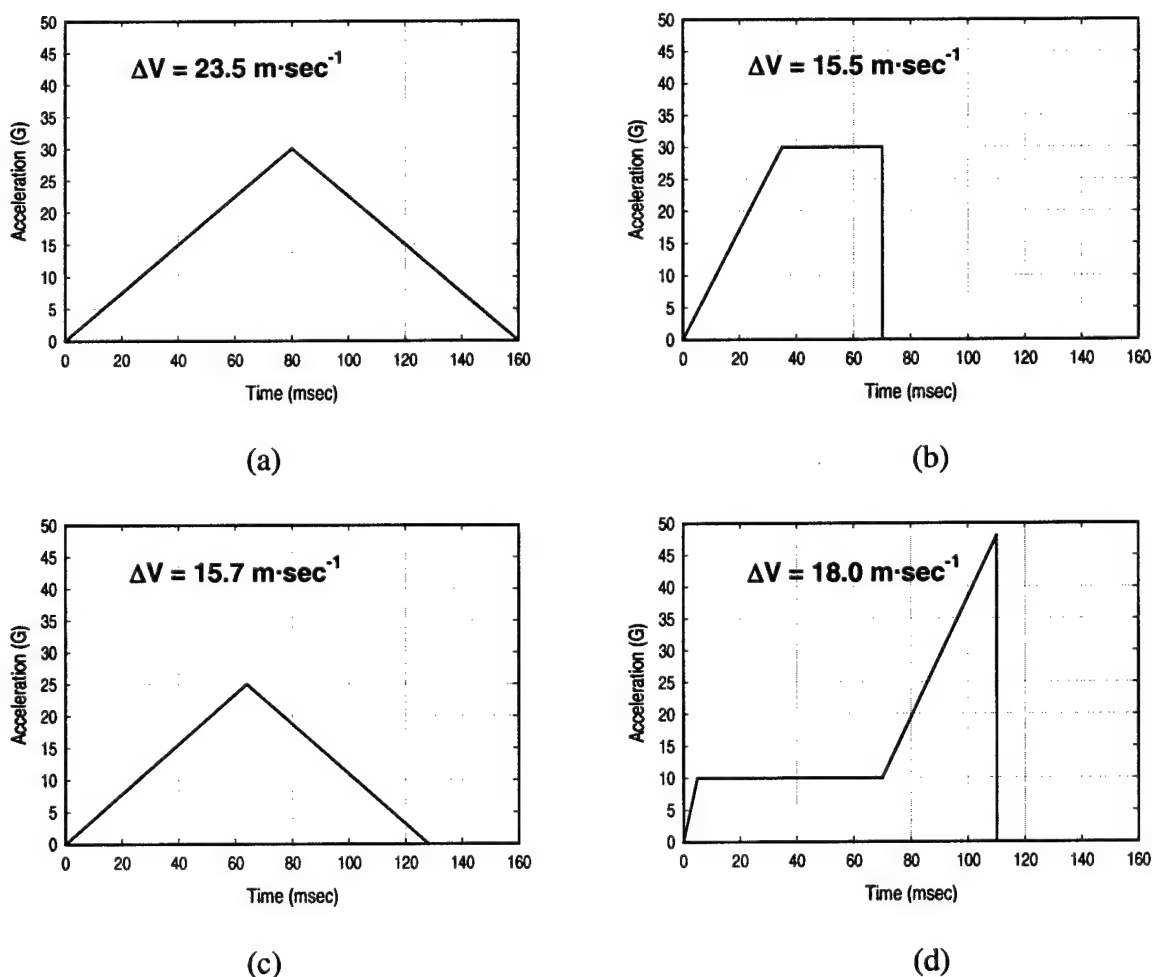


Figure 5-15. Schematics of the acceleration profiles simulated.

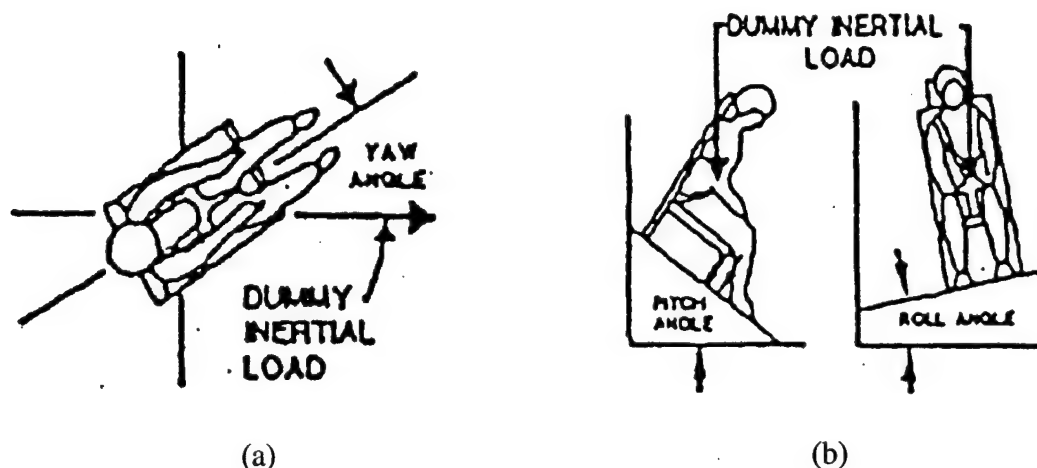


Figure 5-16. Subject orientation.

Restraint system

The pilot and CPG stations of the Apache are equipped with five-point restraint systems. Therefore, a five-point harness was included in the simulations. The harness included two waist belts, two shoulder belts, and one "submarine" belt. Each belt terminated at the same spot on the occupant's lower torso.

To reduce occupant flailing during a crash, the shoulder belts are equipped with inertia reels. These reels are intended to lock automatically when the shoulder strap accelerates at a level greater than 3 G's. However, a recent study conducted by the U.S. Army Aeromedical Research Laboratory (USAARL) has shown that, in some cases, these inertia reels fail to lock at design limits (McEntire, 1992). Therefore, inertia reels in various stages of failure were simulated.

Inertia reel failure was modeled by increasing the initial slack in the shoulder belts. In the ATB program, belts are defined by inputting points of contact between the belt and occupant's torso. The geometric length of the belt is computed from the sum of the distances between successive points on the belt. Initial slack in a belt can also be specified. The initial belt length is then calculated by adding the initial slack to the geometric length (Obergefell, et. al., 1988). To simulate a properly functioning inertia reel, an initial slack of 0.254 cm was input. Specifying initial slack lengths of 12.7 cm and 25.4 cm simulated two intermediate stages of failure. A fully malfunctioning inertia reel was modeled using 38.1 cm of initial slack.

Response parameters

Several response parameters were necessary for this investigation. To aid in determining the risk of impact between the occupant's head and the two displays, the linear and angular positions and velocities of the occupant's head, neck, and upper torso were output from each simulation. In addition, the contact forces generated by the occupant's head impacting the display were output for use in assessing the risk of facial injury. To determine the risk of neck

injury, the forces and moments acting at the occupant's head/neck interface (HNI) were also recorded. These six response parameters included neck extension bending moment ($-M_y$), neck flexion bending moment ($+M_y$), neck axial compression ($-F_z$), neck axial tension ($+F_z$), neck forward shear force ($-F_x$), and neck rearward (aft) shear force ($+F_x$).

Injury assessment

The secondary purpose of this study was to assess the risk of facial and neck injury resulting from simulated helicopter mishaps. Assessing the risk of injury required that individual response parameters be compared to acceptable injury reference values, also referred to as injury thresholds. Then, based on these comparisons, decisions were made regarding the potential for injury. This section will discuss the origin of the injury reference values used in this study, as well as the methodology used to determine the injury risk.

Facial injury reference values

The myriad of bones that make up the facial region of the head allows for a number of different injury mechanisms (Allsop, 1993). These mechanisms range from fractures of the nasal or jawbones to complete craniofacial disjunction in which the face is essentially forced rearward into the skull. Finding the point within this range at which the injury goes from being tolerable to serious is a subjective process. This is due in part to the facts that bone strength and pain thresholds vary among individual aviators.

For this study, the facial injury reference value was based on a percentage of the force necessary to produce craniofacial disjunction. From Welbourne, et. al., the forces necessary to cause simple nasal fractures and craniofacial disjunction were 1875 Newtons (N) and 3760 N, respectively (Allsop, 1993). These values represent 50 percent and 100 percent of the force necessary to cause craniofacial disjunction. Assuming that a simple nasal fracture was not a debilitating injury, 50 percent was thought to be too low a threshold. Also, assuming that craniofacial disjunction was both debilitating and life-threatening, 100 percent represented an unacceptable risk. Therefore, assuming a linear relationship between force and injury risk, the facial injury reference value was taken to be exactly halfway between the two extremes at 75 percent of 3760 N, or 2820 N.

Neck injury reference values

The most commonly accepted injury assessment reference values draw their roots from work performed by General Motors. For more than twenty-five years, General Motors has been conducting automotive crash tests using human cadavers and anthropomorphic test devices such as the Hybrid III dummy. Based on the results of these tests, General Motors devised a set of injury assessment reference values (IARV's) for the small female (5th percentile adult female), the midsize male (50th percentile adult male), and the large male (95th percentile adult male). This set of IARV's contains injury threshold data for the chest, femur, knee, tibia, HNI, and the head (Mertz, 1993).

To determine the risk of occupant injury, the results of the simulations were compared to the IARV's of the midsize male. The IARV's pertinent to this study are those associated with the head/neck interface. This set of reference values deals with six of the response parameters mentioned previously, i.e. neck flexion moment, neck extension moment, axial tension, axial compression, fore shear, and aft shear. The curves defining the IARV's for fore/aft shear, axial tension, and axial compression are shown in Figures 5-17 through 15-19, respectively. The values for neck flexion and extension moment are given in Table 5-4 (Mertz, 1993).

Table 5-4.

Injury assessment reference values for neck flexion and extension moment.

	Small female	Midsize male	Large male
Flexion (N•m)	104	190	258
Extension (N•m)	31	57	78

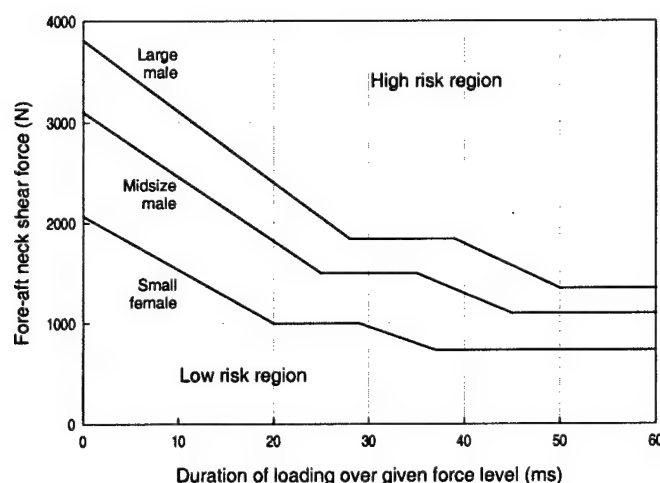


Figure 5-17. Injury assessment reference values for neck fore/aft shear force.

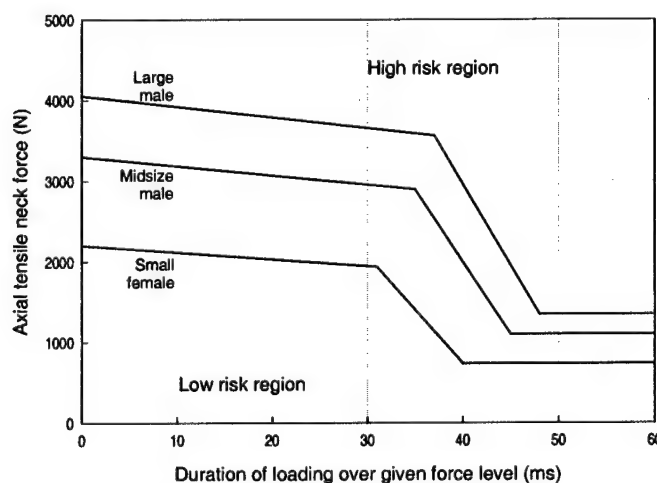


Figure 5-18. Injury assessment reference values for neck axial tension.

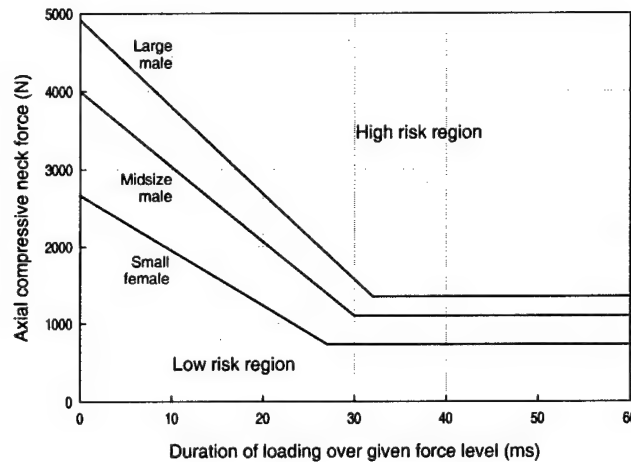


Figure 5-19. Injury assessment reference values for neck axial compression.

Assessment methodology

The assessment method used in this study was based on the peak values of each response parameter. As mentioned previously, the values of contact force and the three forces and three moments acting at the HNI were output at 1-msec intervals for a duration of 300 msec. The peak values for each of the seven response parameters were extracted from their respective time histories. For each response parameter, the peak values were normalized with respect to their associated IARV. Response parameters whose IARV's varied with exposure time, i.e. fore/aft shear and axial tension and compression, were normalized using the value of the IARV corresponding to an exposure time of 0 msec.

These normalized response parameters (NRP's) were then used to assess the occupant's risk of injury. By normalizing, the threshold for each response parameter became 1.0. A NRP value of less than 1.0 indicated that the response parameter in question did not exceed its given IARV. Thus, the risk of injury was judged to be "low." However, if the NRP value reached 1.0 or greater, the particular response parameter exceeded its IARV, and the risk of injury was assessed to be "high."

Conclusions

From the results of this investigation, several conclusions can be drawn. The first two conclusions deal with the effects of fully functional and totally ineffective inertia reels. The final conclusions deal with the influences that harness slack length and impact conditions have on the effectiveness of using the FPD in place of the standard ORT.

The first conclusion is that properly functioning inertia reels are a vital component of the life support system with which the AH-64 is equipped. The harness slack length of 0.254 cm prevented the occupant from flailing after the onset of the crash pulse. This essentially made the positions of the two displays a non-issue. Since the occupant never interacted with either of the displays, none of the response parameters discussed earlier were influence by head/display contact. Thus, no comparisons could be made as to whether the position of the FPD offered any

advantage over that of the standard ORT. For all combinations of impact condition and display type, the risks of impact and facial injury were low due to the lack of head/display contact. However, for some impact conditions, the inertial loads experienced at the HNI were still large enough to cause a risk of serious neck injury.

The second conclusion that can be drawn deals with the simulations involving a harness slack length of 38.10 cm. The 38.10-cm harness slack length was used to model an inertia reel that fails to function at all. The results of these simulations show that the positions of the displays did not have any effect on the risks of impact, facial injury, or neck injury. This was unquestionably due to the excessive occupant motion allowed by the malfunctioning inertia reel. For each impact condition, the risks of impact, facial injury, and neck injury were high for both the standard ORT and the FPD. The results of the simulations involving the 38.10-cm harness slack length show a situation in which the inertia reel prevents harness payout to be both unacceptable and life threatening.

A third conclusion is that the effects of FPD position are dependent on the effectiveness of the inertia reel. This conclusion is best illustrated using impact conditions 3 through 6. At a harness slack length of 12.70 cm use of the FPD lowered the risk of head/display contact and neck injury relative to the risks associated with the standard ORT. These lower risks of impact and neck injury can be attributed to the lack head/FPD contact. For the same impact conditions but at the 25.40-cm harness slack length, contact was made between the head and both display systems. These contacts, in turn, contributed to the risks of head/display contact and neck injury being assessed as high for both the standard ORT and FPD. Since the simulations being considered differed only in harness slack length, it can be seen that the benefits of moving the FPD further away from the occupant are dependent on how well the inertia reels function.

The benefits of using the FPD in place of the standard ORT are also dependent on the type of impact conditions simulated. Consider the risks of facial injury associated with the 25.40-cm harness slack length. For impact conditions 3 and 5, use of the FPD was shown to increase the risk of facial injury over that of the standard ORT. This was due to the fact that the distance between the occupant and the FPD enabled larger impact velocities to be developed. Since impact conditions 4 and 6 were almost identical to conditions 3 and 5, the risks of facial injury were expected to be similar. However, the 10° roll condition present in impact conditions 4 and 6, induced sufficient lateral motion to carry the occupant to the side of the displays rather than directly at them. While the "glancing blows" that resulted made no difference in the facial injury risk associated with the standard ORT, they did lower the facial injury risk associated with the FPD relative to those of impact conditions 3 and 5. This is a clear example of how the type of helicopter mishap being simulated could influence the effectiveness of the FPD at mitigating injury.

In general, based on the six impact conditions considered in this investigation, use of the FPD does not increase the risk of impact, facial injury, or neck injury over that of the standard ORT. For most of the impact conditions, the risks of head/display impact, facial injury, and neck injury were the same or in some cases lower than those resulting from use of the standard ORT.

REFERENCES

Brozoski, T., Brozoski (1999) Mass and Location of Head-Supported Devices Using Articulated Total Body Simulations, UES Inc.

Amir A. Mobasher, Frederick T. Brozoski, B. Joseph McEntire, Nabih M. Alem (1998) Effects of Seat Stroke Distance on the Allowable Mass of Head Supported Devices Fort Rucker, AL: U.S. Army Aeromedical Research Laboratory. USAARL Report No. 98-26.

Nabih M. Alem, Amir A. Mobasher, Frederick T. Brozoski, David G. Beale (1998) Simulations of Head Strikes in Helicopters and the Roles of Restraints, Seat Stroke and Airbags on Their Reduction Fort Rucker, AL: U.S. Army Aeromedical Research Laboratory. USAARL Report No. 98-11.

Amir A. Mobasher, Frederick T. Brozoski (1998) Influence of Airbags on Selection of Mass and CM placements of Head Supported Devices, UES Inc.

Amir A. Mobasher, Frederick T. Brozoski (1998) Effects of optical relay tube (ORT) display modifications on the risk of facial and neck injury, UES Inc.

Amir A. Mobasher, Frederick T. Brozoski, B. Joseph McEntire, Nabih M. Alem (1997) Automation of ATB simulations and analysis to determine head supported CM criteria: UES Inc. and United States Army AeroMedical Research Laboratory, Fort Rucker. Presented at 1997 ATB User's Group Conference.

TASK 6

Biomedical Engineering Research Support for Head Supported Device Mass Properties Design and Operational Criteria

INTRODUCTION

Modern U.S. Army helicopters use the helmet as an integral component of the aircraft control systems. The helmet has evolved from a simple crash protection device to a mounting platform for advanced technologies that greatly increase the effective combat power of the helicopter in the field. The helmets now support such devices as NVG, chemical mask, oxygen system, head-up display (HUD), forward looking infrared (FLIR) display, flash blindness and laser eye protection and weapon aiming systems. All of these devices add weight to the helmet, and displaces the CG of the system. This increased weight and displaced CG add biomechanical stress to the neck and upper body of the pilot, and may also lead to decrements in performance.

In response to the need for investigation of chronic injury development and potential performance decrements, UES researchers instigated the inclusion of measures and methods that addressed the quantification of chronic injury development. A combination of epidemiological techniques and experimental measures produced new information leading towards a dose/response metric in helmet loading and neck fatigue and performance decrement.

A series of studies has been conducted at the USAARL to evaluate the effects of HSD mass properties on biomechanical, physiological and performance responses of male pilots (Butler, 1992; Lantz, 1992; Alem, Meyer, and Albano, 1995). Butler (1992) showed a significant increase in head pitch acceleration response when the total head-supported load exceeded 83 N-cm relative to the atlanto-occipital complex (AOC). The AOC is a functional anatomic structure that represents the C0-C1-C2 joints of the upper cervical spine (Sobotta and Figge, 1974).

Alem et al., (1995) studied performance of male pilots under long exposure (up to 4 hours) to whole body vibration and under four head-supported device (HSD) configurations. They demonstrated that the subject's reaction time to a randomly appearing target increased as the weight moment of the helmet increased beyond 78 N-cm. Another USAARL study by Lantz (1992) showed significant changes in electromyography responses to HSD loading under whole body vibration.

These USAARL studies concluded that the HSD weight moment should not exceed approximately 80 N-cm. Since this conclusion was derived from laboratory experiments with male volunteers as subjects, it was reasonable to expect that the limit would be different for female aviators because of known gender differences in physiology, neck size, and upper body anthropometry (Gordon et al., 1989).

The main objective of this task was to identify safe limits of HSD weight moments that can be tolerated by female aviators without adverse effects on their health and performance. The

approach was to measure and assess biomechanical, cognitive, physiological, and performance parameters associated with the exposure of female subjects to simulated helicopter vibration signatures and different helmet configurations.

INSTRUMENTATION DEVELOPED AND USED

Simulated HSD platform

To simulate various HSD weight moments, a modified aviator helmet was utilized for this study (Figure 6-1). This helmet allowed the investigators to vary weights and centers of mass (CM) precisely and rapidly. The helmet was calibrated for 5 weights (1.4 to 4.1 kg) and 21 CM locations (in the x, y, and z planes). This HSD simulator was used with success for male subjects in previous USAARL experiments and found to be adequate (Butler, 1992; Lantz, 1992; Alem et al., 1995). The appropriate locations of the weights were determined according to the method developed by Barazanji and Dodson (1998). A light assembly was affixed to the top of the helmet (the tube-like structure in Figure 6-1) for the purposes of target tracking.



Figure 6-1. Side view of the helmet simulator.

Accelerometers/bite bar

Under whole body vibration exposure, the head moves in a natural nodding motion in the mid-sagittal plane. This movement consists of two motions: linear motion in the superior-interior (axial) and anterior-posterior (AP) directions and angular motion in the pitch direction about the left-right axis. Since this was a three-degrees-of-freedom motion, at least three

independent accelerometer readings were necessary to solve the kinematics problem. However, a fourth redundant accelerometer was added to simplify the equations and to obtain a robust solution. Thus, four miniature uni-axial accelerometers were mounted strategically on a bite bar (Figure 6-2).

The bite bar developed specifically for this study consisted of a precision-machined, lightweight aluminum alloy mount, approximately 12 cm long and attached to a U-shaped bite plate. This bite plate was fitted to the subject's teeth using dental molding compound one day prior to testing. The accelerometers (Entran model EGAXT) each measured approximately 5 x 4 x 8 mm with a dynamic range of 150 m/s². The bite bar was used during the swept sine vibration testing as explained below in the Procedures section.

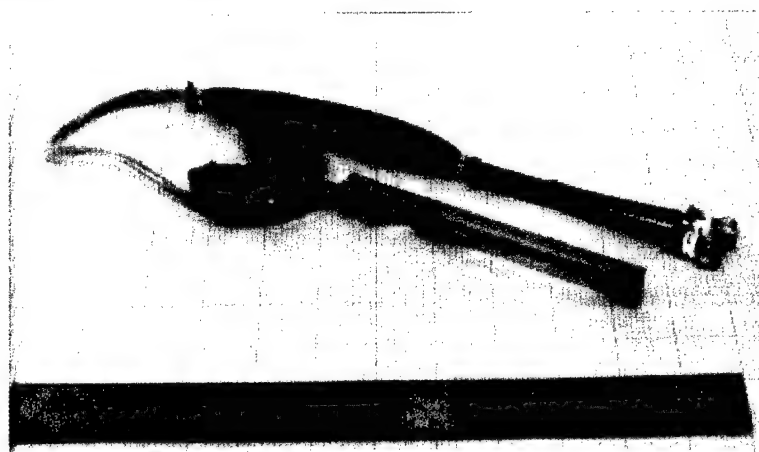


Figure 6-2. Picture of bite bar assembly.

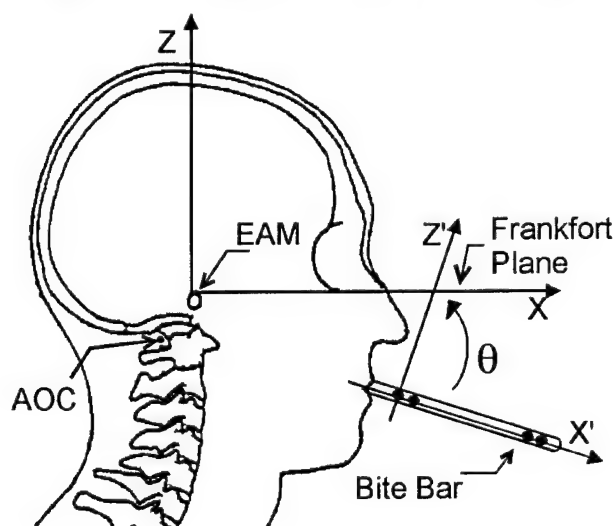


Figure 6-3. Location of bite bar accelerometers with respect to EAM and AOC. EAM represents origin of the anatomical coordinate reference system XZ. θ is a pitch angle relating the bite bar coordinate system X'Z' to XZ. Filled circles on the bite bar represent locations of accelerometers. The X and Z axes denote the AP and axial directions, respectively.

Electromyographic equipment

Measurement of fatigue was achieved by applying electrodes to the trapezius, sternocleidomastoid and splenius capitus. The electrodes were attached to the subject and connected to an amplifier, which then was attached to a recording device.



Figure 6-4. Picture of electrode application.

The pre-amplified EMG signals were amplified further to a range of ± 2.5 volts and were routed to a 14-channel instrumentation VHS tape recorder. Recording speed was set to ensure a bandwidth of at least 250 Hertz. In addition to the analog tape recording, the signals were digitized in real-time as they were recorded. Data acquisition software, SnapMaster, was used for this purpose. The EMG signals were passed through anti-alias filters prior to digitizing. The SnapMaster package was configured as a virtual instrument to detect different light emitting diode (LED) signals and capture at least 2-second data windows (2048 samples). Each window was saved on disk for subsequent spectral analysis.

Response time and tracking

In the head-tracking task, the subject pointed the light source at a target at the center of a moving photocell array placed 2 meters in front of the subject. This target moved horizontally and vertically in a random pattern at a rate of 6 deg/sec measured relative to the subject's eye position. The target array is 32 by 32 photocells, with a resolution of 64 by 64, covering an area of 0.6 m by 0.6 m.

In the target acquisition task, the subject was faced with four target LEDs symmetrically located on the corners of a rectangular semi-circular platform. After an LED turned on, the subject had 5 seconds to aim the collimated light beam on the helmet at the target to 'acquire' it.

A photocell located just below the target turned off the target LED when the light beam struck it for 0.8 seconds. The targets were activated in a random order with a random time interval of 5 to 10 seconds. A target acquisition signal was also recorded on FM analog tape so that myoelectric activity can be correlated with ballistic head motions.

The Multiple Attribute Task Battery (MATB) was the primary cognitive performance task. MATB is a PC-based interactive program designed to simulate a pilot's environment.

PROCEDURES

The general approach of the study was to measure the subject's maximal voluntary contraction against a static load cell, with muscle EMG being recorded before and after the test session. Head acceleration of female subjects in response to swept sine vibration for 12 helmet configurations were measured after the response time and MATB testing, but before the post-session neck muscle EMG testing. The 12 helmet configurations were selected to reflect 3 helmet masses at 4 different CM locations (refer to Table 6-1). The weight moments selected for the study were 55, 70, 80, 95, 110 and 200 N-cm. This approach is a repeated measure design with two factors (helmet mass and helmet CM location). In addition, the design was considered as a repeated measure with helmet weight moment (product of helmet mass and helmet CM location) as the only factor. The subjects were seated in a UH-60 seat that was attached to the USAARL multi-axis ride simulator (MARS) platform. The bite bar was held rigidly in the subject's mouth during the test.

Table 6-1.
Helmet mass properties for the swept sine vibration exposure.

	Helmet ID*	Design helmet mass (kg)	Design helmet CM forward distance relative to the head CM (cm)	Actual helmet mass (kg)	Actual helmet CM forward distance relative to the head CM (cm)	Actual helmet CM forward distance relative to the head AOC (cm)	Helmet weight moment relative to the head AOC (N-cm)
0	H00	No helmet					
1	H2-	2	-2	2.227	-2.76	0.29	6.3
2	H20	2	0	2.227	-0.65	2.40	52.6
3	H22	2	2	2.227	1.16	4.21	92.2
4	H24	2	4	2.227	2.97	6.02	131.9
5	H3-	3	-2	3.150	-2.40	0.65	20.0
6	H30	3	0	3.150	-0.38	2.67	82.5
7	H32	3	2	3.150	1.65	4.70	145.1
8	H34	3	4	3.150	3.67	6.72	207.7
9	H4-	4	-2	4.167	-2.55	0.50	20.5
10	H40	4	0	4.167	-0.67	2.38	97.3
11	H42	4	2	4.167	1.84	4.89	199.8
12	H44	4	4	4.167	3.72	6.77	276.6

* The first digit in the helmet ID reflects the intended (design) total weight of the helmet. The second digit represents the intended (design) location of the helmet CM relative to head CM in the AP direction. For example, H34 has a weight of 3 kg and the helmet CM is located 4 cm in front of head CM. The minus sign in the ID represents the helmet CM location as being 2 cm *behind* head CM. The number "2" is dropped from the ID for convenience. For example, H3- has a weight of 3 kg and the helmet CM is located about 2 cm behind head CM. The reason for this designation is to have compatible comparisons with Butler's male study (1992).

RESULTS

Figure 6-5 shows an example of typical responses of the platform acceleration and the head accelerations of subject #5 for 12 helmet configurations. Note the symmetry in responses between ramp-up and ramp-down phases of the swept sine vibration among all helmet configurations. This allowed averaging the magnitude for both phases of vibration, which was plotted against the input frequency of platform acceleration (Figure 6-5).

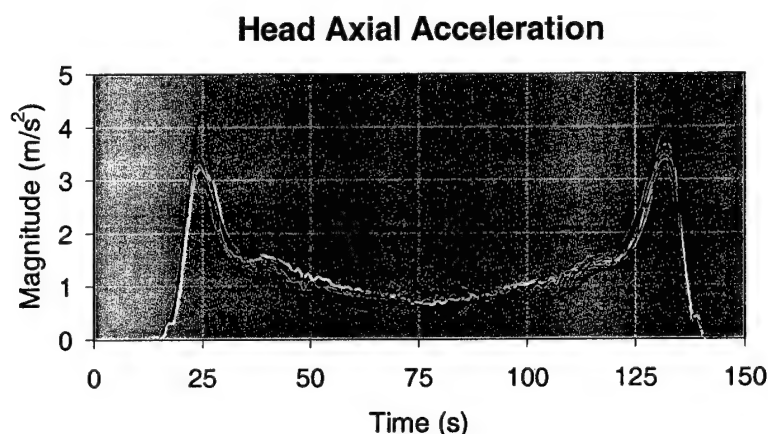


Figure 6-5. Typical vibration responses over time.

Although there was more than one resonant frequency, the first one was considered for this analysis because it was the most dominant. The first resonant frequency and its magnitude were extracted for each helmet load and for each subject. Figure 6-5 shows the first resonant frequency and magnitude of head axial, AP, and pitch accelerations for subject #5, as functions of helmet weight moment relative to AOC.

The pitch acceleration magnitude data were rearranged and plotted in Figure 6-6 (left panel) against helmet weight and CM relative to head AOC. Figure 6-6 also shows the distribution of helmet weight moment versus helmet weight and CM location relative to head AOC.

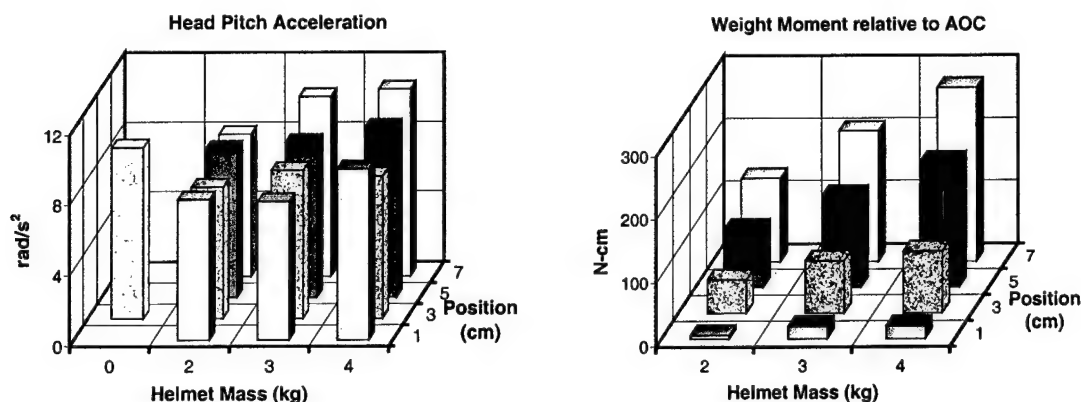


Figure 6-6. Head pitch acceleration (left panel) and helmet weight moment (right panel) are displayed against helmet mass and helmet CM (relative to head AOC). The unloaded (no helmet) case is also shown as the zero mass helmet.

Figures 6-7 and 6-8 show the pitch acceleration magnitude plotted as a 2D chart with all possible interaction scenarios between the design factors. The figures show the pitch acceleration magnitude averaged among helmet CM positions at each weight (Figure 6-7, right plot) and averaged among helmet weights at each CM position (Figure 6-8, right plot).

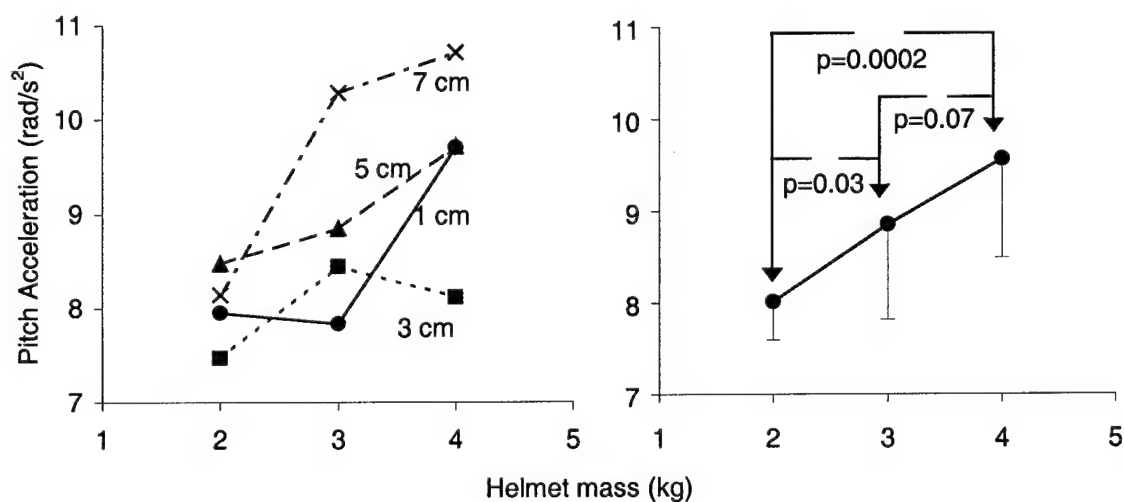


Figure 6-7. Pitch acceleration magnitude versus helmet mass. Averaged among 12 subjects for each helmet CM position relative to head AOC (left plot) and averaged for all helmet CM positions (right plot). Error bars are SD.

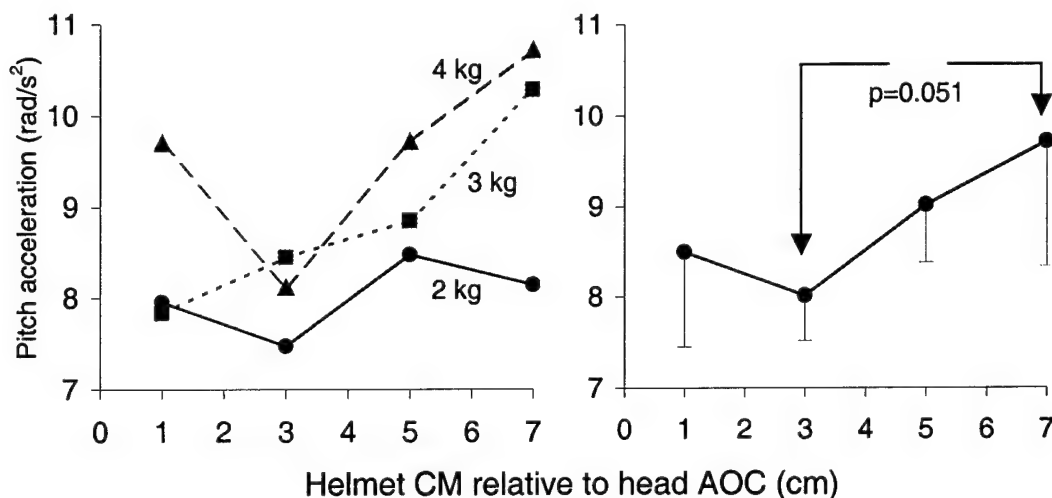


Figure 6-8. Pitch acceleration magnitude versus helmet CM position. Averaged among 12 subjects for each helmet mass (left plot) and averaged for all helmet masses (right plot). Error bars are SD.

The results of the EMG aspect of the testing indicated that the level of fatigue was related to the location of the helmet center of mass.

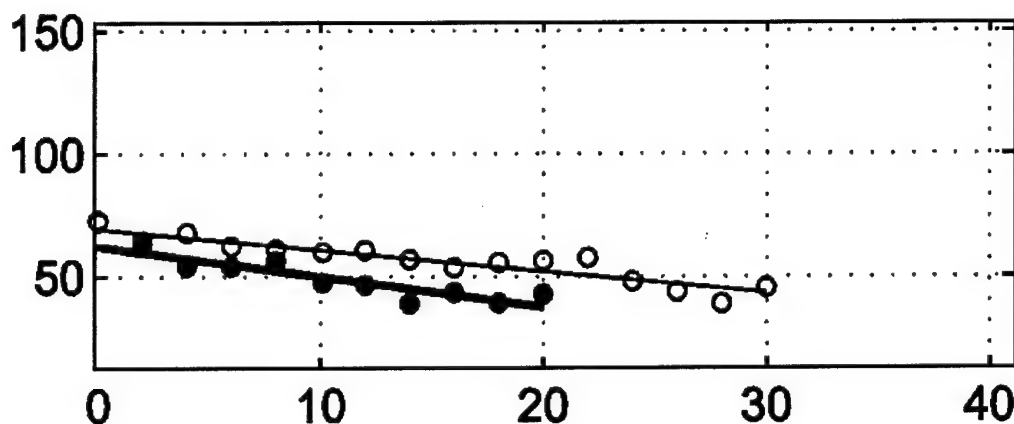


Figure 6-9. Graph of mean power frequency (x, in Hz), over time (y, in seconds) of the EMG with individuals subject's pre-test in open circles and post-test in closed circles.

Figure 6-9 demonstrates how the post-test EMG indicates a greater degree of initial fatigue by way of a lower mean power frequency than the pre-test at the beginning of the efforts, and by the greater rate of mean power frequency decrease over time. Further analysis demonstrated that when the individual factors of head supported mass and center of gravity location were separated, the center of gravity location was the most important factor.

Analysis of the cognitive aspects of the research (the target tracking, locating and MATB) is still under way.

DISCUSSION OF RESULTS

Analysis based on the data shown in Figures 6-7 and 6-8 suggests that the magnitude of head pitch acceleration is the most sensitive parameter to changes in helmet weight moment. This is in general agreement with Butler's (1992) findings for male subjects. Furthermore, ANOVA tests reveal that helmet weight is a more significant factor than helmet CM position in changing pitch acceleration. These upswings of pitch acceleration response from H3- to H4- and from H40 to H4- were also observed in the male aviator but were not significant (Butler 1992). This is an important gender difference, suggesting that negative head loading is more detrimental for females than males. During negative loading, the frontal neck muscles (e.g. sternocleidomastoid) should play the most active role in supporting the head. Thus the gender-difference for negative loading may be attributed to gender-differences in frontal neck muscular characteristics such as density and muscle fiber recruitment.

The results of the EMG aspect of the study showed how the head supported mass configurations resulted in clear indications of fatigue when the center of mass was moved forward.

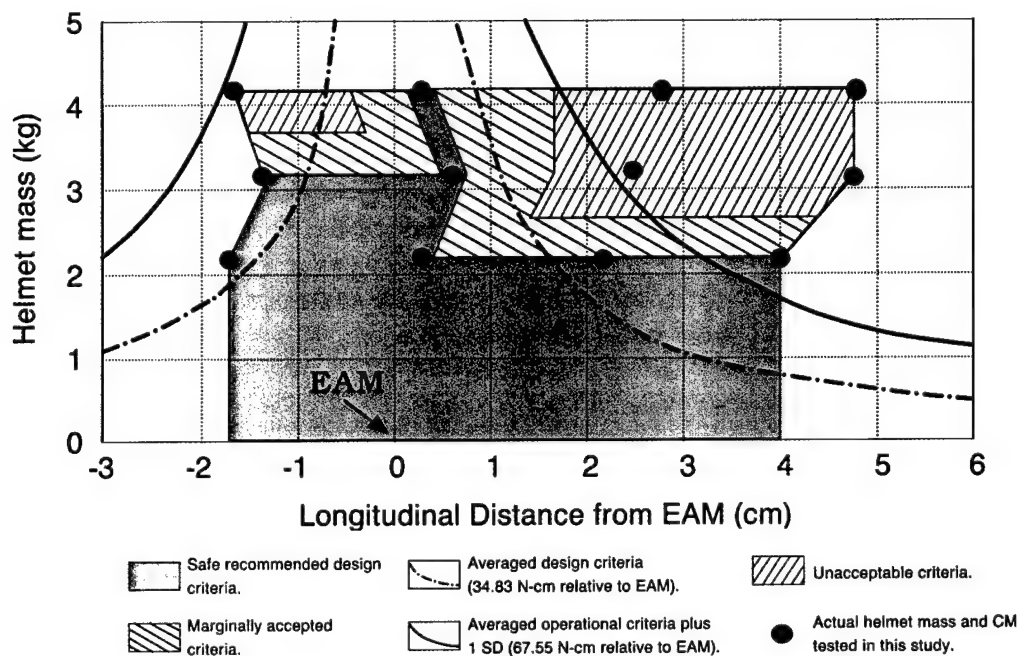


Figure 6-10. Guideline for head supported mass configurations.

The results reported here suggest that head pitch acceleration for the female subjects is the most sensitive response to head-supported devices, compared with AP and axial accelerations. Based on this biomechanical response, we recommend that operational criteria for head-supported devices should follow the shaded areas of Figure 6-10. For extrapolation, the helmet weight moment for female aviators should not exceed the conservative upper-limit of 35 N-cm or the more relaxed upper limit of 68 N-cm, both relative to EAM (91 N-cm and 120 N-cm

relative to AOC, respectively). Indeed, other parts of the study (i.e., neck EMG and performance responses) need to be analyzed in order to assure this recommendation. In general, the design criteria for head-supported devices based on head motion are similar for male and female aviators. However, further studies are needed to address head motion differences between male and female aviators wearing helmets with counterbalance weights.

REFERENCES

- Alem, N.M., Meyer, M.D., and Albano, J.P. (1995). Effects of head supported devices on pilot performance during simulated helicopter rides. Fort Rucker, AL: U.S. Army Aeromedical Research Lab. USAARL Report No. 95-37.
- Barazanji, K. and Dodson, J. (1998). Test and evaluation of the variable weight, variable CG helmet simulator. Fort Rucker, AL: U.S. Army Aeromedical Research Lab. UES, Inc. Report.
- Barazanji, K. and Dodson, J. (1998). Effects of head-supported devices on the biomechanical response of females during whole-body vibration. Fort Rucker, AL: U.S. Army Aeromedical Research Lab. UES, Inc. Report.
- Barazanji, K. and Alem, N. (2000). Effects of head-supported devices on female aviators during simulated helicopter rides. Part I: Biomechanical response. Fort Rucker, AL: US. Army Aeromedical Research Lab. USAARL Report No. 2000-16.
- Butler, B.P. (1992). Helmeted head and neck dynamics under whole-body vibration. Ph.D. dissertation, University of Michigan, Ann Arbor, MI.
- Gordon, C.C., Thomas, C., Clauser, C.E., Bradtmiller, B., McConville, J.T., Tebbetts, I., and Walker, R.A. (1989). Anthropometric survey of U.S. Army Personnel: Methods and summary statistics. Technical Report, Natick/TR-89/044.
- Lantz, S.A. (1992). Analysis of the effects of head-supported mass and random axial whole-body vibration on changes in neck muscle myoelectric activity, posture, and vigilance performance. Final report for contract #DABT01-92-P2326, USAARL.
- Sobotta, V., and Figge, F.H. J. (1974). Atlas of human Anatomy. Vol 1. NY: Hafner Press.

TASK 7

Investigation of Occupant Restraint Issues in Vehicle Occupant Safety and Performance

Subtask A: Head Supported Mass and Soldier Health

INTRODUCTION

Modern U.S. Army helicopters use the helmet as an integral component of the aircraft control systems. The helmet has evolved from a simple crash protection device to a mounting platform for advanced technologies that greatly increase the effective combat power of the helicopter in the field. The helmets now support such devices as NVG, chemical mask, oxygen system, head-up display (HUD), forward looking infrared (FLIR) display, flash blindness and laser eye protection and weapon aiming systems. All of these devices add weight to the helmet, and displaces the CG of the system. This increased weight and displaced CG add biomechanical stress to the neck and upper body of the pilot, and may also lead to decrements in performance. Preliminary results in the area of performance decrements have already shown that the misplacement of the CG does adversely affect the performance of the pilot (Alem, Meyer and Albano, 1995).

UES and the USAARL have completed preliminary studies of HSM effects on operator performance and acute neck injury in rotary-wing operations. Findings in these areas have led to the discovery of such facts as the relationship between helmet CG and task performance (Barazanji and Dodson, 1998) and helmet mass configuration and interaction with airbags (Mobasher and Brozoski, 1998). UES and USAARL investigators have identified the potential for chronic injury development as well. In response to the need for investigation of chronic injury development, UES researchers have instigated the inclusion of measures and methods that address the quantification of chronic injury development. A combination of epidemiological techniques and experimental measures will produce new information leading towards a dose/response metric in helmet loading and neck fatigue and performance decrement. This new approach is well served by existing information gathering taking place at USAARL, as well as coordination with external sources.

In addition to the UES/USAARL research, the US Army Research Institute of Environmental Medicine (USARIEM) has experience with computer models of dismounted soldier activities and injury epidemiology. While the aviation data do not apply directly to the ground environment, the methodology is transferable and in collaboration with USARIEM, will facilitate dismounted, airborne and mounted models. This sub-task is part of an ongoing investigation into the proper planning and execution of research programs, performance testing with human volunteers wearing head-supported devices and cadaver and manikin studies, with the aim of producing predictive models for neck injury and human performance decrements for these environments.

UES researchers are also active in the creation of computer command and data gathering systems, developed for the express purpose of accomplishing this sub-task. Bradley Bumgardner is currently programming C+ code and working with pre-packaged computer programs such as LabView in order to allow centralization of the disparate data sources into a single laptop computer.

BACKGROUND RESEARCH

Researchers Phillips and Petrofsky (1983) performed experiments looking into the effects of various configurations of head supported mass and its distribution. Using a specialized helmet as a platform for mass re-distribution, the overall mass and CG of the helmet system was varied to observe effects on neck muscle fatigue. The researchers found that the neck muscle endurance time is sensitive to changes in weight and the CG location. This work provided information towards the idea that, in terms of neck muscle fatigue, the optimal location for the CG of head-supported mass was approximately 6 cm forward from the atlanto-occipital complex (AOC). Further work in the area tends to focus on the biodynamic responses to whole body vibration (Butler, 1992), or situations where high forces are applied to the neck via the helmet system (Perry, Buhrman and Knox, 1993). There seems to have been little information with respect to the chronic static loading effects on aviator's performance in the general literature.

Presentation of secondary tasks to pilots has been useful in the evaluation of pilots in the UH-60 helicopter simulator. Previous studies in the UH-60 have used presentation of tones (with an appropriate response) to evaluate mental workload of the pilots as they perform standardized maneuvers (Braithwaite et al., 1997).

Building from the base of information provided by the MARS lab studies performed at USAARL, the next phase of investigation is to take the research into more applied environments and adapts the measures accordingly. The physical measures of head vibration response and neck muscular fatigue, the cognitive measures of the MATB and the performance measures of the target acquisition and tracking tasks serve as a solid basis in defining effects of head supported mass on soldiers. This protocol will measure performance variables of the same nature as the original research, but adapted to suit the strengths and limitations of the simulator environment. The measures will be:

- muscular fatigue
- acquisition of targets placed throughout the cabin
- flight performance
- cognitive abilities
- subjective assessment of equipment quality

MATERIALS

HSM attachment platform

To simulate various HSD weight moments, a modified aviator HGU 56P helmet will be utilized for this study. This helmet will allow the investigator to vary its weight and center of mass (CM) precisely and rapidly. Attached to the bottom of the ear cups (bilaterally) are fixtures that have a graduated cylinder protruding forward. Along these cylinders are various weights that may be secured at any point. This allows for the addition of various weights at different distances, thereby allowing control over the location of the helmet system mass and the location of the center of gravity. The graduations in the supporting cylinders allows for accurate replication of the weight placements. The bilateral nature of the fixtures ensures that, for the purposes of this experiment, the center of gravity is relocated along the x-y (sagittal) plane only. Exact measurement of the helmet center of gravity locations as a function of the different weights at different locations (including the head motion tracking equipment attached to the helmet) will be accomplished using the USAARL mass properties measurement machine prior to the experiment.

Table 7a-1.

Describing the experimental weight moments
as a function of head supported weight and CM distance

	Center of mass distance from AOC (cm)			
		2.4	3.9	6.4
Head supported weight (N)	14		55 N.cm	
	22.9	55 N.cm	90 N.cm	147.4 N.cm
	37.5	90 N.cm	147.4 N.cm	

Muscular fatigue

Close coordination with the Naval Air Warfare Center at Patuxent River has allowed for provision of specially designed equipment in the gathering of strength and electromyographic data. Through communications and video teleconferences, the capacities of the Naval Command were found to be complimentary to the goals of this sub-task. To this end, the materials and methods described here are a result of cooperation between USAARL and the NAWC. The exact logistics of gathering and analyzing this data is still a matter of conversation and will be finalized before testing begins.

To monitor muscular electrical activity and muscular fatigue, subjects will wear DelSys, Inc. (Boston, MA) integrated EMG Ag-AgCl surface electrodes over their right and left sternocleidomastoid (below and behind the ear), splenius capitis (on the back of the neck next to the midline under the head harness), and trapezius muscles (at the base of the neck) to record muscular activity. These electrodes are affixed to the skin with adhesive tape and do not

puncture the skin. A reference electrode will be placed over an area remote to the head and neck area, such as the tip of the clavicle (shoulder).

A 100 lb. uniaxial load cell is mounted to the test fixture (Figure 7a-1). The subject's head harness is attached to the load cell via a 1" wide webbing strap. Output data from the load cell is collected by a computer data acquisition system. This system also provides visual and audio feedback of the loads exerted over time. The investigators use the video display to monitor subject progress while audio feedback is provided to the subject to standardize verbal encouragement and cueing to the entire subject pool.

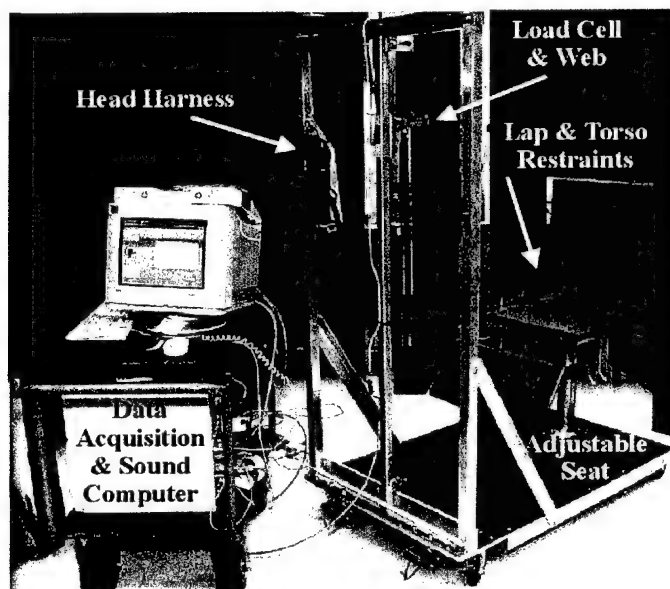


Figure 7a-1. Picture of the strength and electromyographic data equipment.

Randomly appearing targets

This aspect of the testing will involve the presentation of targets to the subject at different locations during level flight while following a lead helicopter. The targets that are to be responded to will be in the form of small display screens strategically placed in a semi-circle around the subject's visual field. These display screens will be controlled by a laptop computer, which will be synchronized with the VAX of the UH-60 simulator. During these trials, only one screen will display the target number; the other screens will be blank. The placement of the screens throughout the cabin will be on the periphery of the pilot's field of view when looking forward (refer to Figure 7a-2).



Figure 7a-2. Locations of proposed target displays (as dots).

UH-60 flight performance data acquisition

The performance of standardized flight maneuvers is a common element when using the UH-60 simulator to observe effects of various conditions. This includes a flight schedule that includes elements of low intensity flights (i.e. straight and level flights, following a lead ship), higher intensity maneuvers (i.e. banking, altitude changes) and a combination of maneuvers and measures scheduled appropriately (i.e. straight and level with the target acquisition task). The variables from the flight (including altitude (barometric and radar), airspeed, heading, attitude (roll, pitch and yaw), vertical speed and X-Y coordinates) will be captured using the simulator software, allowing for errors in flight control to be measured and analyzed during the various phases of the testing protocol.

Psychophysical questionnaire

To supplement the physical and cognitive measures, the subjects will be given a series of questions regarding their psychophysical interactions with the helmets and their perceptions when exposed to the various configurations. There will be three questionnaires used in this study: one to be completed during the flight profile and two to be completed at the end of each test session.

The first questionnaire presented to the subject after the flight profile has been completed is the Simulator Sickness Questionnaire (SSQ). This questionnaire evaluates the subjective sickness symptoms of the subjects, and will be performed using a lap top windows version of the SSQ. The SSQ is a self-report form consisting of 28 items that are rated by the participant in terms of severity on a 4-point scale. Responses from the MSQ will be automatically scored and presented on the computer screen for the medical monitor to examine. This questionnaire will take approximately 5 minutes to administer.

The second end-of-session measure will take the form of paper-based questionnaires that was designed by the experimenters. The questionnaire will be in the format of rating scales to

measure comfort, perception of helmet balance and preferences regarding the mass configuration, plus areas for subjective qualification of the ratings and two open-ended subjective questions. The questions were designed according to accepted practices in the psychological field, including such considerations as the number of possible responses, anchor phrases and balance to avoid ceiling effects. There will also be a small area for an open-ended feedback to obtain the volunteer's opinion on how the mass oriented on their head and any other comments.

The mid-session questions will be administered to the pilots at 50 minutes, 1 hour 50 minutes, 2 hours 50 minutes and 3 hours 50 minutes. These questions will be verbally administered to the pilots and during straight and level flight. These questions will be related to the final questionnaire so as to provide a time history of perceived fatigue and discomfort development over the four-hour flight profile. The questions will ask the pilot to rate elements of their perceived fatigue and discomfort, though the exact nature of the questions will necessarily be different from the final questionnaire, given the potential differences in verbal vs. written questionnaire responses.

PROCEDURES

Muscular Fatigue

For the data trials, strength will be measured in the forward (flexion) and backward (extension) directions and in rotation (right and left). The subject will don a skullcap, the head harness, 3DM, and be restrained in the seat. Subjects will assume a neutral position, defined as a head position of 0° pitch and yaw as measured by a mechanical Cervical Range of Motion device. Before each exertion, subjects will return their heads to the neutral position. Subjects will then be instructed to smoothly pull using head and neck through a predefined angle (30° for extension and forward flexion and 50° for rotation). The weight and maximum angular displacement of the fixture will be measured. In order to ensure consistency within an individual subject's efforts and between subjects, they must reach the required displacement angle at a set rate and time (6° per second). A metronome will be used to supply rate/rhythm cues and the CDAS will indicate aurally when the subject has reached the prescribed displacement angle. Subjects will take 5 s to reach 30° for flexion and extension and 8 s for rotation. If the subject is successful, then they will rest for 45 s while additional weight is placed on the carriage. The subjects will describe their effort using a Borg scale (Borg, 1982).

If the subjects rate their effort 5 or lower, the load will be increased by 5 lb. If the subjects rate their effort 6 or 7, the load will be increased by 2.5 lb. If the subjects rate their effort 8 or 9, the load will be increased by 1 lb. If effort reaches 10, no additional weight will be added. This procedure will be repeated until the subject can no longer reach the required angular displacement or voluntarily stops. At that point, the weight may be reduced, as necessary, to determine the maximal voluntary dynamic effort (MVDE) to within 1 lb. During these exertions, subjects will be instructed to breathe out slowly and steadily during their efforts. During the rest periods, subjects will be free to stretch and/or rub their neck muscles. A rest period of at least 5 minutes will occur between exertions in different directions.

To monitor muscular electrical activity and muscular fatigue, subjects will wear surface electrodes over their right and left sternocleidomastoid (below and behind the ear), splenius capitis (on the back of the neck next to the midline under the head harness), and trapezius muscles (at the base of the neck) to record muscular activity. The electrode leads will be connected to a pre-amplifier, then to a laptop computer that will store and process the information.

After the trials have been completed, the fatigue measures will be taken. Following a minimum 5-minute rest, subjects will be instructed to repetitively pull a load of 70% of MVDE at 6° per second to the prescribed angle (or greater) for as long as they can. A metronome will be used to provide a timing frequency for the repetitions (10 seconds between each repetition). By having a standardized beat, endurance time can be compared between subjects. Auditory cues will be available so that the subjects can gauge their timing and know when they have reached the required displacement. The investigators will terminate the run if the subject is not consistently reaching the required angle or cannot maintain the repetition frequency. The key metric is the overall endurance time. The investigators may provide verbal feedback to the subject during the testing to help with timing if necessary. The endurance tests will be conducted for flexion, extension and right and left rotation with a rest period of at least 10 minutes between each movement.

Randomly appearing targets

This aspect of testing will occur during straight and level flight while following a lead ship. The pilots will be instructed to maintain their attention on the lead ship until instructed to search for the target number and to return their attention to the lead ship after the appropriate number has been responded to. The laptop will be programmed to illuminate one of the displays with a number between 1 and 5. The appropriate response to this signal is the activation of a designated control on the collective the number of times indicated by the signal (1-5). The cue for initiation of the task will be an auditory signal consisting of a tone of 1000 Hz, which lasts for 0.5 seconds. This auditory cue will coincide with the initiation of the display and time recording. Response times will be measured by the time it takes to initiate a response (the first activation of the control, irrespective of the final accuracy of the response) from the presentation of the cue signal. The accuracy of the responses in relation to the target signals will be measured as well.

Psychophysical measurements

The mid-session questionnaires will be presented to the subjects at 50 minutes, 1 hour 50 minutes, 2 hours 50 minutes and 3 hours 50 minutes from the start of the session. These will be administered verbally to the pilots during straight and level flying (to avoid undue distractions in how the pilots report their perceptions, as compared to during NOE flight). The experimenters will record the responses.

The post-session questionnaires to be completed by the pilots will be given to them after they had completed all other tasks within each test session. The subjects will complete the questionnaires before they leave the facility.

CONCLUSION

The protocol developed to achieve this sub-task is currently being prepared for review by the Human Use Committee at Fort Rucker to ensure the safety and health of the volunteers will be protected. Continuing coordination with the Navy Air Warfare Center is ensuring that the potential collaboration will be achievable by both parties with respect to technologies, goals and logistics. There is also continuing development in the area of the technologies being invented for this sub-task, including the variable center of mass platform, target acquisition hardware and computer control systems.

REFERENCES

Alem, N.M., Meyer, M.D., and Albano, J.P. (1995). Effects of head supported devices on pilot performance during simulated helicopter rides. Fort Rucker, AL: U.S. Army Aeromedical Research Laboratory. USAARL Report No. 95-37.

Barazanji, K. and Dodson, J. (1998). Effects of head-supported devices on the biomechanical response of females during whole-body vibration. Fort Rucker, AL: U.S. Army Aeromedical Research Lab. UES, Inc. Report.

Borg, G. (1982). Psychological bases of perceived exertion. *Medicine and Science in Sports Exercise*, 4, 377-381.

Braithwaite, M., Alvarez, E., Jones, H., Higdon, A., Groh, S., Beal, K., Estrada, A. (1997). A helicopter simulator assessment of pilot head movement during various phases of flight. USAARL Technical Report 97-26.

Butler, B.P. (1992). Helmeted head and neck dynamics under whole-body vibration. Ph.D. Dissertation, University of Michigan, Ann Arbor, MI.

Mobashar, AA, Brozoski, FT, McEntire, BJ, and Alem, NM. (1998). Effects of seat stroke distance on the allowable mass of head supported devices. USAARL Technical Report 98-27.

Perry, C., Buhrman, J., Knox, F. (1993). Biodynamic testing of helmet mounted systems. *Proceedings of the Human Factors and Ergonomics Society 37th Annual Meeting*, 79-83.

Phillips CA, Petrofsky JS. Quantitative electromyography: Response of the neck muscles to conventional helmet loading. *Aviat Space Environ Med.* 1983; 54:452-7.

TASK 7

Investigation of Occupant Restraint Issues in Vehicle Occupant Safety and Performance

Subtask B: Vehicular Occupant Restraint Systems

INTRODUCTION

The civilian automotive industry is pursuing numerous new and innovative technologies to enhance occupant safety in the crash environment. Advanced restraint systems (active and passive) are designed against requirements specific to the intended host platform. The army material developer needs biodynamic-based performance criteria and standard assessment methods, to evaluate the safety potential of these systems specifically in the army vehicles. Soldier safety can be enhanced through appropriate adoption of these technologies into army vehicles.

Currently, there is no accepted standard for assessing occupant restraint system performance levels independent of performing expensive vehicle crash tests and platform specific dynamic systems tests. Development of a standard dynamic test methodology, with biomedically relevant performance criteria, could provide a means to critically evaluate improved restraint systems. It would also reduce exploratory developmental cost borne by the material developers and better identify restraint system technologies likely to enhance soldier safety in the crash environment.

Restraint performance trends can often be efficiently and cost effectively studied through the systematic variation of properties within physics based computational models. This can increase the understanding of restraint system performance and their sensitivity to different input variables. Development of computational models representative of innovative restraint systems allow easy application into various vehicle platforms and specific dynamic conditions appropriate for various vehicles.

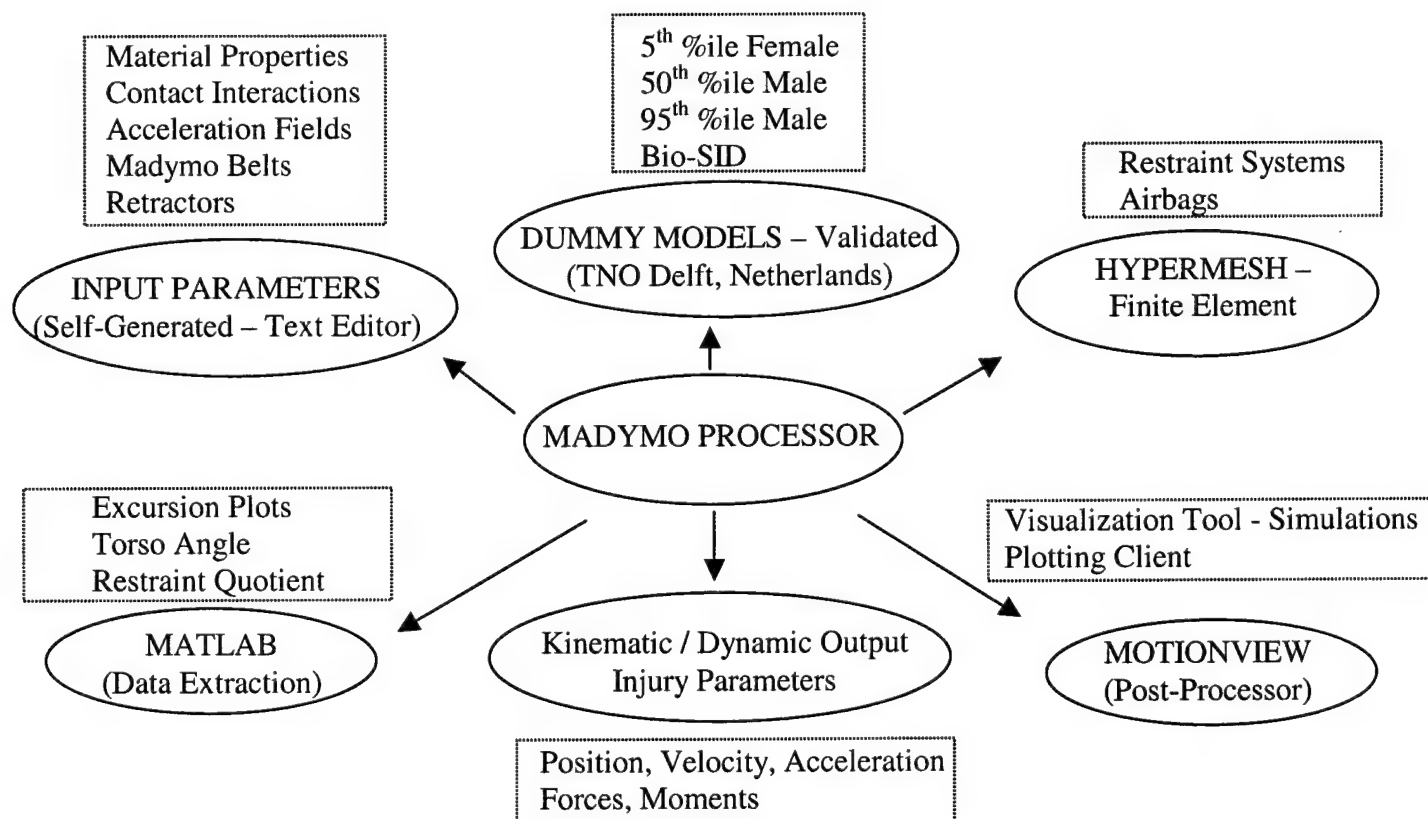
UES, Inc. research in this area supports USAARL in-house research in support of the United States Army Medical Research and Materiel Command's Scientific and Technical Objective F (USAMRMC STO F). STO F is concerned with the investigation of conventional and active (inflatable) restrains on vehicle occupants. Many injuries that occur in tactical vehicle crashes are preventable through use of improved occupant restraint systems. As current inventory vehicles are upgraded and new vehicles are developed, there is an opportunity to implement state-of-the-art safety systems.

METHODOLOGY

The study was conducted in four phases. The first step was to identify the injury parameters that would be considered to evaluate the performance of the restraints. Dynamic testing was planned for a set of restraints that were procured previously through commerce

business daily. Dynamic testing of seat belts using the sled deceleration method is a relatively costly test procedure and the number of tests to validate the quality of a seat belt should be kept to a minimum. The shape, onset rate, peak 'g' and time duration of the deceleration pulse are the parameters that govern the resultant dynamics. In order to reduce the number of tests required for dynamic compliance of seat belts, it is necessary to determine pulse shape, which would produce the greatest loading (relative to each other at a particular peak 'g') in the dummy and the seat belt. Moreover, the pulse shape should be achievable and repeatable in a series of sled tests. To start with the simulations a standard 5-point restraint was modeled in HyperMesh (finite element package). Madymo software was used for multibody simulations. An optimization study was conducted on the mesh density of the finite element model before full-scale simulations were run. Using the optimized mesh for the restraint, three different pulse shapes at two different magnitudes were run to understand the effect on dummy loading. There was a need to select crash pulses that would illuminate restraint system performance keeping the dynamic tests non-destructive. Using the selected pulse shape and varying the magnitude in three different directions, an optimum pulse was selected for the physical dynamic testing of the restraints. Finally, a test plan was prepared to dynamically evaluate restraints that were procured from vendors.

Occupant and restraint system modeling



HUMAN TOLERANCE LIMITS

The study of factors affecting human tolerance, establishing human tolerance limits and other related factors concerning the human interaction with the restraining system were identified for further evaluation, to suit the performance requirement of the restraint system.

IARV's (Injury Assessment Reference Values) to be used for evaluation of the test results are as follows:

Neck Injury Indicator (Nij)

Threshold Value: $N_{ij} = 1$

- Combination of forces and moments on the neck
- Better predictor than NIC which accounts for individual values of forces and moments.
- Also accounts for conditions where forces are high and moments are low or vice versa.
- Threshold limit of $N_{ij} = 1$, possess a 22 % risk of AIS 3 for all occupant sizes.

Thoracic Injury Criteria

Threshold value: Chest Acceleration (3ms) = 60g, Chest Deflection = 63mm

- Thoracic Injury Criteria is a better predictor than Combined Thoracic Index (CTI), even if CTI involves a combination of chest acceleration (3ms) and chest deflection.
- CTI events are not dynamic events i.e., the chest acceleration and max chest deflection events are recorded at different time period.
- Therefore individual values specified by Thoracic Injury Criteria are considered to be the threshold levels.

Viscous Criteria (VC) / Soft Tissue Criterion:

Threshold value: $VC = 1 \text{ m/s}$

- Involves combination of chest deformation and velocity of chest deformation.
- Considered as a better predictor of soft tissue injury for velocities of deformation (*Range: 3m/s to 30 m/s*).
- Threshold limit of $VC = 1\text{m/s}$, possess a 25 % risk of AIS > 3 for all dummy sizes.

Thoracic Trauma Index (TTI):

Threshold value: 4 Door Vehicle = 85g, 2 Door Vehicle = 90g

- To be used in the lateral tests.
- Considers the acceleration values of the ribs and the spine.

Pelvis Injury Criteria:

Threshold value: Pelvis threshold = 130g (50th percentile Male)

- To account for the loading of the pelvis region by the lap belts.
- Considered for evaluation according to FMVSS 208.

Restraint Quotient (RQ):

Threshold Range: $0 < RQ < 1$

- To determine the effectiveness of restraint system from velocity build-up.
- Variation of values within the range assist in manipulating the extent of occupant movement.
- Graphical results help to easily determine the extent of chest and pelvis loading.
- Helps to evaluate conditions like submarining.

Torso Angle Criteria:

Threshold Value: $\alpha = 90$ degrees

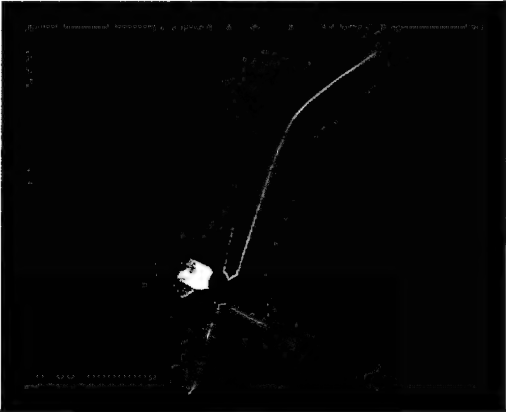
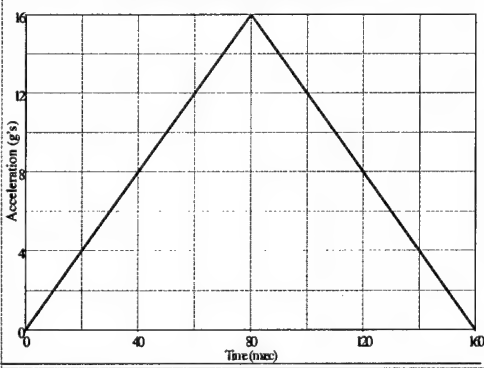
- Evaluation based on the biomechanical quality of the restraint system.
- Optimum position for maximum load bearing is the vertical position.
- Helps to determine the effectiveness of the restraint system in maintaining vertical posture.

A complete description of the injury parameters described above can be found in report 5 (in preparation for USAARL technical Report). The information reported here is garnered from that reporting.

MESH DENSITY OPTIMIZATION

Processing time is a very crucial consideration in computer simulations. Specially, when finite element models are incorporated into simulations, computing time multiplies. Processing time also depends upon the configuration of the computer on which it is run. We used a 800 MHz, single processor Pentium III DELL machine with 512 MB RAM. Preliminary simulations were carried out on this computer to optimize the number of elements in the finite element model of the 5-point restraint. The optimal mesh seed obtained would be used in the later runs for the restraint performance evaluation. Table 7b-1 describes the input parameters for the simulation.

Table 7b-1.
Simulation Parameters

Parameter	Value
Restraint 	5-Point Restraint Shoulder Belt (2): 2" width; 0.043" thick / 25.45" length Lap Harness (2): 2" width; 0.043" thick / 15.24" length Tie-Down (1): 1.75" width; 0.043" thick / 7.5" length Material: Polyester Elongation: 7.5% @ 4000 lbs Pretension: None Slack: (Approx. 5mm)
Simulation Time Duration	300 msec
Integration Time Step	0.005 msec
Acceleration Pulse 	Peak G – 16 g's Change in Velocity - 45 ft/sec Triangular Pulse given to the Dummy Gravity loading given to the Dummy Pulse Duration - 160 msec Onset Rate - 200g/s

The mesh seed was varied in the finite element restraint model, and the injury output parameters were compared. As a rule 'Finer the mesh, better the approximation, but greater the cost'. A finer mesh would produce better results, but would take more processing time. On the other hand, a coarser mesh would not provide so accurate output, but would take less processing time. A break-even point was identified resulting in an optimized solution for both the parameters (time/mesh density). Table 7b-2 gives the mesh characteristics of the five simulations runs carried out for the analysis.

Table 7b-2.
Mesh Characteristics

Simulation	Mesh Seed	Elements	Lap Belt	Shoulder Belt	Tie-down
Simulation 1	9mm	1998	306 (30.6%)	636 (63.7%)	114 (5.7%)
Simulation 2	11 mm	1326	190 (28.7%)	432 (65.2%)	82 (6.18%)
Simulation 3	13 mm	796	118 (29.7%)	248 (62.3%)	64 (8.04%)
Simulation 4	15 mm	582	90 (30.9%)	184 (63.2%)	34 (5.84%)
Simulation 5	18 mm	474	72 (30.4%)	152 (64.1%)	26 (5.49%)

Shoulder belt, lap belt and tie-down belt were modeled and meshed in HyperMesh 4.0. Figure 7b-1 shows the meshed shoulder belt with a mesh seed of 9mm. In all the models the mesh density distribution between the Lap Belt, Shoulder Belt and the Tie-Down Strap was kept approximately the same (Refer Table 7b-2). Table 7b-3 gives the mesh density in terms of elements per inch of the belt. In the case of the 13mm mesh seed simulation, the distribution of the mesh density in the three belts (shoulder, lap and tie-down) is quite consistent.

Table 7b-3.
Mesh Density (Elements/inch of belt length)

	9mm	11mm	13mm	15mm	18mm
Lap Belt Density (2.00" width)	20.08	12.47	7.74	5.91	4.72
Shoulder Belt Density (2.00" width)	24.99	16.97	9.74	7.23	5.97
Tiedown Density (1.75" width)	15.2	10.93	8.53	4.53	3.47

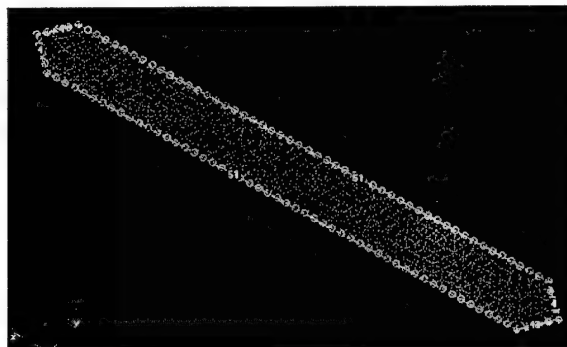


Figure 7b-1. Shoulder Belt Mesh in HyperMesh 4.0.

The meshed belts were exported in a Madymomeshonly.tpl template, to make the madymo program understand the format. Pre-simulations were carried out for each case to get the desired final configuration of the restraint (shoulder/lap/tiedown were done separately) in a loaded position. The mesh output of the presimulations served as an input for the final simulations with prescribed acceleration fields given to the dummy. Figure 7b-2 shows the pre-simulation of the shoulder belt.

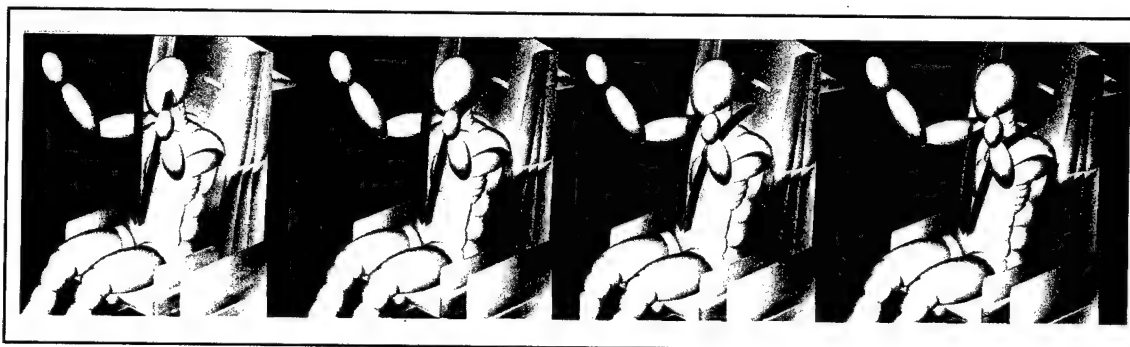


Figure 7b-2. Still Frames of the shoulder belt presimulation.

Observations

Five simulations were run with exactly similar material properties, orientations, acceleration levels, and integration time step. Response parameters consider for evaluation are listed below in Table 7b-4.

Table 7b-4.
Simulation Output

	9mm	11mm	13mm	15mm	18mm
Time (minutes)	38.66	19.68	13.70	11.62	8.53
Elements Lap Belt	306.00	190.00	118.00	90.00	72.00
Elements Shoulder Belt	636.00	432.00	248.00	184.00	152.00
Elements Tiedown	114.00	82.00	64.00	34.00	26.00
ELEMENTS TOTAL	1998.00	1326.00	796.00	582.00	474.00
Peak Head Acc. (m/s*s)	307.41	308.97	305.60	334.52	302.09
Upper Torso (m/s*s)	312.59	294.25	309.92	335.92	305.67
Lower Torso (m/s*s)	339.57	345.34	339.98	309.11	341.22
Lower Lumbar (N)	7016.88	6715.92	6575.37	6540.43	6738.65
Sternum Displacement (mm)	21.74	21.63	21.54	21.77	21.73
Shoulder Belt Load (N)	4143.12	3958.10	4123.82	4368.36	4083.68
Lap Belt Load (N)	5567.2	5643.1	5573.02	5549.99	5622.18
Dynamic Overshoot					
Peak Head Acc. (m/s*s)	1.96	1.97	1.95	2.13	1.92
Upper Torso (m/s*s)	1.99	1.87	1.97	2.14	1.95
Lower Torso (m/s*s)	2.16	2.20	2.16	1.97	2.17

In addition to these parameters, flail in X (frontal) and Z (vertical) was also considered as a deciding factor. Head excursion, upper torso excursion and lower torso excursion was tracked. In the comparison analysis, it was assumed that the 9mm results are the most legitimate and

hence was kept as a benchmark. Deviations from the benchmark values were calculated and analyzed. It is clearly evident that the results from the 13mm mesh seed show the same trend as shown by 9mm output and are not far off. Percentage change for all the outputs has been tabulated below in Table 7b-5.

Table 7b-5.
Percentage Change in the Output

	9mm	11mm	13mm	15mm	18mm
Peak Head Acc. (m/s*s)		0.50	-0.59	8.10	-1.76
Upper Torso (m/s*s)		-6.23	-0.86	6.94	-2.26
Lower Torso (m/s*s)		1.67	0.12	-9.85	0.48
Lower Lumbar (N)		-4.48	-6.71	-7.28	-4.13
Sternum Displ. (mm)		-0.50	-0.93	0.14	-0.04
Shoulder Belt Load (N)		-4.67	-0.47	5.15	-1.45
Lap Belt Load (N)		1.34	0.10	-0.31	0.98
Dynamic Overshoot					
Peak Head Acc. (m/s*s)		0.50	-0.59	8.10	-1.76
Upper Torso (m/s*s)		-6.23	-0.86	6.94	-2.26
Lower Torso (m/s*s)		1.67	0.12	-9.85	0.48

Ideally speaking, 11mm mesh size results should have been closer to the 9mm results. It all depends upon on the structure and the stability of the mesh. 9mm mesh is a fine mesh, which is symmetrical and consistent over the entire belt area. As the mesh grows bigger, the number of elements reduces. The mesh density remains the same but the structure sometimes become unsymmetrical. Depending upon the size of the area, some mesh seeds fit well while others don't. In our case, the 13 mm mesh suits better than the 11/15/18 mm meshes. The computational time was reduced three-fold.

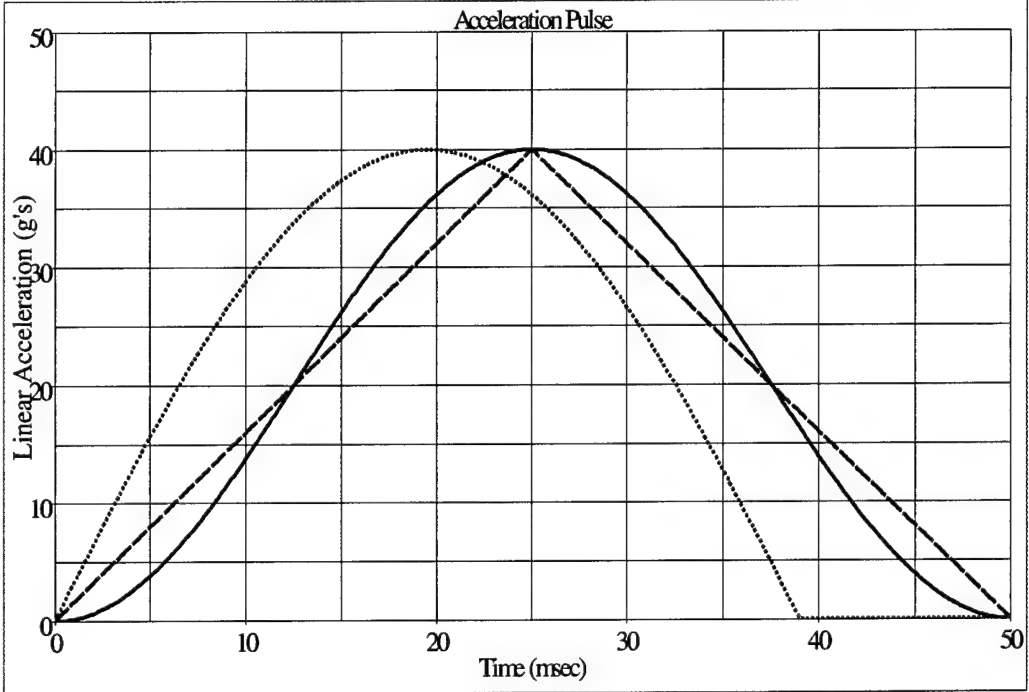
The above-mentioned material has been presented in report 2 (in preparation for USAARL technical report).

SELECTION OF PULSE SHAPES FOR CRASH SIMULATIONS

Introduction

Three different pulse shapes were identified for comparative analysis, viz: triangular, haver-sine and half-sine. Some of the characteristics of these pulses have been listed below in Table 7b-6.

Table 7b-6.
Pulse Characteristics

Pulse	Characteristics
	
Triangular	<ul style="list-style-type: none"> • Constant onset rate • First integral (velocity) = $\frac{1}{2}$ (peak 'g' * pulse duration) • Double integral (distance) = $\frac{1}{2}$ (peak 'g' * pulse duration²)
Haver-Sine	<ul style="list-style-type: none"> • Low initial onset rate; steeper later • First integral (velocity) = $\frac{1}{2}$ (peak 'g' * pulse duration) • Double integral (distance) = $\frac{1}{2}$ (peak 'g' * pulse duration²)
Half-Sine	<ul style="list-style-type: none"> • High initial onset rate; decays later • First integral (velocity) = $\frac{2}{\pi}$ (peak 'g' * pulse duration) • Double integral (distance) = $\frac{2}{\pi}$ (peak 'g' * pulse duration²)

'Velocity change' tables were generated for the three shapes, ranging peak 'g' from 10 to 40, and have been tabulated in Tables 7b-7, 7b-8 & 7b-9. The area under the acceleration curve (energy to be dissipated) for triangular and haversine is exactly the same, but it is 28% more in the case of half-sine. Also, the initial onset rate in the case of a half-sine pulse is steeper than the triangular and the haversine pulses.

Table 7b-7.
Velocity Change Triangular Pulse

Peak G	Pulse Duration			
	50ms	100ms	150ms	200ms
10	8	16	24	32
15	12	24	36	48
20	16	32	48	64
30	24	48	72	96
40	32	64	96	128

Table 7b-8.
Velocity Change Haver-Sine Pulse

Peak G	Pulse Duration			
	50ms	100ms	150ms	200ms
10	8	16	24	32
15	12	24	36	48
20	16	32	48	64
30	24	48	72	96
40	32	64	96	128

Table 7b-9.
Velocity Change Half-Sine Pulse

Peak G	Pulse Duration			
	50ms	100ms	150ms	200ms
10	10.24	20.48	30.72	40.96
15	15.36	30.72	46.08	61.45
20	20.48	40.96	61.45	81.93
30	30.72	61.45	92.17	122.89
40	40.96	81.93	122.89	163.86

Approach

32 ftp 'velocity change' was selected randomly for the comparison of the pulses. In the triangular case, pulses with 40'g' peak (time duration of 50msec) and 10'g' peak (time duration of 200msec) represent 32 fps 'velocity change'. Haver-Sine pulse also follows the same path. Half-Sine pulse time durations had to be computed for 10'g' and 40'g', to attain a velocity change of 32 fps.

$$T = \frac{1.57 * V_o}{32.2 * g}$$

Case-I @ $V_o = 32$ fps; $g = 40$ 'g';

$$T = 39.006 \text{ msec}$$

Case-II @ $V_o = 32$ fps; $g = 10$ 'g';

$$T = 156.024 \text{ msec}$$

List of the pulses to be used in the simulations to analyze the kinematic and dynamic effect in the dummy are given in Table 7b-10.

Table 7b-10.
Pulse Summary

Pulse	Pulse Duration (msec)	Delta V (ft/sec)
10 'g' Triangular	200	32
40 'g' Triangular	50	32
10 'g' Haver-Sine	200	32
40 'g' Haver-Sine	50	32
10 'g' Half-Sine	156.024	32
40 'g' Half-Sine	39.006	32

Simulation Set-up

Frontal impact scenario was modeled with a hybrid III 50th percentile dummy, weighing 172.5 lbs (78.4 Kgs). The seat system was accelerated with the desired pulse in the negative Gx direction (picked from Table 7b-10). The 5-point restraint system was designed in HyperMesh, and the mesh seed size was 13mm in the finite element model. The shoulder harness anchorage angle was zero degrees, the lap belt anchorage angle was 50 degrees and the tiedown belt anchorage angle was 60 degrees, all of them with the horizontal. The shoulder belt anchorage width was 5.2 inches and the lap belt anchorage width was 19 inches. Figure 7b-3 shows the set-up in isometric, top and side details.

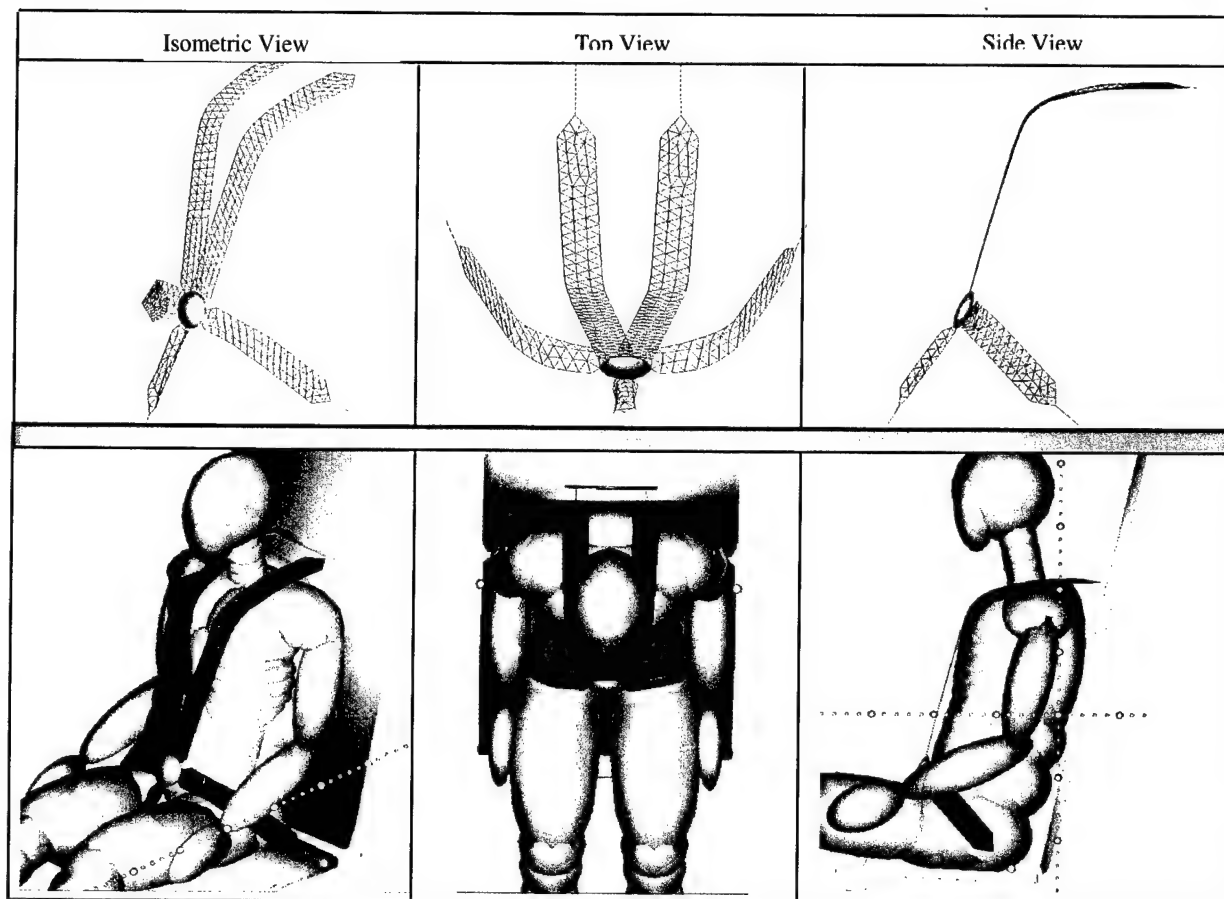


Figure 7b-3. Isometric, top and side view of the restraint system & restrained dummy.

Table 7b-11 gives the specifications of the individual finite element belts and the respective slacks.

Table 7b-11.
Finite Element Belt Specifications

Parameter	Specification
Shoulder Belt (2)	2" width; 0.043" thick 25.89" length
Lap Belt (2)	2" width; 0.043" thick 15.16" length
Tie-Down (1)	1.75" width; 0.043" thick 7.3" length
Material	Polyester Elongation 7.5% @ 4000 lbs
Slack	Shoulder Belt 1" Lap Belt None Tie-Down None

In order to study the effects of the pulse in totality, each pulse condition was simulated for longer time duration than the actual pulse duration. As a thumb rule, all the simulations were run for more than 4 times the pulse duration. The finite element time-step after synchronization with multi-body time step became 5.0E-07, so the simulation took 38 minutes for every 100ms run.

Output Parameters

To compare the effect of different pulses on the kinematics and dynamics of the dummy, output parameters were declared in the input deck of the Madymo program. A detailed list of the desired output is presented below in Table 7b-12.

Table 7b-12.

List of parameters declared in the input deck of Madymo for analysis

Body Part / Restraint	Output
Head	<input type="checkbox"/> Head Acceleration - X direction <input type="checkbox"/> Head Acceleration - Z direction <input type="checkbox"/> Head Acceleration - Resultant <input type="checkbox"/> Head C.G Velocity – Resultant <input type="checkbox"/> Head C.G Impact Force – Resultant <input type="checkbox"/> Head Excursion
Upper Torso	<input type="checkbox"/> Upper Torso Acceleration - X direction <input type="checkbox"/> Upper Torso Acceleration – Z direction <input type="checkbox"/> Upper Torso Acceleration – Resultant <input type="checkbox"/> Upper Torso Excursion
Lower Torso	<input type="checkbox"/> Lower Torso Acceleration - X direction <input type="checkbox"/> Lower Torso Acceleration – Z direction <input type="checkbox"/> Lower Torso Acceleration – Resultant <input type="checkbox"/> Lower Torso Excursion
Restraint	<input type="checkbox"/> Shoulder Belt Load - Resultant <input type="checkbox"/> Lap Belt Load - Resultant <input type="checkbox"/> Tie Down Belt Load – Resultant

Analysis and Discussion

In this section three comparisons shall be made to identify the true nature of the pulses.

Comparison - 40'g' triangular, haver-sine, half-sine pulses

It is clearly evident that an increase in velocity when a constant 'g' level is maintained increases the dynamic overshoot & flail in the body parts and load in the seat belts. This is as it should be, since there is more energy in the moving body to be dissipated and thus the load and the stretch must necessarily increase to accommodate it. As expected, the trends followed by all the pulses are the same. All the pulses lead to the same peak acceleration levels, belt loads and excursion. Kinematics of the dummy and the belt loads due to triangular & haver-sine pulses are

almost in-phase with each other during the onset (triangular lags behind haver-sine during the rearward motion at a much later stage by about 3msec). The mutual overlap is seen in every parameter compared. The kinematics of dummy due to half-sine pulse are slightly different. The time, at which the peak occurs, is 5 msec early than the other two pulse cases. The reason for this could be the high onset rate of the half-sine pulse as compared to others. The acceleration graphs show a sharp peak at around 250msec in every pulse. This is due to the head strike with the headrest. In the case of half-sine pulse, the head hits first and with maximum force, then comes the haver-sine and triangular in sequence with a gap of 5 msec and 3 msec from each other. Although the pulses are of equal energy level, the head undergoes more excursions in case of half-sine pulse. Similar trends are observed in the upper torso accelerations, lower torso accelerations and belt loads.

Comparison - 10'g' triangular, haver-sine, half-sine pulses

The difference in the results of the three pulses is more prominent in the case of 10'g' comparison. The peak value and its timing trends follow the same path as in the previous comparison. Half-sine leads both the pulses all the time, and results in maximum magnitude for all the accelerations and loads. Triangular leads (nominally) haver-sine during the onset till about half the pulse duration by about 5 msec and is then left behind (the gap broadens to 10msec at later stages). The half-sine leads triangular in onset by about 10msec initially during the onset, but this gap increases to about 20 msec during the final stages.

Comparison - 40'g' and 10'g' for all the pulse shapes

The pulses have same ΔV but the peak 'g' and the pulse duration are totally different. The kinematics of the dummy largely depend upon the onset rate. The load level of the seat belts and the dummy kinematics is generally proportionate to the 'g' level if the time base remains nearly constant. Figure 7b-4 shows the three pulse shapes at 10'g' and 40'g' intensity, but same ΔV .

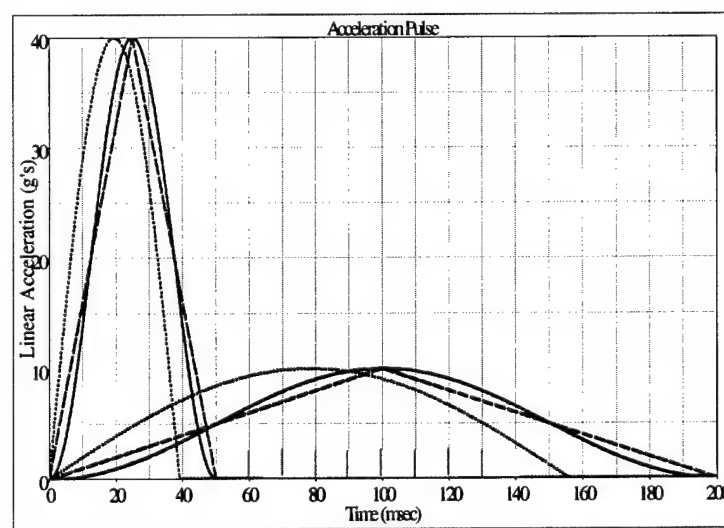


Figure 7b-4. Pulse shapes with same ΔV but different peak 'g'.

In the case of the 40'g' pulses, the onset rate is higher and hence the onset of the kinematics is also quicker. Also, the magnitude of the accelerations and the belt loads is much higher in the case of 40'g' pulse interaction. The interesting point to be noticed was that the dynamic overshoot for 40'g' pulse interaction was around 1.4 (head/upper torso) and for 10'g' interaction, it was 1.7 (head/upper torso). While integrating the shoulder belt load results for the two cases, it was found that energy transferred to the system was almost the same. The results for all the three shapes were plotted and then analyzed, but there is not much difference in the comparison results between the three shapes. The results should not be compared with the test results of sled runs. The conditions of the simulation may not mimic the sled conditions.

Conclusion

We can conclude that for a particular energy level, higher peak'g' (40'g') pulse result is less deviation in the occupant kinematics as compared to lower peak'g' (10'g'). The triangular and haversine pulse conditions tend to move towards in-phase conditions, as the peak'g' increases. Testing the output results using simulation helped in figuring out redundancy encountered with the use of triangular and haversine pulse at higher'g' levels. There is a definite difference seen in the half sine pulse effects because it delivers the same amount of energy in less amount of time. This is due to the steep onset rate for the half-sine pulse. This makes the pulse more severe and at the same time is achievable and repeatable. To model simulations, using a half-sine pulse is advantageous, since it delivers the energy in less amount of time. This helps in cutting down the computational costs. In order to determine the effect of onset of 'g', it is necessary to skew the half-sine pulse changing the point at which the pulse reached the peak.

This work is described in report 3 in preparation for USAARL technical report.

TEST PROTOCOL

Objective

1. Validate standard crash pulse (Figure 7b-5) – The physics based computational modeling software Mathematical Dynamic Modeling (MADYMO) was previously selected and acquired for modeling various restraint systems and crash pulse parameters. Models of a standard seat structure, 5-point restraint harness configuration and mid-size occupant have been developed. These models were exercised in the dynamic environment (series of dynamic input pulses) to predict live system performance. The model was used to evaluate different crash pulse parameters (pulse shape, magnitude, time duration, direction) based on occupant response. A single pulse has been selected for 3 impact directions. Results of the biodynamic simulations will be compared against measured dynamic test performance. This will be a validation effort of the numerical model. The model will then be adapted to different platforms that could best utilize the different innovative restraint technologies to determine if further system utilization studies are warranted.

2. Evaluate restraints' performance (Table 7b-14) – A list of innovative restraint technologies have been acquired through prior Commerce Business Daily (CBD) solicitation. The kinematic and dynamic response of an anthropomorphic test device (ATD) to standard crash pulses when restrained in these pre-selected active and passive restraints will be studied and compared.

Approach

U.S. Army Aeromedical Research Laboratory (USAARL) has planned dynamic sled tests using the Civil Aerospace Medical Institute's (CAMI) horizontal accelerator facility at Oklahoma City, Oklahoma. Restraint systems identified through the CBD announcement have been procured for this evaluation. Additionally, restraint systems typically installed in army aircraft have also been procured to establish baseline performance levels. The research involves study of kinematics and potential injury threats to the occupant in crash accidents. A 50th percentile male hybrid III ATD will be used to collect inertia load and response data. Documented response shall include 3-D motion (head, extremities, upper and lower torso), head accelerations, neck forces and moments, thoracic and seat acceleration and sled pulse.

The input pulse characteristics have been selected on the basis of results obtained from biodynamic simulations carried out for a range of deceleration input pulses using physics based software MADYMO. The pulse characteristics have been selected for maximum dummy flail, but also making sure that decelerative forces are not destructive to the instrumentation or the test hardware.

Test Equipment Description

Seat System

The CAMI seat is a rigid test fixture with seat pan and seat back angles similar to the seats used in rotary wing aircraft. The seat system is used to imitate the seating position of aviators. The seat is comprised of an aluminum seat pan and seat back with restraint system attachment points. Some seat modifications may be required to adapt the test restraint hardware.

Anthropometric Test Device

The USAARL modified Hybrid III ATD (representing the 50th percentile male) will be used for all tests. The modifications consist of an articulated spine, which allows the shoulders to twist about the spinal axis and an internal (self-contained) data acquisition system. For these tests, electrical power will be provided to manikin's instrumentation by an external battery source through an umbilical cable. Data will be downloaded after each test into a laptop computer for storage. The manikin provides the capability to record 32 data channels, of which 30 are instrumented (Table 7b-13).

Table 7b-13.
ATD Instrumentation

Position	Measurement	Axes	Filter CFC*	Channels
Head	Acceleration	X/Y/Z	1000	3
Head	Angular Velocity	Y	600	1
Upper Neck (C1)	Force	X/Y/Z	1000	3
Upper Neck (C1)	Moment	X/Y	600	2
Lower Neck (C7/T1)	Force	X/Y/Z	1000	3
Lower Neck (C7/T1)	Moment	X/Y/Z	600	3
Lower Neck (C7/T1)	Acceleration	X/Y/Z	1000	3
Upper Torso at Sternum	Acceleration	X/Y/Z	1000	3
Lumbar at L5	Force	X/Y/Z	1000	3
Lumbar at L5	Moment	X/Y/Z	1000	3
Lower Torso	Acceleration	X/Y/Z	1000	3
Sled	Acceleration	X	60	1
Total Channels				31

* SAE J211-1 recommendation

The ATD will be dressed only in tight fitting, low friction material. In tests with a Gx (frontal) orientation, the feet of the ATD will be tied down and a supplementary tether will be used to restrain the ATD in case of restraint system failure. In order to evaluate the performance of restraint system, paraphernalia similar to seat cushion and protective clothing gear shall not be used. This is done to eliminate any factor that might add resistance due to friction and interference to the test. The ATD won't be wearing any helmet or any other head mounted device.

Restraint System

A detailed list of restraint systems to be evaluated during this study is given in Table 7b-14. All the restraints and the related hardware/gas generators shall be furnished by USAARL.

Table 7b-14.
List of Restraint Systems to be tested at CAMI horizontal accelerator

Serial #	Restraint System	Test Runs (Days)
1	UH-1 Pilot Safety Restraint Harness	03
2	UH-1 Pilot Safety Restraint Harness with HANS	03
3	UH-1 Pilot Safety Restraint Harness (Modified)	03
4	Inflatabelt	03
5	Co-Axial Restraint	03
6	Smartbelt	03
7	5-way Bolt-in Individual Harness, Latch type buckle	03
8	5-way Bolt-in Y Harness, Latch type buckle	03
9	5-way Wrap-around Individual Harness, Latch type buckle	03
10	5-way Wrap-around Y Harness, Latch type buckle	03
11	Aviation Inflatable Restraint	03
12	Koch & Sons	03
13	HUMMWV 4-Point Restraint	03
14	UH-60 Pilot Safety Restraint Harness	03
15	UH-60 Pilot Safety Restraint Harness with HANS	03*
16	Helo Crew seat Restraint Upgrade Harness	03*
Total Runs		48

* Restraint to be reused for the 3rd test

Slippage of the restraint adjusters will be measured after each test (objective determination by tracking a mark on the restraint before and after the test). No inertial reels will be used in the tests. In passive restraint systems, crash sensors would be placed at suitable locations on the sled, representative of actual locations in aircraft/automobile. This positioning is critical as it plays an important role in triggering the restraint system into action.

Input Pulse

The tests to be conducted are divided into three groups, depending upon the impact orientation. All tests shall be conducted at the CAMI horizontal sled facility with the USAARL provided ATD. Calibration of the CAMI acceleration pulse signature shall be performed prior to conducting the dynamic tests. During calibration, dead weight will be installed on the sled to simulate the weight of the test articles. The ATD instrumentation shall be verified for conformance according to the J211 convention, before the sled runs are conducted. Calibration pulses should have G-onset similar to the desired pulse. Tests will be conducted to simulate a pure horizontal, 30 degrees pitch down and lateral crash scenario (Figure 7b-5).

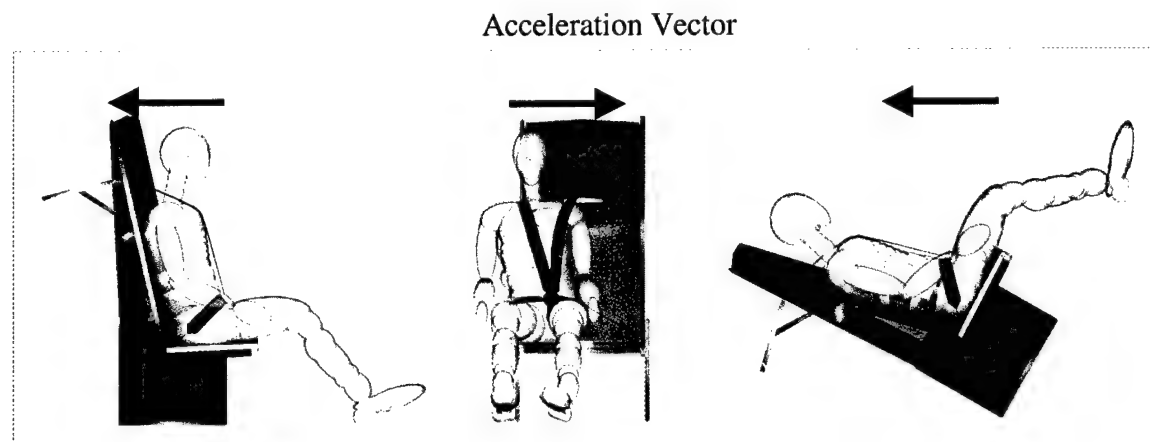


Figure 7b-5. Horizontal, Lateral and 30 degree Pitch down orientations.

The required crash pulse shall be a half-sine shape with a peak of 20 'g' with a resulting velocity change of 42 ft/sec, with onset rate adjusted so as the peak occurs at 50 milliseconds. Figure 7b-6 shows the crash pulse corridor for the sled deceleration pulse. A severe crash pulse cannot be used because of the absence energy attenuators on the seat and also because of the rigid contact surfaces.

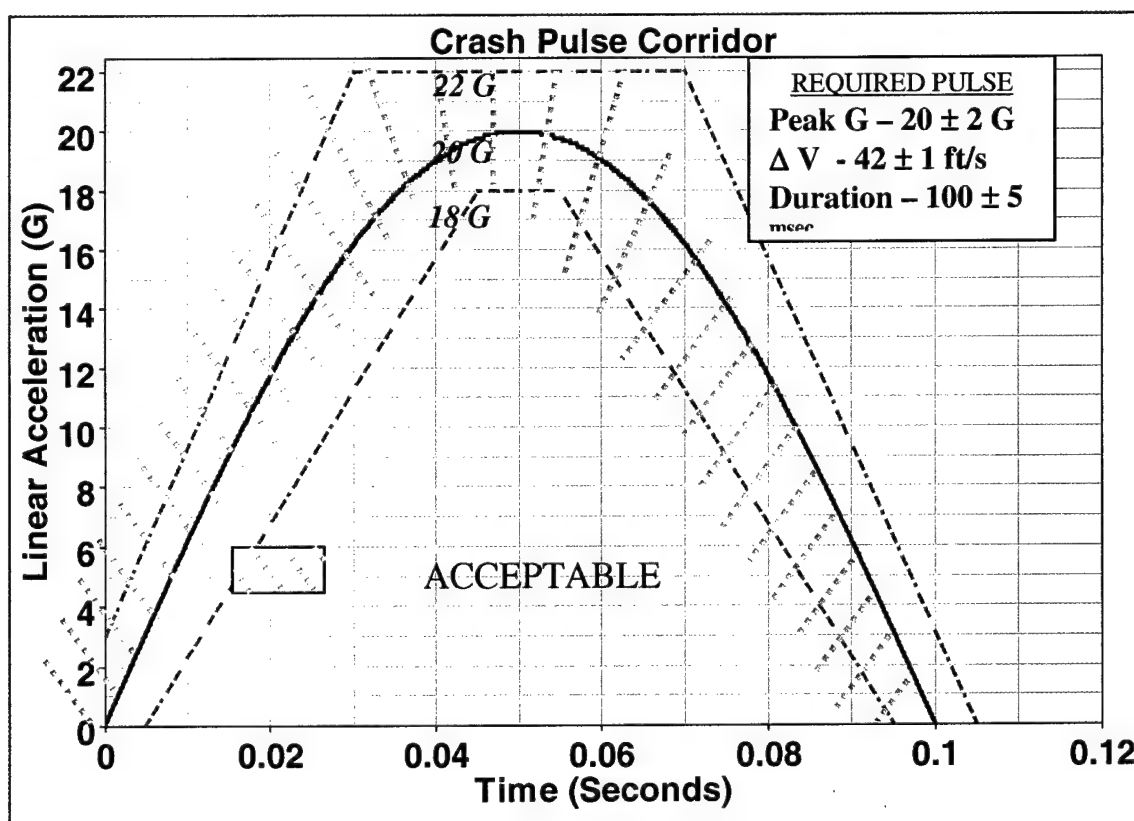


Figure 7b-6. Crash Pulse Corridor (Half-Sine).

Test Procedure

Before conducting a test, proper documentation of the restraint to be tested, seat orientation and the decelerative input pulse will be carried out. The calibration of the input pulse will be confirmed before the run. The restraint will be inspected for any damage or abrasion. The dummy orientation and the seating position will be documented in the measurement chart. The following procedure will be adequate for the initial positioning of the dummy.

1. The ATD will be placed in the center of the seat in as nearly symmetrical position as possible.
2. The ATD back will be against the seat back without clearance.
3. The ATD knees will be separated by 4 inches (inside edge to inside edge).
4. The ATD hands will be placed on the top of the legs, just behind the knees.
5. The ATD feet will be placed flat on the floor, and also such that the centerlines of the lower legs are approximately parallel.
6. The ATD feet will be tied down to the seat floor and a tether will be tied around the lower torso of ATD to the seat back (with sufficient slack so as it doesn't interfere with the forward excursion of ATD).

The optical targets will be put at respective locations (head, shoulder and pelvis), the slack in the belts will be measured and recorded, the electric sensors and the gas generators (in the case of airbag technology) will be placed in the correct location and orientation (as prescribed by the manufacturer) and all the wiring will be checked.

After the preliminary check, the Data Acquisition System (DAS) will be armed (make sure the battery pack is charged). Dummy, restraint and seat will not be disturbed once the DAS is armed. It will be made sure at this point that the LAN is disconnected from the dummy to the computer. Digital camera will be used to take pictures from side, front and oblique (isometric) directions. The distance of the camera lens to the sled will also be recorded.

The high-speed camera lights will be turned ON and the test will be run as the high-speed camera records the event. Test checklist will be used to conduct the tests, for consistency. All the restraints listed in Table 7b-14 will be tested and evaluated at the defined sled pulse. An equal amount of pretension/slack will be introduced in the restraints before the test run (pulling on to the shoulder harness with 1 inch dowels underneath and then taking the dowels out), and the decision for the same will be made at the test site.

Data Collection Requirements

To perform post data analysis, the event has to be documented. There would be three methods in which this documentation will be done.

Data acquisition system

The system has 32 channels that are used to record the events. For uniformity in test conditions, these channels need to be calibrated through software called 'Nanodas' before the

test. A variation in the recording time can be achieved through different combinations of sample rate and number of samples per channel. To prevent false triggering of this system, a back-up trigger option would also be set up. This DAS powered by battery pack is armed to acquire data during the crash event.

After the test, the digital data of the event acquired by DAS will be transferred to a computer. This transfer is facilitated by 'Nanodas'. An interpretation of the recorded data will also be available through the use of graphical option in the software.

In addition to the data acquired from the ATD instrumentation (Table 7b-13), there would be output from the load cells in the harness (belt forces) and the sled acceleration. The CAMI personnel would facilitate this, and the digital data would be given to USAARL on a disc.

High Speed Video Coverage

High-speed digital imaging system recording at 1000 images per second will be used to record the ATD flail in the simulated crash event. Reflective targets shall be placed at desired visible regions (head, upper & lower neck, shoulder, upper extremities and lower torso) to track the excursions. Views from the side, top and oblique would be taken to study the excursions of head, extremities, upper and lower torso.

Still Photo documentation

Still pre- and post- test digital photographic coverage shall be provided as necessary during this test series. A minimum of four pre-test and four post-test still photographs (side, front, top and oblique) will be required for each test. The camera locations and settings shall be standardized to aid in pre- and post- test image analysis (will be done at site).

Data Analysis

All electronic instrumentation data will be filtered in accordance with the Society of Automotive Engineers (SAE) standard J211. Table 7b-15 gives a list of kinematic and dynamic parameters that will be recorded and compared with MADYMO simulation results for validation purposes.

Table 7b-15.
List of performance evaluation parameters

Excursion	Angular Velocity	Linear Acceleration	Forces	Constraint Loads	Injury* Parameters
Head Upper Torso Lower Torso	Head (Y)	Head Upper Torso Lower Torso Seat System	Shoulder Belts Lap Belts T-D Belt	Lower lumbar Lower Neck F/M Upper Neck F/M	Nij TIC Restraint Quotient Torso Angle

* A detailed explanation of each parameter is given in Attachment A

Restraint performance criteria will involve two types of information, one dealing with motion sequence and velocity criteria, and the other, occupant injury assessment. The following requirements will be considered important to the overall quality of occupant restraint:

1. Match the acceleration imposed on the occupant by the restraint system with that of the sled in all crash modes.
2. Begin occupant (torso) deceleration with the smallest possible time delay.
3. Control the kinematics of the occupant.
4. Distribute loads over the body to optimize tolerance.

The requirements represent a complicated and inter-related set of responses that need to be balanced systematically to ensure "overall" occupant restraint in a crash and minimize injury risks in critical body regions. The relative velocity of the occupant with respect to the sled, kinetic energy developed, and the forward displacement and posture of the occupant will be evaluated in terms of potential injuries in a crash. Primarily, study will be done on the occupant kinematic output to study the occupant flail, restraint quotient and torso angle for restraint performance evaluation.

- Occupant flail data shall be extracted from the high-speed video output. TEMA version 2.1 will be used to do the motion analysis. Position versus time for the reflective targets (head, upper & lower neck, shoulder and lower torso) shall be generated for comparative study.
- Restraint Quotient (RQ): It is defined as "A ratio of relative velocity of an occupant on sled at a given instant to the overall change of sled velocity".

$$RQ \text{ (chest/pelvis)} = \frac{\text{Relative velocity of the occupant (chest/pelvis)}}{\text{Overall change of sled}}$$

$$\text{Range: } 0 < RQ < 1$$

RQ is calculated for chest and the pelvis region. Owing to the presence of shoulder and lap belts in respective regions, loading conditions are accounted in these areas.

There exist 3 basic conditions for the RQ:

Condition I: $RQ = 0$	Condition II: $0 < RQ < 1$	Condition III: $RQ \geq 1$
Occupant does not move with respect to sled Relative velocity of occupant with sled equals zero	Occupant moves with respect to sled Relative velocity of occupant with respect to sled exists	Occupant moves with respect to sled Relative velocity equals for occupant and sled
Conclusion: Restraint system is able to totally restrict the forward motion of the occupant	Conclusion: Restraint system shows ability to restrict the forward motion of the occupant Note: Lower RQ is better	Conclusion: Restraint system shows total inability to restrict the forward motion of the occupant

The upper torso and pelvis velocities will be calculated by integrating the filtered acceleration output (CFC 1000) from the upper torso and pelvis accelerometers respectively. The absolute velocities of the upper and lower torso will then be converted to relative velocities (w.r.t sled) by subtracting the sled velocity at each instant. For that the filtered sled acceleration (CFC 60) shall also be integrated to obtain sled velocity data.

- Torso Angle - Torso angle variable helps us to understand the extent to which the upper torso undergoes rotation with respect to the horizontal position.

Ideally the vertical position is regarded as the most optimum position for maximum load bearing. But the probability of being in this position during the crash is very less. So to determine the extent to which the upper torso undergoes rotation in the forward direction, we will account for this variable. The less the rotation from the vertical position, the better is the performance of the restraint system.

- Injury Assessment - Comparison of the dummy Nij values, chest acceleration and compression for different restraints shall be a factor for a better assessment of the restraints.

Organizational Responsibilities

Horizontal Accelerator Personnel Responsibilities

- i. Provide personnel, material and equipment to accomplish the testing described herein.
- ii. Review test schedule.
- iii. Install rigid crashworthy seat to the horizontal accelerator test fixture.
- iv. Provide instrumented ATD(s) in accordance with this test plan.
- v. Provide photographic and video coverage as specified in this test plan.
- vi. Provide a disk of data at the completion of each test day.
- vii. Provide static and dynamic calibration data to project engineer.

Project engineer responsibilities (USAARL)

- i. Provide a test plan.
- ii. Provide anthropometric test device (ATD).
- iii. Provide all restraints, adjusters, sensors, triggering mechanisms and inflators
- iv. Dress, position and adjust ATD.
- v. Participate in and monitor all tests to ensure the test procedures and test results are in accordance with the program objectives.

The information has been procured from the original test protocol prepared to test the hardware procured under the advertisement given in commerce business daily.

BIBLIOGRAPHY AND REFERENCES

Randhawa, H., April 2002 Occupant and Restraint System Modeling, UES Inc. Presentation - AIBS Review of USAARL's Biodynamic Research Program: Fort Rucker, AL: U.S. Army Aeromedical Research Laboratory.

Randhawa, H., Mane, Ketan, 2001 Selection Criteria for Injury Assessment Reference Values (In preparation for USAARL technical report).

Randhawa, H., 2001 Mesh Density Optimization for a standard 5-point restraint using finite element techniques in Madymo (In preparation for USAARL technical report).

Randhawa, H., 2002 Selection of Pulse Shape for Dynamic Crash Simulations in Madymo. (In preparation for USAARL technical report).

Randhawa, H., 2002 Test Protocol for Dynamic Sled Testing at CAMI (In preparation for USAARL technical report/protocol).

Bibliography of Published Reports

Alem, Nabih M., Mobasher, Amir A. Brozoski, Frederick T., Beale David G. (1998) Simulations of Head Strikes in Helicopters and the Roles of Restraints, Seat Stroke and Airbags on Their Reduction, Fort Rucker, AL: USAARL Report No. 98-11.

Alem, Nabih, M. Mobasher, A. Amir, F.T. Brozoski, D.G. Beale (1998). Simulations of Head Strikes in Helicopters and the Roles of Restraints, Seat Stroke and Airbags on Their Reduction. Presented at the 1997 AGARD AMP Specialist's Meeting on Impact Head Injury: Responses, Mechanisms, Tolerance, Treatment and Countermeasures; Mescalero, MN, 1997.

Barazanji, K., Alem, N. 2000 Effects of head-supported devices on female aviators during simulated helicopter rides Part 1: Biomechanical response. USAARL Report No. 2000-16.

Beasley, J. H., Martin, J. S., Klymenko, V., Harding, T. H., Verona, R.W., and Rash, C. E. 1995. A characterization of low luminance static and dynamic modulation transfer function curves for P-1, P-43, and P-53 phosphors. USAARL Report No. 95-29.

Brozoski, T., (1999) Mass and Location of Head-Supported Devices Using Articulated Total Body Simulations, UES Inc.; prepared for Aircrew Protection Division, USAARL under Contract Number: DAMD17-95-C-5095 and presented at the 1998 RTO Human Factors and Medicine Panel (HFM) Symposium, San Diego, USA.

Comperatore, C.A., H. Liberman, A.W. Kirby, B. Adams, and J.S. Crowley. 1996. Melatonin Efficacy in Aviation Missions Requiring Rapid Deployment and Night Operations (Reprint). USAARL Report 97-3.

Harding, H.T., Beasley H.H., Martin, J.S., and Rash, C.E. 1995. Physical evaluation of the Honeywell brass board hardware for the miniature flat panel display for aviation program. *USAARL Lab Report LR95-1-2-1.*

Harding, H.T., Beasley H.H., Martin, J.S., Rash, C.E., 1995. Physical evaluation of integrated helmet and display sighting system (IHADSS) Helmet Display Unit. *USAARL Lab Report 95-32.*

Harding, T. H., Martin, J. S., Beasley, H. H., Rash, C. E. 1996. Figures of merit and performance specifications for the IHADSS and ANVIS. Fort Rucker, AL: U.S. Army Aeromedical Research Laboratory. USAARL Report No. 96-13.

Harding, T. H., Martin, J. S., Beasley, H. H., Rash, C. E., Garrard, J. A. 1996. A survey of flat panel display technologies. Fort Rucker, AL: U.S. Army Aeromedical Research Laboratory. USAARL Report No. 96-19.

Harding, T. H., Martin, J. S., Beasley, H. H., Rash, C. E. 1997. A visual evaluation near the threshold of acuity of five color liquid-crystal flat-Dane1 dismays. Fort Rucker, AL: U.S. Army Aeromedical Research Laboratory. USAARL Report No. 97-29.

Harding, T. H., Beasley, H. H., Martin, J. S., Rash, C. E., McLean, W. E., Mora, J. C., McEntire, B. J., 1998. Optical and biodynamic evaluation of the helmet mounted integrated display sight system (HIDSS) for the RAH-66 Comanche development and validation program phase. Fort Rucker, AL: U.S. Army Aeromedical Research Laboratory. USAARL Report No. 98-22.

Harding, T. H., Martin, J. S., Beasley, H. H., Rash, C. E. 2000. Final Phase One Evaluation of the Microvision, Inc. Aircrew Integrated Helmet System (AIHS) HGU-56P Scanning Laser Display. USAARL Report No. 2001-06.

Harding, T.H., H.H. Beasley, J.S. Martin, and C.E. Rash, 2001. Evaluation of spatial resolution in the Phase II Microvision, Inc. Aircrew Integrated Helmet System HGU-56/P scanning laser display. USAARL Lab Report 2002-01.

Harding, T.H., H.H. Beasley, J.S. Martin, and C.E. Rash, 2002. Evaluation of Pinch Correction in the Phase 2 Microvision, Inc. Aircrew Integrated Helmet System HGU-56/P Scanning Laser Display. USAARL Lab Report 2002-13.

Harding, T.H., V. Klymenko, J.S. Martin and C.E. Rash, 2002. An operational helmet-mounted display model: prediction of visible grayshades and see-through spectral data. *Proceedings of the SPIE, In the press.*

Hsieh, S-J, C.E. Rash, T.H. Harding, H.H. Beasley, J.S. Martin, 1999. Preliminary design of an image quality tester for helmet mounted displays. *USAARL Lab Report* 2000-08.

Hsieh, S-J, C.E. Rash and T.H. Harding, 2001. Design of an image quality tester. *Helmet and Head-Mounted Displays VI*, Lewandowski, Haworth, Girolamo, Rash, Editors. *Proceedings of the SPIE*, 4361, 205 – 212.

Hsieh, S-J, C.E. Rash and T.H. Harding, 2001. Design of an image quality tester. *Helmet and Head-Mounted Displays VI*, Lewandowski, Haworth, Girolamo, Rash, Editors. *Proceedings of the SPIE*, 4361, 205 – 212.

Hsieh, S-J, C.E. Rash, J.C. Mora, T.H. Harding, H.H. Beasley, and J.S. Martin, 2000. Design of Interface and Algorithms for an Image Quality Tester. USAARL Lab Report 2000-26.

Kirby, A.W., C.A. Comperatore, S. Arroya, M. Clayton, C. Ferry, K. Bleser, H. Davis, and R. Beck. 1996. Bedtime Administration of Melatonin to Healthy Females Does Not Alter Menstrual Characteristics. USAARL Lab Report 97-4.

Kirby, A.W. C.A. Comperatore, M. Clayton, P. Rivera, S. Arroya, R. Strickland, N. Garner, R. Bay-Wright, K. Bleser, M. Brock, M. Ledford, D. Wright, C. Ferry, and L. Hein. 1998. The effects of melatonin on menstrual characteristics, prolactin and premenstrual syndrome-like symptoms during a simulated eastward deployment. USAARL Report 98-30.

Kirby, A.W. C.A. Comperatore, M. Clayton, P. Rivera, S. Arroya, R. Bay-Wright, R. Strickland, K. Bleser, M. Brock. Exogenous melatonin: its relationship to prolactin and its efficacy at reducing stress. USAARL Lab Report No. 98-36.

Klymenko, V., T.H. Harding, J.S. Martin, H.H. Beasley and C.E. Rash, 1997. Image quality figures of merit for contrast in CRT and flat panel displays. *USAARL Lab Report* 97-17.

Kymenko, V., T.H. Harding, and C.E. Rash, 1998. Are New Image Quality Figures of Merit Needed for Flat Panel Displays? *USAARL Lab Report* 98-31.

Kymenko, V., T.H. Harding, H.H. Beasley, and C.E. Rash, 1999. The effect of helmet mounted display field-of-view configurations on target acquisitions. USAARL Lab Report 99-19.

Klymenko, V., T.H. Harding, H.H. Beasley, and C.E. Rash, 2001. Visual search performance in HMDs with partial overlapped binocular fields-of-view. USAARL Lab Report 2001-05.

Licina, J., Barazanji, K., Hall, B., Lesniak, J., Murphree, B., (2000). Test and Evaluation Report of the Physio-Control 10-59 Defibrillator/Monitor/Pacemaker Part A: Laboratory Testing. USAARL Report No. 2000-28.

Licina, J., Barazanji, K., Hall, B., Lesniak, J., Murphree, B., (2000). Test and Evaluation Report of the Physio-Control 10-59 Defibrillator/Monitor/Pacemaker Part A: Laboratory Testing. USAARL Report No. 2000-28.

Licina, J.R., Albano, J.P., Reynolds, W.R., Murphree, K.B., Hall, B.D. (1998). Rotary-Wing Airworthiness Certification Evaluation Findings for the Impact Portable Suction System Model 326/326M. USAARL Report No. 98-06.

Licina, J.R., Albano, J.P., Reynolds, W.R., Murphree, K.B., Hall, B.D. (1998). Rotary-Wing Airworthiness Certification Evaluation Findings for the Ivac Medsystem III Infusion Pump Model 2863B. USAARL Report No. 98-07.

Mobasher, Amir A., Brozoski, Frederick T., McEntire, Joseph, Alem, Nabih M., (1998) Effects of Seat Stroke Distance on the Allowable Mass of Head Supported Devices, Fort Rucker, AL: U.S. Army Aeromedical Research Laboratory. USAARL Report No. 98-26.

Mobasher, Amir A., Brozoski, Frederick T., McEntire, Joseph, Alem, Nabih M., (1997) Automation of ATB simulations and analysis to determine head supported CM criteria: UES Inc. and U.S. Army AeroMedical Research Laboratory, Fort Rucker. Presented at 1997 ATB User's Group Conference.

Quattlebaum, M., Licina, J.R. (1996). Test and Evaluation Report of the Omni-Vent Ventilator Model Series D/mri. USAARL Report No. 96-08.

Quattlebaum, M., Licina, J.R. (1996). Test and Evaluation Report of the Impact Ventilator Uni-Vent Model 780. USAARL Report No. 96-10.

Quattlebaum, M., Licina, J.R. (1996). Test and Evaluation Report of the PneuPAC® Ventilator Model PortPAC. USAARL Report No. 96-12.

Randhawa, H., April 2002 Occupant and Restraint System Modeling, UES Inc. Presentation - AIBS Review of USAARL's Biodynamic Research Program: Fort Rucker, AL: U.S. Army Aeromedical Research Laboratory.

Randhawa, H., Mane, Ketan 2001 Selection Criteria for Injury Assessment Reference Values (In preparation for USAARL technical report)

Randhawa, H., 2001 Mesh Density Optimization for a standard 5-point restraint using finite element techniques in Madymo (In preparation for USAARL technical report).

Randhawa, H., 2002 Selection of Pulse Shape for Dynamic Crash Simulations in Madymo. (In preparation for USAARL technical report).

Randhawa, H., 2002 Test Protocol for Dynamic Sled Testing at CAMI (In preparation for USAARL technical report/protocol).

Rash, C. E., Beasley, H. H., Martin, J. S., and Harding, T. H., 1999. Alternate source evaluation for the aircrew integrated helmet system Comanche compatibility program phase IIB. Fort Rucker, AL: U.S. Army Aeromedical Research Laboratory. USAARL Report No. 99-06.

Rash, C. E., Harding, T. H., Martin, J. S., and Beasley, H. H., 1999. Concept phase evaluation of the Microvision, Inc., aircrew integrated helmet system HGU-56P virtual retinal display. Fort Rucker, AL: U.S. Army Aeromedical Research Laboratory. USAARL Report No. 99-18.

Rash, C.E., V. Klymenko, T.H. Harding and J.S. Martin, 2000. Do FPDs need new image-quality metrics?, 2000. *Information Display*, 6/00, 26 - 29.

Rash, C.E., J.S. Martin, H.H. Beasley, and T.H. Harding, 1999. Alternate source evaluation for the aircrew integrated helmet system Comanche compatibility program phase IIB. *USAARL Lab Report* 1999-06.

Rash, C.E. and T.H. Harding, 2002. A proposed laser safety evaluation plan for the Microvision, Inc., scanning laser helmet-mounted display. USAARL Report No. 2003-01.

Rash, C.E. and T.H. Harading, 2002. Power measurements for Microvision, Inc., Aircrew integrated helmet system scanning laser helmet-mounted display. USAARL Report No. 2003-03.